THE UNIVERSITY OF QUEENSLAND

AUSTRALIA

Equiatomic and non-equiatomic Ti-Zr-Nb-Ta refractory medium entropy alloys

Van Thuong Nguyen

B. Eng., M. Eng.

A thesis submitted for the degree of Doctor of Philosophy at

The University of Queensland in 2019

School of Mechanical and Mining Engineering

Abstract

High entropy alloys have been developed over the last two decades and are most commonly defined as synthesizing from five or more principle elements in which the concentration of each element ranges from 5 at.% to 35 at.%. Yeh [1] classified the metallic alloys world into three groups: high entropy alloys (HEAs), medium entropy alloys (MEAs), and low entropy alloys (common metallic alloys). This novel class of MEAs and HEA metallic materials offer a wide range of new alloy composition as well as promising properties for advanced applications such as jet-engine in aerospace and fusion power reactor components [2, 3]. In this thesis, using the high entropy concepts, both new equiatomic and non-equiatomic Ti-Zr-Nb-Ta MEAs have been designed and fabricated as novel candidate alloys for potential bio-applications as well as for structural applications at room temperature and elevated temperatures. A single phase equiatomic Ti-Zr-Nb-Ta MEA was first designed using the empirical rule, assisted with the CAPHAD approach. The equiatomic Ti-Zr-Nb-Ta MEA was fabricated using the arc-melting method and then the effect of homogenization annealing treatments on its microstructure and mechanical properties at room temperature and elevated temperatures was studied. After that, the alloy composition was tailored to obtain lighter and more affordable non-equiatomic Ti-Zr-Nb-Ta MEAs using the atomic mismatch (δ, %) approach. The microstructure and mechanical properties of these non-equiatomic MEAs were studied from room temperature to 1200 °C. The major developments made in this thesis are summarized below.

A novel quaternary equiatomic Ti-Zr-Nb-Ta (δ = 4.8 %) MEA, was redesigned from a quinary equiatomic Ti-Zr-Nb-Ta-Mo (δ = 5.5 %) HEA, for much improved strength-ductility (tensile) combinations by reducing δ through excluding Mo and for potentially improved biocompatibility.

The effect of heat treatment (at 1200ºC for 8 h and 24 h) on the phase stability, microstructure, and mechanical properties of the equiatomic Ti-Zr-Nb-Ta MEA has been investigated in detail. A cuboid-like nanostructure in the matrix and a lamellar structure at the grain boundary region formed after annealing of 8 or 24 hours at 1200ºC. This nanostructure is responsible for a significant increase in compression yield strength from 1100 ± 90 to 1760 MPa ± 25 compared with its as-cast counterpart.

The microstructure and compression behaviours of the homogenised equiatomic Ti-Zr-Nb-Ta ME were investigated at temperatures from 600ºC to 1200ºC. The yield strength, $\sigma_{0.2}$, of the homogenised MEA halved from ~1760 MPa to ~800 MPa, with increasing deformation temperature from room temperature to 600ºC. However, the alloy still exhibited excellent

softening resistance at 1000ºC and 1200ºC; its yield strength still remained ~410 MPa at 1000ºC and ~210 MPa at 1200ºC.

Four non-equiatomic $Ti_{25+x}Zr_{25}Nb_{25}Ta_{25-x}$ (x = 5, 10, 15, 20, in at. %) MEAs were designed using the atomic mismatch approach. These novel MEAs were derived from the equiatomic Ti-Zr-Nb-Ta MEA by replacing part of the Ta content with Ti. Each non-equiatomic MEA solidified as a single solid-solution phase, and their microstructures were characterized in detail and compared with Pandat^{TM} simulation and the empirical rules. In particular, a brittle-to-ductile transition was observed with decreasing Ta content. As a result, both the as-cast $Ti_{40}Zr_{25}Nb_{25}Ta_{10}$ and $Ti_{45}Zr_{25}Nb_{25}Ta_5$ MEAs exhibited excellent tensile strain to fracture (>18%) and tensile strength (>900 MPa) with much reduced density compared with the low-ductility $Ti_{25}Zr_{25}Nb_{25}Ta_{25}$ MEA. Both MEAs are among a very small number of strong and ductile (tensile strain >15%) alloys which have been reported as MEAs or HEAs so far.

High-temperature annealing (at 1200ºC for 8 h) affects the phase stability, microstructure, and mechanical properties of the non-equiatomic $Ta_{25-x}Zr_{25}Nb_{25}Ti_{25+x}$ (x= 5, 10, 15, 20, at. %) MEAs. After homogenisation at 1200ºC, a nano-cuboidal structure formed in the matrix and a secondary phase precipitated at the grain boundary in $Ta_{20}Zr_{25}Nb_{25}Ti_{30}$ (Ta20-HT) and $Ta_{15}Zr_{25}Nb_{25}Ti_{35}$ (Ta15-HT). In contrast, the homogenized $Ta_{10}Zr_{25}Nb_{25}Ti_{40}$ (Ta10-HT) and $Ta_5Zr_{25}Nb_{25}Ti_{45}$ (Ta5-HT) showed a stable single BCC solid-solution phase up to 1200ºC. Both Ta20-HT and Ta15-HT exhibited high yield strength, but limited ductility at room temperature under compression. In contrast, Ta10-HT and Ta5-HT showed excellent ductility at room temperature under both tension and compression.

The collective results of this thesis provide a detailed understanding of the microstructure and mechanical properties of a new group of equiatomic and non-equiatomic TaZrNbTi refractory MEAs. These new alloys, which consist of biocompatible Ti, Nb, Zr, and Ta as principal constituent elements, exhibit promising mechanical properties for both biomedical applications and structural materials.

Declaration by author

This thesis *is composed of my original work, and contains* no material previously published or written by another person except where due reference has been made in the text. I have clearly stated the contribution by others to jointly-authored works that I have included in my thesis.

I have clearly stated the contribution of others to my thesis as a whole, including statistical assistance, survey design, data analysis, significant technical procedures, professional editorial advice, financial support and any other original research work used or reported in my thesis. The content of my thesis is the result of work I have carried out since the commencement of my higher degree by research candidature and does not include a substantial part of work that has been submitted *to qualify for the award of any* other degree or diploma in any university or other tertiary institution. I have clearly stated which parts of my thesis, if any, have been submitted to qualify for another award.

I acknowledge that an electronic copy of my thesis must be lodged with the University Library and, subject to the policy and procedures of The University of Queensland, the thesis be made available for research and study in accordance with the Copyright Act 1968 unless a period of embargo has been approved by the Dean of the Graduate School.

I acknowledge that copyright of all material contained in my thesis resides with the copyright holder(s) of that material. Where appropriate I have obtained copyright permission from the copyright holder to reproduce material in this thesis and have sought permission from co-authors for any jointly authored works included in the thesis.

Publications during candidature

1. **V.T. Nguyen**, M. Qian, Z. Shi, T. Song, L. Huang, J. Zou, Compositional design of strong and ductile (tensile) Ti-Zr-Nb-Ta medium entropy alloys (MEAs) using the atomic mismatch approach, *Materials Science and Engineering: A* 742 (2019) 762-772.
2. **V.T. Nguyen**, M. Qian, Z. Shi, T. Song, L. Huang, J. Zou, A novel quaternary equiatomic Ti-Zr-Nb-Ta medium entropy alloy (MEA), *Intermetallics* 101 (2018) 39-43.
3. L. Huang, M. Qian, L. Wang, Z. Chen, Z. Shi, **V.T. Nguyen**, J. Zou, High-tensile-strength and ductile novel Ti-Fe-N-B alloys reinforced with TiB nanowires, *Materials Science and Engineering: A*, 2017 (708) 285-290.
4. L. Huang, M. Qian, Z. Liu, **V.T. Nguyen**, L. Yang, L. Wang, J. Zou, Preparation of TiB nanowires in Ti metal matrix composites with a network-woven architecture, *Journal of alloys and compounds*, 2017 (735) 2640-2646.

Publications included in this thesis

1. **V.T. Nguyen**, M. Qian, Z. Shi, T. Song, L. Huang, J. Zou, A novel quaternary equiatomic Ti-Zr-Nb-Ta medium entropy alloy (MEA), *Intermetallics* 101 (2018) 39-43 –Chapter 4

Contributor	Statement of contribution
Van Thuong Nguyen (Candidate)	Conception design (80%) Data analysis and interpretation (75%) Paper writing and editing (60%)
Ma Qian	Conception design (10%) Data analysis and interpretation (10 %) Paper writing and editing (20%)
Zhiming Shi	Data analysis and interpretation (5%)
Tingting Song	Data analysis and interpretation (5%)
Liqing Huang	Data analysis and interpretation (5%)
Jin Zou	Conception and design (10%) Analysis and interpretation (10%) Paper writing and editing (20%)

2. **V.T. Nguyen**, M. Qian, Z. Shi, T. Song, L. Huang, J. Zou, Compositional design of strong and ductile (tensile) Ti-Zr-Nb-Ta medium entropy alloys (MEAs) using the atomic mismatch approach, *Materials Science and Engineering: A* 742 (2019) 762-772. - Chapter 5

Contributor	Statement of contribution
Van Thuong Nguyen (Candidate)	Conception design (80%) Data analysis and interpretation (75%) Paper writing and editing (60%)
Ma Qian	Conception design (10%) Data analysis and interpretation (10 %) Paper writing and editing (20%)
Zhiming Shi	Data analysis and interpretation (5%)
Tingting Song	Data analysis and interpretation (5%)
Liqing Huang	Data analysis and interpretation (5%)
Jin Zou	Conception and design (10%) Analysis and interpretation (10%) Paper writing and editing (20%)

Submitted manuscripts included in this thesis:

1. V. T. Nguyen, M. Qian, Z. Shi, X. Q. Tran, D. D. Qu, J. Joseph, D. M. Fabijanic, S. Matsumura, C. Zhang, F. Zhang, J. Zou, **Effect of tantalum content on the phase stability and mechanical of $Ti_{25+x}Zr_{25}Nb_{25}Ta_{25-x}$ medium entropy alloys (MEAs).**

Contributor	Statement of contribution
Van Thuong Nguyen (Candidate)	Conception design (70%) Data analysis and interpretation (50%) Paper writing and editing (50%)
Ma Qian	Conception design (10%) Data analysis and interpretation (20 %) Paper writing and editing (30%)
Zhiming Shi	Data analysis and interpretation (5%)
X. Q. Tran, S. Matsumura	Data analysis and interpretation (5%)
C. Zhang, F. Zhang	Data analysis and interpretation (5%)
D. D. Qu	Data analysis and interpretation (5%)
J. Joseph	Conception design (5%)
D. M. Fabijanic	Conception design (5%)
Jin Zou	Conception and design (10%) Analysis and interpretation (10%) Paper writing and editing (20%)

Contribution by others to the thesis

No contributions by others

Statement of parts of the thesis submitted to qualify for the award of another degree

No work submitted towards another degree has been included in this thesis

Research Involving Human or Animal Subjects

No animal or human subjects were involved in this research.

Acknowledgements

My greatest appreciation goes to my supervisors, Professor Jin Zou and Professor Ma Qian, for their invaluable advice and knowledge, providing encouragement throughout the research and study. Also I would like to express my gratitude to my co-supervisor, Dr Zhiming Shi, for his guidance and advice throughout the whole time. Without them, this whole research study could never run smoothly.

I would like to thank my Ph.D. candidature development committee: Professor Kuzuhiro Nogita and Dr Michael Bermingham, for giving me very good comments throughout my thesis development.

I acknowledge all the staff of Centre for Microscopy and Microanalysis (CMM) at the University of Queensland for their technical support. I have grasped many useful analysis skills from them. I acknowledge the financial support from the IPRS and UQCent for providing my Ph.D. stipend.

It is highlighted that I cannot complete my task without kindly supports from all of staffs of Mechanical and Mining Engineering Laboratory.

Many thanks to my lovely colleges, Dr Mun Teng Soo, Mr Liqing Huang, Mr Xiaolei Shi, Mr Weidi Liu, Mr Han Gao, Mr Sun Qiang in our research group. Without them, most of the analysis and testing results obtained in this study could never be satisfactory.

My special thanks go to all of my friends at The University of Queensland for their amazing friendship, which made my life in Brisbane unforgettable. Their sharing and supports made our life less difficult and more enjoyable.

Most importantly, not to forget, thanks to my parents Tich Nguyen & Long Nguyen; Thao Hoang & An Truong, my wife Diep Hoang, and my little daughter Mai Phuong Nguyen, for their continuous support, encouragement, and understanding during the period of my study.

Financial support

This work was supported by the Australian Research Council (ARC) through ARC LP130100913 and the Baosteel-Australia Joint Research and Development Centre through BA110014LP.

The author also thanks the International Postgraduate Research *Scholarship* (IPRS) Program and UQCent *Scholarship* for providing him with a PhD scholarship.

Keywords

High entropy alloys, medium entropy alloys, solid solution strengthening, high entropy effect, lattice mismatch/distortion, high temperature compression strength, tensile strength.

Australian and New Zealand Standard Research Classifications (ANZSRC)

ANZSRC code: 091207 Metals and Alloys Materials, 100%

Chapter 1Fields of Research (FoR) Classification

FOR code: 0912, Materials Engineering, 100%

Table of Contents

List of figures

List of tables

List of abbreviations

BCC	Body-centered cubic
BSE	Backscattered electron
EBSD	Electron backscatter diffraction
EDS	Energy dispersive X-ray spectroscopy
FCC	Face-centered cubic
FIB	Focused ion beam
HCP	Hexagonal closed-pack
HEA	High entropy alloys
MEA	Medium entropy alloy
MPEA	Multi-principle element alloys
SEM	Scanning electron microscopy
STEM	Scanning transmission electron microscopy
TEM	Transmission electron microscopy
XRD	X-ray diffraction

Chapter 1 Introduction

1.1 Motivation

Conventional metallic alloys are designed based on one principal element, e.g., Ti, Fe, Al, Mg and so on, whose microstructure and properties are tailored by adding minor alloying elements. Their compositions fall in the regions close to the apexes or edges of their phase diagram. In contrast, a new class of metallic alloys has been developed over the last two decades [4, 5], with the motivation of exploring the central region of the multicomponent alloy phase diagram. These alloys are called high entropy alloys (HEAs), and fabricated from a number of principal elements in equiatomic or near-equiatomic fractions. In that regard, they are also referred to as multi-principal-element alloys (MPEAs). Although HEAs have a complex composition, they have a simple microstructure. For instance, the equiatomic FeCrMnNiCo HEA exhibits a single face-centered cubic (FCC) solid solution phase microstructure [5] and so do other reported HEAs [6-12].

Using the HEA concept, Senkov *et al*. [13, 14] fabricated a range of HEAs made from refractory metals, i.e., Mo, Ta, Nb, W, and V in 2010, and in the following years, the number of newly reported refractory HEAs (RHEAs) increased steadily. This class of materials has shown promising properties for various structural and biomedical applications, e.g., ultrahigh strength [9, 12, 15-18], high softening resistance at elevated temperatures [14, 17, 19-21], and excellent corrosion resistance [22, 23]. However, they have also exhibited low ductility at room temperature (RT) and high density [8, 11, 13]. Therefore, extensive attention was paid to them in two major proposed research directions: (*i*) to reduce the density and simultaneously improve the high temperature softening resistance and RT ductility for industrial processing and mobility applications [15, 17, 24-26], and (*ii*) to investigate their bio-applicable properties because RHEAs normally contain bio-compatible elements, e.g., Ti, Nb, Ta, Zr, and Hf [27, 28]. However, a few issues in developing and investigating this metallic class material can be listed as shown in the next section.

1.2 Problem statement

Of the many RHEAs developed or proposed to date, those that are based on alloying with Ti, Zr, Nb, Ta, and Mo have the potential to be used as novel implant alloys, as well as for other structural applications including at elevated temperatures. However, although the equiatomic TiZrNbTaMo showed a good compressive yield strength, its compressive strain was poor (<5%) at room temperature in both the as-cast and annealed (homogenized) conditions [27, 28].

This low ductility essentially excludes it from most load-bearing applications. In addition, regarding biomaterial applications, the cytotoxicity of metals is related to the ion release from the metals to the human body. The released ion concentration of metals is safe to the human body at certain values, above which the material is not biocompatible for biomedical applications. Y. Li *et al.* [29] reported that Mo displays a much lower safe ion concentration than both Ti and Nb for orthopedic applications. Another concern is that the elastic modulus of Mo is remarkably higher than that of each other elements (Ti, Zr, Nb and Ta) in this HEA. Consequently, the equiatomic Ti-Zr-Nb-Ta-Mo HEA exhibited high modulus [27], which is 5-10 times higher than the modulus of human cortical bones. This can cause a severe "stress shielding effect", where the use of an implant device that has significantly higher elastic modulus than that of the bone could result in bone atrophy and therefore loosening of the implant device, and potential fracture of the bone [30]. These shortcomings make this equiatomic Ti-Zr-Nb-Ta-Mo HEA much less competitive than conventional non-HEAs such as Ti-6Al-4V for orthopedic applications.

RHEAs show high compressive strengths at both room temperature and elevated temperatures. However, their density is high (typically > 9 g/cm^3) and ductility is poor at room temperature. Consequently, significant effort has been made to reduce their density but to simultaneously improve their high temperature softening resistance and RT ductility for industrial processing and broader potential (e.g. mobility) applications [15, 17, 24-26]. In that regard, common alloying elements, e.g., Al, Cr, Si, Co, and Ni, have been introduced to replace the heavier metals, e.g., W, Ta in RHEAs [17, 25, 31-34]. However, it should be pointed out that with or without the reduction in density of RHEAs, the formation of intermetallic compounds always deteriorates the room temperature ductility remarkably.

Generally, HEAs are designed in an equiatomic fraction of at least five principal elements in order to maximize the mixing entropy (ΔS_{mix}, J/K mol), which is believed necessary for the formation of a single solid-solution phase in the resultant alloys under normal solidification conditions [3]. However, such HEAs do not always solidify as a single solid-solution phase [2, 34-36], indicating that it is not always stringently necessary to design HEAs in equiatomic fractions. On the other hand, the composition design of a HEA should also aim to achieve desired mechanical or other properties in addition to having a single solid-solution phase by definition.

Most of the refractory HEAs have been fabricated by casting in a water-cooled copper mold where the molten metal solidifies at a high cooling rate, and they are usually investigated in the

as-cast state. Thus, the phases formed and investigated in refractory HEAs are usually at metastable state. In addition, the heat treatment is an important method for tailoring the microstructure structure and mechanical properties of metallic materials. Therefore, the effect of the heat treatment on phase stability and mechanical properties of the HEAs should be investigated in detail. It is worth noting that a number of reports have recently studied the effect of heat treatment on the microstructure of HEAs [37-40].

1.3 Research Objectives

The overall objectives of this thesis are to (i) design and fabricate medium entropy alloys (MEAs) from Ti, Zr, Nb, and Ta system based on the HEA concept, which has novel properties for bio-applications as well as for other structural applications including at elevated temperatures. More specifically, the aims are

1. Using the HEA concept to design and fabricate the (Ti, Zr, Nb, and Ta)-containing MEAs
2. Using the HEA concept to tailor the composition of the designed MEAs for lower alloy cost and density, and to improve their mechanical properties at room temperature.
3. Investigating the effect of heat treatment on the microstructure and mechanical properties at room temperature and elevated temperatures, and the deformation mechanism of the newly designed MEAs.

1.4 Thesis Structure

This PhD thesis is divided into seven chapters:

Chapter 1 Introduction

Chapter 2 Literature review

- Presents and discusses : (1) high entropy alloys (HEAs) concept, (2) core effects of HEAs, (3) motivation of solid-solution phase in HEAs and methods for predicting the formation of solid-solution phase, (4) classification of HEAs and methods for fabricating HEAs, (5) development of refractory HEAs (RHEAs), (6) approaches in designing RHEAs, microstructure and mechanical properties of RHEAs.

Chapter 3 describes the experimental methods used in this study

Chapter 4 studies the microstructure and mechanical properties of a novel equatomic TiZrNbTa MEA which was designed using the HEA concept

Chapter 5 studies the microstructure and mechanical properties of non-equiatomic of $Ta_{(25-x)}Zr_{25}Nb_{25}Ti_{(25+x)}$ medium entropy alloys (MEAs)

Chapter 6 studies the effect of heat treatment on phase stability and mechanical properties of the equiatomic and non-equiatomic $Ta_{(25-x)}Zr_{25}Nb_{25}Ti_{(25+x)}$ MEAs

Chapter 7 summarizes the important outcomes and conclusions in this PhD work. Based on these achievements, some recommendations for future research are provided.

Chapter 2 Literature review

2.1 Concept of high entropy alloys

Conventionally, metallic alloys are developed based on one metal which is chosen for the primary property requirement. Later, minor alloying elements are introduced to the main metals to tailor their microstructure and properties for particular applications. Numerous alloy families have been designed using this strategy, i.e., steels, aluminium alloys, magnesium alloys, and so on. These alloys have been developed with the composition concentrated in the portion close to apexes and edges of their phase diagram, instead of the centre portion of their phase diagram. Therefore, a new class of metallic alloys was developed with the motivation of exploring the central region of the multicomponent alloy phase diagram. A few alloys synthesized in equal atomic fractions from 5 or 6 elemental metals were reported firstly in 2004 [4, 5, 41]. Interestingly, although they have a complex composition, some of them exhibited a single FCC or body-centered cubic (BCC) solid-solution phase in as-cast condition, i.e., $Fe_{20}Cr_{20}Mn_{20}Ni_{20}Co_{20}$ [5], $Cu_{20}Co_{20}Ni_{20}Cr_{20}Fe_{20}$ [4, 41]. These alloys are referred to as multi-principle element alloys (MPEAs) to emphasize the complexity of their composition or as high entropy alloys (HEAs) or medium entropy alloys (MEAs) to emphasize the effect of their high mixing entropy on the formation of the single solid solution phase in their microstructure [4, 5, 41]. Until now, all these terms, MPEAs, HEAs, and MEAs, have been commonly used in the literature for this class of metallic materials.

Perhaps, due to the absence of multi-principle component phase diagrams the definition of HEAs is not firm and consistent. Initially, the HEAs were most commonly defined as having at least five principle elements and concentration of each principle element ranging from 5 % to 35 % [42, 43]. This definition of the HEAs primarily based on their composition with motivation of investigating the alloys with the composition in centre space of their multi-component phase diagram where conventional alloy designs always avoid. According to the Gibbs phase rule, the equilibrium phase number in an alloy system is proportional to the number of components [3, 41]. Hence, a number of phases were thought to form in HEAs, i.e., solid-solution phases and intermetallic compounds. Interestingly, HEAs have a much lower number of phases than expected by the Gibb phase rule and even some of them solidified in a single body-centered cubic (BCC) or FCC solid-solution phase as mentioned above. This was explained that HEAs have a significantly high mixing entropy in the liquid or random solid-solution states, which facilitates the formation of solid-solution phases and prevents the segregation to form intermetallic compounds. Therefore, the term “high entropy alloys” was

used to name this class of materials to emphasize the effect of entropy on the formation of solid-solution phases [1, 44]. In addition, Yeh [1] suggested using Boltzmann's hypothesis to calculate the configurational mixing entropy change per mole of an alloy given by Eq. 2.1 below. Based on this calculation, all metallic alloys could be classified into three groups, namely low entropy alloys (conventional alloys), MEAs and HEAs. It should be noted that a number of alloys which were designed in equiatomic fractions of four principal elements have been considered as HEAs [9-11, 12-14, 18, 20], even though they have ΔS_{mix} of ~1.38R (J/K mole) belonging to MEAs by Yeh's classification [1]. In that regard, the term "MEA" can be controversial but HEAs, MEAs and MPEAs have been used interchangeably in the literature. In general, when the number of principal elements is limited to 3 or 4, researchers often choose to use MEAs. This general selection of terminology has been followed in this thesis. For a detailed discussion of different definitions, please refer to the critical review paper by D.B. Miracle and O.N. Senkov [2].

$$\Delta S_{mix} = -R \sum_{i=1}^{n} c_i ln c_i \qquad \text{(Eq. 2.1)}$$

Where c_i is the atomic fraction of i^{th} element, and R is the gas constant.

2.2 Four HEA core effects

Although HEAs have a complex composition, the microstructure of HEAs generally comprises either solid-solution phases or a mixture of major solid-solution phases and a small amount of the intermetallic compound. Due to this unexpected microstructure of HEAs, four HEA core effects were proposed: (*i*) the high entropy effect, (*ii*) severe lattice distortion effect, (*iii*) sluggish diffusion effect, and (*iv*) cocktail effect. These core effects are briefly introduced below.

2.2.1 High entropy effect

The high entropy effect is used to explain the formation of multi-principle atomic solid-solution phase. It is proposed that increased configurational entropy in equimolar or near-equimolar alloys with a minimum of 5 elements lowers the free energy of solid-solution phases, thereby favouring solid-solution phases over competing intermetallic compounds. In order to prove this concept, the configurational entropy of equimolar alloys containing up to nine principle elements was estimated using Eq. 2.1. Table 2.1 shows that the value of ΔS_{mix} for these equiatomic alloys increases from 1.1R to 2.2R with increasing component element number from 3 to 9. According to Richards' rule, the fusion entropy of pure metals is about ~1.0R at their melting point (Table 2.1). On the other hand, the configuration entropy of the two strong

NiAl and TiAl intermetallic compounds can be estimated from dividing their formation enthalpy by their melting temperature [4, 45]. The configurational mixing entropy of alloy systems with more than 5 principal elements is significantly higher than the fusion entropy of the pure metals. It is in the same range as that of the two strong intermetallic compounds (TiAl and NiAl) (Table 2.1). This indicates that the tendency towards ordering and segregation would be lowered by the high mixing entropy. Consequently, alloys containing a higher number of principle elements would more easily yield the formation of solid-solution phases rather than intermetallic compounds [4].

Table 2.1 Estimated configurational mixing entropy (ΔS_{mix}, J/mole) of equiatomic systems with n components and strong intermetallic compounds (NiAl and TiAl) [4].

Component number (n) or intermetallics	0	3	5	6	9	NiAl	TiAl	Fusion entropy of pure metals
ΔS_{mix}	0	1.1R	1.61R	1.79R	2.2R	1.38R	2.06R	~1.0R

It is worth mentioning that the discussion above only considered the configurational mixing entropy as the main driving force for the formation of a solid-solution phase in HEAs. However, the configurational mixing entropy is an idealized quantity and estimated by assuming that a disordered solid-solution forms in the liquid state or at high temperatures [4, 46]. This does not reflect the fact that the mixing entropy of an alloy can decrease significantly with decreasing temperature and segregations [2]. As a result, it has been shown that the effect of the configurational mixing entropy on the formation of solid-solution phases in HEAs is not as pronounced as other parameters such as mixing enthalpy (ΔH_{mix}, kJ/mol) and atomic mismatch (δ, %) [36, 47, 48]. This indicates that predicting the formation of a solid-solution phase in HEAs cannot just rely on only the ideal configurational mixing entropy. The calculation of the mixing entropy should be improved to show its effect on the formation of solid-solution phases in HEAs.

In the literature, if principal elements are carefully chosen so that the mixing enthalpy for dissimilar atom pairs are not substantially different, single solid-solution alloys could be obtained in the equilibrium state. For example, the FeCoCrMnNi alloy can form a simple FCC solution stable at all annealed temperatures [49, 50]. On the other hand, secondary phase segregations could occur resulting in the formation of other disordered solid solutions or intermetallic phases [51-54]. Also, the largest atomic element in a system tends to segregate out of the solid-solution phase during heat-treatments, e.g., Zr being the largest atom in a

TaZrNbTi MEA segregated into Zr-rich phases after annealing the alloy [6]. Similar phenomena happened in other alloys [38, 39, 55, 56].

2.2.2 Lattice distortion

Traditionally, when an alloying element is added to an alloy, it dissolves into the lattice of the host element or alloy to form a substitutional or interstitial solid-solution, and/or reacts with the alloy components to form intermetallic compounds [57, 58]. The atomic size difference between the host atoms and alloying element atoms causes the lattice distortion surrounding the alloying element atom in the solid-solution phase, which strengthens the parent metal or element. This is called the solid-solution strengthening mechanism [57, 59]. In HEAs, the solid-solution phase consists of a few different elemental atoms which are distributed randomly in a lattice. This indicates that it is impossible to distinguish between solvent and solute atoms in a HEA solid-solution, and most of the atoms in a HEA lattice have different neighbouring atoms. Because of atomic size differences among constituent elements, the HEA lattice inevitably suffers a severe lattice distortion which results in high strength and hardness [41, 43, 46, 60-62]. The severe lattice distortion is an important feature that distinguishes between HEAs and conventional alloys. It serves as the premier strengthening mechanism for these alloys [3, 6, 61], and is often designated as δ, which has been used as an important parameter for designing solid-solution phase HEAs [36, 63]. In that regard, a larger value of δ, which corresponds to the severer lattice distortion, typically offers higher strength, hardness, and high resistance to annealing softening due to the massive solid-solution hardening [3, 61, 64, 69]. Moreover, the severe lattice distortion was also attributed to the decrease in the X-ray diffraction intensity of HEAs [65, 66], lower thermal and electrical conductivity compared with pure component metals [43, 66-68]. The local lattice distortion has been experimentally observed in the microstructure of an equiatomic NbMoTaW HEA using high resolution transmission electron microscopy by Zou et al. [9].

2.2.3 Sluggish diffusion effect

The sluggish diffusion effect proposed that the diffusion in HEAs is sluggish compared with that in conventional alloys [44]. This hypothesis is originated from the difference in atomic configuration between HEAs and the conventional alloys as shown in Figure 2.1(a) and (b). As a result, lattice potential energy along a diffusive pathway in HEAs is fluctuated compared with conventional alloys (Figure 2.1(c)). The fluctuation of lattice potential energy along the diffusion pathway is believed to be obstacles to atom diffusion, which contributes to the sluggish diffusion in HEAs compared to their conventional counterparts [70]. The sluggish

diffusion in HEAs claims to be beneficial for the formation of solid-solution phases in HEAs, which assumes that the disordered solid solutions formed at high temperatures or in the liquid phase remain at low temperatures because the sluggish diffusion prevents the segregation at high temperatures or even during solidification [46]. It was also used to explain the formation of nanostructured HEAs [4, 71], the decelerated grain growth, exceptional phase stability, high softening resistance at elevated temperatures [14, 72, 73], and excellent diffusion barrier [74].

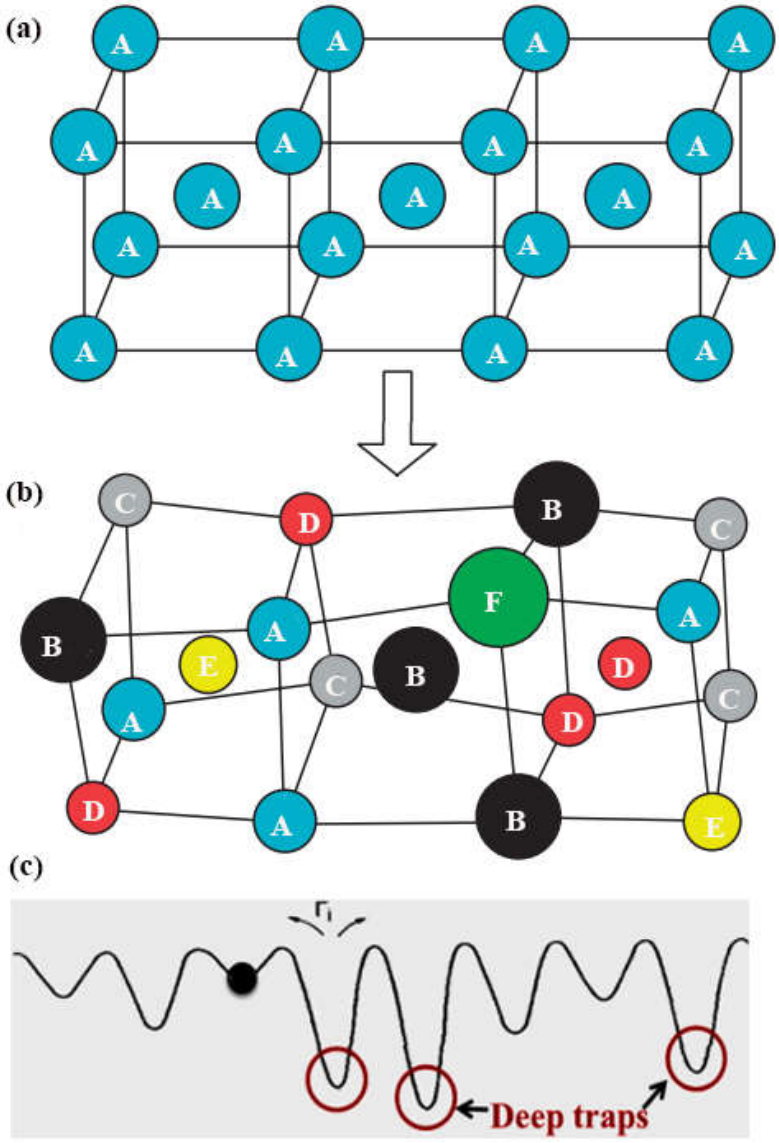

Figure 2.1 Schematic illustrations of BCC crystal structures. (a) Perfect lattice of element A. Adapted with permission from Wiley, from reference [63] (b) the distorted lattice caused by different-sized atoms (A, B, C, D, E, and F) distributed randomly in a BCC lattice due to the atmomic mismatch. Adapted with permission from Wiley, from reference [63]. (c) schematic illustration of the fluctuation of lattice potential energy along a diffusion path for an atom in the lattice. Reproduced with permission from Springer Nature, Jan 30, 2020, from reference [70].

2.2.4 The cocktail effect

The term "cocktail effect" was firstly used by Ranganathan [75], which describes that HEAs are synthesized in a mixture of multi-component metals. Also, the cocktail effect implies that the properties of HEAs are related to constituent elements. For example, Senkov et al. (2010 and 2011) [13, 14] fabricated HEAs from refractory metals, called refractory HEAs. These alloys exhibited higher softening resistance at high temperatures than Ni-based and Co-based superalloys as shown in Figure 2.2, which is attributed to the effect of the high melting point of each refractory metal [14]. Another example is that the density of the refractory HEAs decreases significantly when they were alloyed with the lighter metals and/or lighter metalloids, e.g., Al, Si, and Cr. In addition, the mutual interactions among constituent elements can result in some unexpected properties. For instance, the addition of Al to some Zr-containing refractory HEAs not only reduces their density but also improves their softening resistance at high temperature [17, 31] as well as their oxidation resistance [15]. This is because Al interacts with Zr to form a coherent disordered BCC solid-solution nanoprecipitates in an ordered B2 (Al_xZr_5) matrix, which enhances the mechanical properties of the resultant refractory HEAs at both room temperature and elevated temperatures.

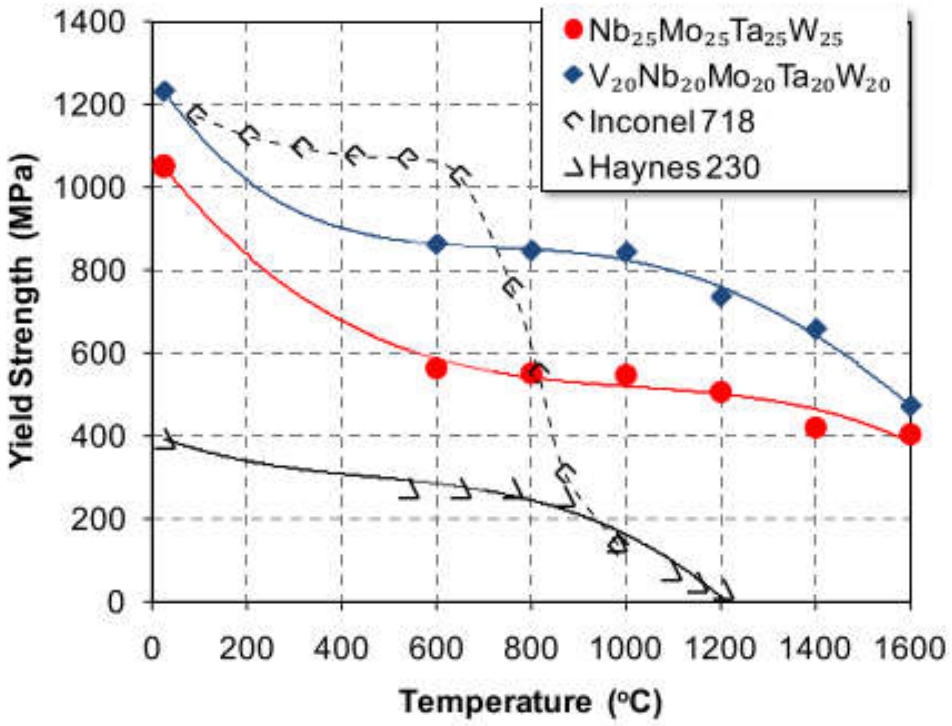

Figure 2.2 Yield strength of $Nb_{25}Mo_{25}Ta_{25}W_{25}$, $V_{20}Nb_{20}Mo_{20}Ta_{20}W_{20}$, superalloy Inconel, and Haynes 230 were as a function of temperature. Reproduced with permission from Elsevier, Jan 29, 2020, from reference [14].

2.3 Formation of solid-solution phases in HEAs

2.3.1 Motivation for solid-solution phases and/or intermetallic compounds

Microstructure is one of the key factors which govern the properties of a metallic material. Since no phase diagram exists for HEAs because of their multi-principal element composition, it is challenging to anticipate their microstructure and mechanical properties. Therefore, it is critical to predict what types of phases (solid-solution phases or intermetallic compounds) could form for a given MEAs or HEAs composition. The intermetallic compounds generally embrittle the alloys, often making processing and machining difficult while the solid-solution phases offer the alloys high damage tolerance [4, 45, 46]. Therefore, a number of HEAs are designed with the purpose of producing HEAs with only solid-solution phases [76]. On the other hand, although intermetallic compounds often embrittle metallic alloys, they can strengthen the alloys significantly. For example, TiB and TiC intermetallic compounds can reinforce titanium to form Ti-TiC/TiB metal matrix composites with excellent strength and good ductility [77, 78]. In that regard, HEAs containing intermetallic compounds should also be investigated but the shape, size and amount of the intermetallic compounds should be controlled to obtain desired mechanical properties.

2.3.2 Empirical rule

In order to predict phase formation in HEAs, an empirical rule was firstly introduced by Zhang et al. [63], which adopted the Hume-Rothery rules and thermodynamic parameters to analyse the phase formation of numerous published multi-component high entropy alloys which cover both bulk metallic glasses (BMGs) and HEAs. The empirical rule was initially based on a few parameters: mixing entropy (ΔS_{mix}, J/K mol), mixing enthalpy (ΔH_{mix}, kJ/mol), and δ (%),. These parameters can be calculated using Eq. 2.1, Eq. 2.2, and Eq. 2.3, respectively.

Mixing enthalpy is calculated based on the regular melt model [79, 166]:

$$\Delta H_{mix} = \sum_{i=1, i\neq j}^{n} \Omega_{ij} c_i c_j \qquad \text{(Eq. 2.2)}$$

Where $\Omega_{ij} = 4\Delta H_{AB}^{mix}$ is the regular melt-interaction parameter between i^{th} and j^{th} elements, and ΔH_{AB}^{mix} is the mixing enthalpy of the binary liquid AB alloys; c_i and c_j are atomic fractions of i^{th} and j^{th} elements, respectively.

Difference in atomic size or atomic mismatch:

$$\delta(\%) = 100\sqrt{\sum_{i=1}^{n} c_i.\left(1-\frac{r_i}{r_a}\right)^2} \quad ; \quad r_a = \sum_{i=1}^{n} c_i r_i \qquad \text{(Eq. 2.3)}$$

Where r_a is the average of atomic radius; c_i and r_i respectively are the atomic fractions and atomic radius of the i^{th} element.

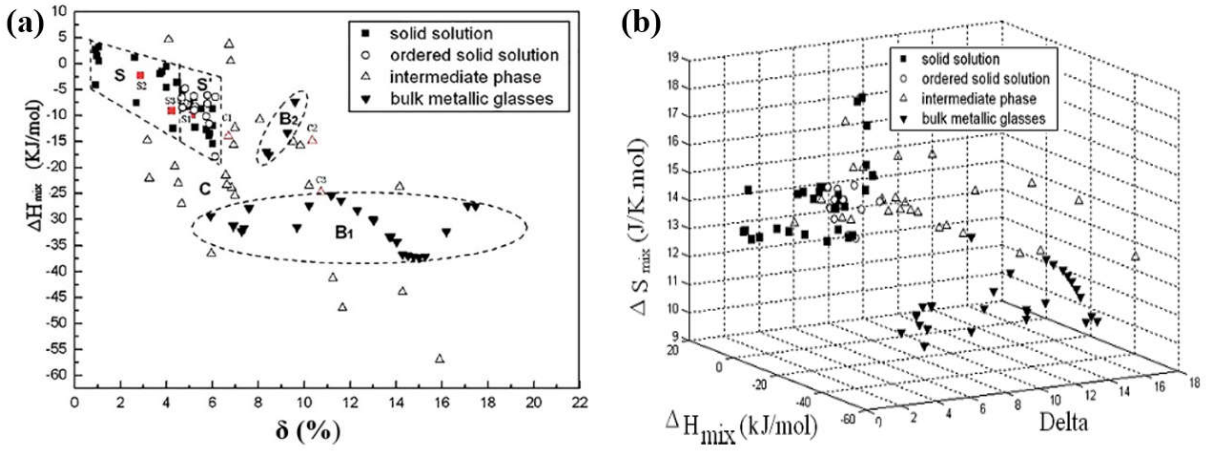

Figure 2.3 (a) Diagram of phase formation of HEAs and BMGs based on the mixing enthalpy and atomic mismatch; (b) the effect of the mixing entropy on the phase formation of multi-component high entropy alloys. Reproduced with permission from Elsevier, Jan 29, 2020, from references [63, 70].

The empirical parameters, i.e., ΔS_{mix}, δ, and ΔH_{mix} were calculated for a large number of BMGs and HEAs, and were analysed in relation with the types of phase (solid-solution, intermetallic, intermediate phase and bulk metallic glasses). The results are plotted in Figure 2.3. Four different regions were clearly observed in Figure 2.3(a), which marked by two polygonal-dash lines for HEAs and two oval-dash lines for BMGs. In general, HEAs always had lower δ and higher ΔH_{mix} than BMGs, which indicates that HEAs and BMGs are well separated by their ΔH_{mix} and δ values. It can also be seen that when the δ was lower than around 4.5%, HEAs exhibited the disordered solid solution phases as shown in the left polygonal regions. This agrees with the Hume-Rothery rules; i.e., when δ is low, the formation of substitutional solid-solutions will be facilitated. When δ ranges from 4.5% to 6.4%, the microstructure of HEAs consists of either a solid solution phase alone or solid solution phases +intermetallic compounds as shown in the right polygonal area. On the other hand, when ΔH_{mix} is lower than -15 kJ/mole or higher than -5 kJ/mole, although the value of δ of the alloys is lower than 4.5%, intermediate phases may form rather than a solid-solution phase. According to Miedema et al. [79], ΔH_{mix}

contributes to the phase formation of the binary alloy system, and either the highly negative or positive ΔH_{mix} facilitates the formation of intermetallic compounds, instead of disordered solid solutions.

In order to evaluate the effect of ΔS_{mix} on phase formation in multi-component high entropy alloys, Figure 2.3(a) is replotted in three dimensions by including ΔS_{mix}. As shown in Figure 2.3(b), HEAs that can exhibit a solid-solution phase microstructure (marked as ■) should satisfy: 12 J/K/mole $\leq \Delta S_{mix} \leq$ 17 J/K/mol. Therefore, based on this statistical analysis, the formation of solid solution phases in HEAs should satisfy 12 J/K/mole $\leq \Delta S_{mix} \leq$ 17 J/K/mol, -15 kJ/mole $\leq \Delta H_{mix} \leq$ -5kJ/mol, and $\delta \leq 6.4\%$ [63, 70].

Later, a few reports [35, 36, 48] also adopted this empirical rule to analyse the phase formation of reported HEAs and BMGs. They found that although some alloys have a high mixing entropy, their microstructure still contains intermetallic compounds and/or solid-solution phase or amorphous phase (Figure 2.4(a)). This indicates that ΔS_{mix} cannot be used as an exclusive rule to predict the phase formation in multi-component. However, the δ- ΔH_{mix} plot shown in Figure 2.4(b) can reasonably predict the formation of the solid-solution phase in multi-component high entropy alloys. Statistically, the solid-solution phases can form when -11.6 kJ/mole $\leq \Delta H_{mix} \leq$ 3.2 kJ/mole and $\delta \leq 6.6\%$. This finding was consistent with previous publications, but stricter than that suggested by Zhang [63].

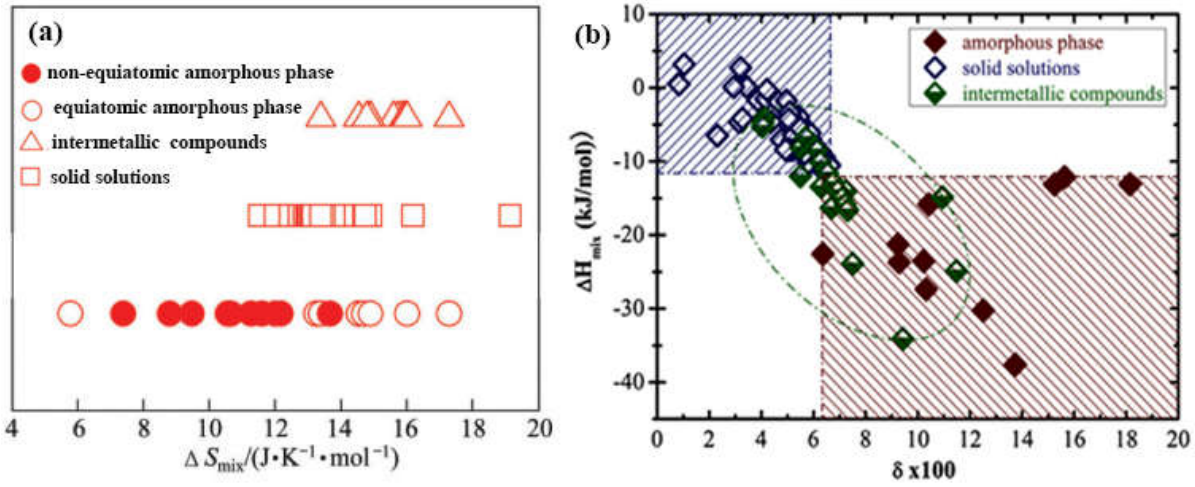

Figure 2.4 (a) phase formation as a function of the mixing entropy, reproduced with permission from Elsevier, Jan 30, 2020, from reference [36]. (b) Phase formation as function of the mixing enthalpy and the atomic mismatch; Reproduced with permission from Taylor & Francis and Springer Nature, Jan 30, 2020, from references [48, 70].

As discussed above, ΔH_{mix} contributes to the phase formation of the binary alloy system, and either too negative or highly positive ΔH_{mix} causes the formation of intermetallic compounds or elemental segregation, respectively, while when the absolute value of ΔH_{mix} is close to zero, the solid-solution phases can form. However, according to the phase rule, if a solid-solution phase possesses the lowest Gibbs free energy, it will be the most stable phase during the solidification. According to the Gibbs equation, ΔH_{mix} and $T\Delta S_{mix}$ are the two factors that contribute to the Gibbs free energy. As discussed above, the high absolute value of ΔH_{mix} could restrain the solid-solution formation, so the absolute value of ΔH_{mix} can be used to describe the resistance for solid-solution formation. On the other hand, the value of ΔS_{mix} is always positive and increases with increasing temperature. Therefore, $T\Delta S_{mix}$ can attain high value at high temperature, which significantly lowers the Gibbs free energy and effectively increases the extent of confusion in an alloy system, thereby facilitating solid-solution formation. As a result, with the idea of combining the effect of both $T\Delta S_{mix}$ and ΔH_{mix} in predicting the formation of the solid-solution phases in HEAs, a new dimensionless parameter, Ω, was proposed by Yang and Zhang [47, 80], and can be calculated using Eq. 2.4 below, because the first phase transformation generally occurs at the liquidus/melting point.

$$\Omega = \frac{T_m \Delta S_{mix}}{\left|\Delta H_{mix}\right|} \quad \text{where: } T_m = \sum_{i=1}^{n} c_i \left(T_m\right)_i \qquad \text{(Eq. 2.4)}$$

where T_m is the nominal melting point of the alloy system while $(T_m)_i$ is the melting point of the i^{th} element.

This statistical analysis relies on the previous publication results for HEAs and BMGs. A δ-Ω plot is shown in Figure 2.5, which indicates that a solid solution phase can form only when both $\Omega \geq 1.1$ and $\delta \leq 6.5$ % are met. This prediction is consistent with previous research about the relationship between solid-solution formation and δ. In addition, when δ is smaller than 3.8 %, only solid solution phases are found. Most BMGs have value of Ω smaller than that of solid solution HEAs but have value of δ greater than that of solid solution HEAs. The boundary of HEAs and BMGs can be well defined by the δ-Ω relationship (Figure 2.5).

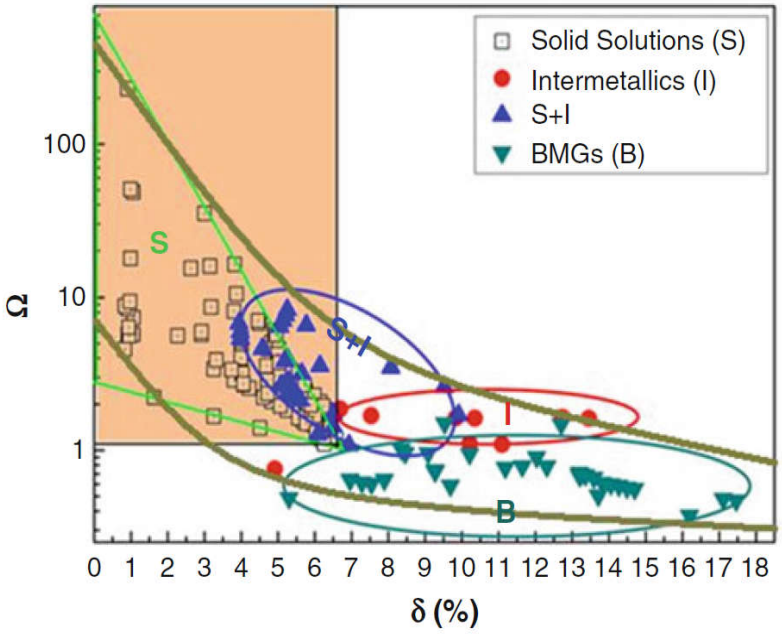

Figure 2.5 Diagram of phase formation of HEAs and BMAs based on the Ω and the atomic size difference. Reproduced with permission from Elsevier, Feb 09, 2020, from reference [47].

Calculating the empirical rule parameters such as ΔS_{mix}, ΔH_{mix}, δ, and Ω [35, 36, 47, 63, 70, 81] just suggests whether HEAs with a given composition could solidify as a solid-solution phase or not. It does not give a prediction about the crystal structure of the solid-solution phase. The solid-solution phases of HEAs that have been reported in the literature can have an FCC or BCC or HCP crystal structure, or a mixture of these structures. HEAs with a FCC structure exhibited good ductility, but their strength is relatively low [82]. In contrast, BCC HEAs show high strength but poor room temperature ductility. Therefore, some research attempted to design the criteria in predicting the crystal structure of the solid-solution phases. Guo *et al.* [83] suggested using valence electron concentration (*VEC*) in predicting the formation of BCC and FCC phases in HEAs. The *VEC* is the total number of total electrons including d electrons involved in the valence band, i.e., *VEC* for pure Ti ([Ar]$3d^2 4s^2$) is 4 and *VEC* for a HEA can be calculated using Eq. 2.5 below. It has been calculated for a number of published HEAs in analysing the crystal structures of the solid-solution phases. Figure 2.6 shows the crystal structures as a function of the *VEC*, which shows that a FCC phase will be stabilized when *VEC* > 8, a mixture of BCC and FCC phases may form when $6.7 \leq VEC < 8$, and a BCC phase will exist when *VEC* < 6.87.

$$VEC = \sum_{i=1}^{n} c_i (VEC)_i \qquad \text{(Eq. 2.5)}$$

where $(VEC)_i$ are the valence electron concentration of element i and c_i is the atomic fraction of atom i^{th}.

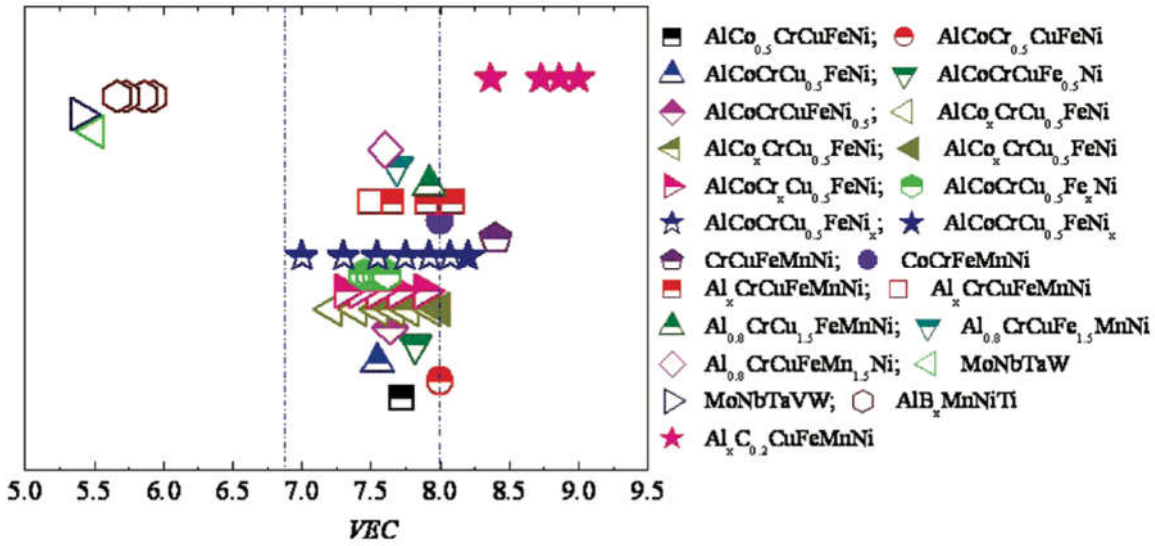

Figure 2.6 Formation of FCC and BCC is as function of valence electron concentration (*VEC*). Fully filled symbols are for FCC phase alloys whereas fully open symbols are for BCC phase alloys, and bottom-half unfilled symbols are for alloys with mixed BCC and FFC phases. Reproduced with permission from Taylor & Francis, Feb 9th 2020, from reference [83].

2.3.3 CALPHAD

The empirical rule has been used extensively in designing HEAs because it is simple and can be used to scan potential HEA candidates quickly. The phase formation in the as-cast condition of a number of HEAs was successfully predicted by the empirical rule [6, 7, 13, 27, 28, 38, 52, 84-87]. However, it failed to predict the phase formation in the equilibrium (annealed) condition. For example, TaNbHfZr HEA exhibited a single BCC solid-solution phase in the as-cast condition, but a secondary phase precipitated during annealing [38]. Therefore, computer-aided phase predictions were developed to solve this issue, and also to assist the experimental design. For example, the CALPHAD approach is commonly used to predict the phase diagram for alloys and has also been adopted to calculate the phase diagram of HEAs, but the main issue in using this method is the lack of a suitable database for HEAs at present, which may be addressed in the future.

2.4 Classification of High Entropy Alloys

About 408 distinct HEAs have been designed by July 2019 from 37 elements across the periodic table such as alkali metal, alkaline earth metals, basic metals, transition metals, lanthanides, metalloids and non-metal [2]. Most HEAs have been designed from using the 3d and 4d transition metals. In general, HEAs can be divided into three groups: HEAs-containing 3d transition metals, refractory HEAs (RHEAs), and light HEAs.

2.4.1 HEAs-containing 3d transition metals

Cantor et al. [5] and Yeh et al. [4] introduced the first HEAs containing 3d-transition metals in 2004. After this breakthrough, much research has been conducted by focusing on the microstructure and mechanical properties of equiatomic HEAs designed from 3d transition metals, i.e., Co, Cr, Cu, Fe, Mn, Ni, and V [50, 85, 88-94]. Later, Al, Si, B, Ti, Mo, Nb and C were introduced to these alloy as alloying elements in order to tailor their microstructure and properties [15, 95-99].

2.4.2 Refractory high entropy alloys (RHEAs)

The refractory HEAs were introduced by Senkov et al. [13] in 2010 with the purpose of exploring new HEAs for high temperature applications, including thermal power plant and aerospace industry. The refractory HEAs are generally fabricated in equiatomic or near-equiatomic fractions from the refractory metals, i.e., Nb, Ta, Hf, Mo, V, W, Zr, Cr, and Ti [10, 21, 28, 38, 100-108]. This alloy family often exhibits high strength, high hardness, and high softening resistance at high temperatures compared with Ni-based superalloys [14]. However, they show high density and poor or little ductility at room temperature, which limits their processing and applications. Therefore, numerous attempts have been made in order to reduce the density while maintaining or improving their properties. The composition of the refractory HEAs has been tailored by replacing the heavy metals, e.g., W and Ta with the lighter metals/metaloids, i.e., V, Cr, Al, and Si, to reduce their density. However, intermetallic compounds were often found to form in these new refractory HEAs, which substantially reduces their ductility at room temperature [15, 17, 25, 31, 32, 34, 109, 110].

2.4.3 Light HEAs

Several studies have been conducted with an ambition to produce light HEAs from light metals e.g., Al, Li, Mg, Be, Sc, and Ti [111-113]. However, these metals have very different melting points for fabrication by melting and casting. Consequently, solid-state approaches such as mechanical alloying have been employed to produce light HEAs. For example, Youssef el al. [111] fabricated a light HEA which has a nominal composition of $Al_{20}Li_{20}$ $Mg_{10}Sc_{20}Ti_{30}$ (at. %) by ball milling. This alloy has a density 2.67 g/cm^3 and exhibits a single FCC phase, and a hardness of 5.9 GPa.

2.5 Fabrication Methods

Three fabrication routes have been used in synthesizing HEAs, namely, liquid route (melting and casting techniques), solid-state route (powder metallurgy), and vapour-state route (deposition methods). The advantages and disadvantages of each approach are discussed below.

2.5.1 Liquid-state Route

The liquid-state route has been the most popular one. Several techniques are categorised as the liquid route, i.e., arc melting [85, 88, 114-116], Bridgman technique [117-120], laser-engineered net shaping (LENS) [121, 122], and induction melting [123-125]. Arc-melting has been extensively used to fabricate HEAs so far because the arc-furnace temperature can exceed 3000 ºC, which is able to melt almost all metals. In addition, metals are generally melted under an argon atmosphere, which limits the contamination during melting and casting processes. However, the torch temperature of the arc-melting furnaces can exceeds 3000 ºC which causes evaporation during melting the low melting/evaporating point metals. As a result, it is difficult to control the composition of alloys containing low melting point metals. Another issue of the liquid-state route is that segregation always happens during solidification, which causes inhomogeneous chemical distribution, coarse dendrite, porosities, and shrinkages [14, 94]. These microstructural defects deteriorate the alloy properties. Therefore, as-cast HEAs have been treated by post-processing, i.e., hot and cold-working and heat treatment to obtain a fine and homogeneous structure and improve their mechanical properties [21, 69, 91, 123].

2.5.2 Solid-state route

Solid-state route means that the alloying reaction happens at temperatures below the melting point of the constituent metals. Mechanical alloying (MA) is a materials processing method which involves the repeated welding, fracturing, and re-welding of a mixture of powder metals, generally in a high-energy ball mill. It has been used widely to produce HEA powders which are then consolidated by compacting and sintering processes [126-145]. It offers a number of advantages that cannot be found in the standard metallurgical practices such as casting and forging. For example, it allows incorporation of alloying elements that are difficult or impossible to combine by conventional methods, also it can produce nanostructured, supersaturated solid-solutions, and amorphous alloys. Although MA offers a variety of advantages in fabricating materials, it shows some disadvantages. For example, it is hard to get high purity powder metals and to avoid contamination during MA processing. However, the effect of these issues can be minimized by proper choice of milling media (composition of ball and vial) and milling in a high-purity inert gas [129, 142]. Some researchers employed an

advanced consolidating method, spark plasma sintering, to consolidate the HEA powder that was synthesized by MA, which produces nanostructured and high compressive strength HEAs [128, 138].

2.5.3 Vapour-state Route

Regarding vapour-state route, two techniques, magnetron sputtering and plasma nitriding, have been adopted to fabricate the thin films of HEAs on the substrate surface. For example, AlMoNbSiTaTiVZr HEA layer was successfully fabricated to investigate its diffusion barrier properties between copper and silicon [146]. In addition, (TiZrNbHfTa)N and (TiZrNbHfTa)C HEAs were deposited on C45 and M2 steel substrates with the purpose of improving the wear resistance of the substrates, and the (TiZrNbHfTa)N and (TiZrNbHfTa)N coating exhibited a significantly higher wear resistance than binary coating (TiC) [147].

2.6 Development of refractory HEAs and their microstructure

2.6.1 Microstructure of refractory HEAs

RHEAs were synthesized from the refractory metals, i.e., group 4B (Ti, Zr, Hf), group 5B (V, Nb, Ta), and group 6B (Mo, W) (Table 2.2), and were primarily developed for high temperature applications [13, 14, 148]. In addition, a few studies proposed RHEAs for bio-medical application [27, 28] as well as for fusion power reactor components [87, 126]. Most studies have focused on the microstructure and properties in the as-cast or as-annealed conditions of RHEAs, and only a few investigated the microstructure and mechanical properties of RHEAs after thermomechanical or heat treatment processing [40, 149-151]. Most RHEAs exhibit a single BCC solid-solution phase microstructure in the as-cast condition, but they can show severe inhomogeneous chemical distributions due to elemental segregation during dendritic solidification. The elemental segregation is generally attributed to the difference in the melting temperature of the constituent metals. The high melting point metals tend to solidify first to form dendrites, hence the low melting metals are forced to be in the inter-dendritic regions [6-11, 13, 27, 28, 32, 54, 61, 100, 105-107, 148, 152-156]. For example, WNbMoTaV RHEA showed a single BCC solid-solution phase and a dendritic microstructure as shown in Figure 2.7. The highest melting point in the WNbMoTaV system is W which was concentrated in the dendritic core, while the lower melting metals (Nb, Mo, and V) are enriched in the interdendritic regions (Figure 2.7).

The BCC solid-solution phase was the most common phase in the microstructure of the reported RHEAs. This could be due to the fact that their constituent metals have a BCC crystal structure

at room temperature or at high temperatures (Table 2.2), and the respective binary phase diagram of the refractory metals shows a high mutual solubility [157]. Besides, several RHEAs show a hexagonal closed-pack (HCP) solid-solution phase [86], which normally contains a high concentration of Hf, Ti, and Zr which have HCP crystal structures at room temperature (Table 2.2).

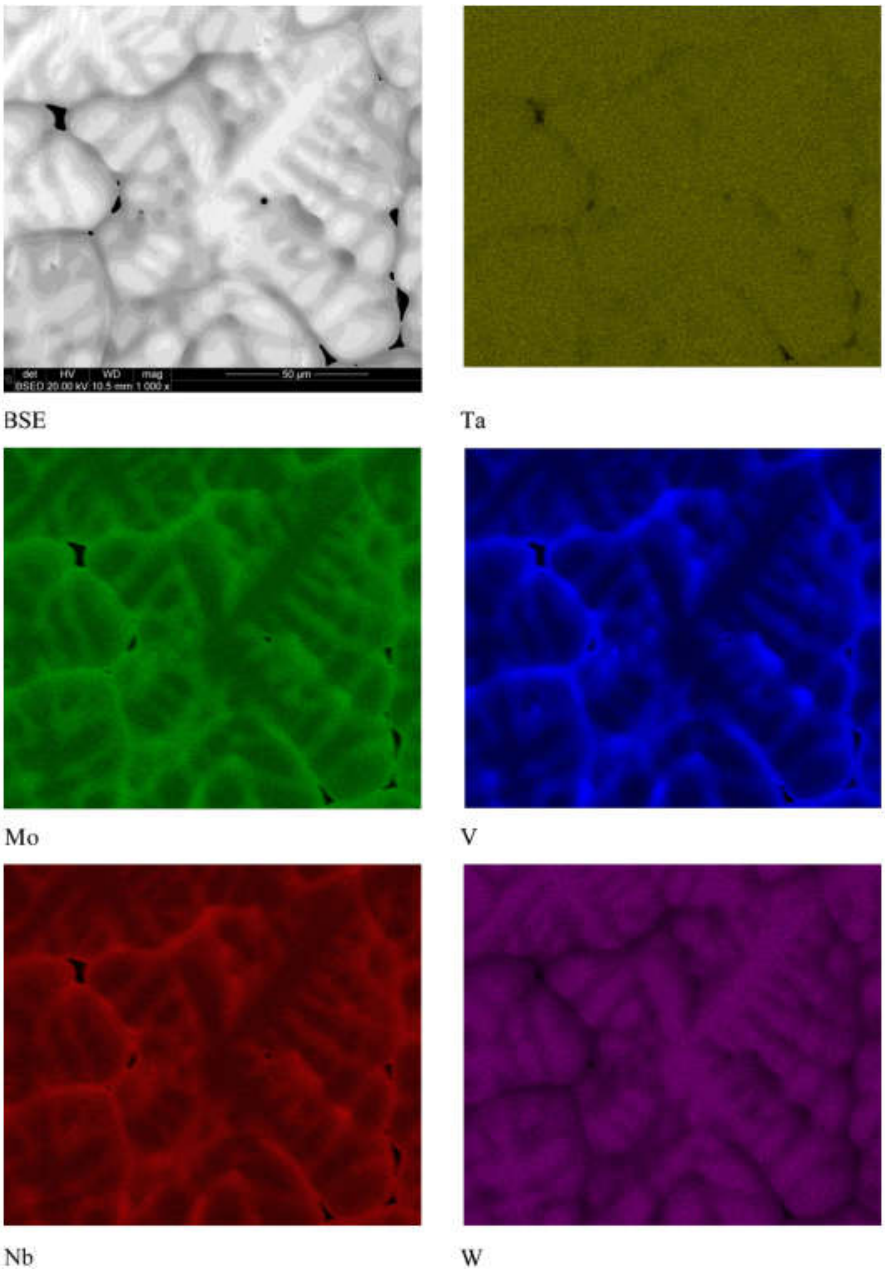

Figure 2.7 EDS mapping of the WNbMoTaV RHEA. W has the highest melting point in the WNbMoTaV alloy system, which is concentrated in the dendritic core, while elements with a lower melting point are enriched in the interdendritic regions. Reproduced with permission from Elsevier, Feb 12th 2020, from reference [13].

2.6.2 Effect of alloying elements on the microstructure of refractory HEAs

RHEAs exhibit high compressive strength at either room temperature or elevated temperatures, but they show a high density and poor room temperature ductility, which limits their applications [2, 3]. Therefore, many researchers attempt to tailor the RHEA compositions to reduce their density by either replacing the heavy metals with lighter ones [20, 25, 31, 32, 84, 158-160] or just introducing new lighter alloying elements [15, 26, 34, 56, 161, 162]. Chromium and aluminium are the two most common alloying elements considered for RHEAs because both Cr and Al are significantly lighter than refractory metals such as W, Ta, and Mo (Table 2.2). In addition, Cr is a high melting point metal, which could maintain the high temperature mechanical properties, and Al is known as a BCC-stabilizer element for Ti, Hf, Zr and HEAs [4]. Although the RHEA density is reduced remarkably by using this approach, new intermetallic compounds are often formed in the microstructure of the resulting RHEAs, which deteriorates the ductility of the resultant RHEAs. For example, Laves phases (C14 or C15) are frequently observed in the RHEAs containing Cr, e.g., CrNbTiVZr, CrNbTiZr [31] or other RHEA systems [20, 25, 34, 163]. The ordered B2 phases found in the RHEAs contained Al and Zr. For example, a cuboidal-like nanostructure surrounded by the secondary ordered B2, Al_xZr_5, was observed in the $AlMo_{0.5}NbTa_{0.5}TiZr$ RHEA [39], as shown in Figure 2.8, which was also observed in the $Al_1Mo_{0.5}Nb_1Ta_{0.5}Ti_1Zr_1$ RHEA [56]. The Al-Zr mixing enthalpy is highly negative as shown in Table 2.2, which indicates a strong interaction between Zr and Al, which has likely caused the formation of the ordered B2-Al_xZr_5 [39, 56].

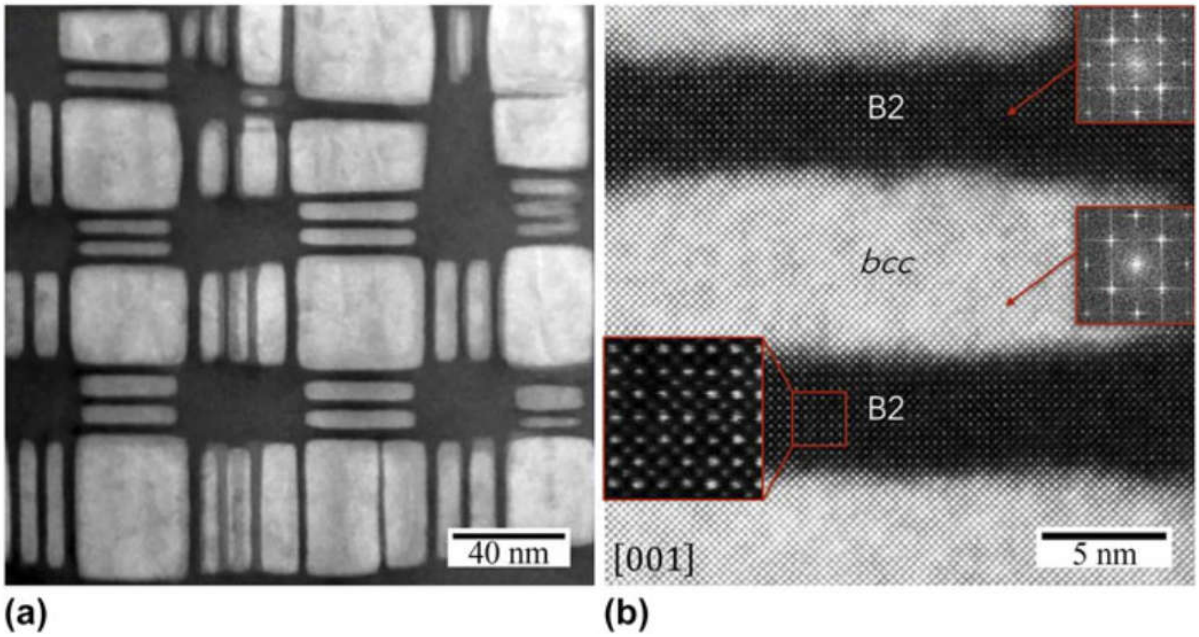

Figure 2.8 STEM-HAADF images of the cuboidal-like nanostructure present inside the grains of Al $AlMo_{0.5}NbTa_{0.5}TiZr$. (a) Bright disordered BCC phase has a cuboid-like nanostructure surrounding by the dark ordered B2 phases- Al_xZr_5. (b) An ordered B2 structure for the dark contrast phase and a disordered BCC structure for the cuboidal-like precipitates were revealed as shown in the corresponding Fast Fourier transforms images marked as red squares. Reproduced with permission from Elsevier, Feb 15, 2020, from reference [39].

Besides, a few researchers have fabricated RHEA-based composites by adding Si to form in-situ silicide, M_5Si_3, as reinforcements [109, 164]. For example, a refractory $HfNbTiVSi_{0.5}$ HEA composite was fabricated from pure elements with a minimum purity of ~99 exhibited a microstructure consisted of a BCC matrix and silicide phases as characterized by XRD and SEM (Figure 2.9). Two publications introduced interstitial alloying elements such as O and N to enhance the mechanical properties of RHEAs [12, 165].

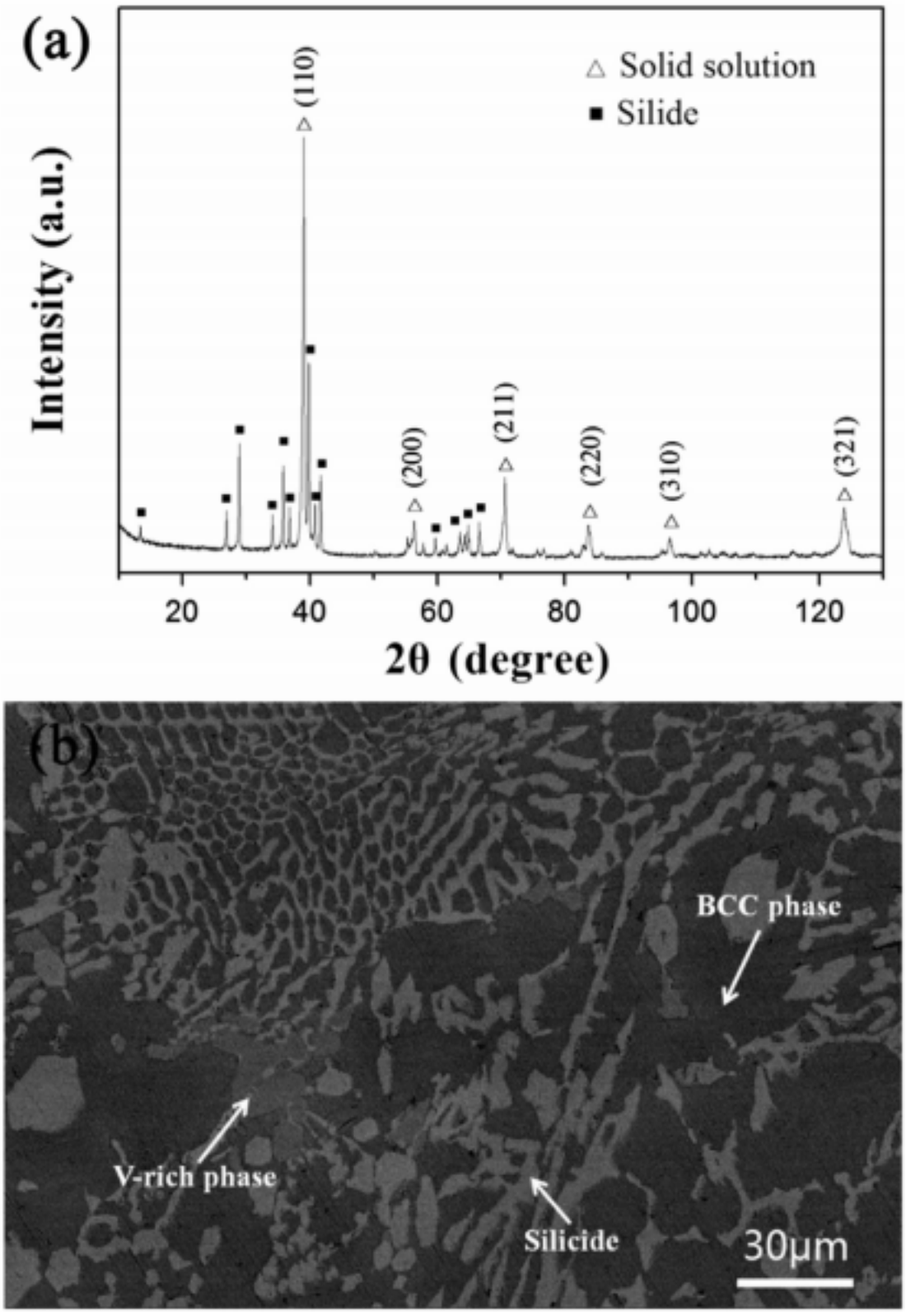

Figure 2.9 (a) XRD patterns of $HfNbTiVSi0_{.5}$ HEA showing the presence of multiphase structure: a BCC solid-solution phase and silide compounds; (b) SEM image of $HfNbTiVSi0_{.5}$ HEA demonstrating a composite structure. Reproduced with permission from Elsevier, Feb 15, 2020, from reference [109].

Table 2.2 Physical and thermodynamic parameters, i.e., metling temperature (T_m, K), atomic radius (r, nm), atomic weight (M, g), mixing enthalpy (ΔH_{mix}^{AB}, kJ/mole) calculated using Miedema's model for atomic pairs between refractory metals, Al, and Si [36, 166].

Elements	**Al**	**Si**	**Ti**	**V**	**Cr**	**Zr**	**Nb**	**Mo**	**Hf**	**W**	**Ta**
Atomic No	13	14	22	23	24	40	41	42	72	74	73
Crystal structure	FCC	diamond	HCP	BCC	BCC	HCP	BCC	BCC	HCP	BCC	BCC
Density (g/cm3)	2.7	2.33	4.5076	6.11	7.14	6.511	8.57	10.28	13.31	19.25	16.65
T_m (K)	933.52	1683.15	1933.15	2163.15	2130.15	2125.15	2741.15	2890.15	2423.15	3683.15	3290
r (nm)	0.1432	0.1153	0.1462	0.1316	0.1249	0.1603	0.1429	0.1363	0.1578	0.1367	0.143
M (g)	26.98	28.09	47.87	50.94	52	91.22	92.91	95.94	178.49	183.84	180.9
ΔH_{mix}^{AB}	**Al**	-19	-30	-16	-10	-44	-18	-5	-39	-2	-19
		Si	-66	-48	-37	-84	-56	-35	-77	-31	-56
			Ti	-2	-7	0	2	-4	0	-6	1
				V	-2	-4	-1	0	2	-1	-1
					Cr	-12	-7	0	-9	1	-7
						Zr	4	-6	0	-9	3
							Nb	-6	4	-8	0
								Mo	-4	0	-5
									Hf	-6	3
										W	-7
											Ta

2.6.3 Effect of heat-treatment on the microstructure of refractory HEAs

An important core effect of HEAs is the severe lattice distortion induced by the random distribution of the constituent elements that vary appreciably in size. As mentioned above, most of the RHEAs have a single BCC solid-solution phase in the as-cast condition, but their microstructure consists of a dendritic structure with elemental segregation that occurs during solidification. Therefore, the lattice distortion effect could be maximized if all elements are homogeneously distributed without segregation to form secondary phases. In addition, RHEAs are often produced by an arc-melting method where the liquid metals solidify at a high cooling rate in a water-cooled copper mould. Consequently, the single solid-solution phase in the as-cast condition is mostly metastable. Therefore, some studies have investigated the phase stability of RHEAs by either homogenization heat treatment [37, 38, 61, 151, 162] or thermomechanical treatment [40]. Some RHEAs show a highly stable BCC phase [9, 10]. For example, the BCC phase of NbMoTaW RHEAs was stable after long annealing at 1800 ºC [9].

While an equiatomic TaNbHfZrTi RHEA was firstly thought to be a stable single BCC solid-solution phase alloy [103, 104, 106, 148, 151], the secondary phase precipitated out after homogenization and aging heat-treatment or thermomechanical treatment [37, 40]. Another example is that, after annealing the as-cast single BCC solid-solution TaNbHfZr alloy, a cuboid-like nanostructure (darker contrast) surrounded by thin strips (lighter contrast) was observed in the TEM images taken along the <100> zone axis, as shown in Figure 2.10 [38]. The formation of the cuboid-like nanostructure is due to the formation of short-range clustering (SRCs) of Zr and Hf during homogenization of the TaNbHfZr RHEA as shown in Figure 2.11 [38]. The formation of Zr and Hf SRCs is likely due to the nature of highly positive mixing enthalpies as well as the large differences in atomic size between Zr (or Hf) and other elements in the TaNbHfZr system.

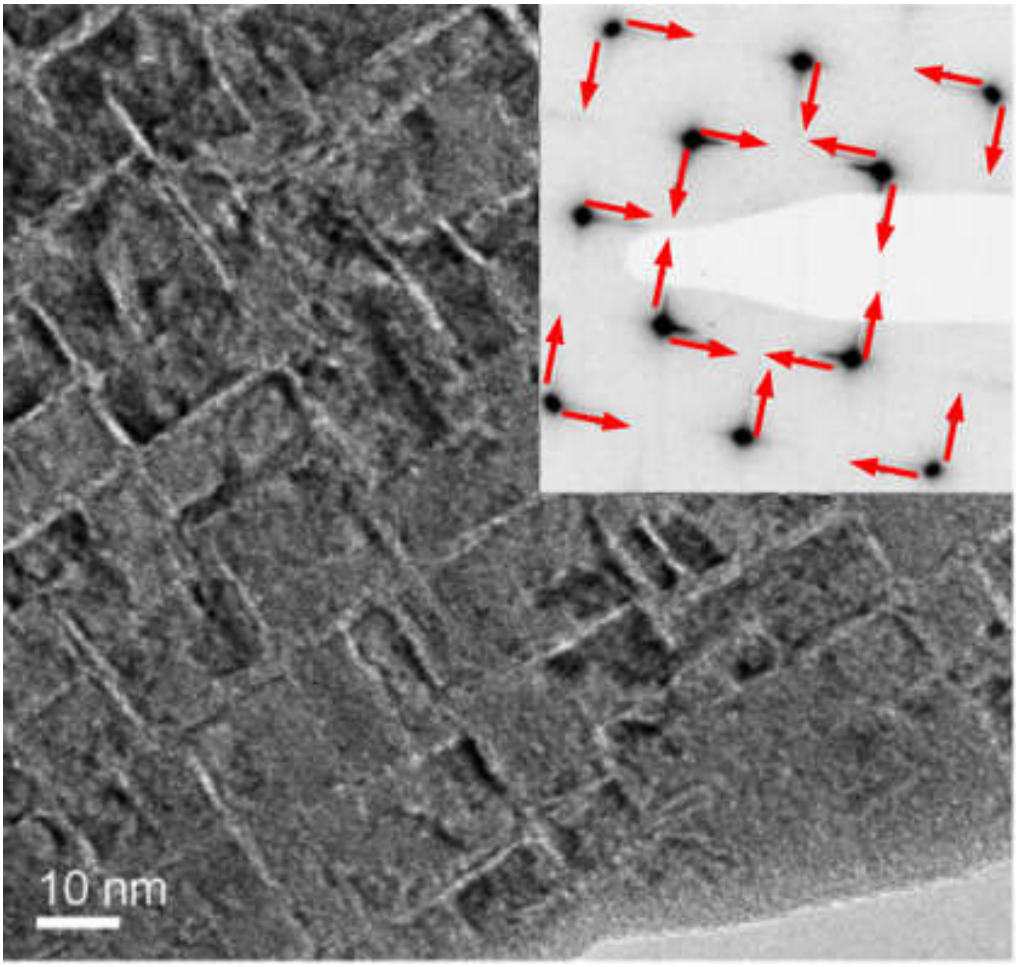

Figure 2.10 High resolution (HR) TEM image of the TaNbHfZr alloy after homogenized for one day. TEM BF image was taken along <100> zone-axis. The inset shows a [001] zone-axis SAED image which reveals an asymmetric nature streak-like diffuse scattering intensity as indicated by red arrows, induced by the formation of (Zr and Hf) SRCs. Reproduced with permission from Elsevier, Feb 15, 2020, from reference [38].

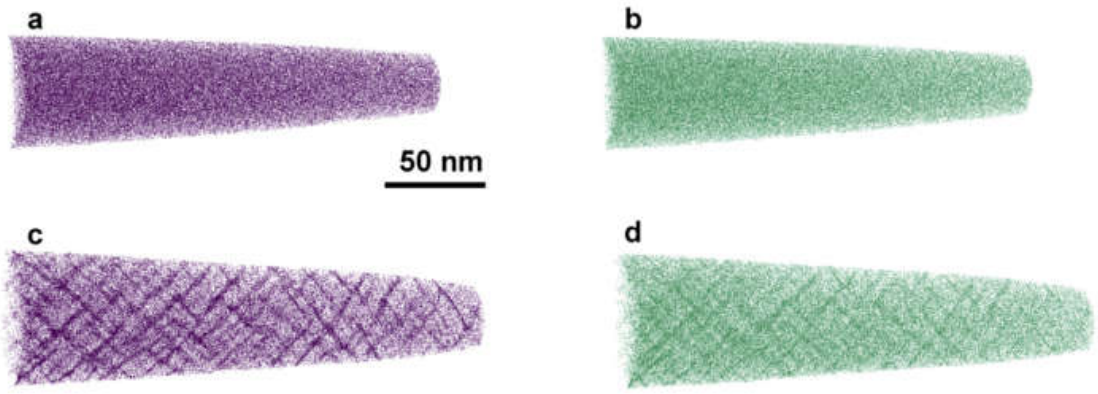

Figure 2.11 Atom map reconstructions from APT analysis: (a) and (b) are the Zr atom and Hf atom maps in as-cast TaNbTiHf, respectively. (c) and (d) are the Zr atom and Hf atom maps in TaNbTiHf alloys after homogenized at 1800 ºC for 6 hours. Reproduced with permission from Elsevier, Feb 15, 2020, from reference [38].

2.7 Mechanical properties of RHEAs

The compressive mechanical properties of most refractory HEAs at room temperature and elevated temperatures were summarized in Table 7 of reference [2]. Due to the lack of tensile ductility, the mechanical properties of most RHEAs were characterised by hardness and compressive testing. At room temperature, RHEAs exhibited high compression yield strength ranging from 879 MPa for HfNbTiZr HEA [10] to 2035 MPa for $Al_{0.5}NbTa_{0.8}Ti_{1.5}V_{0.2}Zr$ HEA, but the compressive strain is rather limited (<5%) [24]. The single phase RHEAs normally show better compression strain and poorer compression stress at room temperature than multiple phase (solid-solution phases and intermetallic compounds) RHEAs. However, the single phase RHEAs show higher softening resistance at elevated temperatures. For instance, single phase MoNbTaVW RHEAs demonstrated a compression stress of ~1246 MPa at room temperature, but its compression stress was ~477 MPa at 1600ºC. In contrast, while the compression stress of multiple phase AlMo0.5NbTa0.5TiZr RHEAs was ultrahigh (~2000 MPa) at room temperature, it dropped to ~255 MPa at 1200ºC. In addition, the majority of RHEAs demonstrated a high density (~8 g/cm^3 or above).

The high-temperature compressive strength of some RHEAs has been compared with three common and widely used superalloys (ICONEL718, MAR-M247, and Haynes 230) as shown in Figure 2.12 [2]. Generally, the yield strength values of refractory HEAs decreases with increasing testing temperatures. However, most of the RHEAs showed a better high-

temperature compressive strength than Haynes 230, and some of them showed higher compressive strengths than superalloy INCONEL 718 and MAR-M 247 at both room temperature and elevated temperatures (Figure 2.12). For instance, MoNbTaW and MoNbTaVW showed compressive yield strengths over 400 MPa at 1600 ^{o}C, which is significantly higher than INCONEL 718 and MAR-M 247 [14]. The high-temperature compression properties of RHEAs are promising for aerospace applications although it may be inappropriate to compare the compression strength of RHEAs with tensile strength of superalloys. In addition, a wide range of additional requirements such as oxidation resistance, fatigue and creep resistance, and processibility have to be accessed for RHEAs in the future.

As mentioned above, RHEAs can exhibit better softening resistance at high temperatures than Ni-based superalloys [14]. However, their limited room-temperature ductility restricts their further processing, while their high density is undesired for many potential applications. Therefore, much effort has been made to improve their room temperature ductility while reducing their density by introducing or replacing heavy refractory metals with lighter Al, Ti and Zr. However, just a few such refractory HEAs have shown good room-temperature tensile strength-ductility combinations as summarized in Table 2.3, e.g., $Hf_{25}Nb_{25}Ti_{25}Zr_{25}$ (at. %) HEA [10], $Ti_{20}Zr_{20}Hf_{20}$ $Nb_{20}Ta_{20}$ (at. %) HEA [107, 148, 167], $Ta_xHfZrTi$ (x=1, 0.6, 0.5, and 0.4) (at. %) [11], $Al_x(HfNbTiZr)_{100-x}$ (x=0, 3, 5, 7, 10, and 12) (at. %) [162]. Although these RHEAs show single solid solution BCC phase microstructure in as-fabricated condition and a good combination of tensile strength and ductility, their density is still over 8 g/cm^3 as shown in Table 2.3. Therefore, in general, the low room-temperature tensile ductility and high density remain to be the major drawbacks of most HEAs reported to date [5-8], in addition to their phase instability when considered for elevated temperature applications [37, 38, 168].

Table 2.3 Tensile properties, fabrication processing and density of reported refractory HEAs.

Alloys	**Processing**	**ρ (g/cm^3)**	**σ_y (MPa)**	**σ_{UTS} (MPa)**	**ε (%)**	**Ref**
HfNbTaTiZr	As-cast, HIP 1200 ºC-207 MPa/2 h, cold rolling 90%-1000ºC/2 h	9.94	1145	1262	9.7	[167]
HfNbTiZr	1300ºC/6 h/slow cooling	8.4	879	969	14.9	[10]
HfNbTiZr	AC	8.4	810	890	8	[103]
Ti35Zr27.5Hf27.5Nb5Ta5	Cold rolling 60-70% - 800&900 ºC/0.5 h	8.48^c	600	960	17	[175]
Hf0.5Nb0.5Ta0.5Ti1.5Zr	As-cast	8.13	903	990	18.8	[176]
Ta0.6ZrHfTi	As-cast	9.5^c	~730	~1080	~20	[11]
Ta0.5ZrHfTi	As-cast	9.4^c	~700	~1080	~29	[11]
Ta0.4ZrHfTi	As-cast	9.2^c	~400	~1080	~30	[11]
AlHfNbTiZr	Cold rolling 80% -1000 ºC/0.5 h	8.4^c	-	~1090	~28	[162]
$Al_3(HfNbTiZr)_{97}$	Cold rolling 80% -1000 ºC/0.5 h	8.3^c	-	~990	~26	[162]
$Al_5(HfNbTiZr)_{95}$	Cold rolling 80% -1000 ºC/0.5 h	8.2^c	-	~950	~26	[162]
$Al_7(HfNbTiZr)_{93}$	Cold rolling 80% -1000 ºC/0.5 h	8.1^c	-	~950	~18	[162]
$Al_{10}(HfNbTiZr)_{90}$	Cold rolling 80% -1000 ºC/0.5 h	7.9^c	-	~825	~16	[162]
$Al_{12}(HfNbTiZr)_{88}$	Cold rolling 80% -1000 ºC/0.5 h	7.8^c	-	~780	~16	[162]
HfNbTiZr	Annealing-cold forging-cold rolling-800 ºC/4 h	8.4	1159	1174	4.7	[151]
HfNbTiZr	Annealing-cold forging-cold rolling-800 ºC/16 h	8.4	1134	1165	7.6	[151]
HfNbTiZr	Annealing-cold forging-cold rolling-800 ºC/64 h	8.4	1094	1110	6.0	[151]
HfNbTiZr	Annealing-cold forging-cold rolling-800 ºC/256 h	8.4	1071	1074	4.6	[151]
HfNbTiZr	Annealing-cold forging-cold rolling-1100 ºC/0.5 h	8.4	1107	1159	13.9	[151]
HfNbTiZr	Annealing-cold forging-cold rolling-1100 ºC/1 h	8.4	1115	1195	18.5	[151]
HfNbTiZr	Annealing-cold forging-cold rolling-1100 ºC/2 h	8.4	1114	1168	12.2	[151]
HfNbTiZr	Annealing - high pressure torsion (HPT)	8.4	-	1900	7.9	[40]
HfNbTiZr	Annealing - HPT-500 ºC/1 h	8.4	-	1520	7.7	[40]
HfNbTiZr	Annealing - HPT-800 ºC/1 h	8.4	-	795	5.0	[40]

HIP: hot isostatic pressing; c: calculated value.

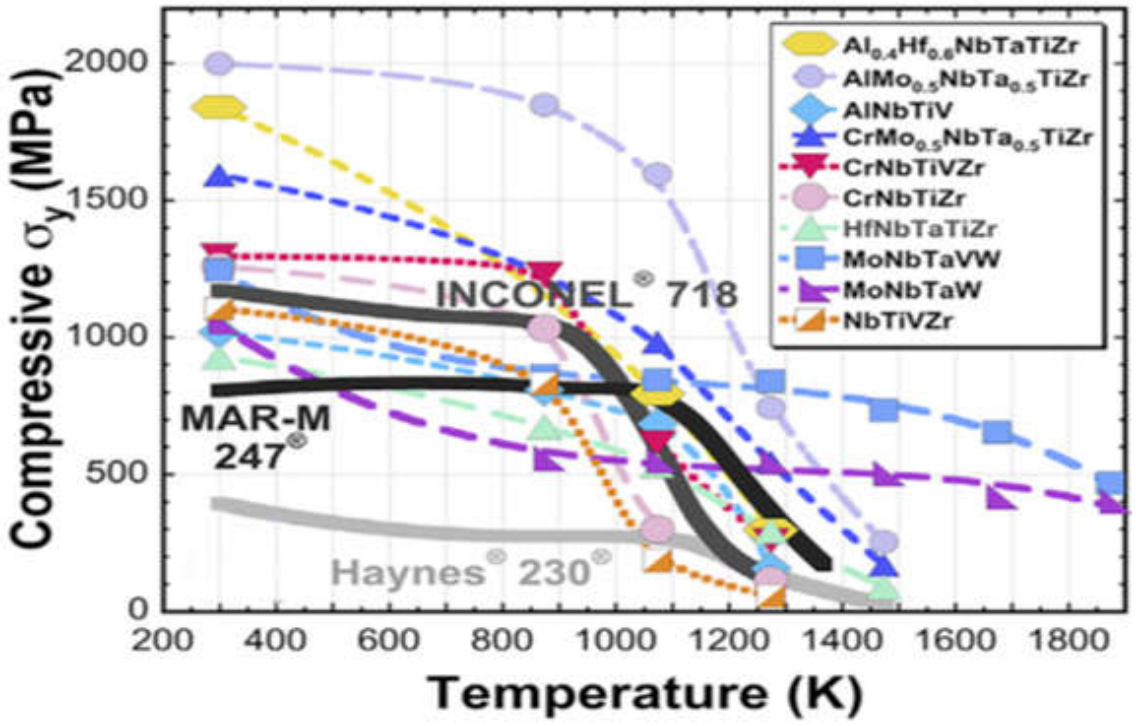

Figure 2.12 Compressive yield strength of refractory HEAs and tensile yield strength of three superalloys (Haynes 230, INCONEL 718 MAR-M 247) are as function of temperature. The data were collected from [15, 17, 31, 32, 108, 172]. Reproduced with permission from Elsevier, Feb 15, 2020, from reference [2].

2.8 Summary and remarks

In summary, the development of HEAs was originally motivated by an idea of investigating the multiple principle element alloys whose compositions are located in the central region of the multi-component phase diagram. Although HEAs have a multi-principal element composition, they generally exhibit a simple microstructure which consists of a single solid-solution phase or a mixture of solid-solution phases or a mixture of solid-solution phase and a small amount of intermetallic compounds. This is not anticipated by the traditional phase rule. Due to this unexpected microstructure of HEAs, four HEA core effects have been proposed: (i) the high entropy effect, (ii) the severe lattice distortion effect, (iii) the sluggish diffusion effect, and (iv) the cocktail effect. The first three core effects were hypothesized-metallurgical properties of HEAs. There have been attempts to quantify these hypothesized core effects of HEAs, but more solid evidence is needed to justify them.

HEAs are commonly categorized into three groups, namely, HEAs-containing the 3d transitional metals, RHEAs and light HEAs. They can be produced using traditional fabrication methods such as arc-melting and induction melting, solid-state route, and vapour-state routes.

The fabrication method is chosen based on the properties of the constituent metals. Of three HEA groups, RHEAs are synthesized from the refractory metals such as Ta, Zr, Nb, Ti, Mo, W, Hf, and Cr, and exhibit promising properties for advanced structural applications and bio-applications. Since they were developed just from 2010, a wide range of compositions, microstructures and properties of RHEAs have not been explored. This is also the major reason for the selection of RHEAs for this study.

Based on the current literature, extensive attention has been paid to the single solid-solution phase HEAs to address the concern that intermetallic compounds embrittle these alloys and make processing difficult. Most reported HEAs have been designed in equiatomic or near-equiatomic fractions with the purpose of maximizing the configurational mixing entropy to benefit the formation of single solid-solution phase. However, this does not always happen according to the literature. Other parameters of the empirical rule such as i.e., δ, Ω, and ΔH_{mix} played an important role in predicting the formation of solid solution phase in HEAs, and the CALPHAD approach becomes a popular tool to predict phase diagram for multi-component element high entropy alloys. Therefore, the primary purpose of this research is to use the empirical rule and the CALPHAD approach to design new refractory MEAs containing premier biocompatible elements for detailed experimental investigation. It is hoped that these new MEAs canexhibit promising mechanical properties for either structural materials or biomedical applications. Since most reported RHEAs alloys have high density (commonly above 8 g/cm^3) and low ductility at room temperature [2], it is important to improve their ductility and reduce their density. Instead of introducing new lighter elements, this thesis focuses on re-designing equiatomic MEAs into non-equiatomic MEAs by gradually replacing heavier constituent element with lighter one to decrease the atomic mismatch for improved ductility and reduced density. Finally, most reported RHEAs are limited to as-cast conditions. The effect of heat treatment on their phase stability and mechanical performance at both room temperature and high temperatures remains largely unexplored. Therefore, in this thesis, the long-term phase stability, microstructure, tensile and compression behaviour of the new designed refractory MEAs at high temperatures will also be investigated, in addition to similar studies at RT.

References

[1] J.W. Yeh, Alloy design strategies and future trends in high-entropy alloys, JOM 65(12) (2013) 1759-1771.

[2] D.B. Miracle, O.N. Senkov, A critical review of high entropy alloys and related concepts, Acta Mater. 122 (2017) 448-511.

[3] Y. Zhang, T.T. Zuo, Z. Tang, M.C. Gao, K.A. Dahmen, P.K. Liaw, Z.P. Lu, Microstructures and properties of high-entropy alloys, Prog. Mater Sci. 61 (2014) 1-93.

[4] J.W. Yeh, S.K. Chen, S.J. Lin, J.Y. Gan, T.S. Chin, T.T. Shun, C.H. Tsau, S.Y. Chang, Nanostructured High-Entropy Alloys with Multiple Principal Elements: Novel Alloy Design Concepts and Outcomes, Adv. Eng. Mater. 6(5) (2004) 299-303.

[5] B. Cantor, I.T.H. Chang, P. Knight, A.J.B. Vincent, Microstructural development in equiatomic multicomponent alloys, Mater. Sci. Eng., A 375–377 (2004) 213-218.

[6] V.T. Nguyen, M. Qian, Z. Shi, T. Song, L. Huang, J. Zou, Compositional design of strong and ductile (tensile) Ti-Zr-Nb-Ta medium entropy alloys (MEAs) using the atomic mismatch approach, Mater. Sci. Eng., A 742 (2019) 762-772.

[7] V.T. Nguyen, M. Qian, Z. Shi, T. Song, L. Huang, J. Zou, A novel quaternary equiatomic Ti-Zr-Nb-Ta medium entropy alloy (MEA), Intermetallics 101 (2018) 39-43.

[8] J.P. Couzinié, G. Dirras, L. Perrière, T. Chauveau, E. Leroy, Y. Champion, I. Guillot, Microstructure of a near-equimolar refractory high-entropy alloy, Mater. Lett. 126 (2014) 285-287.

[9] Y. Zou, S. Maiti, W. Steurer, R. Spolenak, Size-dependent plasticity in an Nb 25 Mo 25 Ta 25 W 25 refractory high-entropy alloy, Acta Mater. 65 (2014) 85-97.

[10] Y.D. Wu, Y.H. Cai, T. Wang, J.J. Si, J. Zhu, Y.D. Wang, X.D. Hui, A refractory Hf25Nb25Ti25Zr25 high-entropy alloy with excellent structural stability and tensile properties, Mater. Lett. 130 (2014) 277-280.

[11] H. Huang, Y. Wu, J. He, H. Wang, X. Liu, K. An, W. Wu, Z. Lu, Phase-Transformation Ductilization of Brittle High-Entropy Alloys via Metastability Engineering, Adv. Mater. (2017).

[12] Z. Lei, X. Liu, Y. Wu, H. Wang, S. Jiang, S. Wang, X. Hui, Y. Wu, B. Gault, P. Kontis, D. Raabe, L. Gu, Q. Zhang, H. Chen, H. Wang, J. Liu, K. An, Q. Zeng, T.G. Nieh, Z. Lu, Enhanced strength and ductility in a high-entropy alloy via ordered oxygen complexes, Nature 563(7732) (2018) 546-550.

[13] O. Senkov, G. Wilks, D. Miracle, C. Chuang, P. Liaw, Refractory high-entropy alloys, Intermetallics 18(9) (2010) 1758-1765.

[14] O. Senkov, G. Wilks, J. Scott, D. Miracle, Mechanical properties of Nb 25 Mo 25 Ta 25 W 25 and V 20 Nb 20 Mo 20 Ta 20 W 20 refractory high entropy alloys, Intermetallics 19(5) (2011) 698-706.

[15] O.N. Senkov, S.V. Senkova, C. Woodward, Effect of aluminum on the microstructure and properties of two refractory high-entropy alloys, Acta Mater. 68 (2014) 214-228.

[16] Y. Zou, H. Ma, R. Spolenak, Ultrastrong ductile and stable high-entropy alloys at small scales, Nat. Commun. 6 (2015) 7748.

[17] O.N. Senkov, S.V. Senkova, D.B. Miracle, C. Woodward, Mechanical properties of low-density, refractory multi-principal element alloys of the Cr–Nb–Ti–V–Zr system, Mater. Sci. Eng., A 565 (2013) 51-62.

[18] S.P. Wang, E. Ma, J. Xu, New ternary equi-atomic refractory medium-entropy alloys with tensile ductility: Hafnium versus titanium into NbTa-based solution, Intermetallics 107 (2019) 15-23.

[19] V. Soni, O. Senkov, B. Gwalani, D. Miracle, R. Banerjee, Microstructural Design for Improving Ductility of An Initially Brittle Refractory High Entropy Alloy, Sci. Rep. 8(1) (2018) 8816.

[20] O. Senkov, S. Rao, K. Chaput, C. Woodward, Compositional effect on microstructure and properties of NbTiZr-based complex concentrated alloys, Acta Mater. 151 (2018) 201-215.

[21] N.N. Guo, L. Wang, L.S. Luo, X.Z. Li, R.R. Chen, Y.Q. Su, J.J. Guo, H.Z. Fu, Hot deformation characteristics and dynamic recrystallization of the MoNbHfZrTi refractory high-entropy alloy, Mater. Sci. Eng. A 651 (2016) 698-707.

[22] Y. Shi, B. Yang, P. Liaw, Corrosion-Resistant High-Entropy Alloys: A Review, Metals 7(2) (2017) 43.

[23] J. Li, X. Yang, R. Zhu, Y. Zhang, Corrosion and Serration Behaviors of TiZr0.5NbCr0.5VxMoy High Entropy Alloys in Aqueous Environments, Metals 4(4) (2014) 597.

[24] O. Senkov, C. Woodward, D. Miracle, Microstructure and properties of aluminum-containing refractory high-entropy alloys, JOM 66(10) (2014) 2030-2042.

[25] N.D. Stepanov, N.Y. Yurchenko, D.V. Skibin, M.A. Tikhonovsky, G.A. Salishchev, Structure and mechanical properties of the AlCrxNbTiV (x = 0, 0.5, 1, 1.5) high entropy alloys, J. Alloys Compd. 652 (2015) 266-280.

[26] N.Y. Yurchenko, N.D. Stepanov, D.G. Shaysultanov, M.A. Tikhonovsky, G.A. Salishchev, Effect of Al content on structure and mechanical properties of the AlxCrNbTiVZr (x=0; 0.25; 0.5; 1) high-entropy alloys, Mater. Charact. 121 (2016) 125-134.

[27] S.P. Wang, J. Xu, TiZrNbTaMo high-entropy alloy designed for orthopedic implants: As-cast microstructure and mechanical properties, Mater. Sci. Eng., C 73 (2017) 80-89.
[28] M. Todai, T. Nagase, T. Hori, A. Matsugaki, A. Sekita, T. Nakano, Novel TiNbTaZrMo high-entropy alloys for metallic biomaterials, Scr. Mater. 129 (2017) 65-68.
[29] Y. Li, C. Wong, J. Xiong, P. Hodgson, C. Wen, Cytotoxicity of titanium and titanium alloying elements, J. Dent. Res. 89(5) (2010) 493-497.
[30] M. Geetha, A.K. Singh, R. Asokamani, A.K. Gogia, Ti based biomaterials, the ultimate choice for orthopaedic implants – A review, Prog. Mater Sci. 54(3) (2009) 397-425.
[31] O.N. Senkov, S.V. Senkova, C. Woodward, D.B. Miracle, Low-density, refractory multi-principal element alloys of the Cr–Nb–Ti–V–Zr system: Microstructure and phase analysis, Acta Mater. 61(5) (2013) 1545-1557.
[32] N.D. Stepanov, D.G. Shaysultanov, G.A. Salishchev, M.A. Tikhonovsky, Structure and mechanical properties of a light-weight AlNbTiV high entropy alloy, Mater. Lett. 142 (2015) 153-155.
[33] H. Chen, A. Kauffmann, B. Gorr, D. Schliephake, C. Seemüller, J.N. Wagner, H.J. Christ, M. Heilmaier, Microstructure and mechanical properties at elevated temperatures of a new Al-containing refractory high-entropy alloy Nb-Mo-Cr-Ti-Al, J. Alloys Compd. 661 (2016) 206-215.
[34] M.G. Poletti, S. Branz, G. Fiore, B.A. Szost, W.A. Crichton, L. Battezzati, Equilibrium high entropy phases in X-NbTaTiZr (X = Al,V,Cr and Sn) multiprincipal component alloys, J. Alloys Compd. 655 (2016) 138-146.
[35] Z. Wang, S. Guo, C.T. Liu, Phase selection in high-entropy alloys: from nonequilibrium to equilibrium, JOM 66(10) (2014) 1966-1972.
[36] G. Sheng, C.T. Liu, Phase stability in high entropy alloys: formation of solid-solution phase or amorphous phase, Prog. Nat. Sci 21(6) (2011) 433-446.
[37] N.D. Stepanov, N.Y. Yurchenko, S.V. Zherebtsov, M.A. Tikhonovsky, G.A. Salishchev, Aging behavior of the HfNbTaTiZr high entropy alloy, Mater. Lett. 211 (2018) 87-90.
[38] S. Maiti, W. Steurer, Structural-disorder and its effect on mechanical properties in single-phase TaNbHfZr high-entropy alloy, Acta Mater. 106 (2016) 87-97.
[39] O.N. Senkov, J.K. Jensen, A.L. Pilchak, D.B. Miracle, H.L. Fraser, Compositional variation effects on the microstructure and properties of a refractory high-entropy superalloy AlMo0.5NbTa0.5TiZr, Mater. Des 139 (2018) 498-511.
[40] B. Schuh, B. Völker, J. Todt, N. Schell, L. Perrière, J. Li, J.P. Couzinié, A. Hohenwarter, Thermodynamic instability of a nanocrystalline, single-phase TiZrNbHfTa alloy and its impact on the mechanical properties, Acta Mater. 142 (2018) 201-212.

[41] J.W. Yeh, S.J. Lin, T.S. Chin, J.Y. Gan, S.K. Chen, T.T. Shun, C.H. Tsau, S.Y. Chou, Formation of simple crystal structures in Cu-Co-Ni-Cr-Al-Fe-Ti-V alloys with multiprincipal metallic elements, Metall. Mater. Trans. A 35(8) (2004) 2533-2536.
[42] M.C. Gao, J.W. Yeh, P.K. Liaw, Y. Zhang, High-Entropy Alloys: *Fundamentals and Applications*, Springer (2016).
[43] B. Murty, J.W. Yeh, S. Ranganathan, High-entropy alloys, Butterworth-Heinemann (2014).
[44] M.H. Tsai, J.W. Yeh, High-entropy alloys: a critical review, Mater. Res. Lett. 2(3) (2014) 107-123.
[45] D.B. Miracle, J.D. Miller, O.N. Senkov, C. Woodward, M.D. Uchic, J. Tiley, Exploration and Development of High Entropy Alloys for Structural Applications, Entropy 16(1) (2014) 494-525.
[46] J.W. Yeh, Recent progress in high entropy alloys, Ann. Chim. Sci. Mat 31(6) (2006) 633-648.
[47] X. Yang, Y. Zhang, Prediction of high-entropy stabilized solid-solution in multi-component alloys, Mater. Chem. Phys. 132(2) (2012) 233-238.
[48] S. Guo, Phase selection rules for cast high entropy alloys: an overview, Mater. Sci. Technol. 31(10) (2015) 1223-1230.
[49] F. Otto, Y. Yang, H. Bei, E.P. George, Relative effects of enthalpy and entropy on the phase stability of equiatomic high-entropy alloys, Acta Mater. 61(7) (2013) 2628-2638.
[50] K.Y. Tsai, M.H. Tsai, J.W. Yeh, Sluggish diffusion in Co–Cr–Fe–Mn–Ni high-entropy alloys, Acta Mater. 61(13) (2013) 4887-4897.
[51] B. Li, Y. Wang, M. Ren, C. Yang, H. Fu, Effects of Mn, Ti and V on the microstructure and properties of AlCrFeCoNiCu high entropy alloy, Mater. Sci. Eng. A 498(1) (2008) 482-486.
[52] J. Morgiel, Z. Świątek, F. Czerwiński, Microstructure and mechanical properties of the new Nb25Sc25Ti25Zr25 eutectic high entropy alloy, Mater. Sci. Eng. A 651 (2016) 590-597.
[53] F. He, Z. Wang, P. Cheng, Q. Wang, J. Li, Y. Dang, J. Wang, C. Liu, Designing eutectic high entropy alloys of CoCrFeNiNb x, J. Alloys Compd. 656 (2016) 284-289.
[54] N.N. Guo, L. Wang, L.S. Luo, X.Z. Li, R.R. Chen, Y.Q. Su, J.J. Guo, H.Z. Fu, Effect of composing element on microstructure and mechanical properties in Mo–Nb–Hf–Zr–Ti multi-principle component alloys, Intermetallics 69 (2016) 13-20.
[55] E. Jumaev, S.H. Hong, J.T. Kim, H.J. Park, Y.S. Kim, S.C. Mun, J.Y. Park, G. Song, J.K. Lee, B.H. Min, T. Lee, K.B. Kim, Chemical evolution-induced strengthening on AlCoCrNi

dual-phase high-entropy alloy with high specific strength, J. Alloys Compd. 777 (2019) 828-834.
[56] J.K. Jensen, B.A. Welk, R.E.A. Williams, J.M. Sosa, D.E. Huber, O.N. Senkov, G.B. Viswanathan, H.L. Fraser, Characterization of the microstructure of the compositionally complex alloy Al1Mo0.5Nb1Ta0.5Ti1Zr1, Scr. Mater. 121 (2016) 1-4.
[57] W.D. .Callister, D.G. Rethwisch, Materials science and engineering: an introduction, Wiley New York (2007).
[58] R. Abbaschian, R.E. Reed-Hill, Physical metallurgy principles, Cengage Learning (2008).
[59] R.E. Smallman, R.J. Bishop, Modern physical metallurgy and materials engineering, elsevier (1999).
[60] Z. Wang, Y. Huang, Y. Yang, J. Wang, C. Liu, Atomic-size effect and solid solubility of multicomponent alloys, Scr. Mater. 94 (2015) 28-31.
[61] C. Lee, G. Song, M.C. Gao, R. Feng, P. Chen, J. Brechtl, Y. Chen, K. An, W. Guo, J.D. Poplawsky, S. Li, A.T. Samaei, W. Chen, A. Hu, H. Choo, P.K. Liaw, Lattice distortion in a strong and ductile refractory high-entropy alloy, Acta Mater. 160 (2018) 158-172.
[62] Z. Li, K.G. Pradeep, Y. Deng, D. Raabe, C.C. Tasan, Metastable high-entropy dual-phase alloys overcome the strength–ductility trade-off, Nature 534(7606) (2016) 227-230.
[63] Y. Zhang, Y.J. Zhou, J.P. Lin, G.L. Chen, P.K. Liaw, Solid-solution phase formation rules for multi-component alloys, Adv. Eng. Mater. 10(6) (2008) 534-538.
[64] F. Tian, L.K. Varga, N. Chen, J. Shen, L. Vitos, Empirical design of single phase high-entropy alloys with high hardness, Intermetallics 58 (2015) 1-6.
[65] C.W. Tsai, Y.L. Chen, M.H. Tsai, J.W. Yeh, T.T. Shun, S.K. Chen, Deformation and annealing behaviors of high-entropy alloy Al 0.5 CoCrCuFeNi, J. Alloys Compd. 486(1) (2009) 427-435.
[66] J.W. Yeh, S.Y. Chang, Y.D. Hong, S.K. Chen, S.J. Lin, Anomalous decrease in X-ray diffraction intensities of Cu–Ni–Al–Co–Cr–Fe–Si alloy systems with multi-principal elements, Mater. Chem. Phys. 103(1) (2007) 41-46.
[67] H.P. Chou, Y.S. Chang, S.K. Chen, J.W. Yeh, Microstructure, thermophysical and electrical properties in AlxCoCrFeNi ($0 \leq x \leq 2$) high-entropy alloys, Mater. Sci. Eng. B 163(3) (2009) 184-189.
[68] Y.F. Kao, S.K. Chen, T.J. Chen, P.C. Chu, J.W. Yeh, S.J. Lin, Electrical, magnetic, and Hall properties of Al x CoCrFeNi high-entropy alloys, J. Alloys Compd. 509(5) (2011) 1607-1614.
[69] Y. Zhang, T. Zuo, Y. Cheng, P.K. Liaw, High-entropy alloys with high saturation magnetization, electrical resistivity, and malleability, Sci. Rep. 3 (2013).

[70] J.W. Yeh, Physical Metallurgy of High-Entropy Alloys, JOM 67(10) (2015) 2254-2261.
[71] T.T. Shun, C.H. Hung, C.F. Lee, Formation of ordered/disordered nanoparticles in FCC high entropy alloys, J. Alloys Compd. 493(1) (2010) 105-109.
[72] C.Y. Hsu, C.C. Juan, W.R. Wang, T.S. Sheu, J.W. Yeh, S.K. Chen, On the superior hot hardness and softening resistance of AlCoCrxFeMo0.5Ni high-entropy alloys, Mater. Sci. Eng. A 528(10) (2011) 3581-3588.
[73] C.W. Tsai, M.H. Tsai, J.W. Yeh, C.C. Yang, Effect of temperature on mechanical properties of Al 0.5 CoCrCuFeNi wrought alloy, J. Alloys Compd. 490(1) (2010) 160-165.
[74] S.Y. Chang, Y.C. Huang, C.E. Li, H.F. Hsu, J.W. Yeh, S.J. Lin, Improved diffusion-resistant ability of multicomponent nitrides: from unitary TiN to senary high-entropy (TiTaCrZrAlRu) N, JOM 65(12) (2013) 1790-1796.
[75] S. Ranganathan, Alloyed pleasures: multimetallic cocktails, Curr. Sci. 85(5) (2003) 1404-1406.
[76] R. Kozak, A. Sologubenko, W. Steurer, Single-phase high-entropy alloys–an overview, Zeitschrift für Kristallographie-Crystalline Materials 230(1) (2015) 55-68.
[77] L. Huang, L. Wang, M. Qian, J. Zou, High tensile-strength and ductile titanium matrix composites strengthened by TiB nanowires, Scr. Mater. 141 (2017) 133-137.
[78] L. Huang, M. Qian, L. Wang, Z.G. Chen, Z. Shi, V. Nguyen, J. Zou, High-tensile-strength and ductile novel Ti-Fe-N-B alloys reinforced with TiB nanowires, Mater. Sci. Eng. A 708 (2017) 285-290.
[79] A.R. Miedema, P.F. de Châtel, F.R. de Boer, Cohesion in alloys — fundamentals of a semi-empirical model, Physica B+C 100(1) (1980) 1-28.
[80] Y. Zhang, X. Yang, P.K. Liaw, Alloy design and properties optimization of high-entropy alloys, JOM 64(7) (2012) 830-838.
[81] Y. Ye, C. Liu, Y. Yang, A geometric model for intrinsic residual strain and phase stability in high entropy alloys, Acta Mater. 94 (2015) 152-161.
[82] F. WANG, Y. Zhang, G. Chen, H.A. Davies, Tensile and compressive mechanical behavior of a A CoCrCuFeNiAl0.5 high entropy alloy , Int. J. Mod. Phys. B 23(06n07) (2009) 1254-1259.
[83] S. Guo, C. Ng, J. Lu, C.T. Liu, Effect of valence electron concentration on stability of fcc or bcc phase in high entropy alloys, J. Appl. Phys. 109(10) (2011) 103505.
[84] Y. Qiu, Y.J. Hu, A. Taylor, M.J. Styles, R.K.W. Marceau, A.V. Ceguerra, M.A. Gibson, Z.K. Liu, H.L. Fraser, N. Birbilis, A lightweight single-phase AlTiVCr compositionally complex alloy, Acta Mater. 123 (2017) 115-124.

[85] Z. Fu, W. Chen, H. Wen, D. Zhang, Z. Chen, B. Zheng, Y. Zhou, E.J. Lavernia, Microstructure and strengthening mechanisms in an FCC structured single-phase nanocrystalline Co 25 Ni 25 Fe 25 Al 7.5 Cu 17.5 high-entropy alloy, Acta Mater. 107 (2016) 59-71.

[86] F. Czerwinski, P. Jochym, L. Litynska-Dobrzynska, Microstructure and mechanical properties of the novel Hf25Sc25Ti25Zr25 equiatomic alloy with hexagonal solid solutions, Mater. Des 92 (2016) 8-17.

[87] X. Xian, Z. Zhong, B. Zhang, K. Song, C. Chen, S. Wang, J. Cheng, Y. Wu, A high-entropy V35Ti35Fe15Cr10Zr5 alloy with excellent high-temperature strength, Mater. Des 121 (2017) 229-236.

[88] F. Otto, A. Dlouhý, K.G. Pradeep, M. Kuběnová, D. Raabe, G. Eggeler, E.P. George, Decomposition of the single-phase high-entropy alloy CrMnFeCoNi after prolonged anneals at intermediate temperatures, Acta Mater. 112 (2016) 40-52.

[89] D.H. Lee, M.Y. Seok, Y. Zhao, I.C. Choi, J. He, Z. Lu, J.Y. Suh, U. Ramamurty, M. Kawasaki, T.G. Langdon, J.I. Jang, Spherical nanoindentation creep behavior of nanocrystalline and coarse-grained CoCrFeMnNi high-entropy alloys, Acta Mater. 109 (2016) 314-322.

[90] J.Y. He, H. Wang, H.L. Huang, X.D. Xu, M.W. Chen, Y. Wu, X.J. Liu, T.G. Nieh, K. An, Z.P. Lu, A precipitation-hardened high-entropy alloy with outstanding tensile properties, Acta Mater. 102 (2016) 187-196.

[91] B. Schuh, F. Mendez-Martin, B. Völker, E. George, H. Clemens, R. Pippan, A. Hohenwarter, Mechanical properties, microstructure and thermal stability of a nanocrystalline CoCrFeMnNi high-entropy alloy after severe plastic deformation, Acta Mater. 96 (2015) 258-268.

[92] D. Ma, M. Yao, K.G. Pradeep, C.C. Tasan, H. Springer, D. Raabe, Phase stability of non-equiatomic CoCrFeMnNi high entropy alloys, Acta Mater. 98 (2015) 288-296.

[93] M. Laurent-Brocq, A. Akhatova, L. Perrière, S. Chebini, X. Sauvage, E. Leroy, Y. Champion, Insights into the phase diagram of the CrMnFeCoNi high entropy alloy, Acta Mater. 88 (2015) 355-365.

[94] K.G. Pradeep, N. Wanderka, P. Choi, J. Banhart, B.S. Murty, D. Raabe, Atomic-scale compositional characterization of a nanocrystalline AlCrCuFeNiZn high-entropy alloy using atom probe tomography, Acta Mater. 61(12) (2013) 4696-4706.

[95] X.D. Xu, P. Liu, S. Guo, A. Hirata, T. Fujita, T.G. Nieh, C.T. Liu, M.W. Chen, Nanoscale phase separation in a fcc-based CoCrCuFeNiAl0.5 high-entropy alloy, Acta Mater. 84 (2015) 145-152.

[96] Z. Tang, T. Yuan, C.W. Tsai, J.W. Yeh, C.D. Lundin, P.K. Liaw, Fatigue behavior of a wrought Al0.5CoCrCuFeNi two-phase high-entropy alloy, Acta Mater. 99 (2015) 247-258.
[97] J.Y. He, W.H. Liu, H. Wang, Y. Wu, X.J. Liu, T.G. Nieh, Z.P. Lu, Effects of Al addition on structural evolution and tensile properties of the FeCoNiCrMn high-entropy alloy system, Acta Mater. 62 (2014) 105-113.
[98] M.A. Hemphill, T. Yuan, G.Y. Wang, J.W. Yeh, C.W. Tsai, A. Chuang, P.K. Liaw, Fatigue behavior of Al 0.5 CoCrCuFeNi high entropy alloys, Acta Mater. 60(16) (2012) 5723-5734.
[99] M.H. Chuang, M.H. Tsai, W.R. Wang, S.J. Lin, J.W. Yeh, Microstructure and wear behavior of AlxCo 1.5 CrFeNi 1.5 Tiy high-entropy alloys, Acta Mater. 59(16) (2011) 6308-6317.
[100] C.C. Juan, K.K. Tseng, W.L. Hsu, M.H. Tsai, C.W. Tsai, C.M. Lin, S.K. Chen, S.J. Lin, J.W. Yeh, Solution strengthening of ductile refractory HfMoxNbTaTiZr high-entropy alloys, Mater. Lett. 175 (2016) 284-287.
[101] M. Heidelmann, M. Feuerbacher, D. Ma, B. Grabowski, Structural anomaly in the high-entropy alloy ZrNbTiTaHf, Intermetallics 68 (2016) 11-15.
[102] B. Gorr, M. Azim, H.J. Christ, H. Chen, D.V. Szabo, A. Kauffmann, M. Heilmaier, Microstructure Evolution in a New Refractory High-Entropy Alloy W-Mo-Cr-Ti-Al, Metall. Mater. Trans. A 47(2) (2016) 961-970.
[103] G. Dirras, L. Lilensten, P. Djemia, M. Laurent-Brocq, D. Tingaud, J.P. Couzinié, L. Perrière, T. Chauveau, I. Guillot, Elastic and plastic properties of as-cast equimolar TiHfZrTaNb high-entropy alloy, Mater. Sci. Eng. A 654 (2016) 30-38.
[104] G. Dirras, H. Couque, L. Lilensten, A. Heczel, D. Tingaud, J.P. Couzinié, L. Perrière, J. Gubicza, I. Guillot, Mechanical behavior and microstructure of Ti20Hf20Zr20Ta20Nb20 high-entropy alloy loaded under quasi-static and dynamic compression conditions, Mater. Charact. 111 (2016) 106-113.
[105] C.C. Juan, M.H. Tsai, C.W. Tsai, C.M. Lin, W.R. Wang, C.C. Yang, S.K. Chen, S.J. Lin, J.W. Yeh, Enhanced mechanical properties of HfMoTaTiZr and HfMoNbTaTiZr refractory high-entropy alloys, Intermetallics 62 (2015) 76-83.
[106] M. Gao, B. Zhang, S. Yang, S. Guo, Senary Refractory High-Entropy Alloy HfNbTaTiVZr, Metall. Mater. Trans. A (2015) 1-13.
[107] J.P. Couzinié, L. Lilensten, Y. Champion, G. Dirras, L. Perrière, I. Guillot, On the room temperature deformation mechanisms of a TiZrHfNbTa refractory high-entropy alloy, Mater. Sci. Eng. A 645 (2015) 255-263.

[108] O.N. Senkov, J.M. Scott, S.V. Senkova, F. Meisenkothen, D.B. Miracle, C.F. Woodward, Microstructure and elevated temperature properties of a refractory TaNbHfZrTi alloy, J. Mater. Sci. 47(9) (2012) 4062-4074.
[109] Y. Zhang, Y. Liu, Y. Li, X. Chen, H. Zhang, Microstructure and mechanical properties of a refractory HfNbTiVSi0.5 high-entropy alloy composite, Mater. Lett. 174 (2016) 82-85.
[110] N.N. Guo, L. Wang, L.S. Luo, X.Z. Li, R.R. Chen, Y.Q. Su, J.J. Guo, H.Z. Fu, Microstructure and mechanical properties of refractory high entropy (Mo 0.5 NbHf 0.5 ZrTi) BCC/M 5 Si 3 in-situ compound, J. Alloys Compd. 660 (2016) 197-203.
[111] K.M. Youssef, A.J. Zaddach, C. Niu, D.L. Irving, C.C. Koch, A Novel Low-Density, High-Hardness, High-entropy Alloy with Close-packed Single-phase Nanocrystalline Structures, Mater. Res. Lett. 3(2) (2015) 95-99.
[112] X. Yang, S. Chen, J. Cotton, Y. Zhang, Phase stability of low-density, multiprincipal component alloys containing aluminum, magnesium, and lithium, JOM 66(10) (2014) 2009-2020.
[113] V.H. Hammond, M.A. Atwater, K.A. Darling, H.Q. Nguyen, L.J. Kecskes, Equal-channel angular extrusion of a low-density high-entropy alloy produced by high-energy cryogenic mechanical alloying, JOM 66(10) (2014) 2021-2029.
[114] L.J. Santodonato, Y. Zhang, M. Feygenson, C.M. Parish, M.C. Gao, R.J. Weber, J.C. Neuefeind, Z. Tang, P.K. Liaw, Deviation from high-entropy configurations in the atomic distributions of a multi-principal-element alloy, Nat. commun. 6 (2015).
[115] B. Gludovatz, A. Hohenwarter, D. Catoor, E.H. Chang, E.P. George, R.O. Ritchie, A fracture-resistant high-entropy alloy for cryogenic applications, Science 345(6201) (2014) 1153-1158.
[116] F. Otto, A. Dlouhý, C. Somsen, H. Bei, G. Eggeler, E.P. George, The influences of temperature and microstructure on the tensile properties of a CoCrFeMnNi high-entropy alloy, Acta Mater. 61(15) (2013) 5743-5755.
[117] Y. Zhang, S. Ma, J. Qiao, Morphology transition from dendrites to equiaxed grains for AlCoCrFeNi high-entropy alloys by copper mold casting and Bridgman solidification, Metall. Mater. Trans. A 43(8) (2012) 2625-2630.
[118] S. Ma, S. Zhang, M. Gao, P. Liaw, Y. Zhang, A successful synthesis of the CoCrFeNiAl0. 3 single-crystal, high-entropy alloy by Bridgman solidification, JOM 65(12) (2013) 1751-1758.
[119] S.G. Ma, S.F. Zhang, J.W. Qiao, Z.H. Wang, M.C. Gao, Z.M. Jiao, H.J. Yang, Y. Zhang, Superior high tensile elongation of a single-crystal CoCrFeNiAl0.3 high-entropy alloy by Bridgman solidification, Intermetallics 54 (2014) 104-109.

[120] T. Zuo, X. Yang, P.K. Liaw, Y. Zhang, Influence of Bridgman solidification on microstructures and magnetic behaviors of a non-equiatomic FeCoNiAlSi high-entropy alloy, Intermetallics 67 (2015) 171-176.
[121] I. Kunce, M. Polanski, J. Bystrzycki, Structure and hydrogen storage properties of a high entropy ZrTiVCrFeNi alloy synthesized using Laser Engineered Net Shaping (LENS), Int. J. Hydrogen Energ. 38(27) (2013) 12180-12189.
[122] I. Kunce, M. Polanski, K. Karczewski, T. Plocinski, K. Kurzydlowski, Microstructural characterisation of high-entropy alloy AlCoCrFeNi fabricated by laser engineered net shaping, J. Alloys Compd. 648 (2015) 751-758.
[123] A.V. Kuznetsov, D.G. Shaysultanov, N.D. Stepanov, G.A. Salishchev, O.N. Senkov, Tensile properties of an AlCrCuNiFeCo high-entropy alloy in as-cast and wrought conditions, Mater. Sci. Eng. A 533 (2012) 107-118.
[124] T.T. Zuo, S.B. Ren, P.K. Liaw, Y. Zhang, Processing effects on the magnetic and mechanical properties of FeCoNiAl0. 2Si0. 2 high entropy alloy, Int. J. Miner. Metall. Mater. 20(6) (2013) 549-555.
[125] G. Laplanche, P. Gadaud, O. Horst, F. Otto, G. Eggeler, E.P. George, Temperature dependencies of the elastic moduli and thermal expansion coefficient of an equiatomic, single-phase CoCrFeMnNi high-entropy alloy, J. Alloys Compd. 623 (2015) 348-353.
[126] O.A. Waseem, H.J. Ryu, Powder Metallurgy Processing of a W(x)TaTiVCr High-Entropy Alloy and Its Derivative Alloys for Fusion Material Applications, Sci. Rep. 7 (2017) 1926.
[127] H.L. Wang, T.X. Gao, J.Z. Niu, P.J. Shi, J. Xu, Y. Wang, Microstructure, thermal properties, and corrosion behaviors of FeSiBAlNi alloy fabricated by mechanical alloying and spark plasma sintering, Int. J. Miner. Metall. Mater. 23(1) (2016) 77-82.
[128] C. Wang, W. Ji, Z. Fu, Mechanical alloying and spark plasma sintering of CoCrFeNiMnAl high-entropy alloy, Adv. Powder Technol. 25(4) (2014) 1334-1338.
[129] Y. Liu, J. Wang, Q. Fang, B. Liu, Y. Wu, S. Chen, Preparation of superfine-grained high entropy alloy by spark plasma sintering gas atomized powder, Intermetallics 68 (2016) 16-22.
[130] O. Maulik, V. Kumar, Synthesis of AlFeCuCrMgx (x = 0, 0.5, 1, 1.7) alloy powders by mechanical alloying, Mater. Charact. 110 (2015) 116-125.
[131] W. Ji, J. Zhang, W. Wang, H. Wang, F. Zhang, Y. Wang, Z. Fu, Fabrication and properties of TiB2-based cermets by spark plasma sintering with CoCrFeNiTiAl high-entropy alloy as sintering aid, J. Eur. Ceram. Soc. 35(3) (2015) 879-886.

[132] W. Ji, W. Wang, H. Wang, J. Zhang, Y. Wang, F. Zhang, Z. Fu, Alloying behavior and novel properties of CoCrFeNiMn high-entropy alloy fabricated by mechanical alloying and spark plasma sintering, Intermetallics 56 (2015) 24-27.
[133] Z. Fu, W. Chen, H. Wen, S. Morgan, F. Chen, B. Zheng, Y. Zhou, L. Zhang, E.J. Lavernia, Microstructure and mechanical behavior of a novel Co 20 Ni 20 Fe 20 Al 20 Ti 20 alloy fabricated by mechanical alloying and spark plasma sintering, Mater. Sci. Eng. A 644 (2015) 10-16.
[134] Z. Chen, W. Chen, B. Wu, X. Cao, L. Liu, Z. Fu, Effects of Co and Ti on microstructure and mechanical behavior of Al0.75FeNiCrCo high entropy alloy prepared by mechanical alloying and spark plasma sintering, Mater. Sci. Eng. A 648 (2015) 217-224.
[135] W. Ji, Z. Fu, W. Wang, H. Wang, J. Zhang, Y. Wang, F. Zhang, Mechanical alloying synthesis and spark plasma sintering consolidation of CoCrFeNiAl high-entropy alloy, J. Alloys Compd. 589 (2014) 61-66.
[136] S. Mridha, S. Samal, P.Y. Khan, K. Biswas, Processing and Consolidation of Nanocrystalline Cu-Zn-Ti-Fe-Cr High-Entropy Alloys via Mechanical Alloying, Metall. Mater. Trans. A 44(10) (2013) 4532-4541.
[137] N. Koundinya, C.S. Babu, K. Sivaprasad, P. Susila, N.K. Babu, J. Baburao, Phase Evolution and Thermal Analysis of Nanocrystalline AlCrCuFeNiZn high entropy alloy produced by mechanical alloying, J. Mater. Eng. Perform. 22(10) (2013) 3077-3084.
[138] Z. Fu, W. Chen, S. Fang, D. Zhang, H. Xiao, D. Zhu, Alloying behavior and deformation twinning in a CoNiFeCrAl 0.6 Ti 0.4 high entropy alloy processed by spark plasma sintering, J. Alloys Compd. 553 (2013) 316-323.
[139] S. Praveen, B.S. Murty, R.S. Kottada, Alloying behavior in multi-component AlCoCrCuFe and NiCoCrCuFe high entropy alloys, Mater. Sci. Eng. A 534 (2012) 83-89.
[140] K.B. Zhang, Z.Y. Fu, J.Y. Zhang, W.M. Wang, S.W. Lee, K. Niihara, Characterization of nanocrystalline CoCrFeNiTiAl high-entropy solid solution processed by mechanical alloying, J. Alloys Compd. 495(1) (2010) 33-38.
[141] S. Varalakshmi, G.A. Rao, M. Kamaraj, B.S. Murty, Hot consolidation and mechanical properties of nanocrystalline equiatomic AlFeTiCrZnCu high entropy alloy after mechanical alloying, J. Mater. Sci. 45(19) (2010) 5158-5163.
[142] S. Varalakshmi, M. Kamaraj, B.S. Murty, Processing and properties of nanocrystalline CuNiCoZnAlTi high entropy alloys by mechanical alloying, Mater. Sci. Eng. A 527(4) (2010) 1027-1030.

[143] S. Varalakshmi, M. Kamaraj, B.S. Murty, Synthesis and characterization of nanocrystalline AlFeTiCrZnCu high entropy solid solution by mechanical alloying, J. Alloys Compd. 460(1) (2008) 253-257.
[144] Y.L. Chen, Y.H. Hu, C.A. Hsieh, J.W. Yeh, S.K. Chen, Competition between elements during mechanical alloying in an octonary multi-principal-element alloy system, J. Alloys Compd. 481(1–2) (2009) 768-775.
[145] Y.L. Chen, Y.H. Hu, C.W. Tsai, C.A. Hsieh, S.W. Kao, J.W. Yeh, T.S. Chin, S.K. Chen, Alloying behavior of binary to octonary alloys based on Cu–Ni–Al–Co–Cr–Fe–Ti–Mo during mechanical alloying, J. Alloys Compd. 477(1) (2009) 696-705.
[146] M.H. Tsai, J.W. Yeh, J.Y. Gan, Diffusion barrier properties of AlMoNbSiTaTiVZr high-entropy alloy layer between copper and silicon, Thin Solid Films 516(16) (2008) 5527-5530.
[147] V. Braic, A. Vladescu, M. Balaceanu, C.R. Luculescu, M. Braic, Nanostructured multi-element (TiZrNbHfTa)N and (TiZrNbHfTa)C hard coatings, Surf. Coat. Technol. 211 (2012) 117-121.
[148] O. Senkov, J. Scott, S. Senkova, F. Meisenkothen, D. Miracle, C. Woodward, Microstructure and elevated temperature properties of a refractory TaNbHfZrTi alloy, J. Mater. Sci. 47(9) (2012) 4062-4074.
[149] A.V. Podolskiy, E.D. Tabachnikova, V.V. Voloschuk, V.F. Gorban, N.A. Krapivka, S.A. Firstov, Mechanical properties and thermally activated plasticity of the Ti30Zr25Hf15Nb20Ta10 high entropy alloy at temperatures 4.2–350K, Mater. Sci. Eng. A 710 (2018) 136-141.
[150] O.N. Senkov, D.B. Miracle, K.J. Chaput, J.P. Couzinie, Development and exploration of refractory high entropy alloys—A review, J. Mater. Res. (2018) 1-37.
[151] O.N. Senkov, A.L. Pilchak, S.L. Semiatin, Effect of Cold Deformation and Annealing on the Microstructure and Tensile Properties of a HfNbTaTiZr Refractory High Entropy Alloy, Metall. Mater. Trans. A 49(7) (2018) 2876-2892.
[152] S.A. Firstov, T.G. Rogul', N.A. Krapivka, S.S. Ponomarev, V.N. Tkach, V.V. Kovylyaev, V.F. Gorban', M.V. Karpets, Solid-solution hardening of a high-Entropy AlTiVCrNbMo alloy, Russ. Metall. 2014(4) (2014) 285-292.
[153] Z.D. Han, N. Chen, S.F. Zhao, L.W. Fan, G.N. Yang, Y. Shao, K.F. Yao, Effect of Ti additions on mechanical properties of NbMoTaW and VNbMoTaW refractory high entropy alloys, Intermetallics 84 (2017) 153-157.
[154] H. Yao, J.W. Qiao, M. Gao, J. Hawk, S.G. Ma, H. Zhou, MoNbTaV Medium-Entropy Alloy, Entropy 18(5) (2016) 189.

[155] H.W. Yao, J.W. Qiao, M.C. Gao, J.A. Hawk, S.G. Ma, H.F. Zhou, Y. Zhang, NbTaV-(Ti,W) refractory high-entropy alloys: Experiments and modeling, Mater. Sci. Eng. A 674 (2016) 203-211.
[156] L. Lilensten, J.P. Couzinié, L. Perrière, A. Hocini, C. Keller, G. Dirras, I. Guillot, Study of a bcc multi-principal element alloy: Tensile and simple shear properties and underlying deformation mechanisms, Acta Mater. 142 (2018) 131-141.
[157] T.B. Massalski, H. Okamoto, P. Subramanian, L. Kacprzak, Binary alloy phase diagrams, 2nd, ASM International, Ohio 2882 (1990).
[158] O. Senkov, S. Senkova, D. Dimiduk, C. Woodward, D. Miracle, Oxidation behavior of a refractory NbCrMo0. 5Ta0. 5TiZr alloy, J. Mater. Sci. 47(18) (2012) 6522-6534.
[159] T.M. Butler, K.J. Chaput, J.R. Dietrich, O.N. Senkov, High temperature oxidation behaviors of equimolar NbTiZrV and NbTiZrCr refractory complex concentrated alloys (RCCAs), J. Alloys Compd. 729 (2017) 1004-1019.
[160] B. Vishwanadh, N. Sarkar, S. Gangil, S. Singh, R. Tewari, G.K. Dey, S. Banerjee, Synthesis and microstructural characterization of a novel multicomponent equiatomic ZrNbAlTiV high entropy alloy, Scri. Mater. 124 (2016) 146-150.
[161] S. Chen, X. Yang, K. Dahmen, P. Liaw, Y. Zhang, Microstructures and Crackling Noise of AlxNbTiMoV High Entropy Alloys, Entropy 16(2) (2014) 870.
[162] Y. Wu, J. Si, D. Lin, T. Wang, W.Y. Wang, Y. Wang, Z. Liu, X. Hui, Phase stability and mechanical properties of AlHfNbTiZr high-entropy alloys, Mater. Sci. Eng. A 724 (2018) 249-259.
[163] F.G. Coury, T. Butler, K. Chaput, A. Saville, J. Copley, J. Foltz, P. Mason, K. Clarke, M. Kaufman, A. Clarke, Phase equilibria, mechanical properties and design of quaternary refractory high entropy alloys, Mater. Des. 155 (2018) 244-256.
[164] Y. Liu, Y. Zhang, H. Zhang, N. Wang, X. Chen, H. Zhang, Y. Li, Microstructure and mechanical properties of refractory HfMo0.5NbTiV0.5Six high-entropy composites, J. Alloys Compd. 694 (2017) 869-876.
[165] Y. Chen, Y. Li, X. Cheng, Z. Xu, C. Wu, B. Cheng, M. Wang, Interstitial Strengthening of Refractory ZrTiHfNb0.5Ta0.5Ox (x=0.05, 0.1, 0.2) High-Entropy Alloys, Mater. Lett. (2018).
[166] A. Takeuchi, A. Inoue, Classification of bulk metallic glasses by atomic size difference, heat of mixing and period of constituent elements and its application to characterization of the main alloying element, Mater. Trans. 46(12) (2005) 2817-2829.
[167] O.N. Senkov, S.L. Semiatin, Microstructure and properties of a refractory high-entropy alloy after cold working, J. Alloys Compd. 649 (2015) 1110-1123.

[168] N.D. Stepanov, D.G. Shaysultanov, R.S. Chernichenko, D.M. Ikornikov, V.N. Sanin, S.V. Zherebtsov, Mechanical properties of a new high entropy alloy with a duplex ultra-fine grained structure, Mater. Sci. Eng. A 728 (2018) 54-62.
[169] X. Yang, Y. Zhang, P.K. Liaw, Microstructure and Compressive Properties of NbTiVTaAlx High Entropy Alloys, Procedia Eng. 36 (2012) 292-298.
[170] O.N. Senkov, C. Woodward, D.B. Miracle, Microstructure and Properties of Aluminum-Containing Refractory High-Entropy Alloys, JOM 66(10) (2014) 2030-2042.
[171] É. Fazakas, V. Zadorozhnyy, L.K. Varga, A. Inoue, D.V. Louzguine-Luzgin, F. Tian, L. Vitos, Experimental and theoretical study of Ti20Zr20Hf20Nb20X20 (X=V or Cr) refractory high-entropy alloys, Int. J. Refract. Met. Hard Mater. 47 (2014) 131-138.
[172] O.N. Senkov, C.F. Woodward, Microstructure and properties of a refractory NbCrMo0.5Ta0.5TiZr alloy, Mater. Sci. Eng. A 529 (2011) 311-320.
[173] N.N. Guo, L. Wang, L.S. Luo, X.Z. Li, Y.Q. Su, J.J. Guo, H.Z. Fu, Microstructure and mechanical properties of refractory MoNbHfZrTi high-entropy alloy, Mater. Des. 81 (2015) 87-94.
[174] O.N. Senkov, G.B. Wilks, J.M. Scott, D.B. Miracle, Mechanical properties of Nb25Mo25Ta25W25 and V20Nb20Mo20Ta20W20 refractory high entropy alloys, Intermetallics 19(5) (2011) 698-706.
[175] L. Lilensten, J.P. Couzinié, J. Bourgon, L. Perrière, G. Dirras, F. Prima, I. Guillot, Design and tensile properties of a bcc Ti-rich high-entropy alloy with transformation-induced plasticity, Mater. Res. Lett. 5(2) (2017) 110-116.
[176] S. Sheikh, S. Shafeie, Q. Hu, J. Ahlström, C. Persson, J. Veselý, J. Zýka, U. Klement, S. Guo, Alloy design for intrinsically ductile refractory high-entropy alloys, J. Appl. Phys. 120(16) (2016) 164902.
[177] D. MA, O. Chung Wo, J. Liu, J. HE, Determination of Young's modulus by nanoindentation, Sci. China Ser. E: Technol. Sci. 47(4) (2004) 398-408.

Chapter 3 Experimental procedures

3.1 Introduction

This thesis is prepared using the publication-based format. Therefore, the experimental procedures will also be briefly discussed in each research chapter. The aims of this chapter are to detail the synthesis and characterization methods which are employed throughout this PhD thesis. Figure 3.1 shows a diagram briefly depicts the experimental procedure in this PhD thesis.

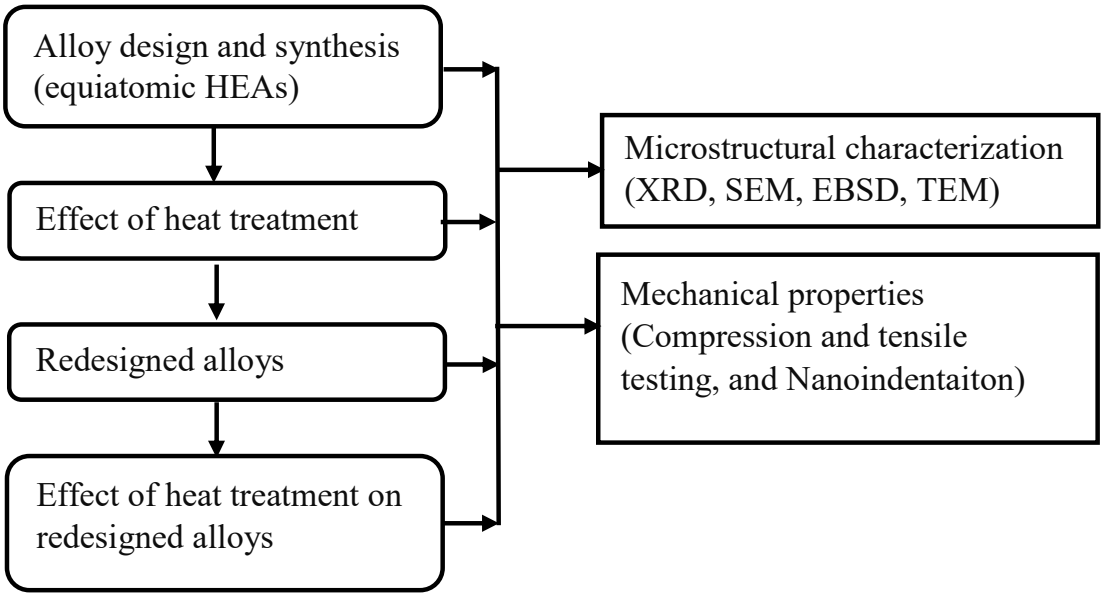

Figure 3.1 Diagram of the experimental procedures throughout this PhD study.

3.2 Alloys Fabrication

3.2.1 Alloys design and raw materials

The alloys in this thesis are designed using the empirical rule to first screen potential alloys that can form a single solid-solution phase as the number of candidates can be numerous. The empirical rule has been discussed in more detail in the literature review chapter. The phase formation in the potential candidate alloys is then assessed using the CALPHAD approach which was performed using the Pandat^{TM} CompuTherm software and the PanNb2019 thermodynamic database. Finally, the chosen alloys are fabricated from pure metals with a minimum purity of 99.95 %. The list of raw materials used in this thesis was shown in Table 3.1.

Table 3.1 List of raw materials used in this thesis.

Pure metals	Form	Suppliers	Purity (%)
Ti	Rod	Alfa Aesar (Australia)	99.95
Zr	Ingots	Shaanxi Getwick Nonferrous Metals Co, LTD	99.95
Nb	Slugs	Alfa Aesar (Australia)	99.95
Ta	Rod	Ningxia Orient Tantalum industry CO., LTD	99.95

3.2.2 Arc-melting and casting procedures

The designed alloys were fabricated using an arc-melter (AM200, Edmund Bühler GmbH) (Figure 3.2(a)) equipped with a water-cooled copper crucible plates with multi-purpose moulds (Figure 3.2(b)) and a generator (Vario hybrid 400-DC-HF). Each alloy composition was prepared in a batch of 20 grams and loaded in the water-cooled copper mould with the order of high melting point metal stacking on top of lower melting point metals to minimize the evaporation. After that, the chamber was closed, evacuated to about 5 Pa by a rotary pump, and then flushed with pure argon. After evacuation and flushing the chamber with the pure argon for two times, the chamber was further evacuated to a high vacuum condition (about 10^{-4} Pa) by a diffusion pump. Finally, the chamber was refilled with the pure argon for the arc-melting process. The materials were then melted by the arc which was controlled by the generator and an arc-driving arm. Pure zirconium/titanium was used as an oxygen getter. The designed alloys were melted six times and flipped after each melting to produce a 20-gram alloy button. The molten alloy was held in the liquid state for 10 minutes during each cycle of melting for chemical homogeneity. Finally, five buttons of each alloy were cast in a rectangle-shape mould to form an alloy ingot which has a rectangular prismatic shape with dimension of 12 mm × 8 mm × 90 mm (thickness of 8 mm) as shown in Figure 3.2. After casting, the ingot was weighed to determine the evaporation.

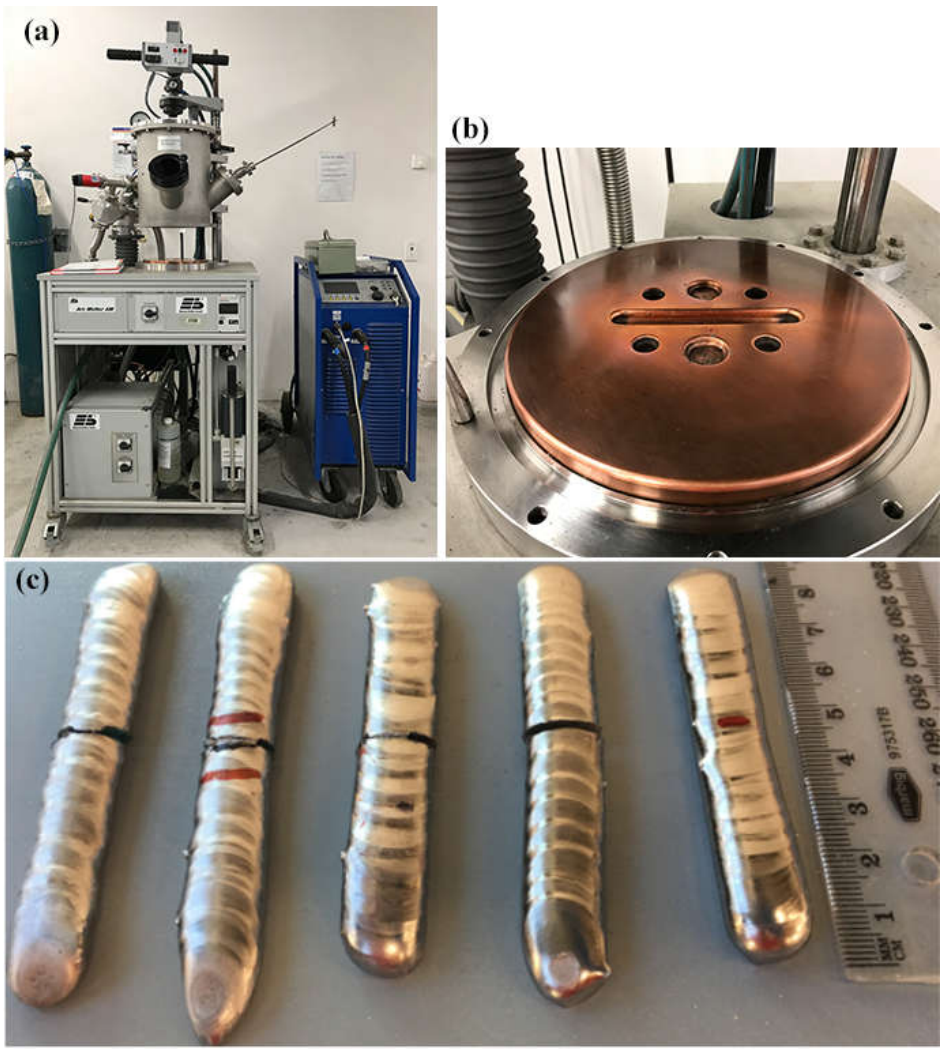

Figure 3.2 (a) Arc Melter AM200 (Edmund Bühler GmbH), (b) Water-cooled copper crucible plate with multi-purpose moulds (for button and rod samples), (c) the as-cast ingots.

3.2.3 Heat treatment

The cast ingot was sectioned to get 2 small ingot samples with dimensions of 12 mm × 8 mm × 45 mm as shown in Figure 3.2(c). One small ingot of each alloy composition was used to study the effect of heat treatment on the microstructure and mechanical properties. A carbolite tube furnace was employed for the heat treatment experiment. Before loading the as-cast ingots into the furnace, they were encapsulated with a box made from pure titanium sponges with the purpose of avoiding oxidation. The as-cast ingots were heat-treated at 1200 ^{o}C at a heating/cooling rate of 4 ^{o}C/min under vacuum condition (10^{-4} Pa).

3.3 Microstructural characterization

In order to characterize the crystal structure and microstructure of the as-cast and as-heat-treated ingots, their cross-sections were mounted using a hot compression method with the PolyFast resin and then ground using SiC papers with the size of the abrasive particles ranging from 40.5 μm to 2.5 μm. The ground surfaces were then polished using a mixture of 20% hydrogen peroxide (H_2O_2) and 80% OP-S NonDry (0.04 μm). Also after compression and tensile testing, the longitudinal cross-section of the deformed samples was prepared as mentioned above for metallographic characterization.

The polished samples were used for determining the crystal structure by X-ray diffraction (XRD). The XRD characterization was conducted using a Bruker D8 Advance MKII with a monochromatic Cu Kα radiation. The XRD patterns were analysed using Pawley method implemented in the software package TOPAS (version 5 Bruker AXS). The microstructural characterization was performed using scanning electron microscopy (SEM) and transmission electron microscopy (TEM). Two SEM models were employed, i.e. JEOL 6610 equipped with an electron backscatter diffraction (EBSD) detector and an energy dispersive X-ray (EDS), and FEI Scios DualBeam FIB-SEM. TEM characterization was performed with a TEM, Philips Tecnai F20 and an aberration-corrected scanning transmission electron microscopy (STEM, JEOL JEM-200CF). TEM specimens were prepared using a focused ion milling (FIB) (Model FEI Scios DualBeam FIB-SEM).

3.4 Density measurement and mechanical Properties

3.4.1 Density measurement

As the material ingot normally exists in irregular shapes, it is difficult to directly measure the accurate volume of the ingot. Therefore, the Archimedes method is used to determine the ingot volume so that the density can be calculated. The density of each fabricated alloy was measured using the Archimedes method as shown in Figure 3.3 below.

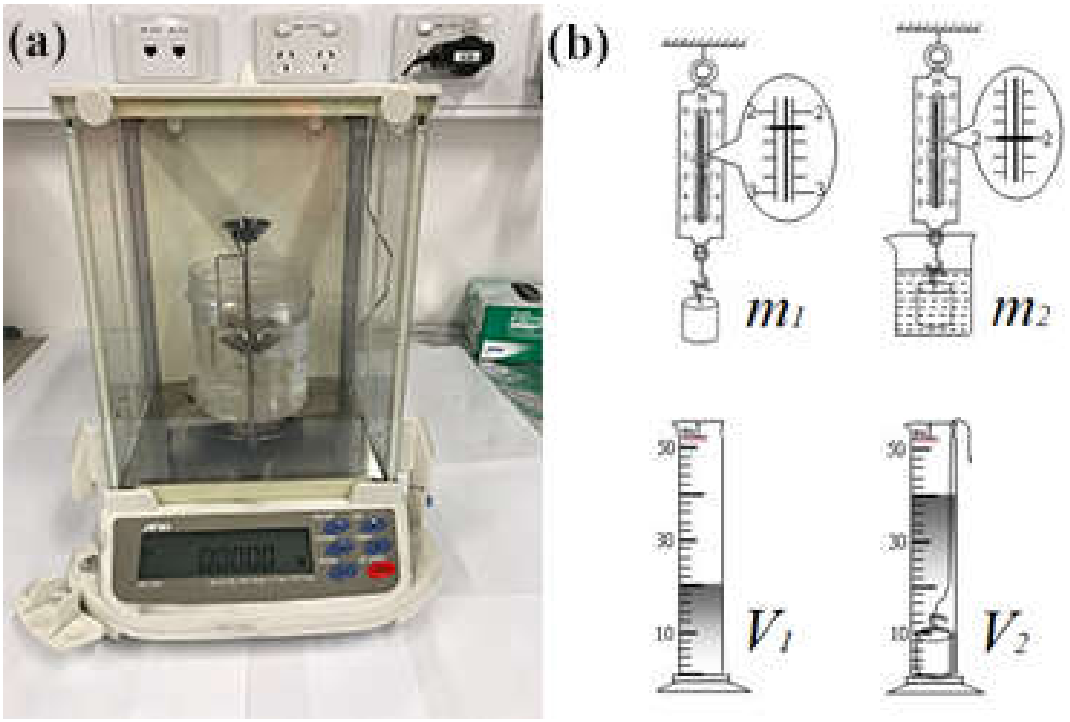

Figure 3.3 (a) the density measurement equipment; (b) mechanism of density measurement by Archimedes method.

The mass of the ingot was measured in the air and in H-Galden fluid by a high accuracy balance which is used to determine the volume (V) of the ingot by the Eq. 3.1 below:

$$V_{ingot} = V_2 - V_1 = \frac{m_2 - m_1}{\rho_l} \qquad \text{(Eq. 3.1)}$$

Where m_2 and m_1 are the weighs of the alloy ingot in the air and in the liquid, respectively, and the value of V_{ingot} calculated by Eq. 3.1 is used to determine ingot density of the alloy.

3.4.2 Nanoindentation

Nanoindentation was conducted using a Hysitron TI900 Triboindenter® to measure the nanoindentation hardness and the modulus of the studied alloys. Samples were ground and polished before performing the nanoindentation testing. A Berkovich indenter with a tip radius less than 100 nm was used to indent on the polished sample surface by gradually increasing the applied load from 0 to 2000 μN. The load was maintained at the peak value (2000μN) and then released. The measurement of load (P) and displacement (h) was recorded automatically. The nanoindentation hardness and modulus (E) were calculated using the Oliver-Pharr method [21, 177].

3.4.3 Tensile and compression properties

a. Compression testing

Cylindrical samples (ϕ3.5 mm ×6 mm) for the compression testing were prepared using an electrical discharging cutting machine. Compression testing at room temperature (~25 ºC) was conducted using an Instron 5584 equipped with an advanced video extensometer (AEV) for strain measurement as shown in Figure 3.4 at a strain rate of 5×10^{-3} s^{-1}. The compression testing at elevated temperatures (600 ºC, 800 ºC, 1000 ºC, and 1200 ºC) was performed with a dilatometer type 805 (DIL805A/D) at a strain rate of 10^{-2} s^{-1}. Before the specimens were compressed, they were heated to desired temperatures by induction coils with a heating rate of 100 ºC/min and then soaked for 15 minutes under a vacuum condition of (~ 9×10^{-3} Pa). The specimen temperature was controlled by a thermocouple welded at a side of the specimens. After reaching 30% compression strain, the compression testing at elevated temperatures was stopped and the compressed specimen was cooled in the air.

Figure 3.4 Compression/tensile testing machine model: Instron 5584.

b. Tensile testing

Tensile testings at room temperature (~25 ºC) were conducted using an Instron 5584 machine equipped with an advanced video extensometer as shown in Fig. 3.4 at a constant strain rate of 5×10^{-3} s^{-1}. Dog-bone shape samples with 1.5 mm thickness, 2.9 mm width, and 8 mm gauge length were prepared using an electrical discharging cutting machine for the tensile testings.

Chapter 4 A Novel Quaternary Equiatomic Ti-Zr-Nb-Ta Medium Entropy Alloy (MEA)

4.1 Chapter overview

An important feature that distinguishes between HEAs and conventional alloys is the severe lattice distortion due to substantial substitutional solid solution, which serves as a premier strengthening mechanism for these alloys. This severe lattice distortion, designated as atomic mismatch (δ), can be used as an important parameter for designing HEAs. A large value of δ, which corresponds to severe lattice distortion, typically offers high strength or hardness but low ductility for refractory HEAs. In principle, a minimum of five elements is required to form a HEA in order to maximize the mixing entropy for the formation of a stable single solid-solution phase. However, the situation can change for refractory metals in that four constituent elements may be sufficient to form a stable single solid-solution phase alloy. Therefore, in the present work, a novel quaternary equiatomic TiZrNbTa medium entropy alloy (MEA) was derived from a quinary equiatomic biocompatible TiZrNbTaMo HEA based on the empirical rule and Pandat^{TM} simulation to obtain a single solid-solution phase MEA. Since TiZrNbTaMo HEA exhibited a high strength but low ductily in both as-cast and as-annealed conditions under compression (<9%), excluding Mo in our new designed MEA can decrease δ, which can then benefit the ductility of the resultant MEA. The quaternary TiZrNbTa MEA was fabricated using arc-melting method from pure Ti, Zr, Nb, and Ta ingots with a purity of 99.95%. The microstructure and mechanical properties of this new MEAs were studied and evaluated details in the as-cast state. We found that the equiatomic TiZrNbTa MEA exhibited a single BCC solid-solution phase in as-cast states. In addition, it shown an excellent combination of compressive strength and ductility at room temperature compared with its counterpart TiZrNbTaMo high entropy alloys. The details on this work are published in *Intermetallics* (vol. 101 (2018): 39-43) and presented in Section 4.2.

4.2 Publication

A Novel Quaternary Equiatomic Ti-Zr-Nb-Ta Medium Entropy Alloy (MEA)

V. T. Nguyen [a], M. Qian [c, *], Z. Shi [a], T. Song [c], L. Huang [a], and J. Zou [a, b, *]

[a] Materials Engineering, [b] Centre of Microscopy and Microanalysis, The University of Queensland, Brisbane, QLD4072, Australia

[c] RMIT University, School of Engineering, Centre of Additive Manufacturing, Melbourne, Victoria 3000, Australia

Abstract

The high strength and low ductility of body-centred cubic (BCC) high entropy alloys (HEAs) both result from the severe lattice-distortion effect as measured by the atomic mismatch (δ). We report a novel quaternary equiatomic Ti-Zr-Nb-Ta (δ = 4.8 %) medium entropy alloy (MEA), redesigned from a quinary equiatomic Ti-Zr-Nb-Ta-Mo (δ = 5.5 %) HEA, for much improved strength-ductility combinations and potentially improved biocompatibility by reducing δ through excluding Mo. The as-cast MEA exhibited a single BCC phase and achieved compressive yield strength of 1100 ± 90 MPa. However, its compression strain to fracture (48 ± 6 %), which is about five times that of the Ti-Zr-Nb-Ta-Mo HEA. Its elastic modulus (116 ± 6 GPa) is similar to that of Ti-6Al-4V.

Introduction

High entropy alloys (HEAs) have received significant attention since the concept was initiated about a decade ago [1, 2]. Up till now, a vast number of HEAs have been designed and fabricated for evaluation. Specific HEAs have exhibited excellent resistance to corrosion [3-5], oxidation [6, 7] and wear [8]. In addition, some compositions have shown superior mechanical properties at cryogenic temperatures [9], room temperature [10-16], or high temperatures [10, 12, 17-21]. Recent studies [4, 22] have reported a pioneering quinary equiatomic Ti-Nb-Zr-Ta-Mo HEA for biomedical applications. Although this HEA showed high compressive yield strengths up to 1400 MPa, its compressive strain is less than 9 % in both the as-cast and annealed (homogenized) conditions. This low ductility essentially excludes it from most load-bearing applications. In addition, Mo displays a much lower safe ion concentration than both Ti and Nb for orthopedic applications [23]. Another concern is that the elastic modulus of Mo (329 GPa) is remarkably higher than that of each other elements (Ti, Zr, Nb and Ta, Table 1) in this HEA. Consequently, the equiatomic Ti-Zr-Nb-Ta-Mo HEA exhibited high modulus (153 GPa) [4],

which is 5-10 times higher than the modulus of human cortical bones, implying a severe "stress shielding effect" [24]. These shortcomings make this equiatomic Ti-Zr-Nb-Ta-Mo HEA much less competitive than conventional non-HEAs such as Ti-6Al-4V for orthopedic applications.

In principle, a minimum of five elements is required from a HEA design standpoint in order to maximize the mixing entropy for the formation of a stable single solid-solution phase [25]. However, the situation can change for refractory metals in that four constituent elements may be sufficient to form a stable single solid-solution phase alloy [10, 14, 26]. Such novel single solid-solution phase alloys are referred to as medium entropy alloys (MEAs) [27] in order to distinguish them from the HEAs. The relaxation of this design rule provides unique flexibility for adjusting the strength and ductility of the resultant MEA due to the reduced atomic mismatch (δ) [12, 25].

In this study, we designed and fabricated a novel quaternary equiatomic Ti-Zr-Nb-Ta MEA from the equiatomic biocompatible Ti-Zr-Nb-Ta-Mo HEA by reducing the value of δ from 5.5 % (HEA) to 4.8 % (MEA) through excluding the constituent element Mo. The purpose was to obtain a strong and ductile MEA with improved biocompatibility. The phase formation in this equiatomic MEA was simulated using both Pandat^{TM} CompuTherm and an established empirical rule. The phase constituent and microstructure were characterized in detail, and its mechanical properties were evaluated.

1. Methods

The quaternary equiatomic Ti-Zr-Nb-Ta MEA was fabricated from individual elemental metals with a minimum purity of 99.95 % using a conventional arc-melting furnace under a titanium-getter argon atmosphere. The alloy button (~20 g) was remelted six times for chemical homogeneity and flipped before each remelting. In addition, the melt was kept in the liquid state for 10 min during each melting. It was cast into a water-cooled copper mould to form a cuboidal bar with dimensions of 25 mm long, 12 mm wide, and 8 mm high. Small cylindrical samples (ϕ3.5 mm × 6.3 mm) were cut from the as-cast bar for compression testing.

Cross-sections of the as-cast alloy bar were ground using SiC papers and polished using a suspension of 80 % OP-S NonDry (0.04 μm) and 20 % of hydrogen peroxide (H_2O_2) for microstructural characterisation. X-ray diffraction (XRD) was used for phase identification. The XRD data were collected on a Bruker D8 Advance MKII using a Cu target tube operated at 40 kV, and analyzed using the Pawley method, which was implemented in the software

package TOPAS (Version 5 Bruker AXS). The microstructure was characterised using scanning electron microscopy (SEM, JOEL 6610, equipped with an energy dispersive spectrometer (EDS) and an electron backscattered diffraction (EBSD) detector), and transmission electron microscopy (TEM, Philips Tecnai F20 FEG-S/TEM). TEM specimens were prepared by focused ion milling (FEI Scious FIB).

Compression testing was performed with an Instron-5588 at room temperature (~25 ^{o}C) at a strain rate of 5×10^{-3} s^{-1}. The hardness was randomly measured at 8 different areas on a polished cross-section surface using nanoindentation (Nanoindenter XP, MTS Systems Corp., Oakridge, TN) with a Berkovich indenter (tip radius < 100 nm).

2. Results and Discussion

Fig. 1a predicts the solidification sequence of the equiatomic Ti-Zr-Nb-Ta MEA using Pandat^{TM} CompuTherm based on the Scheil model [27]. The predicted significant solidification gap (496 ^{o}C) of this alloy suggests that the solute content in the initial solid and the last solid to form can be significantly different if solidified slowly. Fast cooling such as water-cooled copper mould casting is thus necessary to mitigate the chemical inhomogeneity. The Pandat^{TM} simulation shows a fully body-centred cubic (BCC) solid-solution phase, which supports our design expectation. Another method to estimate the phase formation in an HEA is by the use of an empirical rule [25], which is based on the atomic mismatch (δ), mixing enthalpy (ΔH_{mix}), a special dimensionless thermodynamic parameter Ω, and valence electron concentration (VEC). The equations used for calculating these three parameters can be found in Refs. [25, 28, 29]. The empirical rule states that a HEA may solidify as a single solid-solution BCC phase if its four parameters satisfy $\delta \leq 6.6$ %, -11.6 kJ·mol^{-1} < ΔH_{mix} < 3.2 kJ·mol^{-1}, $\Omega \geq 1.1$ and VEC < 6.87 [29]. The calculated values of each parameter for the equiatomic Ti-Zr-Nb-Ta MEA are summarised in Table 1 and the requirements are met.

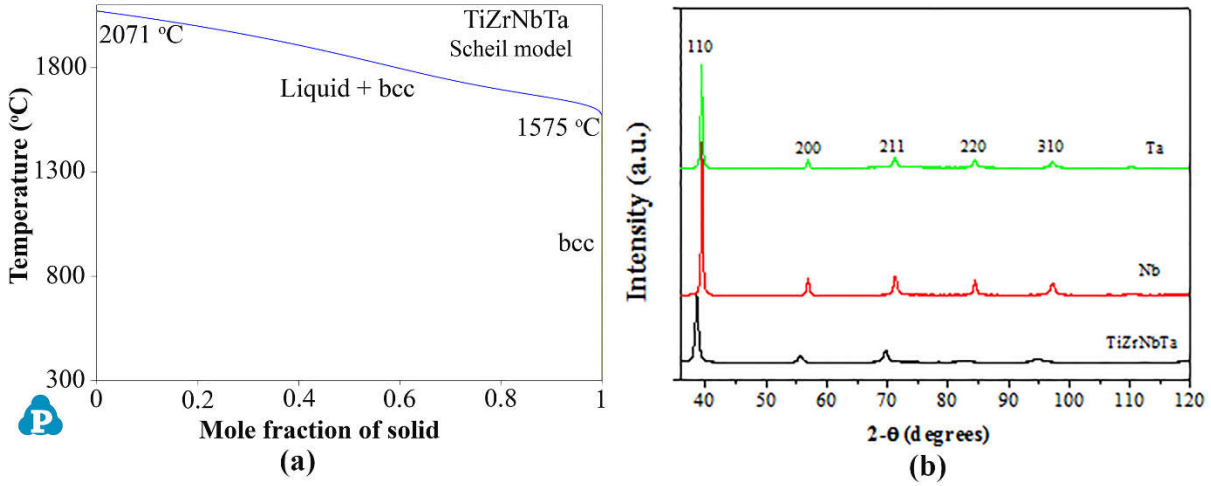

Figure 1 (a) Solidification sequence of the equiatomic Ti-Zr-Nb-Ta MEA by the Scheil model. (b) XRD results of the as-cast equiatomic Ti-Zr-Nb-Ta MEA and the as-received BCC Ta and Nb metals.

Fig. 1b shows the XRD results of the as-cast equiatomic Ti-Zr-Nb-Ta MEA together with those obtained from the two BCC Ta and Nb metals used. The as-cast MEA showed a single BCC phase, in line with the predictions presented above. Its lattice parameter (a_{MEA}) was determined to be 3.368 Å, which is almost identical to the predicted value of 3.365 Å (Table 1) using Vegard's law, i.e., $a = \Sigma c_i a_i$, where c_i and a_i are the molar fraction and lattice parameter of element i, respectively [30]. It is noted that BCC lattice size of Ti and Zr at room temperature was extrapolated from their BCC lattice size at high temperature [4]. The lattice parameters of BCC Ta and Nb were determined to be a_{Ta} = 3.330 Å and a_{Nb} = 3.330 Å, consistent with the PDF card 00-035-0789 for Nb and PDF card 00-004-0788 for Ta. The close similarity between a_{MEA} (3.368 Å) and a_{Ta} (3.330 Å) or a_{Nb} (3.330 Å) suggests that the Ti-Zr-Nb-Ta MEA may have just inherited the same BCC lattice of the refractory Ta and Nb, which together make 50 at.% of the constituent atoms in the MEA. The 1.14 % of increase in a_{MEA} over a_{Ta} or a_{Nb} can be attributed to solid-solution induced expansion by Ti and Zr.

Table 1 Physical, geometric, and thermodynamic properties of Ti, Ta, Nb, Zr, the quaternary Ti-Zr-Nb-Ta MEA and the quinary Ti-Zr-Nb-Ta-Mo HEA.

Parameters or properties		Materials					
		Ti	Zr	Nb	Ta	TiZrNbTa MEA	TiZrNbTaMo HEA [4, 22]
Atomic number		22	40	41	73	-	-
Lattice structure	High temperature	BCC	BCC	BCC	BCC	-	-
	Room temperature	HCP	HCP	BCC	BCC	-	-
*Lattice parameter		3.276	3.582	3.301	3.303	3.365	-
Melting point or liquidus (C^o)		1660	1952	2468	3017	2274	-
Atomic radius (r, nm)		0.1462	0.1603	0.1429	0.1430	-	-
ΔH_{mix} (kJ/mol)		Ti	0	2	1	2.5	-
		Zr	-	4	3		
		Nb	-	-	0		
		Ta	-	-	-		
Dimensionless parameter Ω		-	-	-	-	11.628	-
Atomic mismatch δ(%)		-	-	-	-	4.8	5.5
Valence electron concentration (VEC)		4	4	5	5	4.5	4.8
Elastic modulus, E (GPa)		116	88	105	186	116	153
Vickers microhardness, Hv (GPa)		0.97	0.903	1.32	0.873	-	-
Yield strength (MPa)		195	280	240	170	-	1400

* Note: BCC lattice parameter at room temperature [4].

Fig. 2a shows the representative microstructure of the as-cast MEA in the backscattered electron (BSE) mode. The uneven contrast (Z-contrast) reflects the difference in composition between the dendrite and the inter-dendritic regions due to constitutional segregation during solidification. This is further shown in Fig. 2b. Fig. 2c shows EDS mapping results of the constituent elements, in which the dendrite was enriched with Ta due to its higher melting point, whereas higher concentrations of Zr, Ti, and Nb were observed in the inter-dendritic regions. The EBSD phase analysis shown in Fig. 2(d, e) confirmed the presence of only the BCC phase in the as-cast MEA. The grain size was evaluated from the grain orientation map and determined to be ~150 μm.

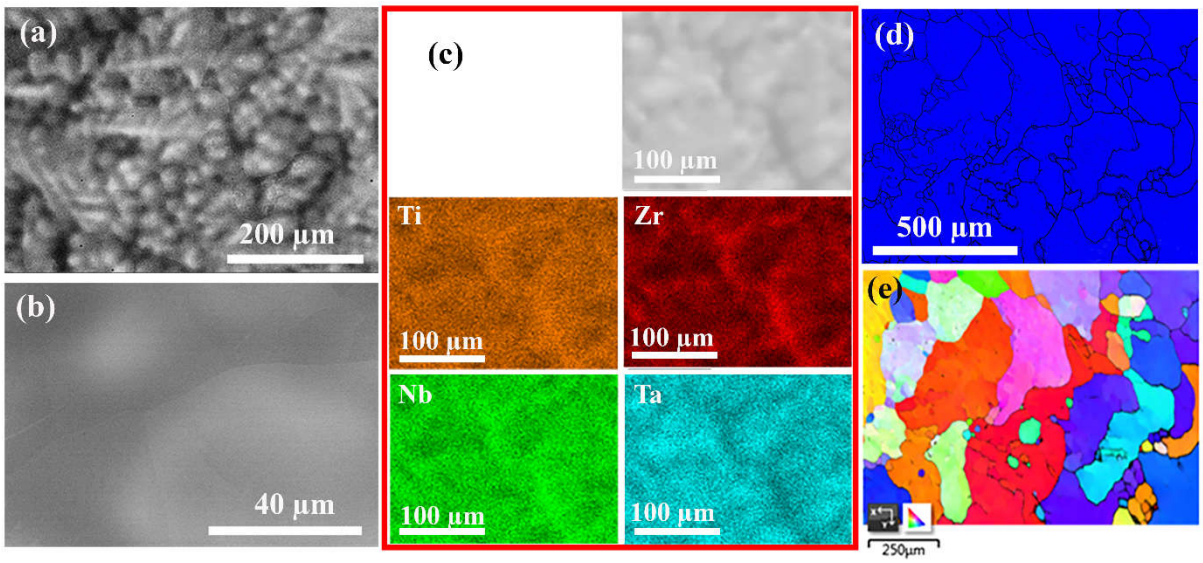

Figure 2 SEM characterization of the as-cast Ti-Zr-Nb-Ta MEA: (a) SEM-BSE image; (b) a zoom-in view of the grain boundary area; (c) SEM image and corresponding EDS maps; (d) EBSD-phase mapping; and (e) grain orientation map.

Since a secondary phase may form in the grain boundary (GB) areas and is often not detectable by XRD due to its small volume fraction, TEM investigations were performed on a number of GB areas in the as-cast MEA to clarify this concern. Fig. 3a shows a bright-field (BF) TEM image taken from a typical GB area in the as-cast MEA, and the inset displays a selected area electron diffraction (SAED) pattern taken along the [001] zone-axis from the dark grain in Fig. 3a. A high-resolution TEM (HRTEM) image of a selected GB area is shown in Fig. 3b. No second phase was observed under BF-TEM or HRTEM images, which is consistent with XRD, SEM, and EBSD results. The EDS mapping results shown in Fig. 3c revealed that the distribution of each constituent element (Ti, Zr, Nb, and Ta) in the GB area is essentially homogeneous.

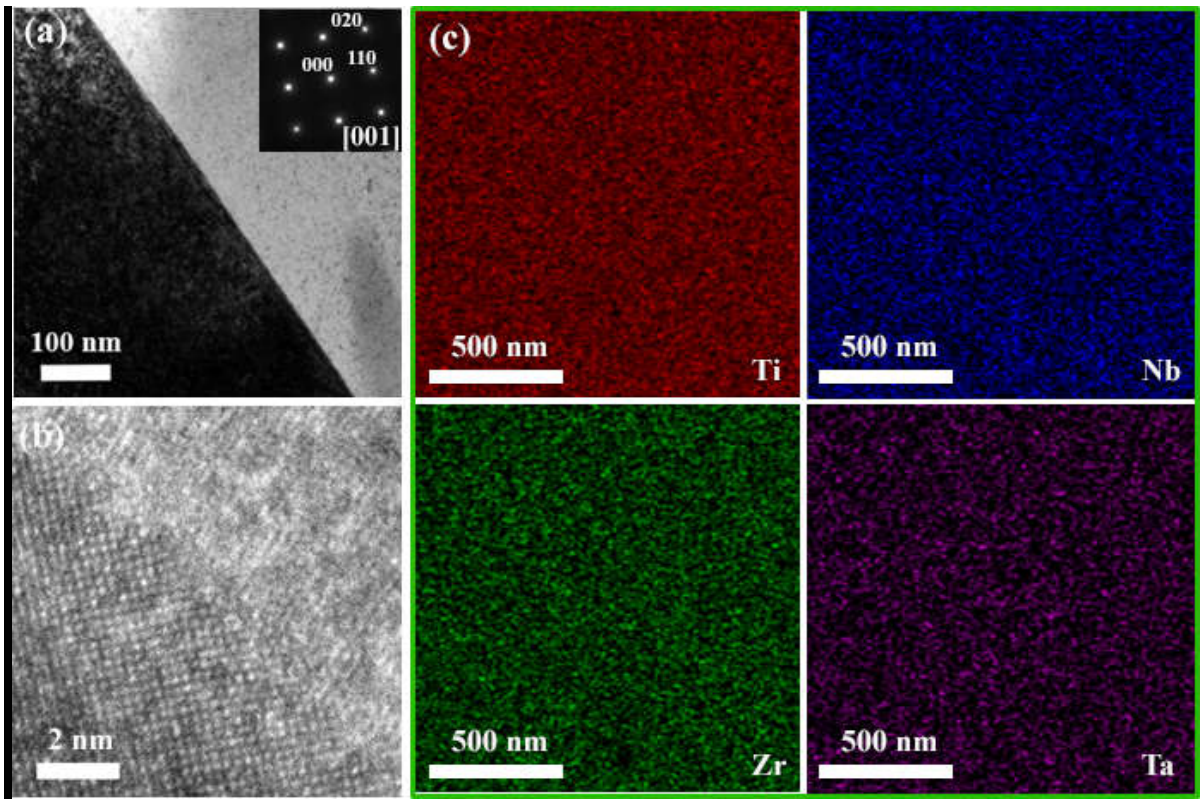

Figure 3 TEM characterization of the as-cast Ti-Zr-Nb-Ta MEA: (a) bright field TEM image of a grain boundary area, and SAED pattern of the dark grain obtained along the [001] zone axis; (b) HRTEM image of the grain boundary; and (c) EDS maps of the grain boundary area.

Fig. 4a shows the true stress-strain curves measured from the as-cast Ti-Zr-Nb-Ta MEA at room temperature. After yielding starts under compression, the diameter of the sample will keep increasing. In the initial stage, the strength increases with increasing compressive strain due to work hardening development. After reaching the maximum, the strength normally starts to decrease due to the substantial increase in the diameter of the sample. This is shown in all the three-compressive strength-strain curves. However, the rate of decrease in strength after reaching the maximum is distinctly different. If the axis of the cylindrical sample is kept the same as the axis of the compressive load, the compressive stress will first increase steadily and then decrease as shown in curve 1. However, if the axis of the cylindrical sample becomes slightly off or no longer parallel to the axis of the compressive load, the sample under compression will start tilting at the time when reaching about the maximum strength. This tilting leads to an accelerated rate in the decrease of the strength as shown in curve 2 and 3.

The compressive yield strength and strain achieved 1100 ± 90 MPa and 48 ± 6 %, respectively. The exclusion of Mo resulted in a decrease of the atomic mismatch δ from 5.5 % for the quinary

Ti-Zr-Nb-Ta-Mo HEA to 4.8 % for the quaternary Ti-Zr-Nb-Ta MEA. According to Tian *et al* [31], the hardness of a HEA is proportional to δ. As a result, the yield strength of the Ti-Zr-Nb-Ta MEA is lower than that of the Ti-Zr-Nb-Ta-Mo HEA. On the other hand, solid-solution alloys generally experience a strength-ductility trade-off, which is intrinsic of the interactions between the solute atoms and dislocations. In that regard, the reduced atomic mismatch or solid-solution strengthening effect due to the removal of Mo increased the compressive strain five times, i.e. from < 9 % for the quinary Ti-Zr-Nb-Ta-Mo HEA to 48 ± 6 % for the quaternary Ti-Zr-Nb-Ta MEA. It should be noted that despite the exclusion of Mo, the compressive yield strength of the MEA (1100 ± 90 MPa) is still clearly higher than that of the benchmark biomedical titanium alloy Ti-6Al-4V (970 MPa [32]). The novel MEA thus shows an excellent combination of compressive strength and ductility in the as-cast state.

Fig. 4b displays the load-displacement curves obtained by nanoindentation of the as-cast MEA. The nanoindentation hardness and modulus (E) of the as-cast Ti-Zr-Nb-Ta MEA were calculated using the Oliver-Pharr method as used in Ref. [33]. The hardness was determined to be 4.6 ± 0.2 GPa due to the strong solid-solution strengthening effect compared with the hardness of each elemental metal listed in Table 1. The modulus was calculated to be 116 ± 6 GPa, which is clearly lower than that of the quinary Ti-Zr-Nb-Ta-Mo HEA (153 GPa) [4], but comparable to that of the benchmark Ti-6Al-4V (113 GPa [32]).

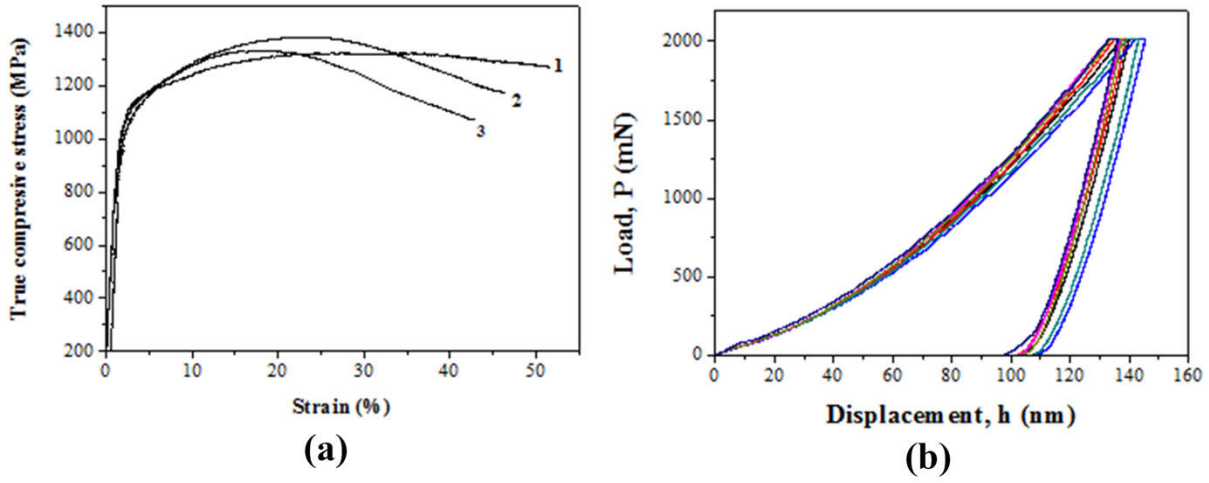

Figure 4 Mechanical properties of the as-cast Ti-Zr-Nb-Ta MEA at room temperature: (a) true compression stress-strain curve and (b) nanoindentation results.

3. Conclusions

In summary, an equiatomic quaternary Ti-Zr-Nb-Ta MEA has been designed and fabricated by reducing the atomic mismatch (δ) of the equiatomic quinary Ti-Zr-Nb-Ta-Mo (δ= 5.5 %) HEA by excluding the constituent element Mo. The resultant as-cast Ti-Zr-Nb-Ta MEA showed an excellent combination of compressive yield strength and ductility. In particular, its compressive strain is four times better (48 ± 6 %) than that of the original equiatomic quinary Ti-Zr-Nb-Ta-Mo HEA, whilst its yield strength (>1000 MPa) is clearly higher than that of the benchmark Ti-6Al-4V for orthopaedic applications. In addition, the elastic modulus of the equiatomic Ti-Zr-Nb-Ta MEA is lower than that of the quinary Ti-Zr-Nb-Ta-Mo HEA and comparable to that of Ti-6Al-4V. These properties make this MEA a promising candidate for biomedical applications.

Acknowledgement

This work was supported by the Australian Research Council (ARC) through ARC LP130100913 and the Baosteel-Australia Joint Research and Development Centre through BA110014LP. VTN thanks the International Postgraduate Research *Scholarship* (IPRS) Program for providing him with a PhD scholarship. The Australian Microscopy & Microanalysis Research Facility is acknowledged for providing characterization facilities.

References

[1] B. Cantor, I.T.H. Chang, P. Knight, A.J.B. Vincent, Microstructural development in equiatomic multicomponent alloys, Mater. Sci. Eng. A 375–377 (2004) 213-218.

[2] J.W. Yeh, S.J. Lin, T.S. Chin, J.Y. Gan, S.K. Chen, T.T. Shun, C.H. Tsau, S.Y. Chou, Formation of simple crystal structures in Cu-Co-Ni-Cr-Al-Fe-Ti-V alloys with multiprincipal metallic elements, Metall. Mater. Trans. A 35(8) (2004) 2533-2536.

[3] J. Li, X. Yang, R. Zhu, Y. Zhang, Corrosion and Serration Behaviors of TiZr0.5NbCr0.5VxMoy High Entropy Alloys in Aqueous Environments, Metals 4(4) (2014) 597.

[4] S.P. Wang, J. Xu, TiZrNbTaMo high-entropy alloy designed for orthopedic implants: As-cast microstructure and mechanical properties, Mater. Sci. Eng. C 73 (2017) 80-89.

[5] Y.J. Hsu, W.C. Chiang, J.K. Wu, Corrosion behavior of FeCoNiCrCu x high-entropy alloys in 3.5% sodium chloride solution, Mater. Chem. Phys. 92(1) (2005) 112-117.

[6] O. Senkov, S. Senkova, D. Dimiduk, C. Woodward, D. Miracle, Oxidation behavior of a refractory NbCrMo0. 5Ta0. 5TiZr alloy, J. Mater. Sci 47(18) (2012) 6522-6534.

[7] B. Gorr, F. Müller, M. Azim, H.J. Christ, T. Müller, H. Chen, A. Kauffmann, M. Heilmaier, High-Temperature Oxidation Behavior of Refractory High-Entropy Alloys: Effect of Alloy Composition, Oxid. Met. (2017) 1-11.

[8] A. Poulia, E. Georgatis, A. Lekatou, A. Karantzalis, Dry Sliding Wear Response of MoTaWNbV High Entropy Alloy, Adv. Eng. Mater. 19(2) (2017).

[9] B. Gludovatz, A. Hohenwarter, D. Catoor, E.H. Chang, E.P. George, R.O. Ritchie, A fracture-resistant high-entropy alloy for cryogenic applications, Science 345(6201) (2014) 1153-1158.

[10] O. Senkov, G. Wilks, J. Scott, D. Miracle, Mechanical properties of Nb 25 Mo 25 Ta 25 W 25 and V 20 Nb 20 Mo 20 Ta 20 W 20 refractory high entropy alloys, Intermetallics 19(5) (2011) 698-706.

[11] H. Huang, Y. Wu, J. He, H. Wang, X. Liu, K. An, W. Wu, Z. Lu, Phase Transformation Ductilization of Brittle High-Entropy Alloys via Metastability Engineering, Adv. Mater. (2017).

[12] Y. Zhang, T.T. Zuo, Z. Tang, M.C. Gao, K.A. Dahmen, P.K. Liaw, Z.P. Lu, Microstructures and properties of high-entropy alloys, Prog. Mater Sci. 61 (2014) 1-93.

[13] O.A. Waseem, H.J. Ryu, Powder Metallurgy Processing of a W(x)TaTiVCr High-Entropy Alloy and Its Derivative Alloys for Fusion Material Applications, Sci. Rep 7 (2017) 1926.

[14] H.W. Yao, J.W. Qiao, M.C. Gao, J.A. Hawk, S.G. Ma, H.F. Zhou, Y. Zhang, NbTaV-(Ti,W) refractory high-entropy alloys: Experiments and modeling, Mater. Sci. Eng. A 674 (2016) 203-211.

[15] S. Maiti, W. Steurer, Structural-disorder and its effect on mechanical properties in single-phase TaNbHfZr high-entropy alloy, Acta Mater. 106 (2016) 87-97.

[16] N.N. Guo, L. Wang, L.S. Luo, X.Z. Li, R.R. Chen, Y.Q. Su, J.J. Guo, H.Z. Fu, Effect of composing element on microstructure and mechanical properties in Mo–Nb–Hf–Zr–Ti multi-principle component alloys, Intermetallics 69 (2016) 13-20.

[17] O. Senkov, J. Scott, S. Senkova, F. Meisenkothen, D. Miracle, C. Woodward, Microstructure and elevated temperature properties of a refractory TaNbHfZrTi alloy, J. Mater. Sci 47(9) (2012) 4062-4074.

[18] O.N. Senkov, S.V. Senkova, D.B. Miracle, C. Woodward, Mechanical properties of low-density, refractory multi-principal element alloys of the Cr–Nb–Ti–V–Zr system, Mater. Sci. Eng. A 565 (2013) 51-62.

[19] N.D. Stepanov, D.G. Shaysultanov, G.A. Salishchev, M.A. Tikhonovsky, Structure and mechanical properties of a light-weight AlNbTiV high entropy alloy, Mater. Lett. 142 (2015) 153-155.

[20] N.N. Guo, L. Wang, L.S. Luo, X.Z. Li, R.R. Chen, Y.Q. Su, J.J. Guo, H.Z. Fu, Hot deformation characteristics and dynamic recrystallization of the MoNbHfZrTi refractory high-entropy alloy, Mater. Sci. Eng. A 651 (2016) 698-707.
[21] C.C. Juan, M.H. Tsai, C.W. Tsai, C.M. Lin, W.R. Wang, C.C. Yang, S.K. Chen, S.J. Lin, J.W. Yeh, Enhanced mechanical properties of HfMoTaTiZr and HfMoNbTaTiZr refractory high-entropy alloys, Intermetallics 62 (2015) 76-83.
[22] M. Todai, T. Nagase, T. Hori, A. Matsugaki, A. Sekita, T. Nakano, Novel TiNbTaZrMo high-entropy alloys for metallic biomaterials, Scripta Mater. 129 (2017) 65-68.
[23] Y. Li, C. Wong, J. Xiong, P. Hodgson, C. Wen, Cytotoxicity of titanium and titanium alloying elements, J. Dent. Res 89(5) (2010) 493-497.
[24] M. Geetha, A.K. Singh, R. Asokamani, A.K. Gogia, Ti based biomaterials, the ultimate choice for orthopaedic implants – A review, Prog. Mater. Sci 54(3) (2009) 397-425.
[25] Y. Zhang, Y.J. Zhou, J.P. Lin, G.L. Chen, P.K. Liaw, Solid-solution phase formation rules for multi-component alloys, Adv. Eng. Mater. 10(6) (2008) 534-538.
[26] O. Senkov, G. Wilks, D. Miracle, C. Chuang, P. Liaw, Refractory high-entropy alloys, Intermetallics 18(9) (2010) 1758-1765.
[27] J.W. Yeh, Alloy design strategies and future trends in high-entropy alloys, JOM 65(12) (2013) 1759-1771.
[28] G. Sheng, C.T. Liu, Phase stability in high entropy alloys: formation of solid-solution phase or amorphous phase, Prog. Nat. Sci 21(6) (2011) 433-446.
[29] S. Guo, Phase selection rules for cast high entropy alloys: an overview, Mater. Sci. Technol. 31(10) (2015) 1223-1230.
[30] A.R. Denton, N.W. Ashcroft, Vegard's law, Phys. Rev. A 43(6) (1991) 3161.
[31] F. Tian, L.K. Varga, N. Chen, J. Shen, L. Vitos, Empirical design of single phase high-entropy alloys with high hardness, Intermetallics 58 (2015) 1-6.
[32] ASM Aerospace Specification Metals, Titanium Ti-6Al-4V (Grade 5), Annealed. http://asm.matweb.com/search/SpecificMaterial.asp?bassnum=mtp641 (Accessed April 2018)
[33] D. MA, O. Chung Wo, J. Liu, J. HE, Determination of Young's modulus by nanoindentation, Sci. China. Ser. E 47(4) (2004) 398-408.

Chapter 5 Compositional design of strong and ductile (tensile) Ti-Zr-Nb-Ta medium entropy alloys (MEAs) using the atomic mismatch approach

5.1 Chapter overview

In previous chapter, an equiatomicTiZrNbTa MEA was successfully fabricated and exhibited an excellent combination of compressive strength and ductility at room temperature compared to the counterpart TiZrNbTaMo HEA, but its density was high (8.9 ± 0.02 g/cm^3). Therefore, new non-equiatomic $Ti_{25+x}Zr_{25}Nb_{25}Ta_{25-x}$ MEAs with single solid solution phase were designed using atomic mismatch approach and verified by the empircal rule and Pandat^{TM} simulation before experimental study. This newly designed MEAs was aimed for a view of achieving strong and ductile MEAs with lower density and cost. All new non-equiatomic MEAs were fabricated, microstructurally characteraterized, and mechanically evaluated in details as published in *Journal of Materials Science Engineering A* (vol. 742 (2019): 762-772) and shown in section 5.2. These new MEAs depicted a single BCC solid-solution phase after being fabricated by the arc-melting method. The density decreased remarkably from ~8.9 g/cm^3 ($Ti_{25}Zr_{25}Nb_{25}Ta_{25}$) to ~6.6 g/cm^3 ($Ti_{45}Zr_{25}Nb_{25}Ta_5$). The conventional strength-ductility trade-off was observed when increasing replacement of Ta with Ti. At room temperature, the tensile strength decreased, but tensile strain increased significantly, which attributes to the decrease of atomic mismatch when decreasing Ta content. This work contributes an improved knowledge in designing non-equiatomic MEA or HEA containing Ti, Zr, Nb, and Ta.

5.2 Publication

Compositional design of strong and ductile (tensile) Ti-Zr-Nb-Ta medium entropy alloys (MEAs) using the atomic mismatch approach

V. T. Nguyen [a], M. Qian [c, *], Z. Shi [a], T. Song [c], L. Huang [a], and J. Zou [a, b, *]

[a] Materials Engineering, [b] Centre of Microscopy and Microanalysis, The University of Queensland, Brisbane, QLD4072, Australia

[c] RMIT University, School of Engineering, Centre of Additive Manufacturing, Melbourne, Victoria 3000, Australia

Abstract

New non-equiatomic $Ti_{(25+x)}$-Zr_{25}-Nb_{25}-$Ta_{(25-x)}$ (x = 0, 5, 10, 15, 20, in at. %) medium entropy alloys (MEAs) have been designed using the atomic mismatch approach and fabricated through a conventional arc-melting process. These novel MEAs were derived from a recently developed equiatomic Ti-Zr-Nb-Ta MEA by gradually replacing its Ta content with Ti. Each non-equiatomic MEA solidified as a single solid-solution phase, which was characterized in detail and compared with Pandat^{TM} simulation and empirical rules. Systematic tensile mechanical property data revealed the existence of a brittle-to-ductile transition for Ti-Zr-Nb-Ta MEAs, i.e., when 15 at.% of Ta in the equiatomic Ti_{25}-Zr_{25}-Nb_{25}-Ta_{25} MEA was replaced by Ti to become a Ti_{40}-Zr_{25}-Nb_{25}-Ta_{10} MEA. The transition occurs corresponding to a small reduction in atomic mismatch from 4.72% to 4.65% but a signficant drop in nanoindentation hardness from 4.2 GPa to 3.5 GPa. In particular, both the as-cast Ti_{40}-Zr_{25}-Nb_{25}-Ta_{10} and Ti_{45}-Zr_{25}-Nb_{25}-Ta_5 MEAs exhibited excellent tensile strain to fracture (>18%) and tensile strength (>900 MPa) with much reduced density compared to the brittle Ti_{25}-Zr_{25}-Nb_{25}-Ta_{25} MEA. They are both among a very small number of strong and ductile (tensile strain >15%) HEAs reported to date. Their tensile mechanical properties can be further tuned by adjusting the atomic mismatch of the resulting single solid-solution phase in conjunction with the improved understanding of the microstructures of these MEAs.

1. Introduction

In the recent decade, significant efforts have been made towards developing high entropy alloys (HEAs) or multi-principal-element alloys [1-9]. In general, HEAs are designed in an equiatomic fraction of at least five principal elements in order to maximize the mixing entropy, which is believed necessary for the formation of a single solid-solution phase in the resultant alloys under

normal solidification conditions [10]. However, such HEAs do not always solidify as a single solid-solution phase [11-14], indicating that it is not always stringently necessary to design HEAs in equiatomic fractions. On the other hand, the composition design of an HEA should also aim to achieve desired mechanical or other properties in addition to having a single solid-solution phase by definition. After all, it is their competitive properties that will matter rather than the number of the phases in these new alloys.

Refractory HEAs are HEAs that contain high melting-point elements as principal constituent elements. They have received much attention due to their excellent compressive strengths at both room and elevated temperatures [15-17], high corrosion resistance, and good bio-compatibility [18, 19]. However, they show high density and low ductility at room temperature [17, 18, 20-22]. Consequently, much effort has been made to design lower density refractory HEAs by replacing high-density elements with low-density ones while keeping their equiatomic nature. While such effort can noticeably reduce density, the resultant HEAs often contain undesired intermetallic phases, which deteriorate their ductility [11, 16, 23-26]. Therefore, instead of introducing new element(s) to a single solid-solution phase HEA, which has the risk of leading to undesired intermetallics, another option is to shift the focus of the compositional design from equiatomic to non-equiatomic. Such a strategy can avoid or minimize the formation of unexpected intermetallics while offering the potential to improve the mechanical properties of the HEAs.

An important feature that distinguishes between HEAs and conventional alloys is the severe lattice distortion due to substantial substitutional solid solution, which serves as the premier strengthening mechanism for these alloys [10, 27]. This severe lattice distortion, designated as atomic mismatch (δ), can be used as an important parameter for designing HEAs [28]. A large δ, which corresponds to severe lattice distortion, typically offers high strength or hardness but low ductility of refractory HEAs [10, 27]. Hence, it is possible that the strength and ductility of a HEA can be tuned through adjusting or optimizing the value of δ. The equiatomic Ti-Zr-Nb-Ta is a recently developed medium entropy alloy (MEA) [29], which solidifies as a single body-centred cubic (BCC) phase and exhibits high compressive strength but low tensile strain. Of the four constituent elements, Ti is the lightest and most inexpensive element whereas Ta is the heaviest and most costly one. In addition, if Ta is partially replaced with Ti, δ decreases. Therefore, there is a possibility that such Ti-enriched while Ta-depleted non-equiatomic Ti-Zr-Nb-Ta MEAs can achieve balanced tensile strengths and ductility with lower density and cost.

In this study, new non-equiatomic Ti-Zr-Nb-Ta MEAs are designed using the Pandat^{TM} software and established empirical rules [14, 28, 30], with a view of achieving strong and ductile MEAs with lower density and cost. These newly designed non-equiatomic MEAs are fabricated through a conventional arc-melting approach and their microstructures and tensile mechanical properties are characterised in detail. It is found that an appropriate δ reduction can stabilize the single solid-solution MEAs and transform the brittle equiatomic Ti-Zr-Nb-Ta MEA into strong and ductile (tensile) MEAs.

2. Experimental

Table 1 lists the nominal compositions of the designed $Ti_{(25+x)}$-Zr_{25}-Nb_{25}-$Ta_{(25-x)}$ MEAs with x = 0, 5, 10, 15, 20 (all in at. %), denoted respectively as Ti25, Ti30, Ti35, Ti40, and Ti45. They were fabricated from elemental metals with a minimum purity of 99.95 wt. % using an arc-melting furnace under a titanium-gettered argon atmosphere. The alloy buttons (~20 g) were remelted six times and flipped after each remelting. The melt was held for 10 min during each remelting for homogenisation. The fully prepared melt was cast into a rectangle water-cooled copper mould to produce a cuboidal bar of 13 mm in width, 8 mm in thickness, and 50 mm in length. 5 dog-bone-shaped tensile specimens with thickness of 1.5 mm, gauge length of 8 mm, and width of 2.9 mm were machined from the as-cast bars by electrical discharge wire cutting. The entire surfaces of the tensile specimens were ground with 600 grit SiC papers in order to remove the heat-affected layer caused by cutting. Tensile testing was carried out at a strain rate of 5×10^{-3} s^{-1} at room temperature (~25 ºC). A minimum of three tensile specimens of each alloy were tested using an Instron 5584 EM Frame machine equipped with a video extensometer. Nanoindentation hardness was randomly performed on a polished surface at eight different areas at room temperature (~25 ºC) using a nanoindenter (MTS Systems Corp., Oakridge, TN) with a Berkovich indenter (tip radius <100 nm).

In order to investigate the phase stability, a sample cut from each alloy ingot was annealed at 1200 ºC for 8 h in a vacuum of ~10^{-4} Pa, heated and cooled at 4 ºC/min. Specimens for metallographic examination were ground with SiC papers and polished using a suspension of 80% OP-S NonDry (0.04 μm) and 20% of hydrogen peroxide (H_2O_2). X-ray diffraction (XRD) (model Bruker D8 Advance MKII with monochromatic Cu Kα radiation) was used for phase identification. The XRD data were analyzed using the Pawley method implemented in the software package TOPAS (version 5 Bruker AXS). The microstructures were characterized using scanning electron microscopy (SEM) and transmission electron microscopy (TEM, Philips Tecnai F20). Two SEM systems were used: FEI Scios DualBeam FIB-SEM and JEOL

6610 SEM equipped with an electron backscatter diffraction (EBSD) detector and an energy-dispersive X-ray spectroscopy (EDS) detector. All TEM specimens were prepared using an FEI Scios DualBeam FIB.

Table 1: Compositions and thermodynamic parameters of the designed non-equiatomic $Ti_{(25+x)}$-Zr_{25}-Nb_{25}-$Ta_{(25-x)}$ MEAs (x = 0, 5, 10, 15, 20, all in at. %)

MEAs	Composition (at. %)				S_{mix}	δ	H_{mix}	a
	Ti	Zr	Nb	Ta	J/(K.mole)	(%)	kJ/mol	(Å)
Ti25	25	25	25	25	11.5	4.84	2.5	3.365
Ti30	30	25	25	20	11.4	4.78	2.44	3.364
Ti35	35	25	25	15	11.1	4.72	2.36	3.362
Ti40	40	25	25	10	10.7	4.65	2.26	3.361
Ti45	45	25	25	5	10	4.58	2.14	3.36
Atomic radii (Å)	1.462	1.603	1.429	1.43	-	-	-	-

S_{mix}: mixing entropy; δ: atomic mismatch; H_{mix}: mixing enthalpy; a: lattice parameter predicted by Vegard's law.

3. Results and Discussion

3.1 Phase formation by the Pandat^{TM} simulation and the empirical rules and comparison with XRD results

In order to achieve single-solid solution non-equiatomic MEAs, the Pandat modelling tool was used in conjunction with the empirical rules that are based on the δ, mixing entropy (ΔS_{mix}) and mixing enthalpy (ΔH_{mix}), where their values can be estimated using equations given in Refs. [14, 28, 30]. Table 1 lists their estimated values for the designed alloys. In general, the smaller the value of δ and the closer the value of ΔH_{mix} to zero, the more likely a single solid-solution phase will form in the expected HEA [13, 14, 30]. As shown in Table 1, both δ and ΔH_{mix} decrease with increasing replacement of Ta by Ti, which is in favour of the formation of a single-solid solution phase. In addition, the binary phase diagrams for the Ti-Zr, Ti-Nb, Ti-Ta, Zr-Nb, Zr-Ta, and Nb-Ta alloys all predict the formation of an exclusive BCC phase at high temperatures.This intrinsic nature is expected to facilitate the formation of a single solid-solution BCC phase in the designed non-equiatomic MEAs.

In this study, each MEA fabricated by arc melting solidified in a water-cooled copper mould at a high cooling rate. The Scheil model [31] can be employed to simulate this non-equilibrium solidification process of each MEA using Pandat^{TM} CompuTherm and the PanTi

thermodynamic database. Fig. 1a shows the Pandat^{TM} prediction of the solidification sequences for Ti30, Ti35, Ti40 and Ti45 MEAs. A full solid-solution BCC phase was predicted for each MEA, consistent with expectations based on the empirical rules. In addition, a wide solidification range ($T_{liquidus}$-$T_{solidus}$) was predicted for each MEA (Ti30: 410ºC; Ti35: 375ºC; Ti40: 311ºC; and Ti45: 246ºC). This implies that the BCC phase can have a distinct difference in composition in the initial and late stages of solidification. Fig. 1b predicts the compositional development in the remaining liquid phase (enriched in Zr and Ti but depleted in Ta) during solidification of the Ti30 MEA. In contrast, Fig. 1c predicts the compositional development in the BCC phase, which is enriched in Ta in the beginning but becomes enriched in Zr and Ti in the late stage of solidification.

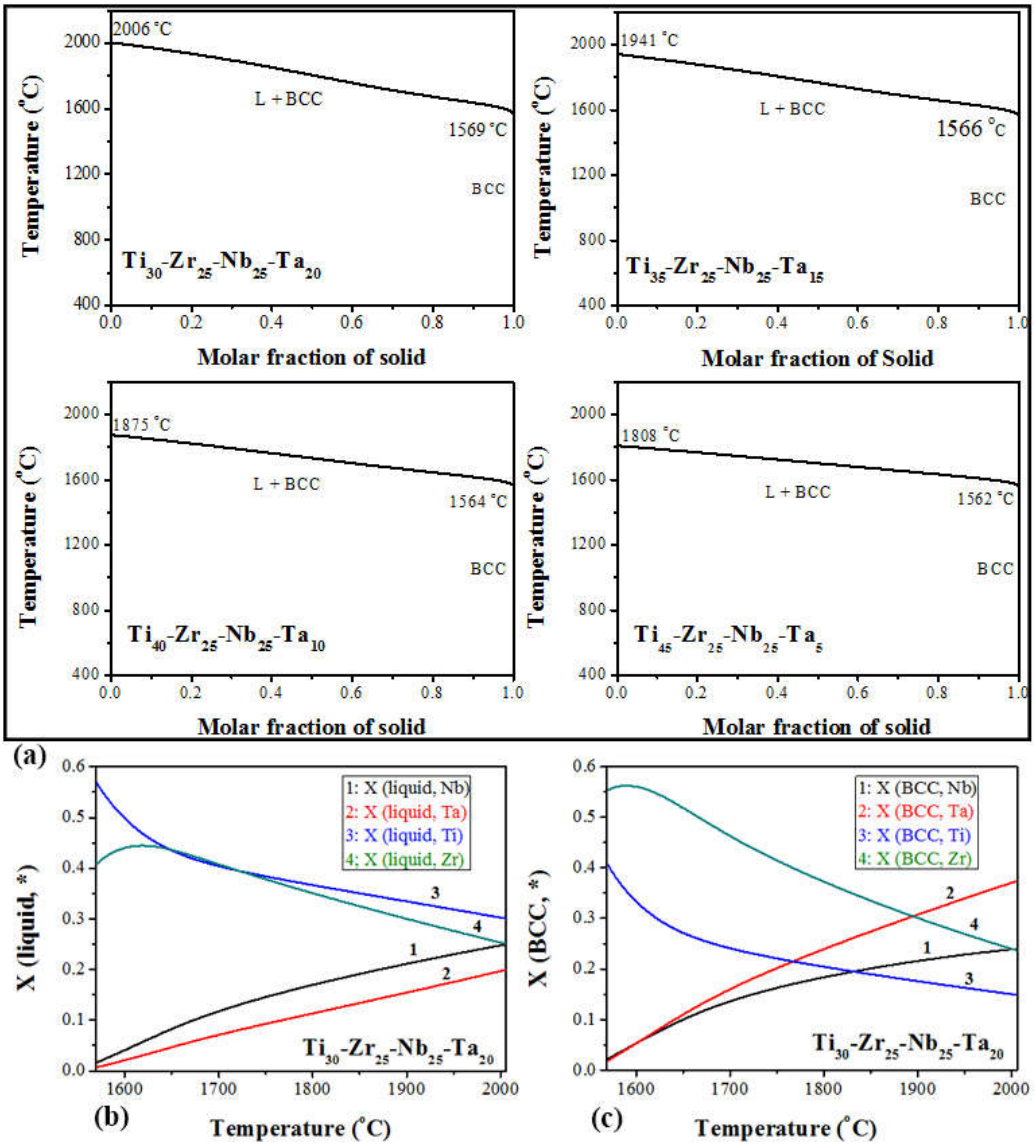

Figure 1 (a) Solidification of the Ti-Zr-Nb-Ta MEAs predicted using the Scheil model. Fig 1b and c predict respectively the elemental content in the liquid and the elemental content in the BCC phase as a function of temperature for Ti30.

Fig. 2a shows the XRD data obtained from the as-cast Ti25, Ti30, Ti35, Ti40 and Ti45 MEAs and the BCC Nb and Ta metals. The lattice parameters of BCC Ta and Nb were determined to be a_{Ta} = 3.330 Å and a_{Nb} = 3.330 Å, which are almost identical to the values given by the PDF cards of 00-004-0788 (Ta) and 00-035-0789 (Nb). This confirmed the accuracy of the XRD facility used in this study. As shown in Fig. 2a, only one BCC phase was detected in each MEA. This indicates that replacing Ta by Ti up to 20 at. % is still able to retain the single BCC phase, despite a clear decrease in S_{mix} (Table 1). This agrees well with the simulation results and the empirical rule. Fig. 2b shows the zoom-in (110) diffraction peak for all five MEAs, which shift towards higher 2θ values with increasing replacement of Ta by Ti due to lattice relaxation or smaller values of δ (Table 1). This phenomenon is consistent with the Vegard's law.

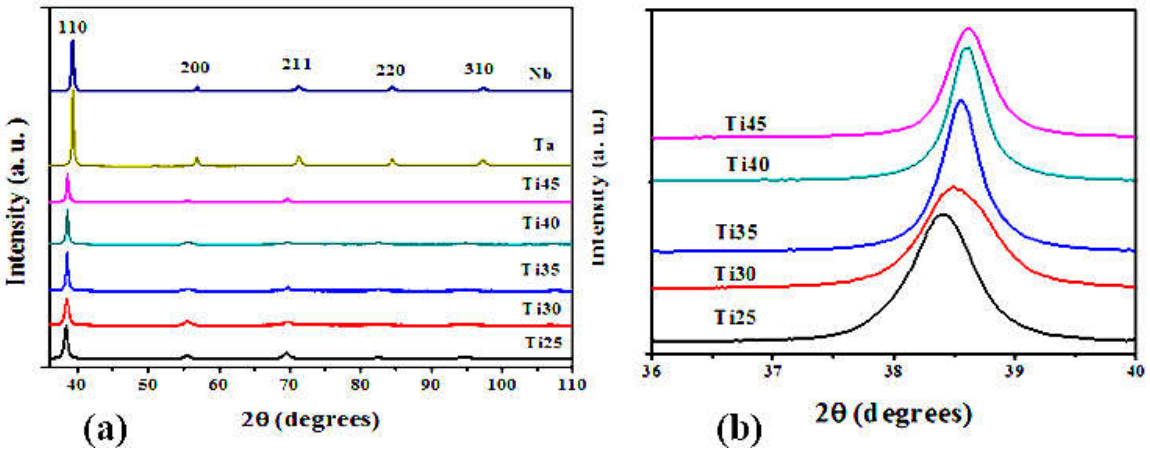

Figure 2 (a) XRD results of the as-cast Ti25, Ti30, Ti35, Ti40 and Ti45 MEAs and the BCC Nb and Ta metals used. (b) Zoom-in (110) diffraction peaks showing peak position shift.

3.2 Density

Density is an important property for the anticipated applications of these MEAs. The density of each MEA was determined using the Archimedes method while the calculated density was calculated from the following equation [26, 32]:

$$\rho = \frac{\sum c_i A_i}{\sum \frac{c_i A_i}{\rho_i}}, \quad (1)$$

Where c_i, A_i, and ρ_i are the concentration, atomic weight and density of the i^{th} element, respectively.

Fig. 3 compares these two density results, which are highly consistent with each other. These results have also confirmed that Eq. (1) can be highly accurate for predicting the density of a multi-component solid-solution alloy. As expected, the density decreases noticeably with replacing Ta by Ti. For example, the density of the Ti25 MEA is 8.92±0.02 g/cm^3 compared to 6.63±0.02 g/cm^3 for Ti45.

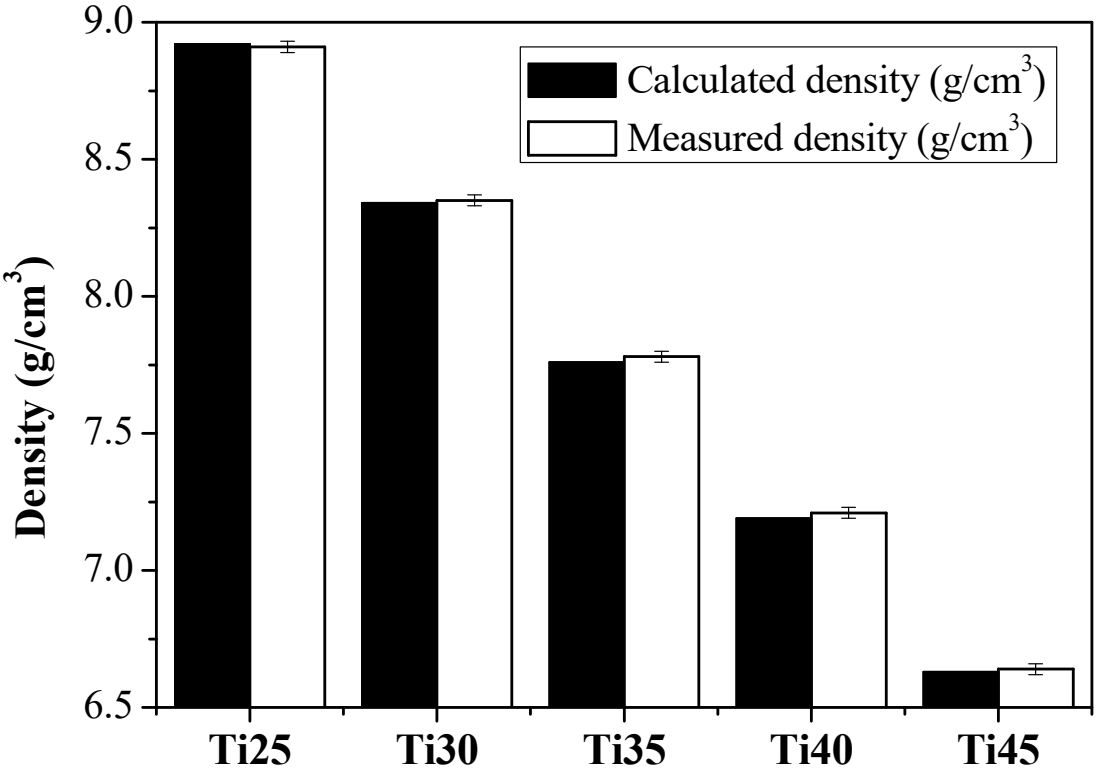

Figure 3 Calculated and measured densities of as-cast Ti25, Ti30, Ti35, Ti40 and Ti45 MEAs.

3.3 Microstructure

Fig. 4a depicts representative backscattered-electron (BSE) SEM images of the as-cast Ti30, Ti35, Ti40, and Ti45 MEAs and their corresponding zoom-in images to show selected grain boundary areas. A dendritic microstructure was prominent in each as-solidified MEA. Owing to constitutional segregation during solidification, most grains showed an uneven Z-contrast in each MEA. These observations show that all four non-equiatomic MEAs have solidified in a similar fashion (dendritic solidification), although the dendrite size is different.

Fig. 4b shows the EDS line-scan profiles of Ti30, Ti35, Ti40, and Ti45 MEAs taken from the arrowed regions in Fig. 4a while Table 2 summarises the results. They confirmed that the dendritic arms are enriched in Ta and Nb due to their high melting point metals while Ti and

Zr are enriched in the inter-dendritic regions. The chemical fluctuation between the dendrite and inter-dendritic region of Ti30 MEA (Fig. 4b) agrees qualitatively with the predicted results shown in Fig. 1b and c. It was also found that the fluctuation in the composition profiles of Ti, Nb, and Ta decreases significantly with increasing replacement of Ta by Ti (Fig. 4b and Table 2). This is due to the decrease of the solidification gap by reducing the concentration of Ta, the highest melting point element in this MEA system as discussed in the previously (Section 3.1). In addition, owing to the high mixing enthalpies of Zr-X (X: Ta, Nb, and Ta) and the distinct difference in atomic size between Zr and X (Table 3), Zr prefers to stay in the remaining liquid and becomes enriched in the inter-dendritic regions.

Table 2: Compositions of the Ti30, Ti35, Ti40, and Ti45 MEAs by SEM-EDS analysis.

Alloys or Elements		**Ti (at. %)**	**Zr (at. %)**	**Nb (at. %)**	**Ta (at. %)**
Ti30	Average	31 ± 2	24 ± 5	25 ± 3	20 ± 5
	Dendrite	29 ± 1	18 ± 1	28 ± 1	26 ± 2
	Inter-dendrite	33 ± 1	28 ± 3	23 ± 1	16 ± 3
Ti35	Average	35 ± 2	25 ± 5	25 ± 2	15 ± 4
	Dendrite	34.7 ± 0.3	20.4 ± 0.2	27.3 ± 0.2	17.6 ± 0.2
	Inter-dendrite	38.9 ± 0.3	31.5 ± 0.9	20.6 ± 0.7	9.0 ± 0.7
Ti40	Average	42 ± 1	25 ± 2	24 ± 1	9 ± 1
	Dendrite	41.0 ± 0.2	23 ± 0.2	25.8 ± 0.2	10.2 ± 0.2
	Inter-dendrite	42.2 ± 0.6	27 ± 2	23 ± 1	8 ± 1
Ti45	Average	46 ± 1	26 ± 2.3	23.5 ± 2.2	4.7 ± 0.9
	dendrite	45 ± 0.1	23.7 ± 0.5	25.7 ± 0.4	5.6 ± 0.3
	Inter-Dendrite	46.1± 0.9	27 ± 3	22 ± 2	4 ± 1

Table 3: The mixing enthalpy values (H_{mix}, kJ/mol) calculated using Miedema's model for atomic pairs between constituent elements in Ti-Zr-Nb-Ta alloy system [33].

Element	Ti	Zr	Nb	Ta
Ti	-	0	2	1
Zr	-	-	4	3
Nb	-	-	-	0

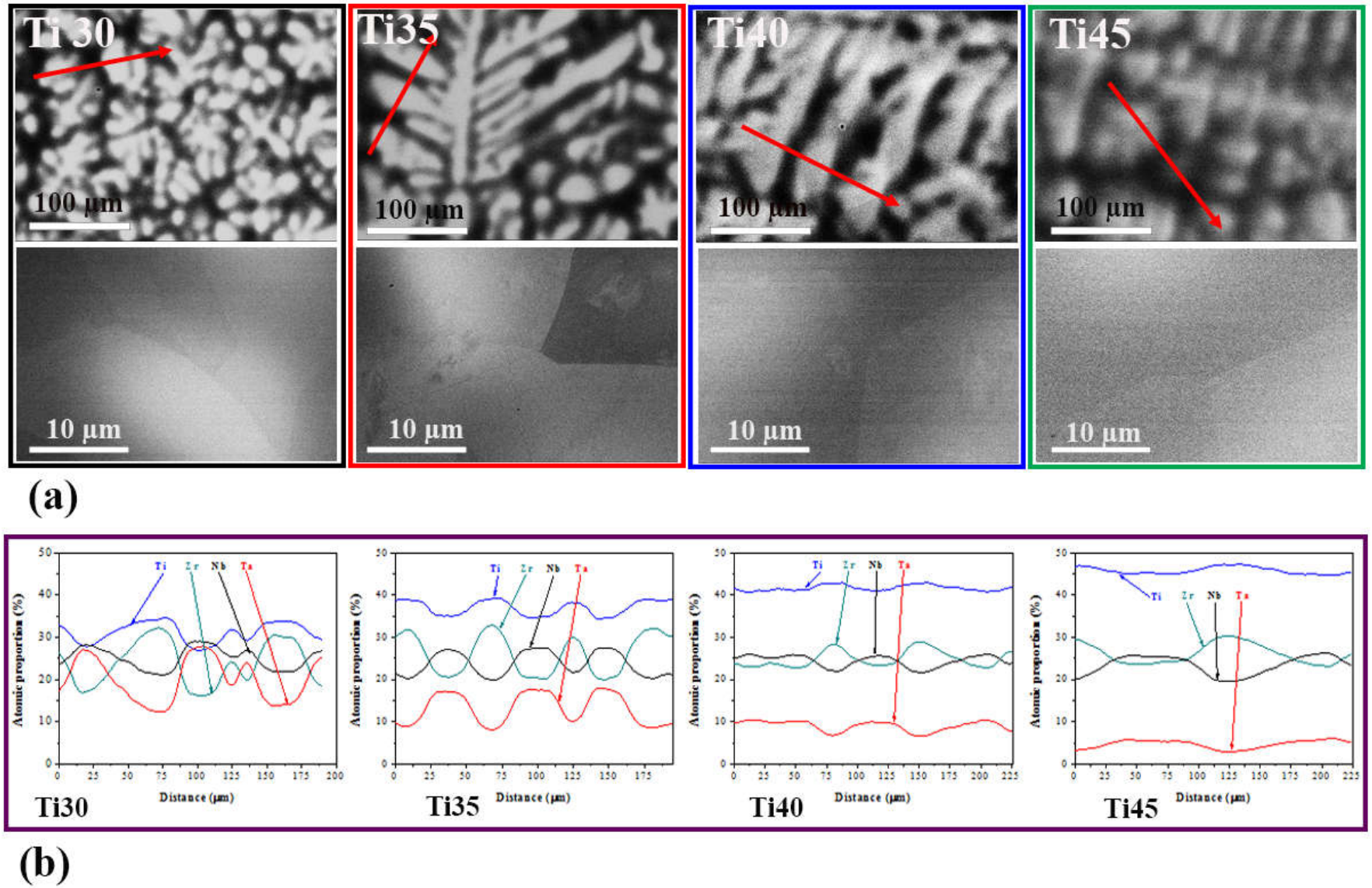

Figure 4 (a) BSE SEM images at low magnification and zoom-in observations of selected grain boundary areas in Ti30, Ti35, Ti40, and Ti45 MEAs; (b) EDS line-scan composition profiles of Ti30, Ti35, Ti40, and Ti45 MEAs taken from the arrowed regions in Fig 4a.

Fig. 5 shows BSE-SEM images obtained from the grain boundary (GB) areas in the annealed Ti25, Ti30, Ti35, Ti40, and Ti45 MEAs (annealed at 1200 ºC for 8 h). GB segregation was noticeable in the annealed Ti25, Ti30, Ti35 MEAs, but absent in the annealed Ti40 and Ti45 MEAs. In addition, the GB segregation was more severe in the annealed Ti25 and Ti30 MEAs than in the annealed Ti35 MEA. This indicates that the BCC phase is stabilized by replacing Ta with Ti, and an approximate minimum replacement of 15 % Ta is necessary. The replacement reduces the value of δ (Table 1), fortifying the empirical rule in designing stable single solid-solution phase HEAs [10]. EDS analyses indicate that the GB segregation is related to Zr, which can be attributed to its largest atomic radius in this alloy system and the high mixing enthalpies of Zr-X alloys (X: Ta, Nb, and Ta).

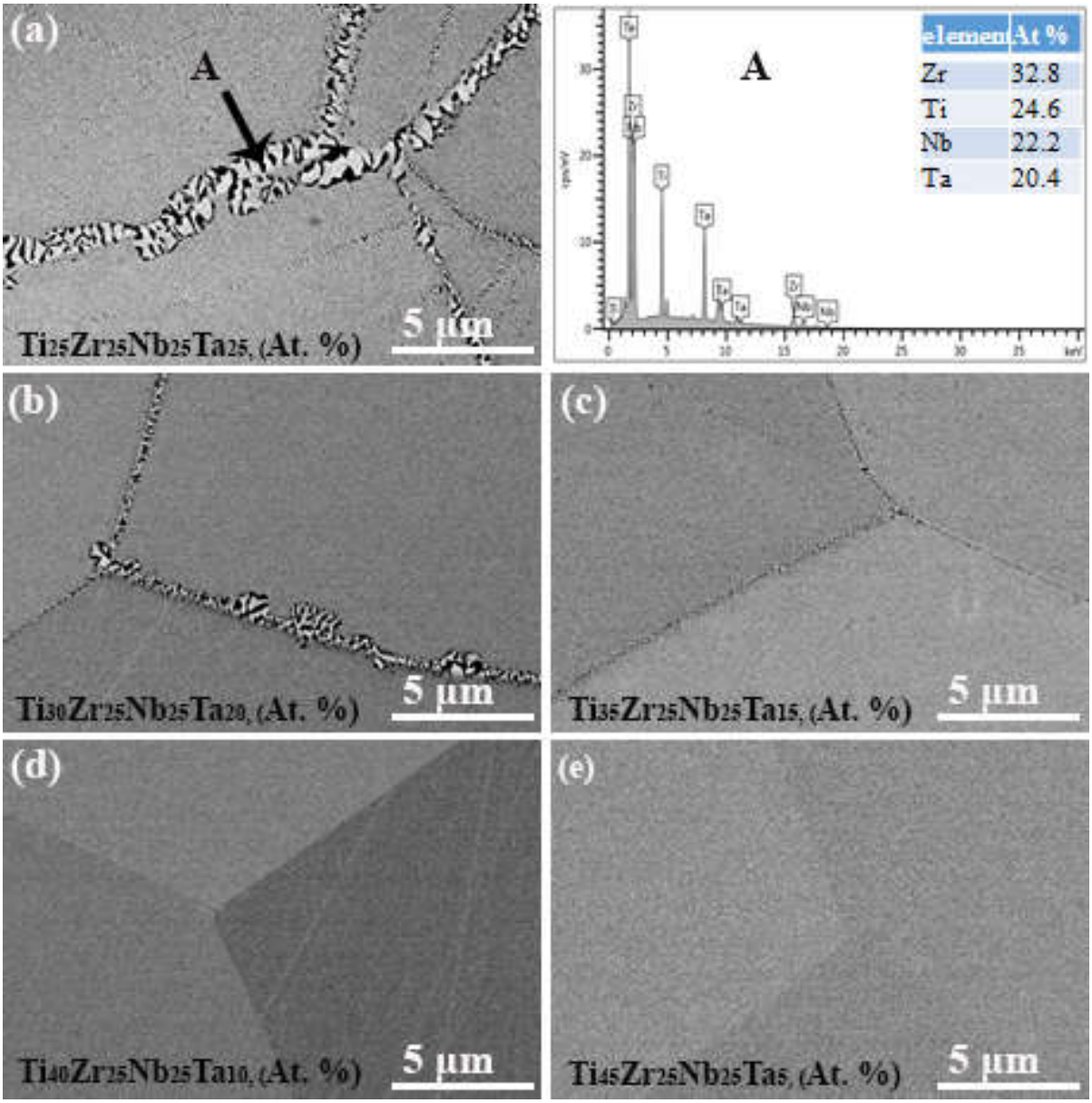

Figure 5 BSE-SEM images of annealed MEAs of (a) Ti25; (b) Ti30; (c) Ti35; (d) Ti40; (d) Ti45.

Fig. 6a shows the EBSD phase analysis results, which further confirmed the single BCC phase in all MEAs. The grain orientation maps shown in Fig. 6b suggest a similar grain structure for the as-cast MEAs. Despite the high cooling rate (water-cooled copper mould), the grains are coarse in size (~250 μm), which is not surprising due to the high casting temperature determined by the high liquidus temperature of each MEA (Fig. 1a). In addition, uneven contrast is observed in the grain orientation map in all MEAs, suggesting the existence of sub-grains with low-angle grain boundaries.

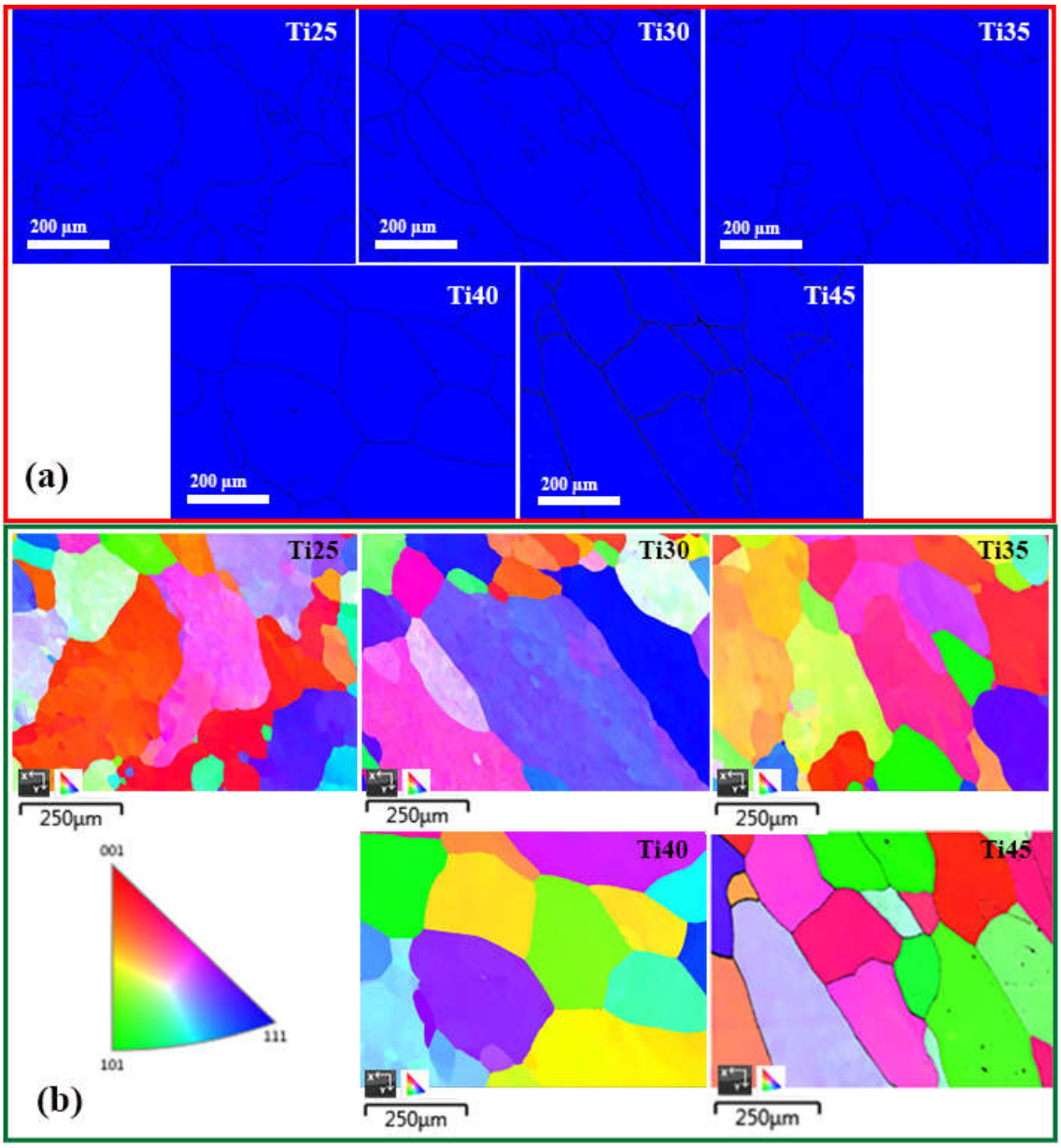

Figure 6 EBSD mapping for as-cast MEAs: (a) shows phase maps of as-cast Ti25, Ti30, Ti35, Ti40, and Ti45 MEAs. Blue colour in these phase map indicates BCC crystal structure. (b) shows grain orientation maps of as-cast MEAs.

Secondary phases often form in the inter-dendritic regions during the solidification of a highly concentrated alloy due to solute segregation. Such phases are not always detectable by XRD or EBSD because of their low volume fraction. Hence, GB areas were investigated by TEM in all MEAs. Fig. 7 shows representative bright-field (BF) TEM images taken from selected GB areas in the as-cast Ti30, Ti35, Ti40, and Ti45 MEAs. No secondary phase was observed. The inset in each BF-TEM image shows a selected area electron diffraction (SAED) pattern, which was taken from the dark grain (after titling the dark grain to the [001] zone-axis of BCC structure) in each image. No diffraction spots for ordered solid-solution phases were observed in all SAED patterns, indicating that the BCC phase is just a disorder solid-solution phase. Fig. 8 shows the EDS mapping results of a selected GB area in the as-cast Ti30 MEA. The distribution of each principal element (Ti, Zr, Nb, and Ta) was found to be essentially homogeneous.

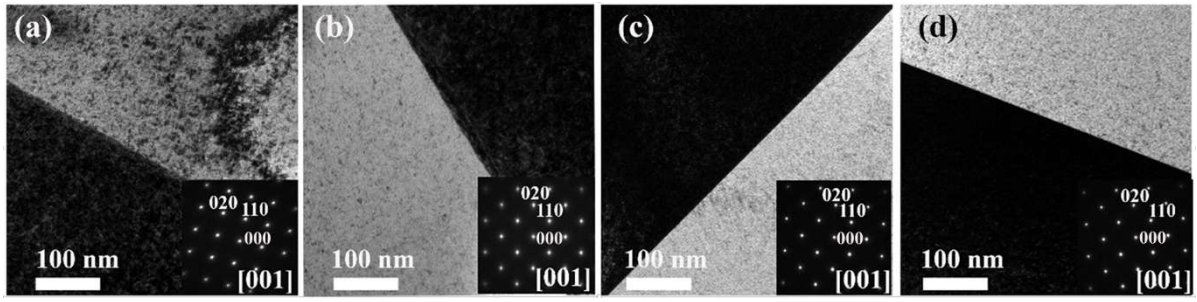

Figure 7 BF-TEM images with insets showing [001] zone-axis SAED patterns taken from the dark grain of each selected grain boundary area in as-cast MEAs of (a) Ti30; (b) Ti35; (c) Ti40; and (d) Ti45.

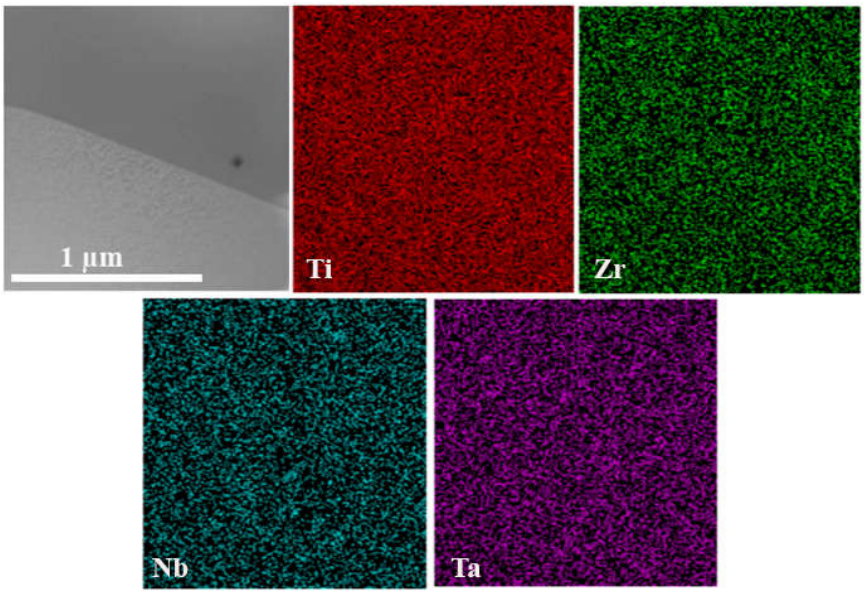

Figure 8 BF-TEM image and EDS mapping results of a selected GB area in as-cast Ti45 MEA. The distribution of Ti, Zr, Nb, and Ta was found essentially to be homogeneous at the GB area.

3.4 Mechanical Properties

3.4.1 Tensile properties

Fig. 9a shows the true tensile stress-strain curves for the Ti25, Ti30, Ti35, Ti40, and Ti45 MEAs at room temperature. A clear transition was observed between Ti35 and Ti40, where Ti25, Ti30, and Ti35 MEAs all exhibited poor tensile strain (0-5%) but both Ti40 and Ti45 achieved high tensile strain of >18% with good tensile strength (>900 MPa).

Table 4 compares the yield strength, ultimate tensile strength, strain at failure, and density for Ti40 and Ti45 MEAs with nine refractory HEAs reported in the literature [6, 34-38]. To our best knowledge, our Ti40 and Ti45 MEAs are among the very few HEAs and MEAs reported to date that are both strong and highly ductile (tensile). In addition, they offer much lower densities than those HEAs listed in Table 4 while the tensile strengths are comparable.

Fig. 9b displays the load-displacement curves obtained by nanoindentation of the as-cast MEAs. The displacement increases with increasing the replacement of Ta by Ti. The nanoindentation hardness calculated using the Oliver-Pharr method [39, 40] shows 4.6 ± 0.2 GPa for Ti25, 4.4 ± 0.2 GPa for Ti30, 4.2 ± 0.2 GPa for Ti35, 3.5 ± 0.1 GPa for Ti40, and 3.3 ± 0.1 GPa for Ti45. The decrease of nanoindentation hardness corresponds to the reduced solid-solution strengthening effect due to the replacement of Ta by Ti, or the reduction in δ. The reduction in nanoindentation hardness is gradual from both Ti25 to Ti30 and Ti40 to Ti45 but sharp from Ti35 to Ti40 MEA.

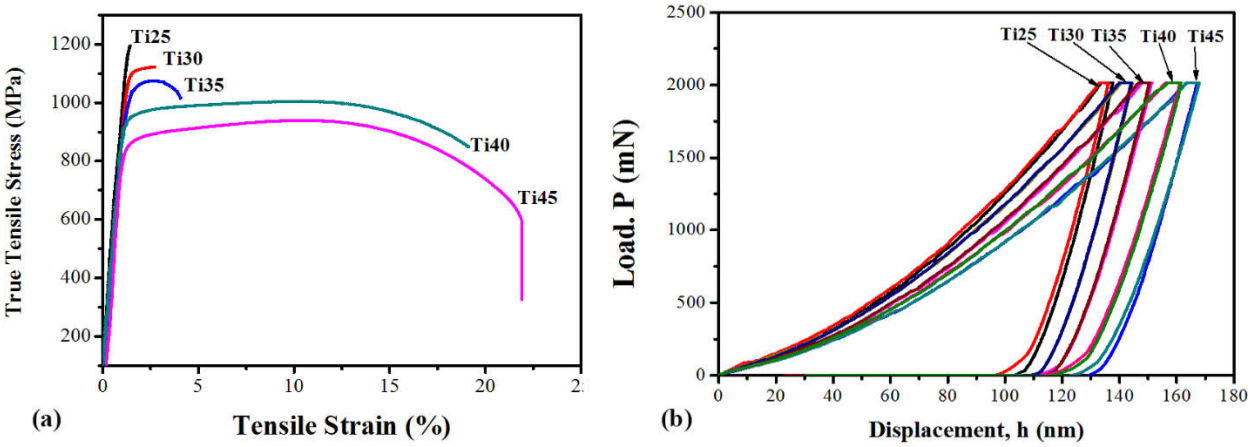

Figure 9 (a) True tensile strength-tensile strain curves for Ti25, Ti30, Ti35, Ti40, and Ti45 MEAs at room temperature (~25ºC); (b) Nanoidentation results.

Table 4 Comparison of the tensile properties of Ti40, Ti45 and reported refractory HEAs.

Alloys	Processing	ρ (g/cm^3)	σ_y (MPa)	σ_{UTS} (MPa)	ε (%)	Ref
HfNbTaTiZr	As-cast, HIP 1200 ^{o}C-207 MPa/2 hours, cold rolling 90%-1000^{o}C/2hours	9.94	1145	1262	9.7	[34]
HfNbTiZr	1300^{o}C/6hours/slow cooling	8.4	879	969	14.9	[35]
HfNbTiZr	AC	8.4	810	890	8	[36]
Ti35Zr27.5Hf27.5Nb5Ta5	Cold rolling 60-70% - 800&900 ^{o}C/30 minutes	8.48^c	600	960	17	[37]
Hf0.5Nb0.5Ta0.5Ti1.5Zr	As-cast	8.13	903	990	18.8	[38]
Ta0.6ZrHfTi	As-cast	9.5^c	~730	~1080	~20	[6]
Ta0.5ZrHfTi	As-cast	9.4^c	~700	~1080	~29	[6]
Ta0.4ZrHfTi	As-cast	9.2^c	~400	~1080	~30	[6]
Ti40	As-cast	7.2	910	1040	18	This study
Ti45	As-cast	6.6	790	910	22	This study

HIP: hot isostatic pressing; c: calculated value.

Fig. 10 shows representative SEM images taken from the tensile fracture surfaces of Ti25, Ti30, Ti35, Ti40, and Ti45 MEAs. Cleavage fracture and inter-granular fracture are prominent for Ti25, Ti30, and Ti35 MEAs (low ductility in Fig. 9), whereas dimpled fracture is observed in Ti40 and Ti45 MEAs, consistent with their high tensile strain to fracture (Fig. 9).

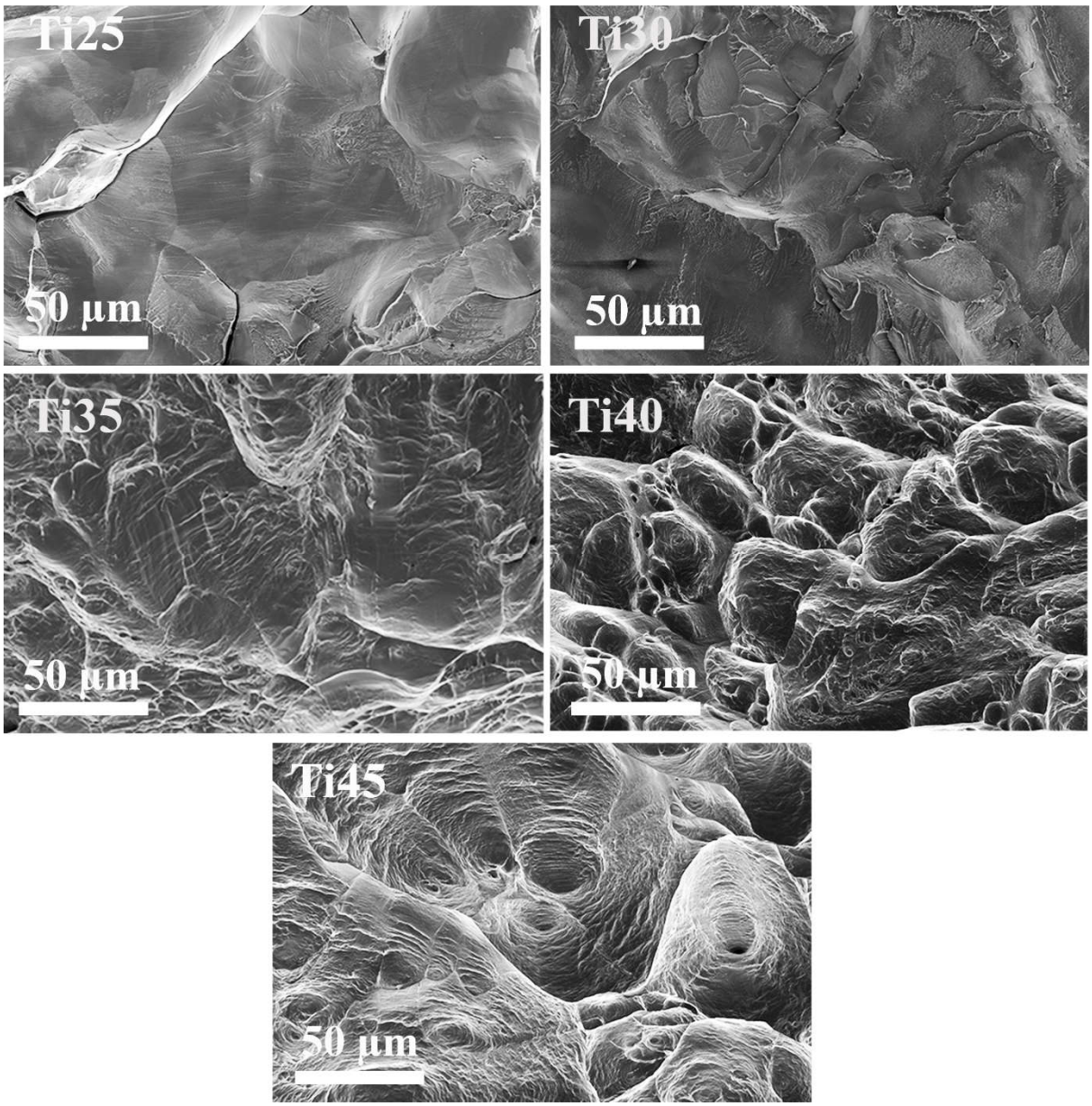

Figure 10 Representative tensile fracture surfaces of Ti25, Ti30, Ti35, Ti40, and Ti45 MEAs.

3.4.2 The brittle-ductile transition

In this study, the tensile stress-strain curves shown in Fig. 9(a) suggest the existence of a brittle-ductile transition for the Ti-Zr-Nb-Ta alloy system. The key alloy design parameter used in this research was δ, which can be calculated using the following equation [14, 28].

$$\delta(\%) = 100\sqrt{\sum_{i=1}^{n} c_i.\left(1-\frac{r_i}{r_a}\right)^2} \quad \text{with} \quad r_a = \sum_{i=1}^{n} c_i r_i \tag{2}$$

Where r_a is the average atomic radius; and c_i and r_i are respectively the atomic fraction and atomic radius of the i^{th} element.

Since δ provides a measure of the solid-solution strengthening effect in HEAs [10, 20], Fig. 11 plots the measured tensile strength and ductility as a function of δ. Replacing Ta with Ti in the equiatomic Ti-Zr-Nb-Ta MEA resulted in a progressive decrease in δ (Table 1). A decrease in δ reduces the solid-solution strengthening effect and allows dislocations to move more easily in the BCC lattice than in a highly distorted lattice of the same BCC phase. Consequently, the tensile strength decreases but the ductility improves noticeably with decreasing δ, as shown in Fig. 11. It is clear from Fig. 11 that the tensile strength and ductility can be tuned over a broad range for Ti-Nb-Zr-Ta MEAs by replacing Ta by Ti for different performance requirements.

It is noted that the tensile ductility jumped from ~5% (Ti35) to ~18% (Ti40) while the atomic mismatch δ decreased only slightly from 4.72% to 4.65%. Indeed, in principle, the atomic mismatch δ corresponds to strength rather than ductility. However, as pointed out earlier, the nanoindentation hardness dropped from 4.2 ± 0.2 GPa for Ti35 to 3.5 ± 0.1 GPa for Ti40 compared with a gradual change from Ti25 to Ti30, Ti30 to Ti35, and Ti40 to Ti45. Hence, there is a clear mismatch between δ and nanoindentation hardness over the composition range from Ti35 to Ti40. In other words, the atomic mismatch δ failed to completely reflect the change in solid solution strengthening from Ti35 (4.2 ± 0.2 GPa) to Ti40 (3.5 ± 0.1 GPa). This means that the calculation of δ should be improved. The significant drop in nanoindentation hardness from Ti35 to Ti40 indicates much reduced solid-solution strengthening due to the replacement of 5 at.% Ta by 5 at.% Ti, which corresponded to a substantial increase in tensile ductility from ~5% to ~18%.

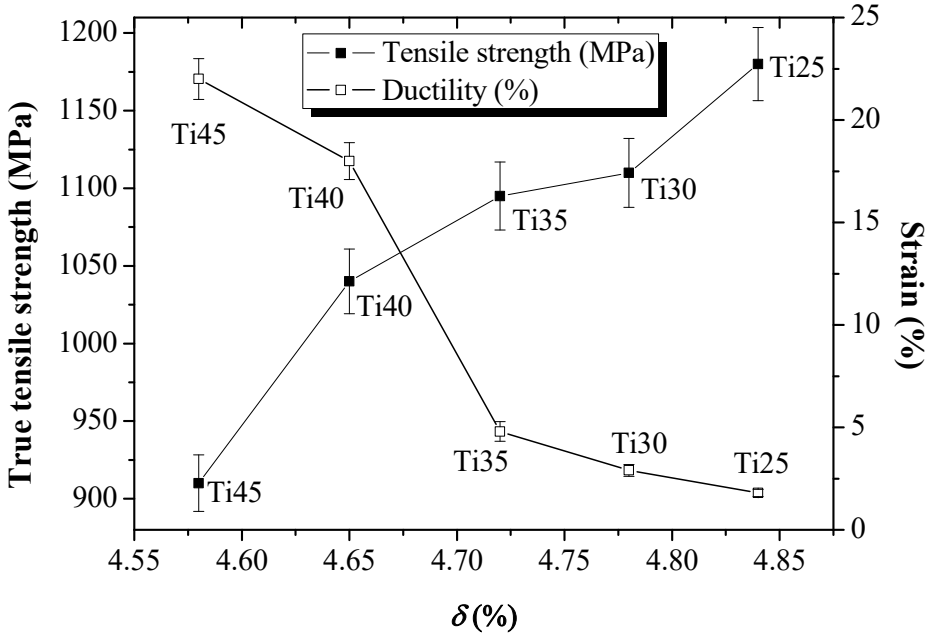

Figure 11 Tensile strength and ductility versus atomic mismatch (δ) in as-cast Ti25, Ti30, Ti35, Ti40, and Ti45 MEAs.

To further understand the ductile deformation mechanism, a sample of Ti40 MEA after tensile testing was investigated in detail using SEM, EBSD and TEM. The observations are shown in Fig. 12. Fine lamellae in the matrix grains are observed (Fig. 12 a and c), which are identified to be micro-sized shear bands (Fig. 12 b and e) due to significant plastic deformation. Similar feature was observed in the ductile equiatomic TiHfZrTaNb HEA [41]. No phase segregation was found (Fig. 12d). TEM characterization confirmed this. Fig. 12f is a BF-TEM image showing shear bands with a thickness of 2-3 μm and Fig. 12g is a [001] zone-axis SAED pattern (a single BCC phase) taken from a dark band in Fig. 12f. In addition, Fig.12h is a TEM image showing a typical shear band boundary. The EDS mapping results of Ti, Zr, Nb and Ta are shown in Fig. 12 (i-l). The distribution of each element is homogeneous. The observation of significant shear bands in the Ti40 MEA sample after tensile testing is consistent with the high tensile ductility measured. However, the exact underlying mechanism for the change in the deformation mode from Ti35 to Ti40 needs to be further investigated. As reported previously [27, 42, 43], unconventional dislocation lines were found in HEAs due to the severe lattice distortion, which implies that a distinctly different deformation mechanism may have operated in these alloys.

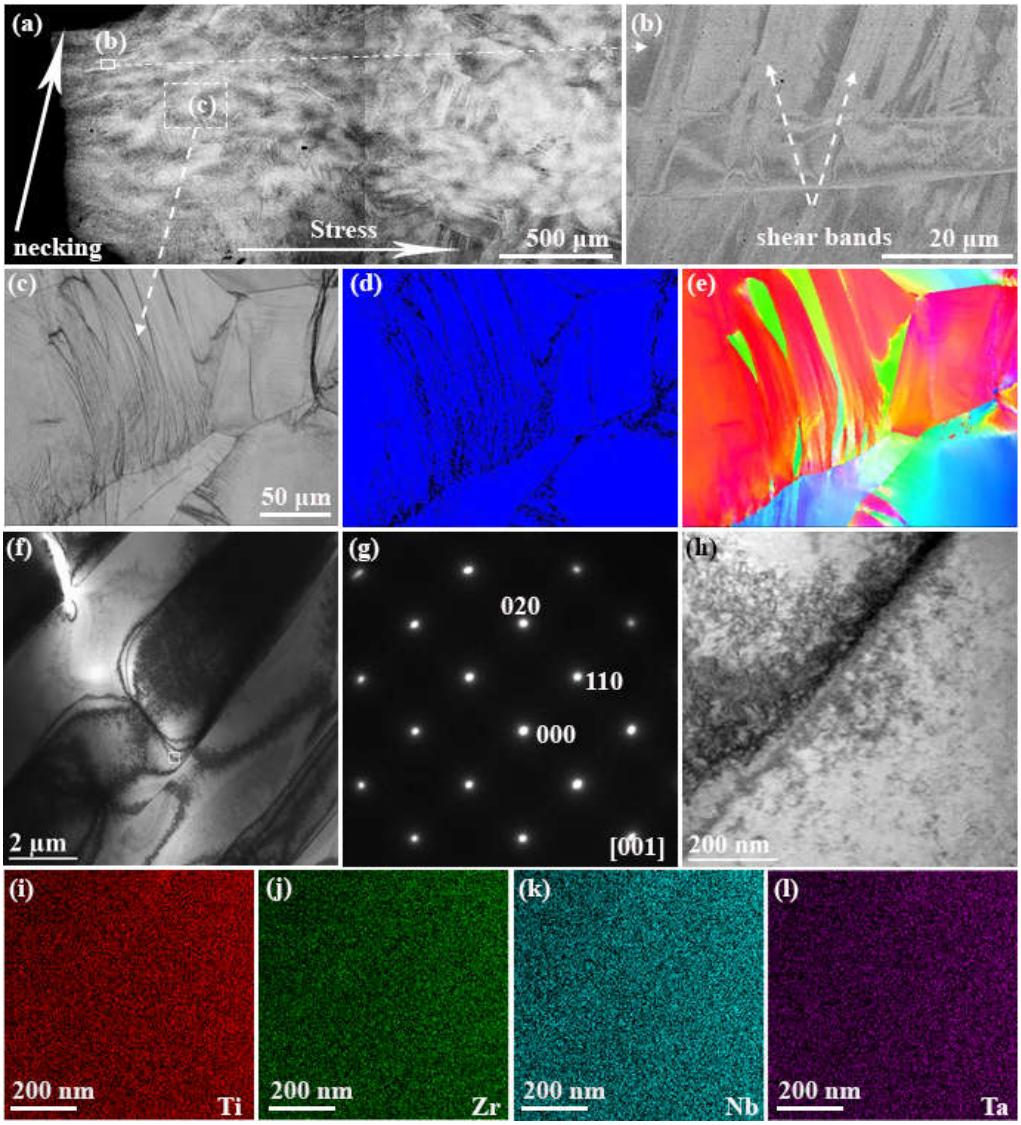

Figure 12 (a) SEM backscattered montage along the longitudinal cross-section of a Ti40 MEA sample from the tensile fractured surface. (b) A closer view of (a). (c), (d), and (e) are the band-contrast, phase map, and grain orientation map of the area marked out in (a). (f) is a BF-TEM image taken from a selected lamella in (c). (g) is a SAED pattern of the dark bands in (e) showing a single BCC phase. (h) is a bright field TEM image of the area from which EDS mapping of Ti , Zr, Nb, Ta was performed and shown in (i-l).

4. Conclusions

In this study, new non-equiatomic $Ti_{(25+x)}$-Zr_{25}-Nb_{25}-$Ta_{(25-x)}$ (x = 0, 5, 10, 15, 20, in at. %) MEAs were designed, fabricated, and characterised. All designed new alloys solidified as a single BCC phase under conventional arc-melting and water-cooled copper-mould cooling conditions. The impact of the atomic mismatch δ on the tensile properties of these non-equiatomic Ti-Zr-Nb-Ta MEAs was studied systematically for the first time. The value of δ

showed a strong correlation with both the tensile strength and ductility of Ti-Zr-Nb-Ta MEAs. In particular, a brittle-ductile transition was observed when the value of δ was decreased from 4.72% to 4.65% by a replacement of 5 at.% Ta with 5 at.% Ti, which corresponds to a signficant drop in nanoindentation hardness from 4.2 GPa to 3.5 GPa. As a result, both Ti_{40}-Zr_{25}-Nb_{25}-Ta_{10} (at. %) and Ti_{45}-Zr_{25}-Nb_{25}-Ta_5 (at. %) MEAs achieved tensile strain to fracture of >18% and tensile strength of >900 MPa in the as-cast state. They are both among a very small number of strong and ductile (tensile strain >15%) HEAs reported to date. Their tensile strength-ductility combination can be tuned over a broad range by replacing Ta by Ti due to the reduction of δ. These novel Ti-Zr-Nb-Ta MEAs are useful additions to the existing alloy database on Ti, Nb, Zr, and Ta.

Acknowledgements

This work was supported by the Australian Research Council (ARC) through ARC LP130100913 and the Baosteel-Australia Joint Research and Development Centre through BA110014LP. VTN thanks the International Postgraduate Research Scholarship (IPRS) Program for providing him with a PhD scholarship. M. Qian further acknowledges the support from the Australian-India Strategic Research Fund. The Australian Microscopy & Microanalysis Research Facility is acknowledged for providing characterization facilities.

Data Availability statement

The raw/processed data required to reproduce these findings cannot be shared at this time due to technical or time limitations.

References

[1] B. Cantor, I.T.H. Chang, P. Knight, A.J.B. Vincent, Microstructural development in equiatomic multicomponent alloys, Mater. Sci. Eng. A 375–377 (2004) 213-218.

[2] J.W. Yeh, S.K. Chen, S.J. Lin, J.Y. Gan, T.S. Chin, T.T. Shun, C.H. Tsau, S.Y. Chang, Nanostructured High-Entropy Alloys with Multiple Principal Elements: Novel Alloy Design Concepts and Outcomes, Adv. Eng. Mater. 6(5) (2004) 299-303.

[3] T.T. Shun, L.Y. Chang, M.H. Shiu, Microstructures and mechanical properties of multiprincipal component CoCrFeNiTi x alloys, Mater. Sci. Eng. A 556 (2012) 170-174.

[4] K.B. Zhang, Z.Y. Fu, J.Y. Zhang, W.M. Wang, H. Wang, Y.C. Wang, Q.J. Zhang, J. Shi, Microstructure and mechanical properties of CoCrFeNiTiAl x high-entropy alloys, Mater. Sci. Eng. A 508(1) (2009) 214-219.

[5] K.Y. Tsai, M.H. Tsai, J.W. Yeh, Sluggish diffusion in Co–Cr–Fe–Mn–Ni high-entropy alloys, Acta Mater. 61(13) (2013) 4887-4897.
[6] H. Huang, Y. Wu, J. He, H. Wang, X. Liu, K. An, W. Wu, Z. Lu, Phase-Transformation Ductilization of Brittle High-Entropy Alloys via Metastability Engineering, Adv. Mater. (2017).
[7] Z. Li, K.G. Pradeep, Y. Deng, D. Raabe, C.C. Tasan, Metastable high-entropy dual-phase alloys overcome the strength–ductility trade-off, Nature 534(7606) (2016) 227-230.
[8] Y. Zou, J.M. Wheeler, H. Ma, P. Okle, R. Spolenak, Nanocrystalline High-Entropy Alloys: A New Paradigm in High-Temperature Strength and Stability, Nano Lett. 17(3) (2017) 1569-1574.
[9] H.W. Yao, J.W. Qiao, M.C. Gao, J.A. Hawk, S.G. Ma, H.F. Zhou, Y. Zhang, NbTaV-(Ti,W) refractory high-entropy alloys: Experiments and modeling, Mater. Sci. Eng. A 674 (2016) 203-211.
[10] Y. Zhang, T.T. Zuo, Z. Tang, M.C. Gao, K.A. Dahmen, P.K. Liaw, Z.P. Lu, Microstructures and properties of high-entropy alloys, Prog. Mater. Sci. 61 (2014) 1-93.
[11] M.G. Poletti, S. Branz, G. Fiore, B.A. Szost, W.A. Crichton, L. Battezzati, Equilibrium high entropy phases in X-NbTaTiZr (X = Al,V,Cr and Sn) multiprincipal component alloys, J. Alloys Compd. 655 (2016) 138-146.
[12] D.B. Miracle, O.N. Senkov, A critical review of high entropy alloys and related concepts, Acta Mater. 122 (2017) 448-511.
[13] Z. Wang, S. Guo, C.T. Liu, Phase selection in high-entropy alloys: from nonequilibrium to equilibrium, JOM 66(10) (2014) 1966-1972.
[14] G. Sheng, C.T. Liu, Phase stability in high entropy alloys: formation of solid-solution phase or amorphous phase, Prog Nat Sci-Mater 21(6) (2011) 433-446.
[15] O.A. Waseem, H.J. Ryu, Powder Metallurgy Processing of a W(x)TaTiVCr High-Entropy Alloy and Its Derivative Alloys for Fusion Material Applications, Sci. Rep 7 (2017) 1926.
[16] O.N. Senkov, S.V. Senkova, D.B. Miracle, C. Woodward, Mechanical properties of low-density, refractory multi-principal element alloys of the Cr–Nb–Ti–V–Zr system, Mater. Sci. Eng. A 565 (2013) 51-62.
[17] O. Senkov, G. Wilks, J. Scott, D. Miracle, Mechanical properties of Nb 25 Mo 25 Ta 25 W 25 and V 20 Nb 20 Mo 20 Ta 20 W 20 refractory high entropy alloys, Intermetallics 19(5) (2011) 698-706.
[18] M. Todai, T. Nagase, T. Hori, A. Matsugaki, A. Sekita, T. Nakano, Novel TiNbTaZrMo high-entropy alloys for metallic biomaterials, Scr. Mater. 129 (2017) 65-68.

[19] S.P. Wang, J. Xu, TiZrNbTaMo high-entropy alloy designed for orthopedic implants: As-cast microstructure and mechanical properties, Mater. Sci. Eng. C 73 (2017) 80-89.
[20] S. Maiti, W. Steurer, Structural-disorder and its effect on mechanical properties in single-phase TaNbHfZr high-entropy alloy, Acta Mater. 106 (2016) 87-97.
[21] Y. Zhang, Y. Liu, Y. Li, X. Chen, H. Zhang, Microstructure and mechanical properties of a refractory HfNbTiVSi0.5 high-entropy alloy composite, Mater. Lett. 174 (2016) 82-85.
[22] C.C. Juan, M.H. Tsai, C.W. Tsai, C.M. Lin, W.R. Wang, C.C. Yang, S.K. Chen, S.J. Lin, J.W. Yeh, Enhanced mechanical properties of HfMoTaTiZr and HfMoNbTaTiZr refractory high-entropy alloys, Intermetallics 62 (2015) 76-83.
[23] Y. Qiu, Y.J. Hu, A. Taylor, M.J. Styles, R.K.W. Marceau, A.V. Ceguerra, M.A. Gibson, Z.K. Liu, H.L. Fraser, N. Birbilis, A lightweight single-phase AlTiVCr compositionally complex alloy, Acta Mater. 123 (2017) 115-124.
[24] N.Y. Yurchenko, N.D. Stepanov, D.G. Shaysultanov, M.A. Tikhonovsky, G.A. Salishchev, Effect of Al content on structure and mechanical properties of the AlxCrNbTiVZr (x=0; 0.25; 0.5; 1) high-entropy alloys, Mater. Charact. 121 (2016) 125-134.
[25] N.D. Stepanov, D.G. Shaysultanov, G.A. Salishchev, M.A. Tikhonovsky, Structure and mechanical properties of a light-weight AlNbTiV high entropy alloy, Mater. Lett. 142 (2015) 153-155.
[26] O.N. Senkov, S.V. Senkova, C. Woodward, D.B. Miracle, Low-density, refractory multi-principal element alloys of the Cr–Nb–Ti–V–Zr system: Microstructure and phase analysis, Acta Mater. 61(5) (2013) 1545-1557.
[27] C. Lee, G. Song, M.C. Gao, R. Feng, P. Chen, J. Brechtl, Y. Chen, K. An, W. Guo, J.D. Poplawsky, S. Li, A.T. Samaei, W. Chen, A. Hu, H. Choo, P.K. Liaw, Lattice distortion in a strong and ductile refractory high-entropy alloy, Acta Mater. 160 (2018) 158-172.
[28] Y. Zhang, Y.J. Zhou, J.P. Lin, G.L. Chen, P.K. Liaw, Solid-solution phase formation rules for multi-component alloys, Adv. Eng. Mater. 10(6) (2008) 534-538.
[29] V.T. Nguyen, M. Qian, Z. Shi, T. Song, L. Huang, J. Zou, A novel quaternary equiatomic Ti-Zr-Nb-Ta medium entropy alloy (MEA), Intermetallics 101 (2018) 39-43.
[30] S. Guo, Phase selection rules for cast high entropy alloys: an overview, Mater. Sci. Technol. 31(10) (2015) 1223-1230.
[31] M.C. Gao, J.-W. Yeh, P.K. Liaw, Y. Zhang, High-Entropy Alloys: *Fundamentals and Applications*, Springer 2016.
[32] O. Senkov, G. Wilks, D. Miracle, C. Chuang, P. Liaw, Refractory high-entropy alloys, Intermetallics 18(9) (2010) 1758-1765.

[33] A. Takeuchi, A. Inoue, Classification of bulk metallic glasses by atomic size difference, heat of mixing and period of constituent elements and its application to characterization of the main alloying element, Mater. Trans. 46 (12) (2005) 2817-2829.
[34] O.N. Senkov, S.L. Semiatin, Microstructure and properties of a refractory high-entropy alloy after cold working, J. Alloys Compd. 649 (2015) 1110-1123.
[35] Y.D. Wu, Y.H. Cai, T. Wang, J.J. Si, J. Zhu, Y.D. Wang, X.D. Hui, A refractory Hf25Nb25Ti25Zr25 high-entropy alloy with excellent structural stability and tensile properties, Mater. Lett. 130 (2014) 277-280.
[36] G. Dirras, L. Lilensten, P. Djemia, M. Laurent-Brocq, D. Tingaud, J.P. Couzinié, L. Perrière, T. Chauveau, I. Guillot, Elastic and plastic properties of as-cast equimolar TiHfZrTaNb high-entropy alloy, Mater. Sci. Eng. A 654 (2016) 30-38.
[37] L. Lilensten, J.-P. Couzinié, J. Bourgon, L. Perrière, G. Dirras, F. Prima, I. Guillot, Design and tensile properties of a bcc Ti-rich high-entropy alloy with transformation-induced plasticity, Mater. Res. Lett. 5(2) (2017) 110-116.
[38] S. Sheikh, S. Shafeie, Q. Hu, J. Ahlström, C. Persson, J. Veselý, J. Zýka, U. Klement, S. Guo, Alloy design for intrinsically ductile refractory high-entropy alloys, J. Appl. Phys. 120(16) (2016) 164902.
[39] W.C. Oliver, G.M. Pharr, An improved technique for determining hardness and elastic modulus using load and displacement sensing indentation experiments, J. Mater. Res. 7(6) (1992) 1564-1583.
[40] D. MA, O. Chung Wo, J. Liu, J. HE, Determination of Young's modulus by nanoindentation, Sci. China. Ser. E 47(4) (2004) 398-408.
[41] G. Dirras, H. Couque, L. Lilensten, A. Heczel, D. Tingaud, J.P. Couzinié, L. Perrière, J. Gubicza, I. Guillot, Mechanical behavior and microstructure of Ti20Hf20Zr20Ta20Nb20 high-entropy alloy loaded under quasi-static and dynamic compression conditions, Mater. Charact. 111 (2016) 106-113.
[42] C. Lu, T. Yang, K. Jin, N. Gao, P. Xiu, Y. Zhang, F. Gao, H. Bei, W.J. Weber, K. Sun, Y. Dong, L. Wang, Radiation-induced segregation on defect clusters in single-phase concentrated solid-solution alloys, Acta Mater. 127 (2017) 98-107.
[43] F. Granberg, K. Nordlund, M.W. Ullah, K. Jin, C. Lu, H. Bei, L.M. Wang, F. Djurabekova, W.J. Weber, Y. Zhang, Mechanism of Radiation Damage Reduction in Equiatomic Multicomponent Single Phase Alloys, Phys. Rev. Lett. 116(13) (2016) 135504.

Chapter 6 The effect of Ta content and heat treatment on the phase stability and mechanical properties of the non-equiatomic $Ta_{(25-x)}Zr_{25}Nb_{25}Ti_{(25+x)}$ medium entropy alloys

6.1 Chapter overview

In previous chapters, Chapter 4 first assessed the equiatomic TiZrNbTa medium entropy alloy (MEA) (chapter 4), which exhibited a single BCC phase, substantial compressive ductility (46 ± 6%) and excellent yield strength (1100 ± 90 MPa) at RT in the as-cast state. On this basis, Chapter 5 investigated non-equiatomic $Ta_{25-x}Zr_{25}Nb_{25}Ti_{25+x}$ (x = 5, 10, 15, 20, at.%) MEAs by partially replacing Ta with Ti to reduce both density and cost. This resulted in high tensile ductility (22%) in the as-cast state at RT with good yield strength (> 900 MPa). However, the current evaluation of the $Ta_{25-x}Zr_{25}Nb_{25}Ti_{25+x}$ MEA system is limited to as-cast and as-printed conditions, both being featured by a single BCC phase as per the design rules. The phase stability of the BCC phase and its potential phase transformations have not been explored yet. In particular, both binary Nb-Zr and Ta-Zr systems can undergo spinodal decomposition at high temperatures as according to their phase diagrams. Considering that Ti is analogous to Zr in many aspects, $Ta_{25-x}Zr_{25}Nb_{25}Ti_{25+x}$ MEAs have the potential to display similar phase transformation features. In that regard, it may offer a different pathway for the creation of novel microstructures for this promising MEA system. This chapter investigates the effect of Ta content and annealing treatment on the phase stability, microstructure and mechanical properties of as-cast $Ta_{25-x}Zr_{25}Nb_{25}Ti_{25+x}$ (x = 0-20 at.%) MEAs from RT to 1200 °C. In addition, their deformation mechanisms at RT and microstructural evolution under compression at elevated temperatures are characterized. After annealing at 1200°C for either 8 h or 24 h, a nanocuboidal structure was formed in the microstructure of $Ta_{25-x}Zr_{25}Nb_{25}Ti_{25+x}$ MEAs containing ≥15 at.% Ta (Ta25, Ta20, and Ta15 MEAs), while the microstructure of lower Ta containing MEAs (Ta10 and Ta5 MEAs) was stable with a single solid-solution BCC phase. As-heat-treated Ta25 (Ta25-HT) exhibited an ultrahigh compressive yield strength ($\sigma_{0.2}$) at room temperature (~1760 MPa) and excellent softening resistance at elevated temperatures, e.g., $\sigma_{0.2}$ retained at ~410 MPa at 1000 °C and ~210 MPa at 1200 °C. In addition, both Ta20-HT and Ta15-HT exhibited a high compression yield strength, but limited ductility at room temperature. On the other hand, Ta10-HT and Ta5-HT showed excellent ductility at room temperature in both tension and compression conditions. The tensile strain and tensile strength at room temperature were ~22.5% and 893 ± 20 MPa for Ta10-HT, and ~27.5% and 750 ± 20 MP for Ta5-HT. respectively.

6.2 Publication

The effect of tantalum content and heat treatment on the phase stability and mechanical properties of $Ta_{(25-x)}Zr_{25}Nb_{25}Ti_{(25+x)}$ medium entropy alloys at different temperatures

V. T. Nguyen [a], M. Qian [b,*], Z. Shi [a], X. Q. Tran [c], D. D. Qu [a], J. Joseph [d], D. M. Fabijanic [d], S. Matsumura [c], C. Zhang [e], F, Zhang[e], J. Zou [a,f*]

[a] *School of Mechanical and Mining Engineering, The University of Queensland, Brisbane, Queensland 4072, Australia*

[b] *Centre of Additive Manufacturing, School of Engineering, RMIT University, Melbourne, Victoria 3000, Australia*

[c] *Department of Applied Quantum Physics and Nuclear Engineering, Kyushu University, Fukuoka 819-0395, Japan*

[d] *Institute for Frontier Materials, Deakin University, Waurn Ponds 3216, Australia*

[e] *CompuTherm LLC, 8401 Greenway Blvd., Suite 248, Middleton, WI 53562, USA*

[f] *Centre of Microscopy and Microanalysis, The University of Queensland, Brisbane, Queensland 4072, Australia*

Abstract

$Ta_{25-x}Zr_{25}Nb_{25}Ti_{25+x}$ (x = 0-20, at.%) is a promising new medium entropy alloy (MEA) system. This study investigates the effect of the Ta content and annealing treatment on the phase transformation and mechanical properties of the MEAs from this system from room temperature (RT) to 1200°C. After annealing at 1200 °C for 8 h, the single solid-solution body-centred cubic (BCC) phase in the as-cast $Ta_{25}Zr_{25}Nb_{25}Ti_{25}$, $Ta_{20}Zr_{25}Nb_{25}Ti_{30}$, and $Ta_{15}Zr_{25}Nb_{25}Ti_{35}$ transformed into an extremely high number density of Ta- and Nb-rich BCC nanocuboids (~$10^3/\mu m^2$, BCC1) in a nanostrip-like Zr-rich (~70 at.%Zr) BCC matrix (BCC2). Conversely, the single BCC phase was retained in both $Ta_{10}Zr_{25}Nb_{25}Ti_{40}$ and $Ta_5Zr_{25}Nb_{25}Ti_{45}$ after annealing. The phase separation arises from three primary reasons: (i) the atomic mismatch dependent phase stability (affected significantly by the Ta content), (ii) the highly positive mixing enthalpy of both Ta-Zr and Nb-Zr (strong tendency to separation between each pair), and (iii) the 3-4 orders of magnitude higher mobility of Zr than Ta, Nb and Ti in these MEAs (kinetically driven). Detailed CALPHAD predictions of phase stability and compositions agreed with experimental observations for the high Ta (≥15 at.%) MEAs but differed from those for the low Ta (≤10 at.%) MEAs. The predicted diffusion distance of Zr (~4.1 nm) based on the CALPHAD data corresponds to the measured Zr-rich (~70 at.%) nanostrip width (3 ± 2 nm). The nanocuboidal structure exhibited 112<111>-type of twinning deformation under

compression at RT while shear-band dominated deformation occurred in the single BCC phase. The $Ta_{25}Zr_{25}Nb_{25}Ti_{25}$ MEA retained yield strength of ~410 MPa at 1000ºC and ~210 MPa at 1200ºC. The microstructural evolution during compression at elevated temperatures was characterised and discussed in detail.

Keywords: tantalum, zirconium, medium entropy alloys (MEAs), high entropy alloys (HEAs), nanocuboidal, mechanical properties.

1. Introduction.

Refractory high entropy alloys (RHEAs) were first introduced by Senkov *et al* in 2010 [1], and synthesized from high-melting-point metals including Hf, Ta, Nb, Zr, Ti, V, W, Mo and Cr. They have shown a range of promising properties such as ultrahigh strength [2-8], resistance to softening at elevated temperatures [5, 9-12], and excellent corrosion resistance [13, 14]. However, they usually exhibit low ductility at room temperature (RT) under both tension and compression conditions [1, 15, 16], in addition to their high density. Consequently, much effort has been made to reduce their density and improve their RT ductility without sacrificing their high temperature properties for both broader potential applications and more practical industrial processing [2, 5, 17-19]. The first major group of RHEAs that contain Ta, Nb, Zr and Ti include Al0.4Hf0.6NbTaTiZr [2], Al0.3NbTaTi1.4Zr1.3 [17], AlNbTa0.5TiZr0.5 [20], AlMo0.5NbTa0.5TiZr0.5 [20], .Al0.5Mo0.5NbTa0.5TiZr [20], Al0.25NbTaTiZr [20], and AlMo0.5NbTa0.5TiZr [2, 17, 20]. In these RHEAs, Al was first introduced to reduce density [2], but it was soon found that Al also significantly improved their strengths [2, 17, 20]. These Al-containing RHEAs similarly exhibited low ductility at RT under compression and even after hot isostatic pressing (HIP). However, after HIP at 1200°C and further annealing at 1200°C, a unique microstructure, featured by a disordered body-centred cubic (BCC) nanocuboidal phase in an ordered BCC matrix, was observed in Al0.3NbTaTi1.4Zr1.3 [17], Al0.5Mo0.5NbTa0.5TiZr [20], Al0.25NbTaTiZr [20], and AlMo0.5NbTa0.5TiZr [20] RHEAs. Spinodal decomposition was proposed to be responsible according to Senkov *et al.* [21]. This microstructure enhanced the strength at temperatures up to 1000°C but resulted in compressive ductility of less than 5% at RT [20].

Of the high-melting-point elements specified above, Ti, Ta, Zr, and Nb are the premier biocompatible metals for load-bearing bone implant applications [22, 23], as well as for other structural applications including at elevated temperatures [2, 17, 20]. Hence, we first assessed the equiatomic TiZrNbTa medium entropy alloy (MEA) [24], which showed substantial

compressive ductility (46 ± 6%) and excellent yield strength (1100 ± 90 MPa) at RT in the as-cast state, compared with other HEAs containing these four elements [22, 23]. On this basis, we further investigated non-equiatomic $Ta_{25-x}Zr_{25}Nb_{25}Ti_{25+x}$ (x = 5, 10, 15, 20, at.%) MEAs by partially replacing Ta with Ti to reduce both density and cost [25]. This resulted in high tensile ductility (22%) in the as-cast state at RT with good yield strength (> 900 MPa) [25]. The high ductility means that these alloys can be cast or additively manufactured (fusion) into intricate thin-walled parts without microcracking, which commonly occurs in low ductility materials such as TiAl alloys unless a high powder bed temperature (≥ 1000 °C) is used [26]. Indeed, a recent study has confirmed that $Ta_{25-x}Zr_{25}Nb_{25}Ti_{25+x}$ MEAs can be easily manufactured by additive manufacturing (single BCC phase) [27]. This reinforces the good manufacturability of this MEA system for potential practical applications.

The current evaluation of the $Ta_{25-x}Zr_{25}Nb_{25}Ti_{25+x}$ MEA system is limited to as-cast and as-printed conditions [24, 25, 27], both being featured by a single BCC phase as per the design rules. The phase stability of the BCC phase and its potential phase transformations have not been explored yet. In particular, both binary Nb-Zr and Ta-Zr systems can undergo spinodal decomposition at high temperatures [21]. Considering that Ti is analogous to Zr in many aspects, $Ta_{25-x}Zr_{25}Nb_{25}Ti_{25+x}$ MEAs have the potential to display similar phase transformation features or just distinctly different types. In either case, it may offer a different pathway for the creation of novel microstructures for this promising MEA system. This study investigates the effect of Ta content and annealing treatment on the phase stability, microstructure and mechanical properties of as-cast $Ta_{25-x}Zr_{25}Nb_{25}Ti_{25+x}$ (x = 0-20 at.%) MEAs from RT to 1200 °C. In addition, their deformation mechanisms at RT and microstructural evolution under compression at elevated temperatures are characterized. The purpose is twofold: to further explore the potential of this new MEA system and to advance the fundamental knowledge base for the design of HEAs with Ta, Zr, Nb and Ti as principal constituent elements.

2. Experimental procedure

2.1 Materials and sample preparation

Five $Ta_{25-x}Zr_{25}Nb_{25}Ti_{25+x}$ (x = 0, 5, 10, 15, 20, at.%, equiatomic at x = 0) MEAs were prepared by arc-melting of pure metals of Ti, Zr, Nb, and Ta (all in 99.95wt.% purity) in a Ti-oxygen-getter argon atmosphere. They are designated by their Ta content as Ta25 ($Ta_{25}Zr_{25}Nb_{25}Ti_{25}$), Ta20 ($Ta_{20}Zr_{25}Nb_{25}Ti_{30}$), Ta15 ($Ta_{15}Zr_{25}Nb_{25}Ti_{35}$), Ta10 ($Ta_{10}Zr_{25}Nb_{25}Ti_{40}$) and Ta5 ($Ta_5Zr_{25}Nb_{25}Ti_{45}$). To ensure chemical homogeneity, each MEA ingot (~20 g) was remelted six times and kept in the liquid state for 10 min during each remelting cycle before it was flipped

for next remelting. The melt was eventually cast in a rectangle water-cooled copper mould to form a cuboidal bar with dimensions of 100 ×13 × 8 mm^3 (thickness: 8 mm). The as-cast bars were annealed at 1200ºC for 8 h in a vacuum of (1-3) × 10^{-4} Pa and cooled to RT (heating and cooling: 4ºC/min). These heat-treated alloys are designated with the suffix "HT". In addition, the equiatomic Ta25 MEA was annealed at 1200ºC for 24 h (heating and cooling: 4ºC/min), designated as Ta25-HT24, to study the effect of annealing time on microstructure.

2.2 Microstructural characterization

Samples cut from each MEA bar were mechanically ground and polished for metallographic examination. Constituent phases were identified using X-ray diffraction (XRD) with monochromatic Cu Kα radiation (Bruker D8 Advance MKII). An FEI Scios DualBeam FIB-SEM (scanning electron microscopy) system, equipped with an electron backscatter diffraction (EBSD) detector and an energy-dispersive X-ray spectroscopy (EDS) detector, was used for characterization. Transmission electron microscopy (TEM) (JEOL JEM 200CF, and Philips Tecnai F20) was employed for additional microstructural characterization using specimens prepared by the FIB-SEM system.

2.3 Mechanical testing

Nanoindentation was conducted on as-polished cross-sections of each sample in eight randomly selected regions with a Berkovich indenter (tip radius < 100 nm, MTS Systems Corp., Oakridge, TN). Dog-bone-like tensile specimens (gauge length: 8 mm; width: 2.9 mm; thickness: 1.3 mm) and cylindrical compressive specimens (Φ3.5 mm × 6 mm) were prepared by wire cutting. Three tests were performed for each condition at a strain rate of 5×10^{-3} s^{-1} on an Instron 5584 EM Frame machine equipped with a video extensometer for both tensile and compressive testing at RT (~25ºC).

Compression testing at elevated temperatures was performed only for the Ta25-HT24 MEA using a dilatometer (TA Instruments, DIL805A/D type 805) at a strain rate of 10^{-2} s^{-1}. Each specimen was first heated to 600, 800, 1000, and 1200°C at 120ºC/min by induction coils in a vacuum of ~9×10^{-3} Pa and soaked for 15 min at each temperature to ensure a uniform temperature distribution. The specimen temperature was monitored via a thermocouple welded to it. The compression testing was terminated at 30% compressive strain at each temperature, followed by cooling at 50 ºC/s to RT.

2.4 Thermal analysis and Pandat simulation

Differential scanning calorimetry (DSC) was conducted on samples of Ta25-HT24, Ta20-HT, Ta15-HT, Ta10-HT, and Ta5-HT MEAs using a Netzsch STA 409 in a high-purity argon gas flow to identify their characteristic solid-state phase transformation temperatures. All samples were heated to 1400^{o}C at 10^{o}C/min, held for 1 h, and then cooled at 10^{o}C/min to RT. To better understand the phase transformations in the $Ta_xTi_{50-x}Nb_{25}Zr_{25}$ MEA system, its equilibrium phase diagrams were calculated using the CALPHAD approach [35, 36] through the Pandat^{TM} software [28, 29] and the PanNb2019a thermodynamic + atomic mobility database. There are six binary (Nb-Ta, Nb-Ti, Nb-Zr, Ta-Ti, Ta-Zr, and Ti-Zr) and four ternary (Nb-Ta-Ti, Nb-Ta-Zr, Nb-Ti-Zr, and Ta-Ti-Zr) sub-systems involved in this quaternary system. The self-diffusion coefficient of each element within the BCC phase was taken from the reference book [30]. Although experimental data on the diffusion in the above sub-systems are limited, Liu *et al* have assessed the atomic mobility in the BCC Nb-Ta [31], Nb-Ti [32], Nb-Zr [33], Ta-Ti [34], and Ti-Zr [35] alloys. Their assessments were adopted in our current modelling work with modifications for consistency and compatibility. The descriptions of all other constituent binary and ternary systems were obtained via extrapolation.

3. Results

3.1 Constituent phases in as-cast and as-annealed MEAs

Fig. 1 (a) shows the XRD patterns obtained from the five MEAs in both the as-cast and as-annealed conditions. An exclusive BCC phase was detected in each MEA in both conditions. Fig. 1 (b) is a closer view of the (110) peak for each alloy, confined to the 2Θ range of 36-42°. The (110) peak position for Ta25, Ta20, and Ta15 shifted towards higher 2Θ values after annealing, indicating shrinkage in the BCC lattice, possibly due to local redistribution of elements. However, no shift was observed in the (110) peak position for both Ta5 and Ta10 MEAs after annealing, implying more stable BCC phase compositions.

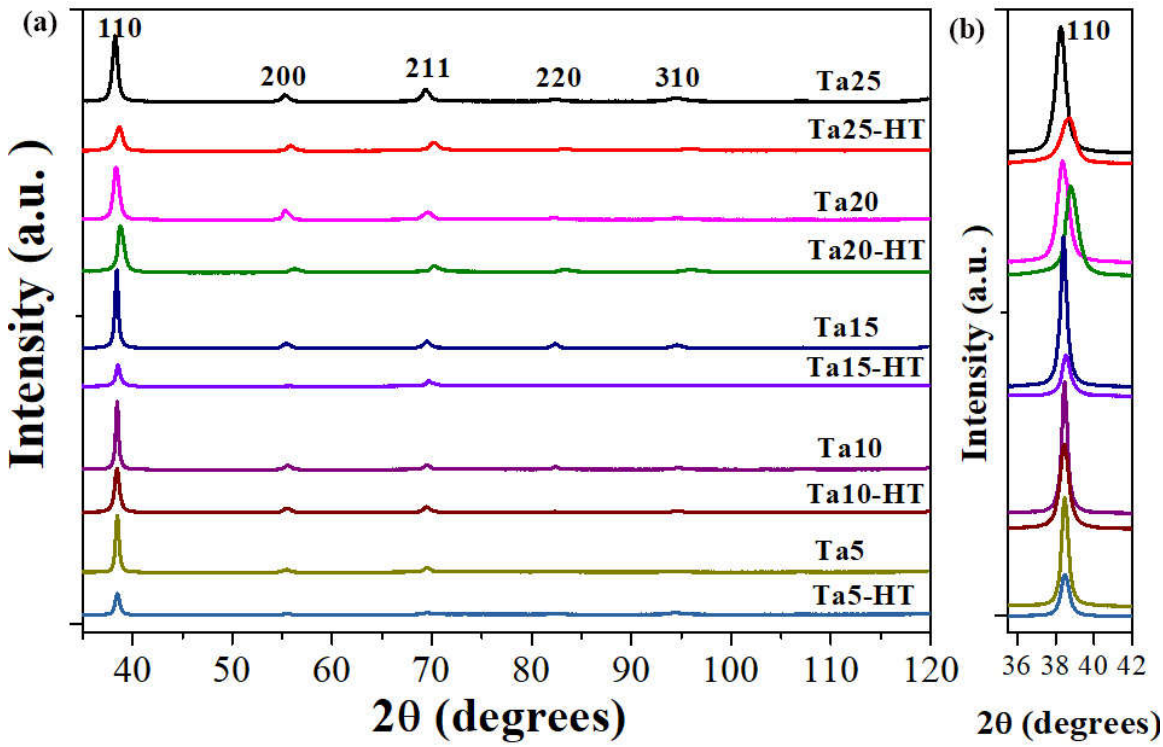

Figure 1 (a) XRD patterns for Ta25, Ta20, Ta15, Ta10 and Ta5 MEAs in as-cast and as-annealed states (HT: annealed at 1200 ºC for 8 h in vacuum), and (b) zoomed-in (110) peaks in (a).

3.2 Microstructural characteristics of as-cast and as-annealed $Ta_{25-x}Zr_{25}Nb_{25}Ti_{25+x}$ MEAs

The as-cast microstructure of each MEA has been investigated previously [25]. A dendritic microstructure was observed for each case (Fig. S1 in Supporting Information), with Ta being enriched in the dendrites because it is the highest melting point element in the Ta, Zr, Nb, and Ti alloy system. The microstructure of each MEA after annealing at 1200 ºC for 8 h is shown in Fig. 2 (a-e). The as-cast dendritic structure was retained to a certain extent in Ta25-HT (Fig. 2 a) and Ta20-HT (Fig. 2 b) due to their higher Ta content but absent in the lower Ta content Ta15-HT (Fig. 2 c), Ta10-HT (Fig. 2 d), and Ta5-HT (Fig. 2 e) MEAs. Detailed compositional analyses by EDS line-scans confirmed the distribution of Ta and the nominal composition of each alloy as well (Fig. S2 and Table S1).

A closer inspection of the microstructure of each annealed MEA revealed distinct features. A unique basket-weave-like nanostructure was observed throughout the interior of each grain in Ta25-HT (Fig. 2 a″), Ta20-HT (Fig. 2 b″) and Ta15-HT (Fig. 2 c″), in addition to a grain boundary (GB) lamellar structure (Fig. 2 (a′, b′, c′)). However, neither feature was observed in Ta10-HT (Fig. 2 d′, d″) and Ta5-HT (Fig. 2 e′, e″). Clearly, Ta25-HT, Ta20-HT and Ta15-HT MEAs have undergone specific phase transformations.

Similarly, the basket-weave-like nanostructure was observed in Ta25-HT24 that was annealed at 1200 ºC for 24 h, as shown in Fig. 3 (a, a′). A high angle annular dark-field (HAADF) image was taken along the <001> BCC zone-axis of the nanocuboids as shown in Fig. 3 (a′′). It is revealed that the nanostructure is composed of an extremely high number density of nanocuboids (~$10^3/\mu m^2$) with an average size of 28 ± 10 nm, separated by the nanostrip-like matrix with an average strip width of 3 ± 2 nm. Fig. 3 (b, c) shows the corresponding EDS mapping and line-scan profiles from the area marked in Fig. 3 (a′′), which identified that the nanostrip-like matrix is Zr-enriched (~70 at.%Zr) and depleted of Ta and Nb. They are comparable to the nanostrip-like Zr- and Hf-rich regions observed in the annealed equiatomic TaNbHfZr HEA, referred to as local short-range clusterings (SRCs) by the authors of Ref. [36].

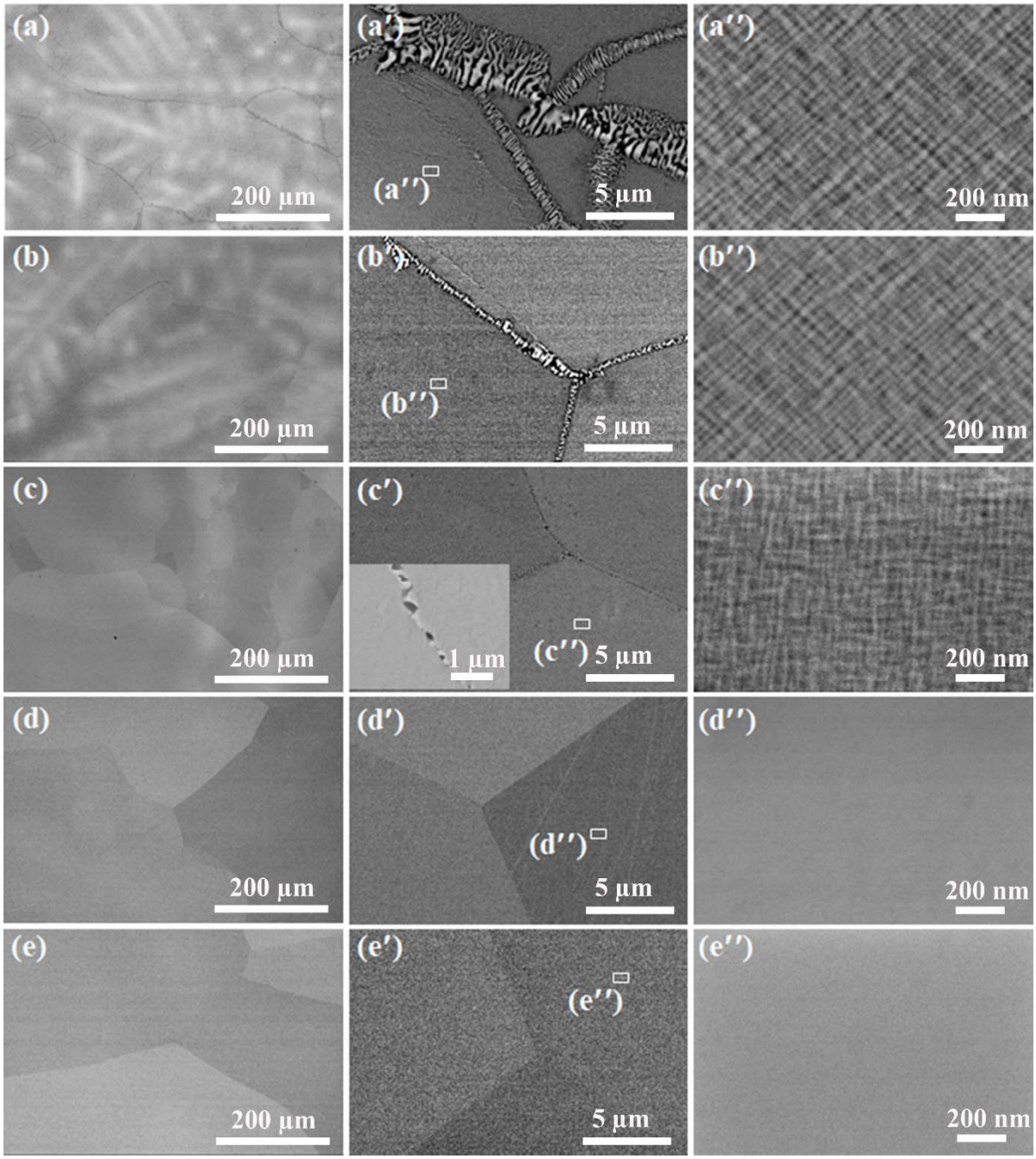

Figure 2 SEM-BSE images of representative microstructures of $Ta_{25-x}Zr_{25}Nb_{25}Ti_{25+x}$ (x = 0-20, at.%) MEAs after annealing at 1200 ºC for 8 h. The magnification increases from the left to the right for each MEA: (a, a′, a′′) Ta25-HT; (b, b′, b′′) Ta20-HT; (c, c′, c′′) Ta15-HT; (d, d′, d′′) Ta10-HT; and (e, e′, e′′) Ta5-HT. The interior of each grain in Ta25-HT, Ta20-HT and Ta15-HT MEAs exhibited a unique basket-weave-like nanostructure (Fig. 2 a′′-c′′), which is absent in Ta10-HT and Ta5-HT (Fig. 2 d′′-e′′).

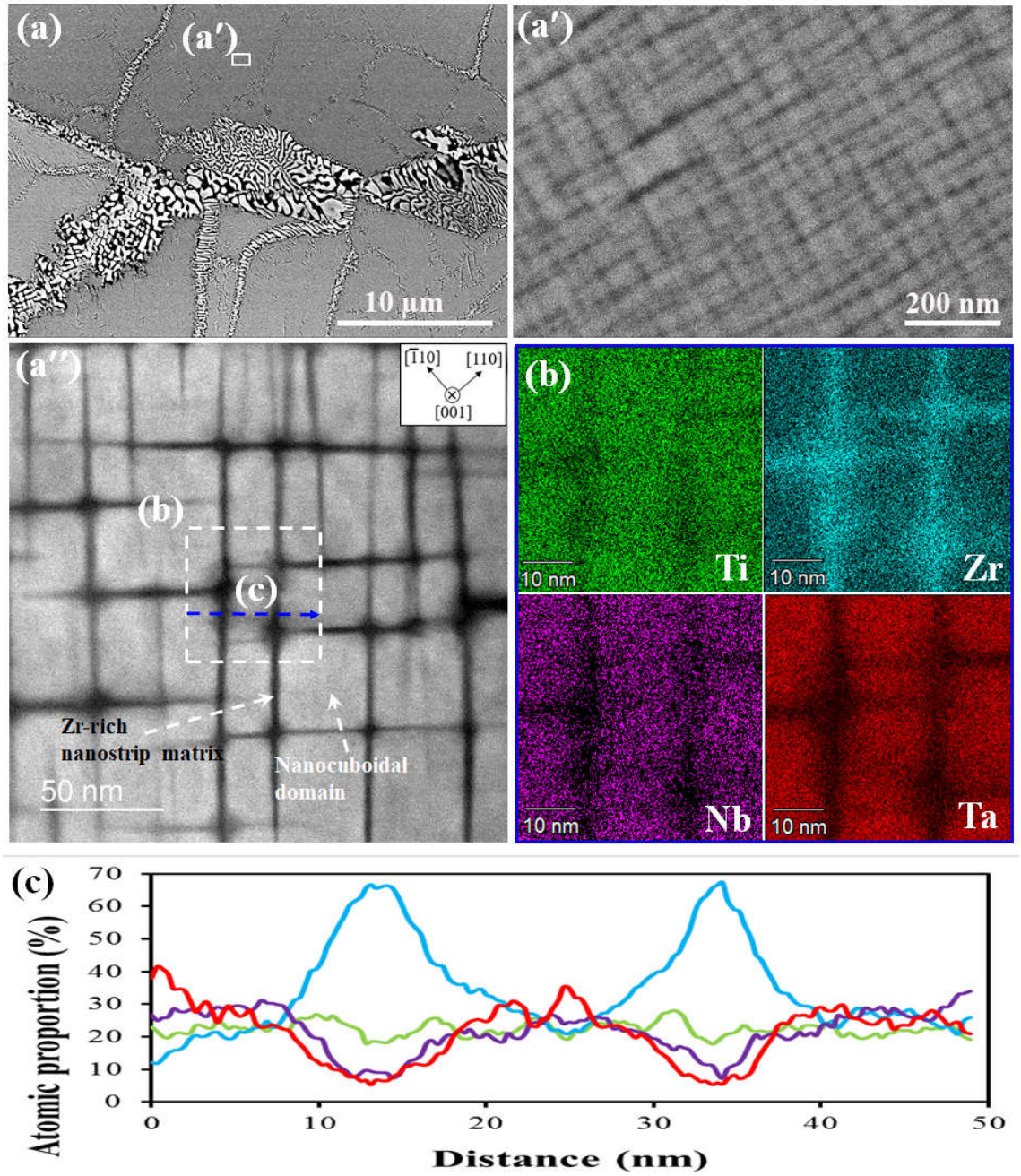

Figure 3 (a) SEM-BSE image of the microstructure of Ta25-HT24 MEA; (a′) magnified view of the area marked in (a); (a″) a HAADF view of the basket-weave-like nanostructure in (a′), revealing its nanocuboidal structure, where the [001] zone axis of the nanocuboids was parallel to the electron beam; (b) STEM-EDS mapping of the nanocuboidal structure marked in (a″); and (c) EDS line-scan profiles across the blue arrow in (a″).

Further detailed high resolution (HR) HAADF characterisation of both the nanocuboidal phase and the matrix phase observed in the Ta25-HT24 MEA is shown in Fig. 4. Fig. 4 (a) is a [001] zone-axis HAADF image taken from a nanocuboidal region. The dark contrast of the nanostrip-like matrix is due its high Zr content (lower-Z-number vs. Nb and Ta). The [001] zone axis

selected area electron diffraction (SAED) pattern exhibited noticeable asymmetric diffuse scattering (Fig. 4 a′), where the Bragg spots stretched towards the shorter reciprocal vectors as indicated by the red arrows in Fig. 4 (a′). Fig. 4 (b, c) shows HR HAADF views of the two interfacial regions marked in Fig. 4 (a), which indicated that the lattice fringes bent from the BCC-cuboidal phase to the Zr-rich matrix. Their corresponding Fast Fourier transforms (FFTs) are given in Fig. 4 (b′, c′). The asymmetric diffuse intensities around the spots in the FFT resembles the diffuse scattering detected by the SAED (Fig. 4 a′), but the streak-like features stretched towards only one principal crystallographic axial direction in each FFT image. This is because Fig. 4b′ was taken from an upright nanostrip (Fig. 4 b) while Fig. 4 (c′) from a horizontal nanostrip (Fig. 4 c). The diffuse intensity in the FFT images and the lattice fringe bending can be attributed to the formation of the short-range clustering of Zr (the largest atom in this system) in the nanostrip-like matrix phase. Similar diffuse scattering was observed in the equiatomic TaNbHfZr HEA and attributed to the short-range clustering of Hf and Zr [36].

The characteristic nanocuboidal structure also formed in Ta25-HT, Ta20-HT, and Ta15-HT as observed by HRTEM (Fig. 5 (a-c)) but is absent in both Ta10-HT and Ta5-HT (Fig. 5 (d, e)). There is a clear trend that the nanocuboidal structure became less prominent with decreasing Ta content until its absence in Ta10-HT. Streak-like diffuse scattering was similarly observed in the [001] zone axis SAED patterns taken from the nanocuboidal regions in Ta25-HT, Ta20-HT, and Ta15-HT (see white arrows in the insets of Fig. 5 (a-c)). In addition, the lattice fringes bent from the nanocuboids to the Zr-rich nanostrip-like matrix (Fig. 5 (a′-c′)). The corresponding FFTs, shown in Fig. 5 (a′′-c′′), displayed similar streak-like diffuse intensities to that discussed earlier (Fig. 4). All these features were absent in both Ta10-HT (Fig. 5 (d′, d′′)) and Ta5-HT (Fig. 5 (e′, e′′)) due to the absence of the nanocuboidal structure.

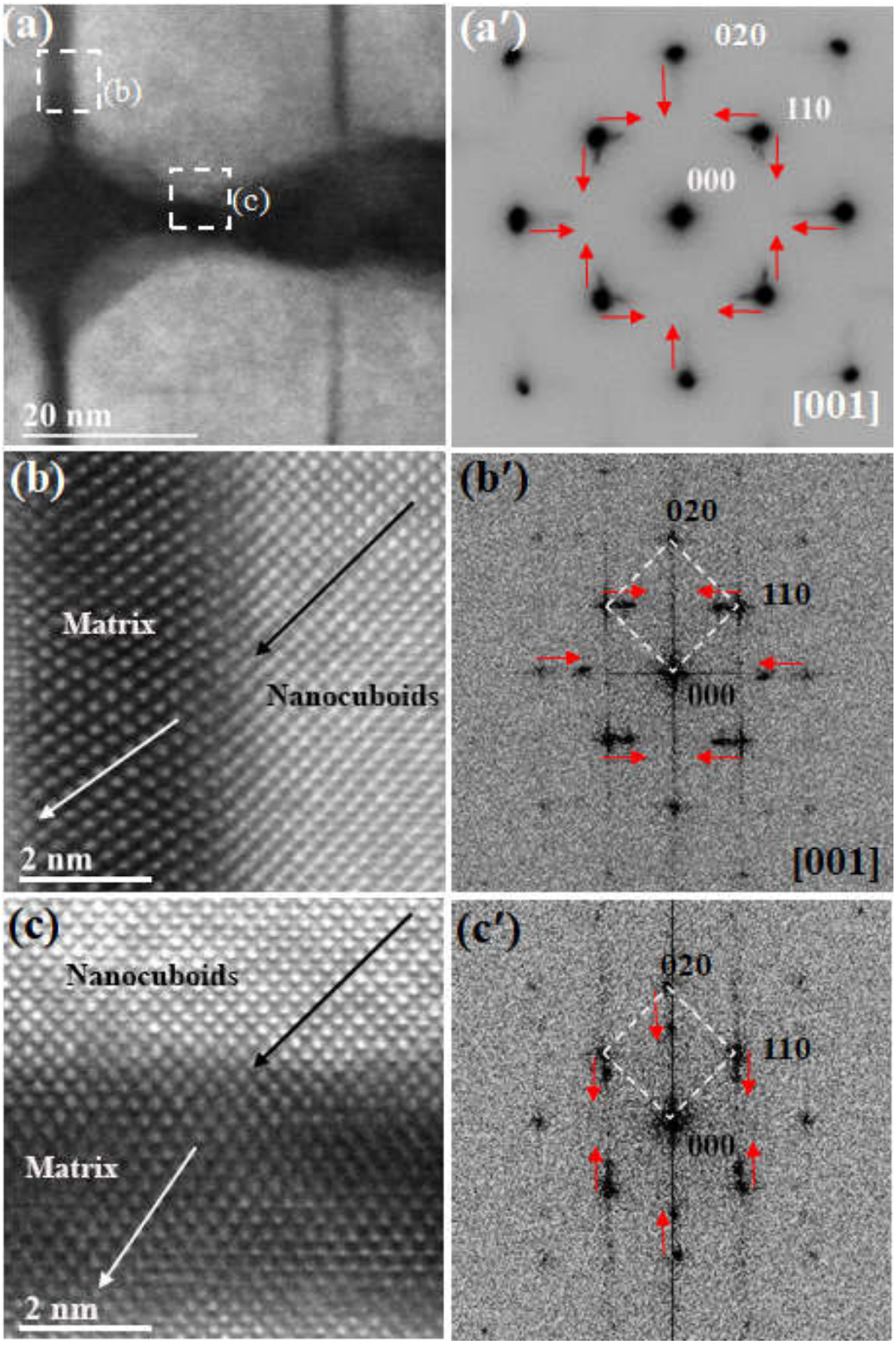

Figure 4 Detailed STEM characterization of the nanocuboidal structures in the Ta25-HT24 MEA. (a) a HAADF view of the nanocuboidal structure imaged along the [001] crystallographic zone axis. (a′) shows the [001] zone axis SAED pattern of the nanocuboidal structure. (b-c) are HR HAADF images from corresponding regions marked in (a) while (b′-c′) are the corresponding FFTs of (b-c).

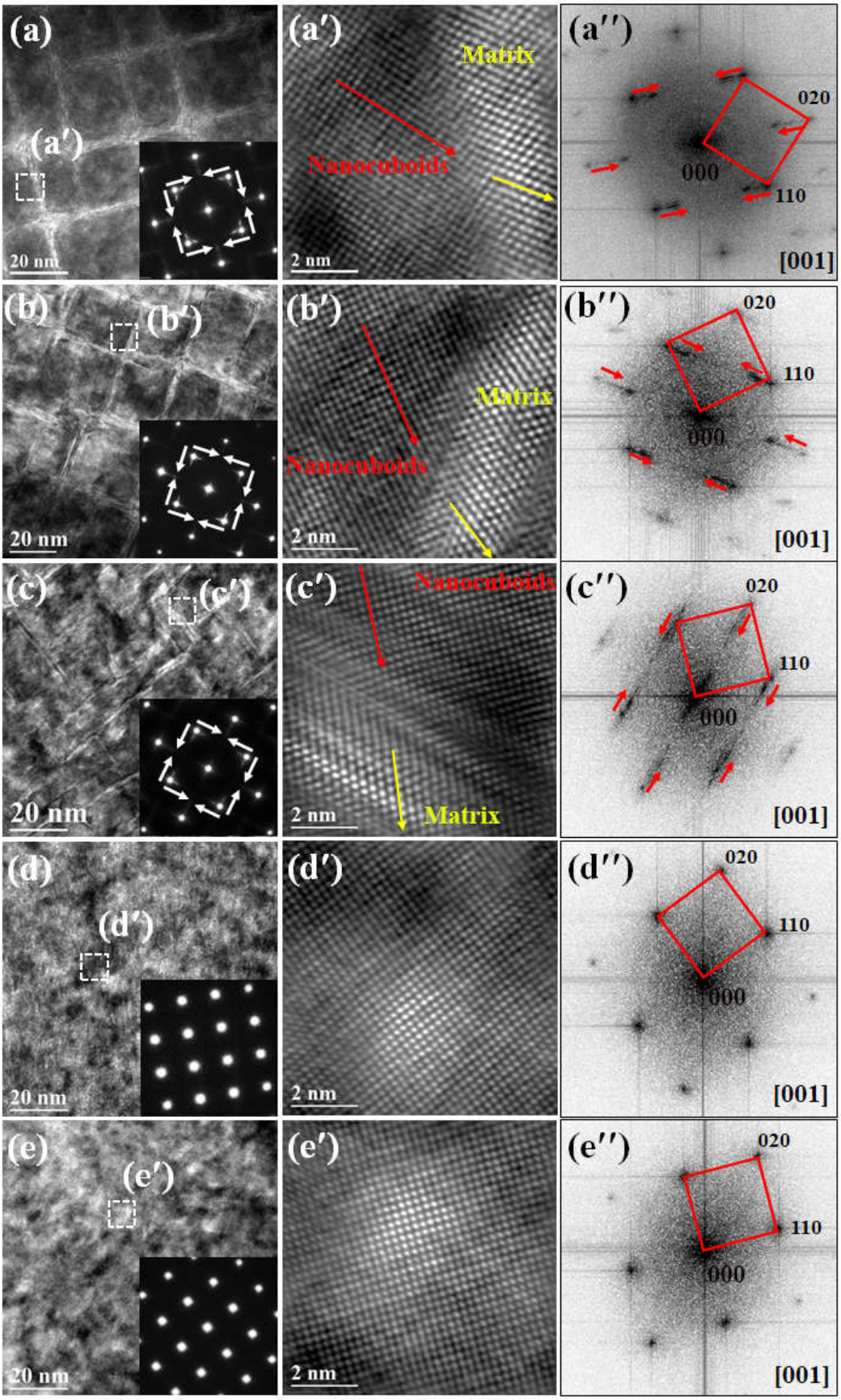

Figure 5 HRTEM images taken from the nanocuboids/matrix regions of (a) Ta25-HT, (b) Ta20-HT, (c) Ta15-HT, (d) Ta10-HT and (e) Ta5-HT MEAs. (a′-e′) are zoomed-in images from corresponding regions marked in (a-e) while (a″-e″) are the corresponding FFTs of (a′-e′).

Fig. 6 presents the TEM-EDS characterisation results of the GB lamellar structure shown in Fig. 3a. It consists of a Zr-rich phase and a Nb- and Ta-rich phase as shown in Fig. 6a. As with the Zr-rich nanostrips in the nanocuboidal structure, the Zr-rich lamella contains ~70 at.% Zr (see Fig. S3) and has a BCC lattice structure. This was identified from the [011], [113], and [001] SAED patterns shown in Fig. 6 (d-f) taken from the circled area in Fig. 6b and the TEM dark-field (DF) image (Fig. 6c) taken using the 200 diffraction spot in Fig. 6d. The Nb- and Ta-rich lamella also has a BCC lattice structure, according to the [001], [111], and [113] zone-axis SAED patterns shown in Fig. 6 (h-j), taken from the circled lamella in Fig. 6g. The GB lamellar structures observed in Ta20-HT and Ta15-HT are similar (see Fig. S4).

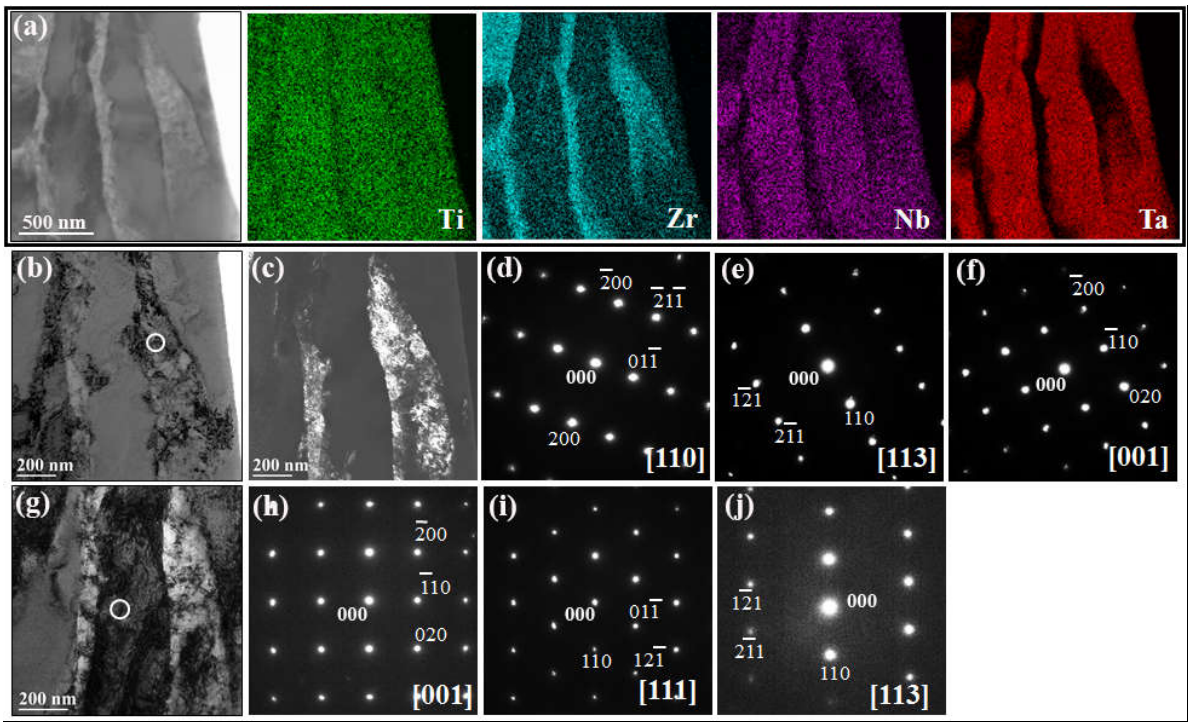

Figure 6 TEM-EDS characterization of the GB lamellar structure in the Ta25-HT24 MEA. (a) TEM-EDS elemental mapping. (b) TEM-BF image of a Zr-rich lamella containing the circle imaged along the [011] zone axis; (c) TEM-DF image taken using the (200) diffraction spot in (d); (d, e, f) SAED patterns taken from the circled region in the Zr-rich lamella in (b) along the [110], [113] and [001] zone axes; (g) TEM-BF view of Nb- and Ta- rich lamella containing a the circle imaged along the [001] zone axis; and (h, i, j) BCC SAED patterns taken from the lamella marked in (g).

3.2 Thermal analysis and Pandat^{TM} simulation

DSC analyses and Pandat^{TM} simulation were performed to understand the phase transformation related to the formation of the nanocuboidal phase. Fig. 7 summarises the DSC results for each

MEA. A phase transformation event was detected for Ta25-HT24 over the temperature range from ~629 °C to ~664 °C in a time frame of ~210 s (Fig. S5 a). A similar event was observed for Ta20-HT from ~604 °C to ~636 °C over a period of ~190 s (Fig. S5 b) but was absent in Ta15-HT, Ta10-HT and Ta5-HT MEAs due to either the reduced transformation intensity or just absence of transformation.

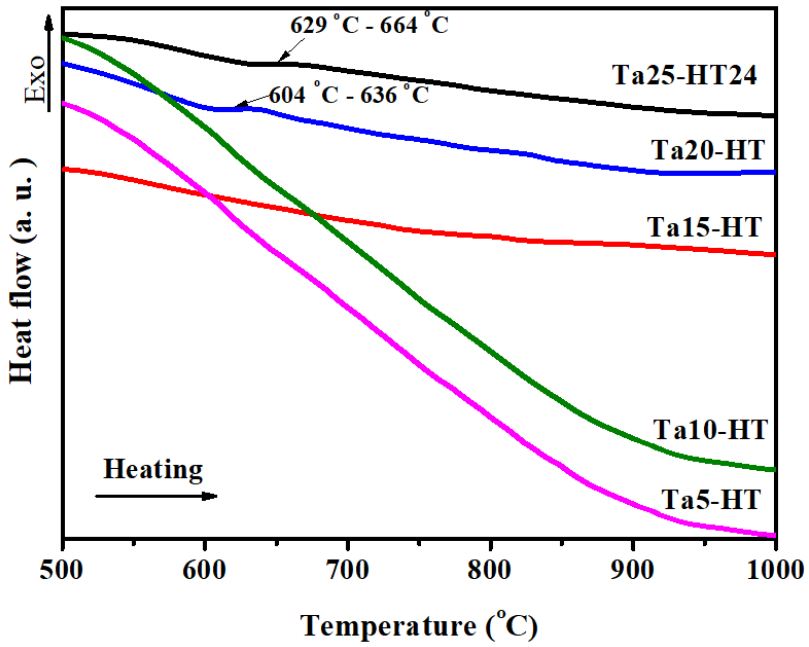

Figure 7 Differential scanning calorimetry (DSC) analyses of the annealed MEAs

Fig. 8a shows the equilibrium phase diagram for the $Ta_{25-x}Zr_{25}Nb_{25}Ti_{25+x}$ system calculated using the Pandat^{TM} software and PanNb2019a database, while the temperature-phase fraction diagrams for each MEA are given in Fig. 8 (b-f). All five MEAs are predicted to be thermodynamically stable as a single solid-solution BCC phase (BCC#1) over a wide temperature range, e.g., 677-1889°C for Ta25 and 500-1733°C for Ta5. Also, Fig. 8a predicted the formation of a second BCC phase (BCC#2) for each MEA at lower temperatures, e.g., below 677°C for Ta25 (DSC: 629-664 °C, Fig. 7), 610°C for Ta20 (DSC: 604-636 °C, Fig. 7), 560°C for Ta15, 520°C for Ta10, and 500°C for Ta5. In addition, the BCC#1 and BBC#2 phases are predicted to be Ta- and Nb-rich and Zr-rich, respectively, as shown in Fig. 8(g, h), for Ta25 (Fig. S6 shows similar predictions for Ta20 and Ta15). In addition, the fraction of the Zr-rich BCC#2 phase decreases noticeably with decreasing Ta content, e.g., from ~0.45 for Ta25 to ~0.39 for Ta15, and then to ~0.04 for Ta5 at 500 °C (Fig. 8 (b-f)). These predictions agree well with the experimental observations discussed above. However, there is a discrepancy, i.e., the Zr-rich BCC#2 phase was observed in neither Ta10-HT nor Ta5-HT while predicted to form in both MEAs below 500 °C (Fig. 8a).

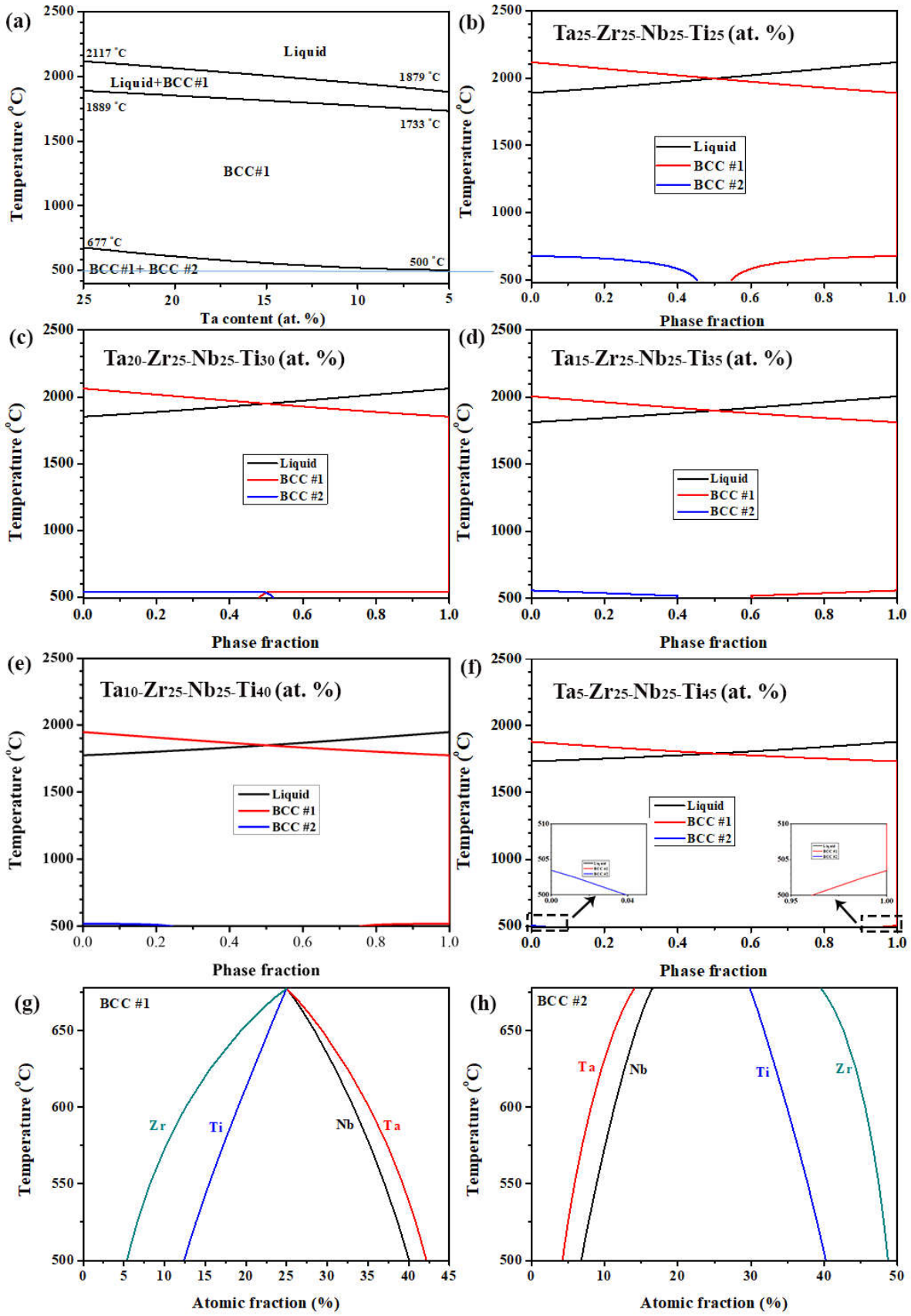

Figure 8 Phase diagram of the $Ta_{25-x}Zr_{25}Nb_{25}Ti_{25+x}$ system with the Ta content ranging from 5% to 25%. Calculated temperature-phase fraction diagrams for (b) Ta25 ($Ta_{25}Zr_{25}Nb_{25}Ti_{25}$), (c) Ta20 ($Ta_{20}Zr_{25}Nb_{25}Ti_{30}$), (d) Ta15 ($Ta_{15}Zr_{25}Nb_{25}Ti_{35}$), (e) Ta10 ($Ta_{10}Zr_{25}Nb_{25}Ti_{40}$), (f) Ta5 ($Ta_5Zr_{25}Nb_{25}Ti_{45}$); and solubility of each element in (g) BCC#1 and (h) BCC#2 of Ta25 MEA.

3.3 Effect of Ta content on mechanical properties and deformation mechanisms at RT

Fig. 9 (a) shows representative compression stress-strain curves for each MEA at RT. The yield strength decreased sharply with decreasing Ta content, accompanied by a clear increase in compressive strain. For example, the Ta25-HT24 MEA exhibited a yield strength of 1760 ± 30 MPa while Ta5-HT achieved only 790 ± 10 MPa. The nanoindentation results obtained from each MEA are presented in Fig. 9 (b). As expected, at the same applied load, the displacement increased with decreasing Ta content (i.e., decrease in hardness). The nanoindentation hardness and elastic modulus were calculated using the Oliver-Pharr method [23]. Table 1 summarises the compression and nanoindentation properties of each MEA. The nanoindentation elastic modulus is generally consistent with the elastic modulus obtained from compressive testing.

Tensile testing was also performed for each MEA. Although Ta25-HT24, Ta25-HT, Ta20-HT, and Ta15-HT MEAs showed good compressive ductility (Fig. 9(a)), their tensile ductility at RT was insufficient and fracture occurred before yielding. In contrast, both Ta5-HT and Ta10-HT exhibited high tensile ductility and reached ~27.5% and ~22.5%, respectively. Thus, only the tensile stress-strain curves for Ta5-HT and Ta10-HT are plotted in Fig. 9c to compare with their as-cast tensile properties. After annealing, both Ta5-HT and Ta10-HT showed higher ductility but lower tensile strengths than the respective as-cast Ta5 and Ta10 MEAs.

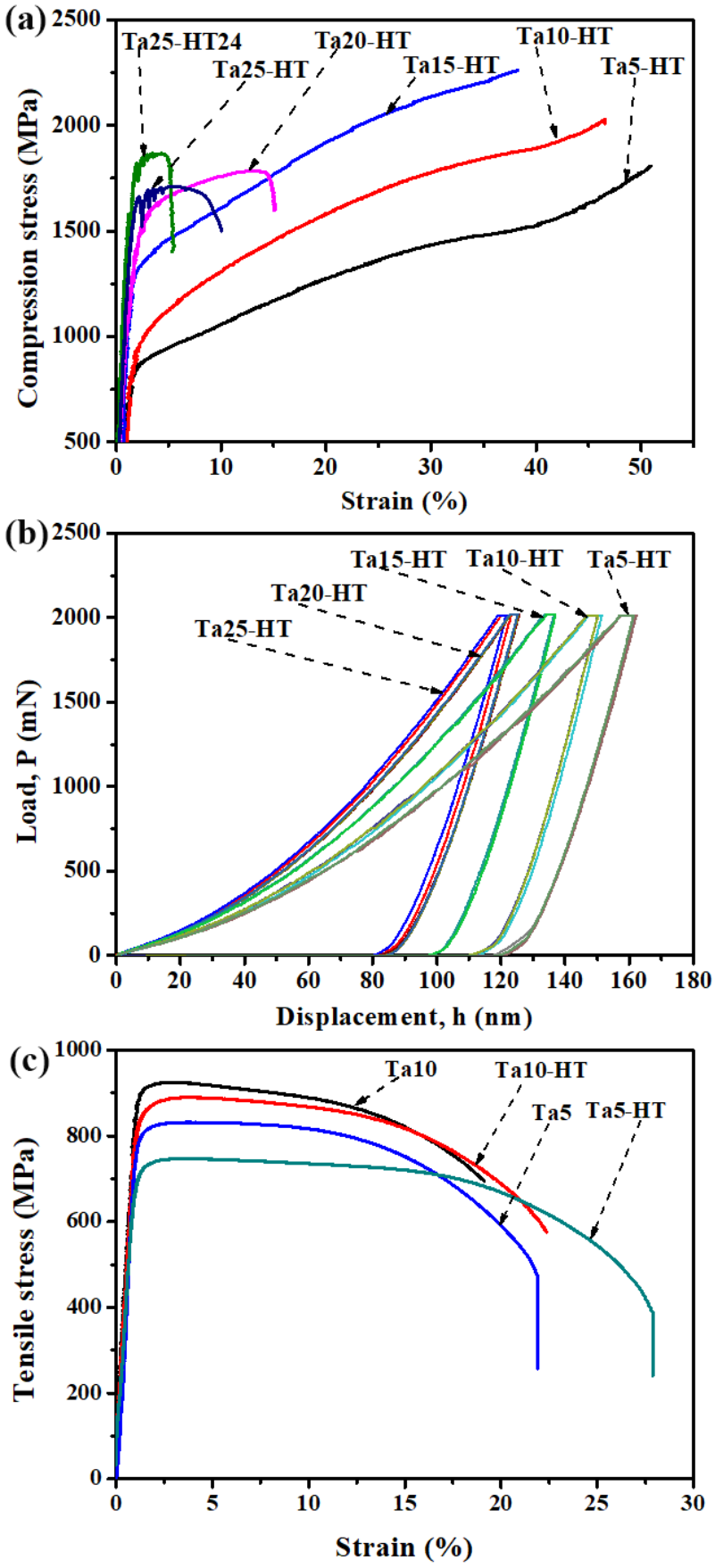

Figure 9 (a) Compressive stress-strain curves of Ta25-HT24, Ta25-HT, Ta20-HT, Ta15-HT, Ta10-HT, and Ta5-HT at RT. (b) Load vs. displacement curves by nanoindentation at RT. (c) Tensile stress-strain curves of Ta10 and Ta5 in both as-cast and as-annealed states at RT.

Table 1 Nanoindentation, compressive and tensile properties of annealed MEAs

MEAs	Nanoindentation hardness (GPa)	Elastic modulus (nanoindentation) (GPa)	Elastic modulus (compression) (GPa)	Compressive yield strength (MPa)	Tensile yield strength (MPa)
Ta25-HT24	-	-	115 ± 4	1760 ± 30	-
Ta25-HT	5.9 ± 0.1	114 ± 2	112 ± 3	1550 ± 30	-
Ta20-HT	5.7 ± 0.1	110 ± 2	98 ± 5	1410 ± 20	-
Ta15-HT	4.5 ± 0.2	106 ± 2	94 ± 5	1300 ± 30	-
Ta10-HT	3.7 ± 0.1	100 ± 1	86 ± 5	880 ± 20	853 ± 20
Ta5-HT	3.4 ± 0.1	87 ± 4	85 ± 4	790 ± 10	726 ± 20

The fracture surfaces of Ta25-HT24 after compression testing at RT are inclined at 38~40^{o} to the loading axis (Fig. 10 a), which are close to the maximum resolved shear stress direction (45^{o}) under uniaxial compression [37]. Microcracks were found to initiate and propagate along the GB lamellar structure (Fig. 10 b), which resulted in intergranular fracture (arrows in Fig. 10 c), although pockets of dimple fracture (Fig. 10 d) were observed as well. The GB lamellar structure is largely responsible for the low ductility of this alloy.

TEM characterisation of the Ta25-HT24 MEA after compression at RT, shown in Fig. 11, revealed the (112)<111>-type of twinning (Fig. 11 (a, b)), which seems to have initiated from the GB regions and then spread through the nanocuboidal structure as shown in Fig. 11 (c, d). Similar twinning deformation was observed in Ta20-HT (Fig. S7).

The two low Ta MEAs, Ta10-HT and Ta5-HT, which both showed high compressive and tensile ductility at RT (Fig. 9c), displayed a different deformation mechanism at RT as shown in Fig. 12. After reaching 50% compressive strain, the deformed microstructure in both MEAs consisted of fine deformation-shear bands (30-450 nm wide) (Fig. 12 (a, b)). The slightly curved shear bands (dash-lines in Fig. 12) are due to the interactions between the shear bands and restrictions by the GBs under substantial compression strain (~50%). Similar shear-band deformation features have been observed in other RHEAs [38, 39].

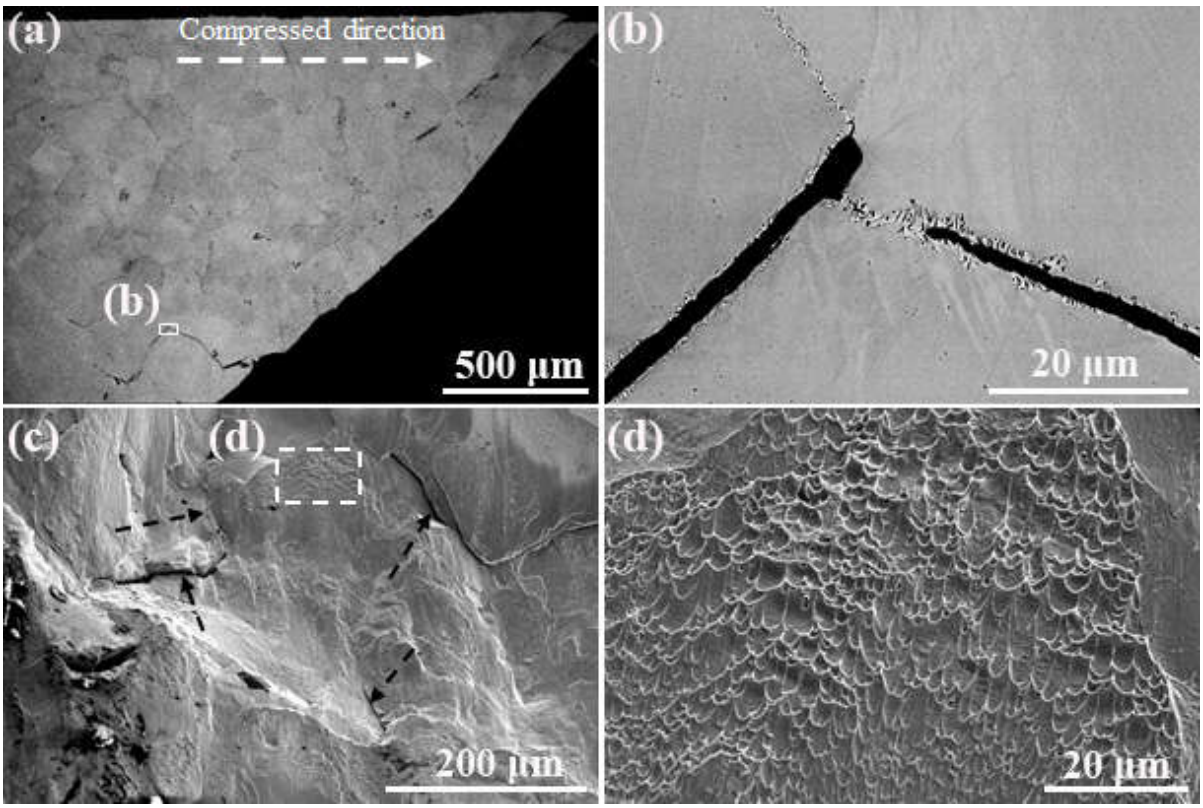

Figure 10 (a) SEM-BSE image of a cross-section containing the fracture surface from a Ta25-HT24 specimen after compression testing at RT, (b) a zoomed-in image of the area marked in (a), (c) representative fracture surface of Ta25-HT24 after compression, and (d) a zoomed-in view of the area marked in (c).

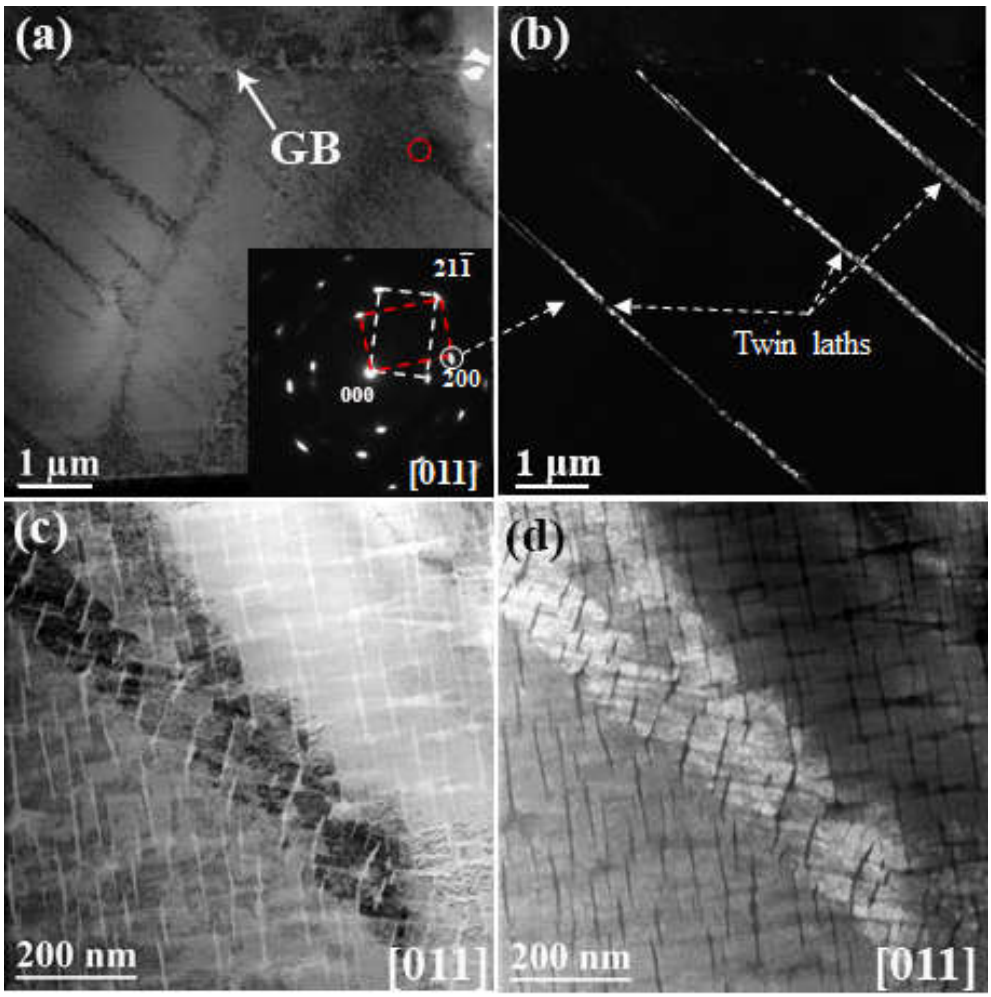

Figure 11 TEM characterization of Ta25-HT24 MEA after compression at RT. (a) TEM-BF image and an inset showing the SAED pattern taken from the red circle region in (a); (b) TEM-DF image from the 200 diffraction spot (twinning) marked in (a); (c) STEM-BF and (d) STEM-HAADF images taken from a single twinning lath.

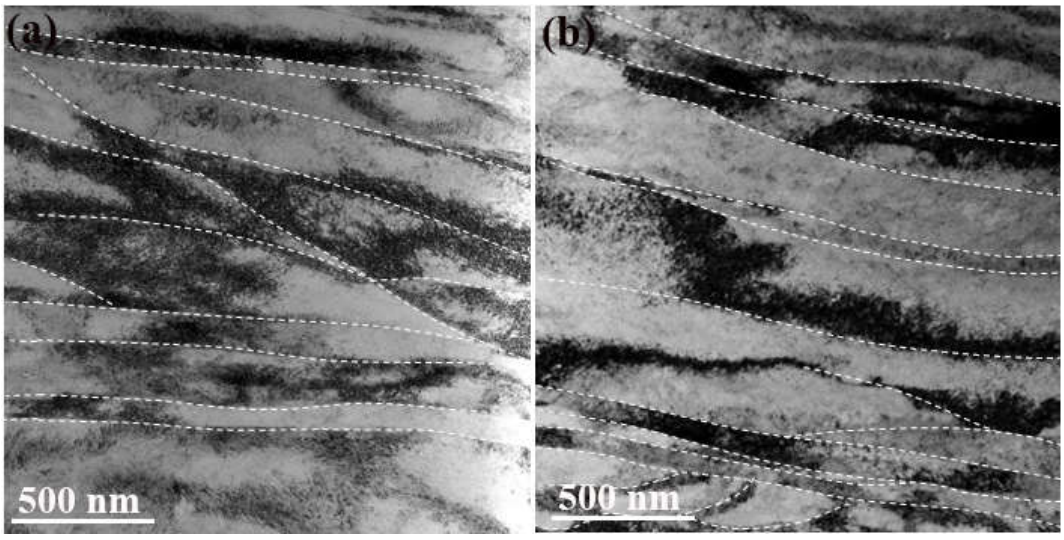

Figure 12 TEM images of (a) Ta10-HT and (b) Ta5-HT after compression strain to 50% at RT.

3.4 Microstructural evolution and mechanical properties of Ta25-HT24 at 600-1200ºC

Considering the similarity between the nanocuboidal structure shown in Fig. 3a″ and the micro-cuboidal structure of Ni-based superalloys, the Ta25-HT24 MEA containing ~$10^3/\mu m^2$ of nanocuboids (extremely high density) was compressed at 600-1200ºC. The results are shown in Fig. 13a. Table 2 lists the yield strength ($\sigma_{0.2}$) at 0.2% strain and the strengths at 5% (σ_5) and 20% (σ_{20}) strain from RT to 1200ºC. Also listed are the properties of other RHEAs for comparison. At both 600ºC and 800ºC, Ta25-HT24 exhibited a clear hardening stage from yielding ($\sigma_{0.2}$) to σ_5 (Table 2). The strength reached 893 MPa at 5% strain at 600ºC. Softening occurred afterwards as can be seen from the reduction of σ_5 to σ_{20}. At 1000ºC, the yield strength reached ~410 MPa, which was higher than that of most reported RHEAs (Table 2), except AlMo0.5NbTa0.5TiZr [2] and those containing W and Mo [9]. At 1200ºC, the alloy retained a nearly constant strength of ~200 MPa without showing cracking at 30% strain. Fig. 13b shows a specimen compressed at 1200ºC to 30% strain, which exhibited a symmetric barrelling shape with homogeneous and harmonic macroscopic deformation.

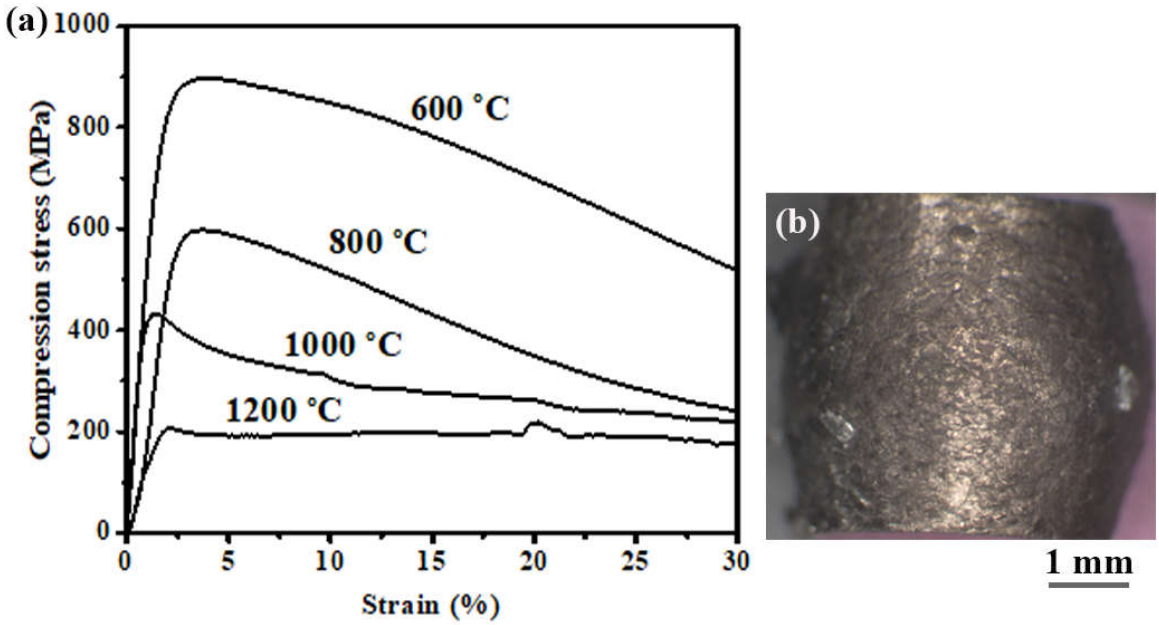

Figure 13 (a) Engineering stress-strain curves of the Ta25-HT24 MEA compressed at different temperatures. (b) A photograph of a specimen after it was compressed at 1200ºC to 30% strain.

Table 2 Compression properties of the Ta25-HT24 MEA at elevated temperatures (yield stress: $\sigma_{0.2}$, stress at 5% strain: σ_5) and the yield stress at elevated temperatures of reported RHEAs.

Alloys	**Properties**	**25 (ºC)**	**600 (ºC)**	**800 (ºC)**	**1000 (ºC)**	**1200 (ºC)**	**Ref**
Ta25-HT24	$\sigma_{0.2}$ (MPa)	1760	813	550	410	210	This study
	σ_5 (MPa)	1886	893	588	351	193	
	σ_{20} (MPa)	-	698	348	261	196	
NbTiV2Zr	$\sigma_{0.2}$ (MPa)	918	571	240	72	-	[5, 40]
NbTiVZr	$\sigma_{0.2}$ (MPa)	1105	843	187	58	-	[5, 40]
CrNbTiZr	$\sigma_{0.2}$ (MPa)	1260	1035	300	115	-	[5, 40]
CrNbTiVZr	$\sigma_{0.2}$ (MPa)	1298	1230	615	259	-	[5, 40]
AlNbTiV	$\sigma_{0.2}$ (MPa)	1020	810	685	158	-	[18]
HfMoNbTiZr	$\sigma_{0.2}$ (MPa)	1575	-	825	635	187	[41]
Al0.4Hf0.6NbTaTiZr	$\sigma_{0.2}$ (MPa)	1841	-	796	298	-	[2]
AlMo0.5NbTa0.5TiZr	$\sigma_{0.2}$ (MPa)	2000	-	1597	745	225	[2]
AlNb1.5Ta0.5Ti1.5Zr0.5	$\sigma_{0.2}$ (MPa)	1280	-	728	403	-	[17]
MoNbTaW	$\sigma_{0.2}$ (MPa)	1058	561	552	548	506	[9]
MoNbTaVW	$\sigma_{0.2}$ (MPa)	1246	862	846	842	735	[9]

The deformation of Ta25-HT24 at elevated temperatures showed distinct features. Fig. 14a is a STEM-BF image of a typical GB region in the alloy after uniaxial compression at 600ºC to 30% strain. The GB lamellar structure (Fig. 3a and Fig. 6) disappeared and was replaced by an ultrafine nano-equiaxed grain structure (grain size: ~90 nm), indicative of recrystallisation. Fig. 14b displays a closer view of the deformed nanocuboidal region, in which the [001] zone-axis of the nanocuboids was parallel to the electron beam. The nanocuboidal structure was retained after 30% compressive deformation at 600ºC but became distorted and coarsened. STEM-EDS elemental mapping revealed that the recrystallized GB region consisted of mixed Zr-rich nanograins and Nb- and Ta-rich nanograins (Fig. 14 (c, d)).

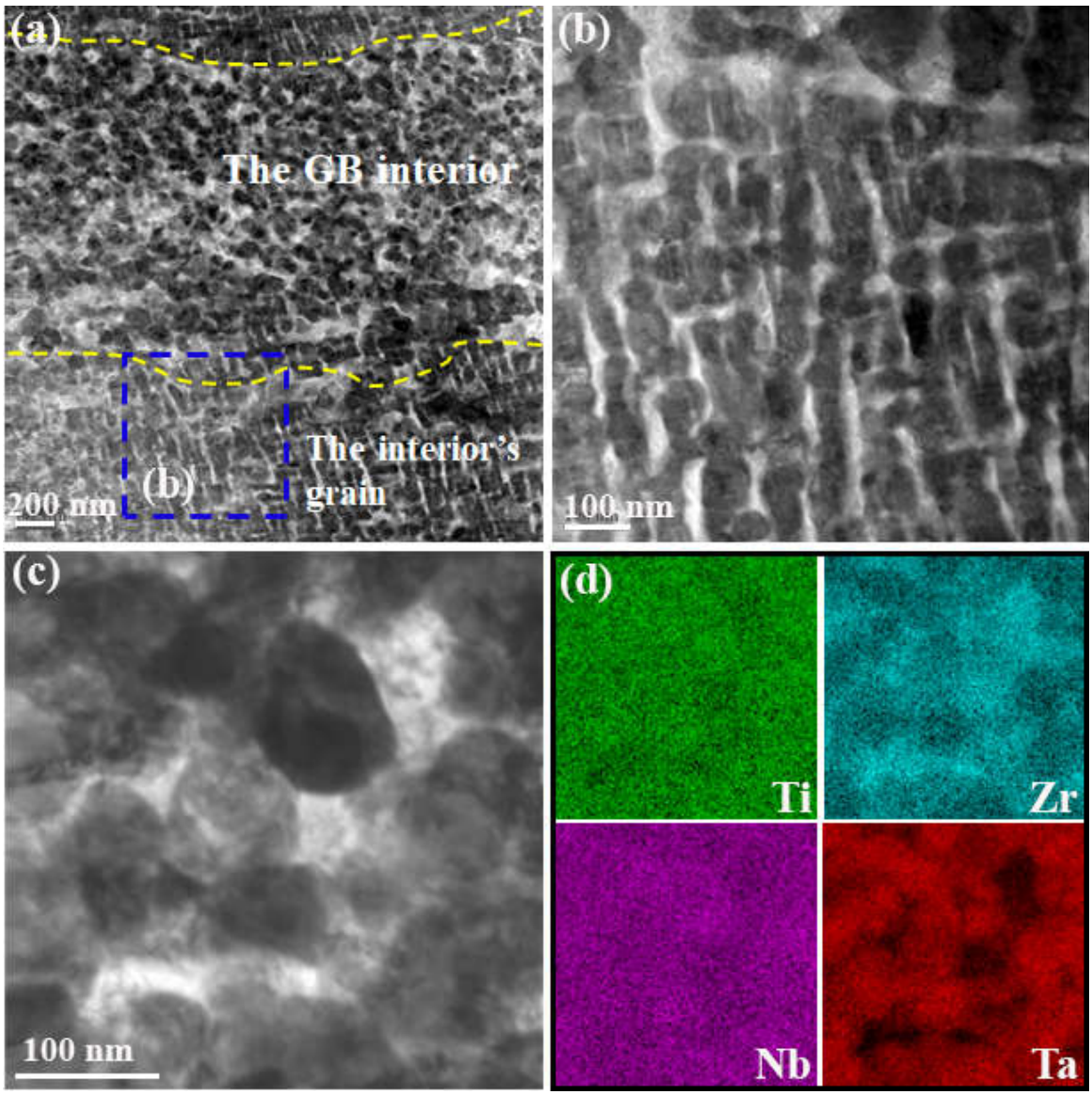

Figure 14 Ta25-HT24 compressed at 600ºC to 30% strain. (a) STEM-BF image of a GB region; (b) zoomed-in image of an area marked in (a); (c) STEM-BF image and (d) corresponding EDS mapping of the recrystallized GB equiaxed grains.

When compressed at 1200 ºC, a fine equiaxed-grain structure was similarly observed along the GBs, but its grain size was increased to 2-5 μm due to the much higher deformation temperature. Fig. 15 (a, b) shows the EBSD image quality (IQ) and inverse pole figure (IPF) images of a longitudinal cross-section of the Ta25-HT24 alloy compressed at 1200ºC to 30% strain. The EBSD-IPF illustrates the continuous change in crystal orientation (i.e., in colour) induced by plastic deformation. No nanocuboidal structure survived after compression at 1200ºC, where only a few dislocations were observed in the grains (Fig. 15 (c, d)). The same was observed when the material was compressed at 800ºC and 1000ºC (Figs. S8-S9). Unlike the nanocuboidal grains, the fine grain structure in the GB areas contained dislocation walls (Fig. 15e) and the composition became reasonably homogeneous compared to before compression (Fig. 6).

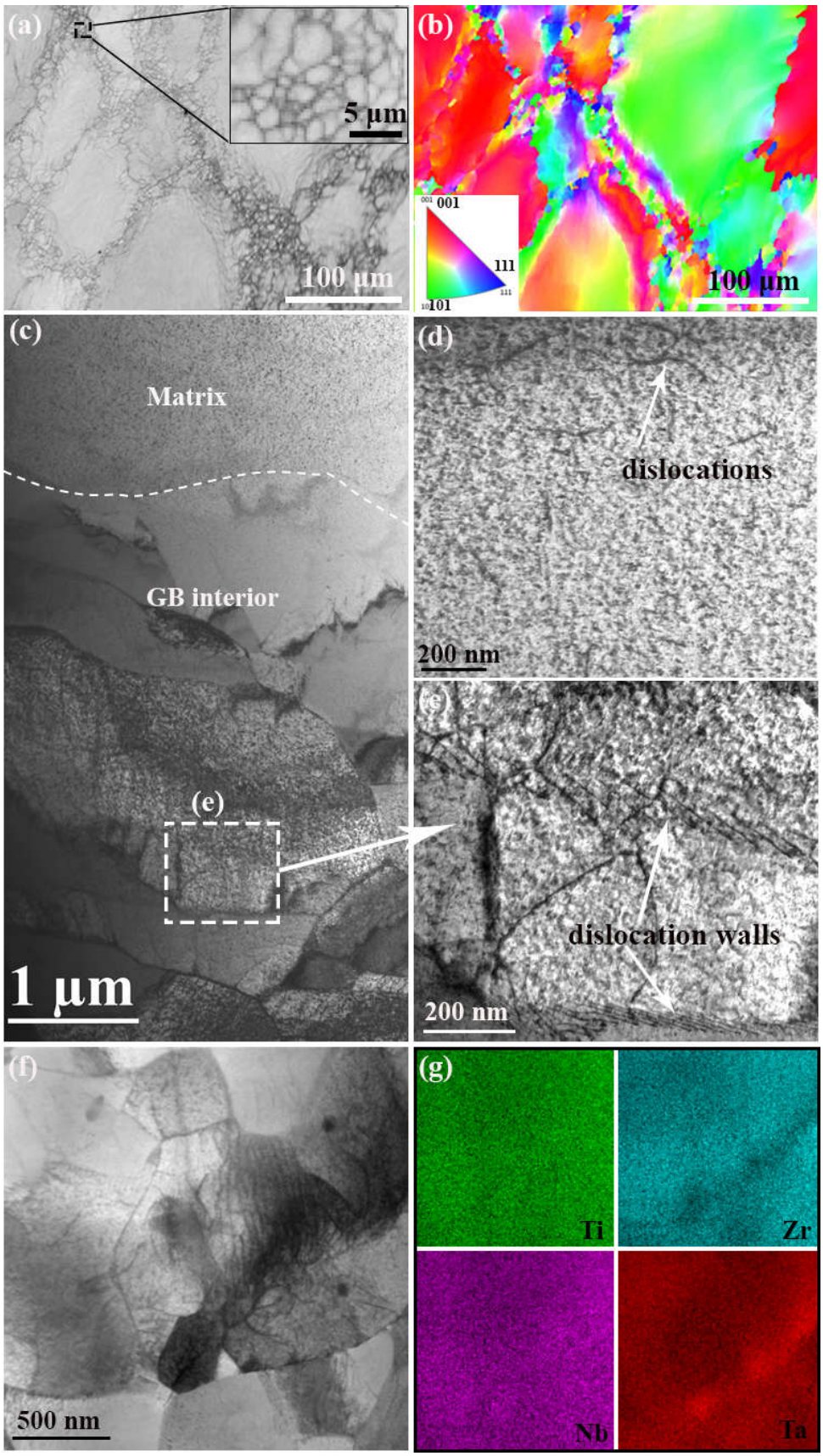

Figure 15 Ta25-HT24 compressed at 1200 ºC to 30% starin. (a) and (b) are the EBSD-IQ and EBSD-IPF images, respectively. (c) A TEM-BF image of a representative GB region. (d) and (e) are zoomed-in TEM-BF images of the grain interiors and the GB area. (f) is a STEM-BF image and (g) is the corresponding STEM-EDS mapping of a GB area.

4. Discussion

4.1 The effect of Ta content on phase stability in $Ta_{25-x}Zr_{25}Nb_{25}Ti_{25+x}$ MEAs

The phase formation in a HEA depends on the atomic mismatch (δ%), mixing enthalpy (H_{mix}, kJ/mol), thermodynamic property (measured by the dimensionless parameter Ω), and valence electron concentration (VEC) from all the constituent elements, in addition to solidification conditions. The empirical rules state that a HEA tends to solidify as a single solid-solution BCC phase with $\delta \leq 6.6\%$, $-11.6\ \text{kJ}\cdot\text{mol}^{-1} < \Delta H_{mix} < 3.2\ \text{kJ}\cdot\text{mol}^{-1}$, $\Omega \geq 1.1$, and $VEC < 6.87$ [42-45]. Table 3 lists the parameters for the five MEAs of this study. They all satisfy the requirements to solidify as a single BCC solid-solution phase for each MEA, consistent with both the XRD results (Fig. 1) and metallographic observations (Fig. S1).

Table 3 Empirical design parameters for each MEA in this study.

MEA	**Ta25**	**Ta20**	**Ta15**	**Ta10**	**Ta5**
Atomic mismatch, $\boldsymbol{\delta}$ **(%)***	4.8	4.78	4.72	4.65	4.58
Mixing enthalpy, $\boldsymbol{H_{mix}}$ **(kJ/mol)**	2.5	2.44	2.36	2.26	2.14
Valence electron concentration, ***VEC***	4.5	4.45	4.4	4.35	4.3
Dimensionless Thermodynamic parameter, $\boldsymbol{\Omega}$	11.6	11.5	11.3	11	10.5

*: Calculated from the atomic radii (Å) [46]: 1.462 (Ti), 1.603 (Zr), 1.429 (Nb), 1.430 (Ta).

The as-solidified single solid-solution BCC phase is, however, metastable in each MEA. It will transform into two different BBC phases at lower temperatures under slow cooling conditions according to Fig. 8, one being Ta- and Nb-rich (BCC1, Fig. 8g) and the other being Zr-rich (BCC2, Fig. 8h). Indeed, this was observed in Ta25-HT, Ta20-HT and Ta15-HT (BCC1 nanocuboids + BCC2 nanostrips, Figs. 4-9), but not in the two lower Ta content Ta10-HT and Ta5-HT MEAs. The influence of Ta content is discussed below.

As shown in Table 3, the values of δ, VEC, $|\Delta H_{mix}|$ and Ω all decrease with decreasing Ta content, which corresponds to increased stability of the as-solidified single solid-solution BCC phase. This agrees with the CALPHAD prediction that both the phase separation temperature and the phase fraction of the Zr-rich BCC2 phase will decrease with decreasing Ta content (Fig. 8 (a-f)). In other words, the single BCC phase in Ta10-HT and Ta5-HT is more stable than that in Ta25-HT, Ta20-HT and Ta15-HT. The mixing enthalpy between each pair of constituent

elements is indicative of their bonding energy [44, 47]. Table 4 lists the calculated mixing enthalpy of each pair in the Ti-Nb-Zr-Ta system. Both ΔH_{Zr-Nb}^{mix} (4 kJ/mole) and ΔH_{Zr-Ta}^{mix}(3 kJ/mole) are highly positive compared with ΔH_{Zr-Ti}^{mix}(0 kJ/mole) and ΔH_{Ta-Nb}^{mix} (0 kJ/mole). This means that Zr would intrinsically tend to separate from Ta and Nb. A similar phenomenon was observed in AlCoCrCuFeNi HEAs, in which a Cu-rich phase formed by segregation after an annealing treatment due to the highly positive mixing enthalpies of Cu-X (X = Fe, Cr, Co, Ni) [48]. Another factor is that Zr is much larger in size than each of Ti, Ta, and Nb (Table 3). These combined effects caused Zr atoms to segregate or cluster together as a nanostrip-like phase (~70 at.%) between the Nb- and Ta-rich nanocuboids. The rejection of Zr from the BCC lattice in these MEAs after annealing led to lattice shrinkage and therefore shifted the XRD peaks towards higher 2Θ values. Accordingly, the absence of phase separation in Ta10-HT and Ta5-HT is due to the enhanced phase stability of the BCC phase in each alloy because of their low values of δ, VEC, $|\Delta H_{mix}|$ and Ω.

Table 4 Mixing enthalpy $\left(\Delta H_{A-B}^{mix}\right)$ of each pair in the Ti-Nb-Zr-Ta system by Miedema's model [8, 46, 47].

Mixing enthalpy	Elements	**Ti**	**Zr**	**Nb**	**Ta**
ΔH_{A-B}^{mix} (kJ/mole)	**Ti**	-	0	2	1
	Zr	0	-	4	3
	Nb	2	4	-	0
	Ta	1	3	0	-

The phase separation discussed above was accompanied by redistribution of each element, especially Zr, whose concentration in the BCC2 phase reached ~70 at.% (Fig. 3). This implies that Zr atoms have high mobility in these MEAs. To understand the diffusion kinetics, Fig. 16 shows the predicted diffusivity of each element in the equiatomic $Ta_{25}Zr_{25}Nb_{25}Ti_{25}$ (Ta25) from 500 °C to 1200 °C using the CALPHAD approach, where below 677°C the single BCC phase separates into BCC1+BCC2. The predictions indicate that Zr diffuses ~3-4 orders of magnitude faster than other elements. As identified in Section 3.4, the phase separation period in Ta25-HT24 is ~210 s. Accordingly, the calculated diffusion distance of Zr at 677°C for 210 s based on Fig. 16 is ~4.1 nm, which is comparable to the average Zr-rich nanostrip (BCC2) width (3.16 ± 1.58 nm). This confirms the kinetic feasibility for the phase separation observed.

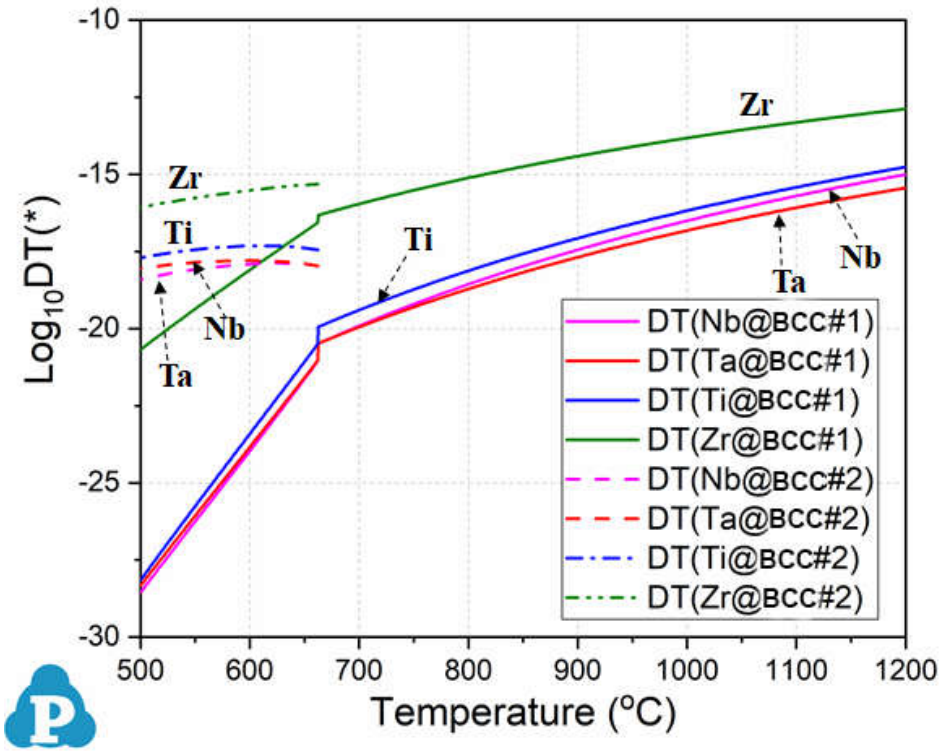

Figure 16 Diffusivity of each element in the equiatomic TaNbTiZr (Ta25) from 500 °C to 1200 °C determined by the CALPHAD approach (D: diffusion coefficient; T: temperature). (*) represents each element in both BCC#1 and BCC#2.

The atomic mismatch (δ) is known to significantly affect the strength of a HEA but it has been challenging to isolate the influence of δ due to other contributing factors such as compositional segregation, grain size, and residual stress. In this study, both Ta10-HT and Ta5-HT (Fig. 2) exhibited a single solid-solution BCC phase with a homogeneous composition and a similar grain size (Fig. S10). Therefore, the noticeable difference in their yield strength under both tension (853 vs. 726 MPa, Table 1) and compression (880 vs. 790 MPa, Table 1) can be attributed to the reduction in δ from 4.65% (Ta10-HT) to 4.58% (Ta5-HT, Table 3). This provides quantitative evidence for the high effectiveness of δ in affecting strength.

4.2 Deformation mechanism at RT and microstructural evolution under compression at high temperatures

Twining is common in the deformation of hexagonal closed-pack metals [49] but uncommon in bulk BCC materials. Exceptions are when BCC metals are deformed at high strain rates or low temperatures [49, 50] or when their microstructure is composed of nanoscaled BCC grains, which require high deformation stresses. For example, twinning-dominated deformation was

identified in nanoscaled BCC tungsten at RT by in situ compression in a HRTEM set-up [51]. The reason was attributed to the high stresses that are generated in nanoscaled BCC crystals due to dislocation starvation and exhaustion hardening [51]. In this study, the nanocuboidal Ta25-HT24 and Ta20-HT MEAs both exhibited (112)<111>-type of twinning deformation at RT (Fig. 11 and Fig. S7). In contrast, the single BCC Ta10-HT and Ta5-HT MEAs showed shear-band-dominated deformation at RT (Fig. 12), consistent with other single phase refractory HEAs [38, 52-55]. The different deformation mechanisms arise from their different microstructures. Both Ta25-HT24 and Ta20-HT MEAs contain an extremely high number density of nanocuboidal BBC phases, which recorded a hardness value of 5.9 ± 0.1 GPa (Table 1), indicative of the high stress generated in each nanocuboid. Hence, deformation of each hard nanocuboidal BCC phase in Ta25-HT24 and Ta20-HT can be regarded as being similar to that of each nanoscaled BCC tungsten grain [51]. Accordingly, the proposed dislocation starvation and exhaustion hardening mechanism [51] can be used to explain the twinning-dominated mechanism observed in Ta25-HT24 and Ta20-HT MEAs. It should be noted that twinning-dominated deformation has led to excellent compressive ductility in other HEAs [16, 54-56]. However, both Ta25-HT24 and Ta20-HT showed relatively low ductility at RT, which can be attributed to their GB lamellar structures. This is supported by the intergranular fracture surfaces of the Ta25-HT24 MEA (Fig. 10 (b, c)).

The formation of the fine equiaxed grains along the GB areas in Ta25-HT24 when compressed at 600°C (Fig. 14 a) can be attributed to localized dynamic recrystallization. The solidus temperature ($T_{solidus}$) of the Ta25 MEA is 2162 K (1889 ºC) according to the Pandat^{TM}, and the compression temperature (873 K/ 600ºC) is greater than 0.4 $T_{solidus}$ of the alloy. Localized dynamic recrystallization is also responsible for the softening stage in the stress-strain curves as observed by other researchers [12, 57]. The nearly constant compressive strength at 1200°C with increasing compressive strain (Fig. 13a) can be attributed to the dynamic equilibrium between work-hardening and softening [12, 54].

No shear bands or dislocations were observed in the nanocuboidal structure in Ta25-HT24 (Fig. 14b) when compressed at 600°C, which indicates the high resistance of the nanocuboids to deformation up to 600°C. As predicted by Fig. 8 (a, b), the Ta25 MEA will enter the single BCC phase region at temperatures above ~677ºC. Hence, when compressed at ≥ 800°C, the nanocuboidal structure will become a single solid-solution BCC phase, assisted with the compressive stress applied. On the other hand, the subsequent fast cooling (50ºC/min) after the

compression testing suppresses the re-separation of the BCC phase when cooled below 677ºC. Hence, the nanocuboidal structure disappeared in the samples after compression at ≥ 800°C. Conversely, compression at 600ºC, which is below 677ºC, retained the nanocuboidal structure, but due to the severe plastic deformation and stress-enhanced diffusion [58], the retained nanocuboidal structure exhibited distortion and coarsening (Fig. 15 (a, b)).

5. Conclusions

In this study, the effect of Ta content and heat treatment on the phase stability, microstructure, and mechanical properties of five $Ta_{25-x}Zr_{25}Nb_{25}Ti_{25+x}$ (x = 0, 5, 10, 15, 20, in at.%) MEAs was studied in detail. The following conclusions can be drawn.

- The $Ta_{25-x}Zr_{25}Nb_{25}Ti_{25+x}$ (x = 0, 5, 10, 15, 20, in at.%) MEAs solidified as a single solid-solution BCC phase in the copper-mould-cast condition. However, after annealing at 1200 °C for 8 h, followed by cooling at 4 ºC/min, an extremely high number density of nanocuboids (~$10^3/\mu m^2$) formed in $Ta_{25}Zr_{25}Nb_{25}Ti_{25}$ (Ta25-HT), $Ta_{20}Zr_{25}Nb_{25}Ti_{30}$ (Ta20-HT), and $Ta_{15}Zr_{25}Nb_{25}Ti_{35}$ (Ta15-HT) along with a nanostrip-like matrix phase between the nanocuboids. In contrast, the solid-solution BCC phase was retained in both $Ta_{10}Zr_{25}Nb_{25}Ti_{40}$ (Ta10-HT) and $Ta_5Zr_{25}Nb_{25}Ti_{45}$ (Ta5-HT) after the same annealing.
- The nanocuboids (28 ± 10 nm square) are a Ta- and Nb-rich BCC phase (BCC1) while the nanostrips (3 ± 2 nm thick) are a Zr-rich BCC phase (~70 at.% Zr). The nanocuboids show high nanoindentation hardness in the equiatomic Ta25 (5.9 ± 0.1 GPa) compared with 3.4 ± 0.1 GPa of the single solid-solution BCC phase in Ta10-HT and Ta5-HT.
- Thermodynamic simulation predicts a phase transformation process from BCC to BCC1 + BCC2 during cooling of each MEA, where the separation temperature decreases from 677 °C to 500ºC with decreasing Ta content from 25 at.% to 5 at.%. The predictions agree with the experimental observations in high Ta content (≥15 at.%) MEAs but differ from the those observed in the low Ta content (≤10 at.%) MEAs.
- The phase separation can be attributed to three principal reasons: (i) the atomic mismatch-dependent phase stability, which is affected significantly by the Ta content, (ii) the highly positive mixing enthalpy between Ta and Zr and Nb and Zr, which implies the strong tendency to separation between each pair, and (iii) the 3-4 orders of magnitude higher mobility of Zr than Ta, Nb and Ti in the single solid-solution BCC phase, which enables the separation to form Zr-rich (~70 at.%) nanostrips. The calculated diffusion distance of Zr (4.1 nm) is comparable to the measured Zr-rich nanostrip width (3 ± 2 nm).

- The change in microstructure due to different Ta contents results in a distinct change in deformation mechanisms at RT. The characteristic nanocuboids-nanostrip structure (Ta25-HT, Ta20-HT and Ta15-HT) exhibited a 112<111>-type of twinning deformation under compression at RT. In contrast, shear-band dominated deformation occurred in the single solid-solution BCC phase in both Ta10-HT and Ta5-HT at RT.
- At RT, Ta25-HT24, Ta25-HT, Ta20-HT, and Ta15-HT exhibited high compressive yield strength from 1300 ± 30 MPa (Ta15-HT) to 1760 ± 30 MPa (Ta25-HT24), while Ta10-HT and Ta-5HT showed excellent ductility in both tension and compression conditions with good tensile yield strengths (893 ± 20 MPa for Ta10-HT and 750 ± 20 MPa for Ta5-HT).
- At elevated temperatures, the Ta25-HT24 MEA exhibited excellent softening resistance due to its unique extremely high density nanocuboidal structure. Its compression yield strength, $\sigma_{0.2}$, retained ~410 MPa at 1000ºC and ~210 MPa at 1200ºC. The microstructure of Ta25-HT24 after compression at 1200ºC is composed of coarse matrix grains (~200 μm) and fine equiaxed grains (~2-5 μm) in the grain boundary regions. This new microstructure needs further assessment.

Acknowledgments

This work was supported by the Australian Research Council (ARC) through ARC LP130100913 and the Baosteel-Australia Joint Research and Development Centre through BA110014LP. V. T. Nguyen thanks the International Postgraduate Research *Scholarship* (IPRS) Program for providing him with a Ph.D scholarship. The Australian Microscopy & Microanalysis Research Facility is acknowledged for providing characterization facilities. M. Qian and D. M. Fabijanic further acknowledge the support from the Australian-India Strategic Research Fund (AISRF53731).

References

[1] O. Senkov, G. Wilks, D. Miracle, C. Chuang, P. Liaw, Refractory high-entropy alloys, Intermetallics 18(9) (2010) 1758-1765.

[2] O.N. Senkov, S.V. Senkova, C. Woodward, Effect of aluminum on the microstructure and properties of two refractory high-entropy alloys, Acta Mater. 68 (2014) 214-228.

[3] Y. Zou, S. Maiti, W. Steurer, R. Spolenak, Size-dependent plasticity in an Nb 25 Mo 25 Ta 25 W 25 refractory high-entropy alloy, Acta Mater. 65 (2014) 85-97.

[4] Y. Zou, H. Ma, R. Spolenak, Ultrastrong ductile and stable high-entropy alloys at small scales, 6 (2015) 7748.

[5] O.N. Senkov, S.V. Senkova, D.B. Miracle, C. Woodward, Mechanical properties of low-density, refractory multi-principal element alloys of the Cr–Nb–Ti–V–Zr system, Mater. Sci. Eng. A 565 (2013) 51-62.
[6] S.P. Wang, E. Ma, J. Xu, New ternary equi-atomic refractory medium-entropy alloys with tensile ductility: Hafnium versus titanium into NbTa-based solution, Intermetallics 107 (2019) 15-23.
[7] Z. Lei, X. Liu, Y. Wu, H. Wang, S. Jiang, S. Wang, X. Hui, Y. Wu, B. Gault, P. Kontis, D. Raabe, L. Gu, Q. Zhang, H. Chen, H. Wang, J. Liu, K. An, Q. Zeng, T.G. Nieh, Z. Lu, Enhanced strength and ductility in a high-entropy alloy via ordered oxygen complexes, Nature 563(7732) (2018) 546-550.
[8] D.B. Miracle, O.N. Senkov, A critical review of high entropy alloys and related concepts, Acta Mater. 122 (2017) 448-511.
[9] O. Senkov, G. Wilks, J. Scott, D. Miracle, Mechanical properties of Nb 25 Mo 25 Ta 25 W 25 and V 20 Nb 20 Mo 20 Ta 20 W 20 refractory high entropy alloys, Intermetallics 19(5) (2011) 698-706.
[10] V. Soni, O. Senkov, B. Gwalani, D. Miracle, R. Banerjee, Microstructural Design for Improving Ductility of An Initially Brittle Refractory High Entropy Alloy, Sci. Rep. 8(1) (2018) 8816.
[11] O. Senkov, S. Rao, K. Chaput, C. Woodward, Compositional effect on microstructure and properties of NbTiZr-based complex concentrated alloys, Acta Mater. 151 (2018) 201-215.
[12] N.N. Guo, L. Wang, L.S. Luo, X.Z. Li, R.R. Chen, Y.Q. Su, J.J. Guo, H.Z. Fu, Hot deformation characteristics and dynamic recrystallization of the MoNbHfZrTi refractory high-entropy alloy, Mater. Sci. Eng. A 651 (2016) 698-707.
[13] Y. Shi, B. Yang, P. Liaw, Corrosion-Resistant High-Entropy Alloys: A Review, Metals 7(2) (2017) 43.
[14] J. Li, X. Yang, R. Zhu, Y. Zhang, Corrosion and Serration Behaviors of TiZr0.5NbCr0.5VxMoy High Entropy Alloys in Aqueous Environments, Metals 4(4) (2014) 597.
[15] J.P. Couzinié, G. Dirras, L. Perrière, T. Chauveau, E. Leroy, Y. Champion, I. Guillot, Microstructure of a near-equimolar refractory high-entropy alloy, Mater. Lett. 126 (2014) 285-287.
[16] H. Huang, Y. Wu, J. He, H. Wang, X. Liu, K. An, W. Wu, Z. Lu, Phase-Transformation Ductilization of Brittle High-Entropy Alloys via Metastability Engineering, Adv. Mater. (2017).

[17] O. Senkov, C. Woodward, D. Miracle, Microstructure and properties of aluminum-containing refractory high-entropy alloys, JOM 66(10) (2014) 2030-2042.
[18] N.D. Stepanov, N.Y. Yurchenko, D.V. Skibin, M.A. Tikhonovsky, G.A. Salishchev, Structure and mechanical properties of the AlCrxNbTiV (x = 0, 0.5, 1, 1.5) high entropy alloys, J. Alloys Compd. 652 (2015) 266-280.
[19] N.Y. Yurchenko, N.D. Stepanov, D.G. Shaysultanov, M.A. Tikhonovsky, G.A. Salishchev, Effect of Al content on structure and mechanical properties of the AlxCrNbTiVZr (x=0; 0.25; 0.5; 1) high-entropy alloys, Mater. Charact. 121 (2016) 125-134.
[20] O.N. Senkov, J.K. Jensen, A.L. Pilchak, D.B. Miracle, H.L. Fraser, Compositional variation effects on the microstructure and properties of a refractory high-entropy superalloy AlMo0.5NbTa0.5TiZr, Mater. Des. 139 (2018) 498-511.
[21] O.N. Senkov, D.B. Miracle, K.J. Chaput, J.-P. Couzinie, Development and exploration of refractory high entropy alloys—A review, J. Mater. Res. (2018) 1-37.
[22] M. Todai, T. Nagase, T. Hori, A. Matsugaki, A. Sekita, T. Nakano, Novel TiNbTaZrMo high-entropy alloys for metallic biomaterials, Scr. Mater. 129 (2017) 65-68.
[23] S.-P. Wang, J. Xu, TiZrNbTaMo high-entropy alloy designed for orthopedic implants: As-cast microstructure and mechanical properties, Mater. Sci. Eng. C 73 (2017) 80-89.
[24] V.T. Nguyen, M. Qian, Z. Shi, T. Song, L. Huang, J. Zou, A novel quaternary equiatomic Ti-Zr-Nb-Ta medium entropy alloy (MEA), Intermetallics 101 (2018) 39-43.
[25] V.T. Nguyen, M. Qian, Z. Shi, T. Song, L. Huang, J. Zou, Compositional design of strong and ductile (tensile) Ti-Zr-Nb-Ta medium entropy alloys (MEAs) using the atomic mismatch approach, Mater. Sci. Eng. A 742 (2019) 762-772.
[26] H.P. Tang, G.Y. Yang, W.P. Jia, W.W. He, S.L. Lu, M. Qian, Additive manufacturing of a high niobium-containing titanium aluminide alloy by selective electron beam melting, Mater. Sci. Eng. A 636 (2015) 103-107.
[27] H. Dobbelstein, E.L. Gurevich, E.P. George, A. Ostendorf, G. Laplanche, Laser metal deposition of compositionally graded TiZrNbTa refractory high-entropy alloys using elemental powder blends, Addit. Manuf. 25 (2019) 252-262.
[28] Pandat^{TM}, Thermodynamic Calculations and Kinetic Simulations, CompuTherm LLC, Middleton, WI - 53562.
[29] W.S. Cao, S.L. Chen, F. Zhang, K.S. Wu, Y. Yang, Y.A. Chang, R. Schmid-Fetzer, W.A. Oates, PANDAT software with PanEngine, PanOptimizer and PanPrecipitation for multi-component phase diagram calculation and materials property simulation, Calphad 33(2) (2009) 328-342.

[30] G. Neumann, C. Tuijn, Self-diffusion and impurity diffusion in pure metals: Handbook of experimental data, Elsevier, 525 B Street, Suite 1900, San Diego, CA 92101-4495, USA, 2009.
[31] Y. Liu, G. Wang, J. Wang, Z. Kang, Mobilities and diffusivities for bcc Nb-W, Nb-Ta, Zr-Mo and Zr-Hf alloys, J. Alloys .Compd. 555 (2013) 381-389.
[32] Y. Liu, T. Pan, L. Zhang, D. Yu, Y. Ge, Kinetic modeling of diffusion mobilities in bcc Ti-Nb alloys, J. Alloys Compd. 476 (2009) 429-435.
[33] Y. Liu, L. Zhang, T. Pan, D. Yu, Y. Ge, Study of diffusion mobilities of Nb and Zr in bcc Nb-Zr alloys, Calphad 32 (2008) 455-461.
[34] Y. Liu, L. Zhang, Y. Du, J. Wang, D. Liang, Study of atomic mobilities and diffusion characteristics in bcc Ti-Ta and Ta-W alloys, Calphad 34 (2010) 310-316.
[35] Y. Liu, L. Zhang, D. Yu, Computational Study of Mobilities and Diffusivities in bcc Ti-Zr and bcc Ti-Mo Alloys, J. Phase Equilib. Diffus. 30(4) (2009) 334-344.
[36] S. Maiti, W. Steurer, Structural-disorder and its effect on mechanical properties in single-phase TaNbHfZr high-entropy alloy, Acta Mater. 106 (2016) 87-97.
[37] R.E. Smallman, R.J. Bishop, Modern physical metallurgy and materials engineering, elsevier (1999).
[38] G. Dirras, H. Couque, L. Lilensten, A. Heczel, D. Tingaud, J.P. Couzinié, L. Perrière, J. Gubicza, I. Guillot, Mechanical behavior and microstructure of Ti20Hf20Zr20Ta20Nb20 high-entropy alloy loaded under quasi-static and dynamic compression conditions, Mater. Charact. 111 (2016) 106-113.
[39] G. Dirras, L. Lilensten, P. Djemia, M. Laurent-Brocq, D. Tingaud, J.P. Couzinié, L. Perrière, T. Chauveau, I. Guillot, Elastic and plastic properties of as-cast equimolar TiHfZrTaNb high-entropy alloy, Mater. Sci. Eng. A 654 (2016) 30-38.
[40] O.N. Senkov, S.V. Senkova, C. Woodward, D.B. Miracle, Low-density, refractory multi-principal element alloys of the Cr–Nb–Ti–V–Zr system: Microstructure and phase analysis, Acta Mater. 61(5) (2013) 1545-1557.
[41] N. Guo, L. Wang, L. Luo, X. Li, Y. Su, J. Guo, H. Fu, Microstructure and mechanical properties of refractory MoNbHfZrTi high-entropy alloy, Mater. Des. 81 (2015) 87-94.
[42] S. Guo, Phase selection rules for cast high entropy alloys: an overview, Mater. Sci. Technol. 31(10) (2015) 1223-1230.
[43] Z. Wang, S. Guo, C.T. Liu, Phase Selection in High-Entropy Alloys: From Nonequilibrium to Equilibrium, JOM 66(10) (2014) 1966-1972.
[44] X. Yang, Y. Zhang, Prediction of high-entropy stabilized solid-solution in multi-component alloys, Mater. Chem. Phys. 132(2) (2012) 233-238.

[45] Y. Zhang, T.T. Zuo, Z. Tang, M.C. Gao, K.A. Dahmen, P.K. Liaw, Z.P. Lu, Microstructures and properties of high-entropy alloys, Prog. Mater Sci. 61 (2014) 1-93.
[46] G. Sheng, C.T. Liu, Phase stability in high entropy alloys: formation of solid-solution phase or amorphous phase, Prog. Nat. Sci-Mater. 21(6) (2011) 433-446.
[47] A. Takeuchi, A. Inoue, Classification of bulk metallic glasses by atomic size difference, heat of mixing and period of constituent elements and its application to characterization of the main alloying element, Mater. Trans. 46(12) (2005) 2817-2829.
[48] M.A. Hemphill, T. Yuan, G.Y. Wang, J.W. Yeh, C.W. Tsai, A. Chuang, P.K. Liaw, Fatigue behavior of Al 0.5 CoCrCuFeNi high entropy alloys, Acta Mater. 60(16) (2012) 5723-5734.
[49] Y.T. Zhu, X.Z. Liao, X.L. Wu, Deformation twinning in nanocrystalline materials, Prog. Mater Sci. 57(1) (2012) 1-62.
[50] Q. Yu, Z.W. Shan, J. Li, X. Huang, L. Xiao, J. Sun, E. Ma, Strong crystal size effect on deformation twinning, Nature 463(7279) (2010) 335.
[51] J. Wang, Z. Zeng, C.R. Weinberger, Z. Zhang, T. Zhu, S.X. Mao, In situ atomic-scale observation of twinning-dominated deformation in nanoscale body-centred cubic tungsten, Nat. Mater. 14 (2015) 594.
[52] O.N. Senkov, A.L. Pilchak, S.L. Semiatin, Effect of Cold Deformation and Annealing on the Microstructure and Tensile Properties of a HfNbTaTiZr Refractory High Entropy Alloy, Metall. Mater. Trans. A 49(7) (2018) 2876-2892.
[53] C. Lee, G. Song, M.C. Gao, R. Feng, P. Chen, J. Brechtl, Y. Chen, K. An, W. Guo, J.D. Poplawsky, S. Li, A.T. Samaei, W. Chen, A. Hu, H. Choo, P.K. Liaw, Lattice distortion in a strong and ductile refractory high-entropy alloy, Acta Mater. 160 (2018) 158-172.
[54] O. Senkov, J. Scott, S. Senkova, F. Meisenkothen, D. Miracle, C. Woodward, Microstructure and elevated temperature properties of a refractory TaNbHfZrTi alloy, J. Mater. Sci. 47(9) (2012) 4062-4074.
[55] O.N. Senkov, S.L. Semiatin, Microstructure and properties of a refractory high-entropy alloy after cold working, J. Alloys Compd. 649 (2015) 1110-1123.
[56] Z. Li, C.C. Tasan, K.G. Pradeep, D. Raabe, A TRIP-assisted dual-phase high-entropy alloy: Grain size and phase fraction effects on deformation behavior, Acta Mater. 131 (2017) 323-335.
[57] O.N. Senkov, C. Zhang, A.L. Pilchak, E.J. Payton, C. Woodward, F. Zhang, CALPHAD-aided development of quaternary multi-principal element refractory alloys based on NbTiZr, J. Alloys Compd. 783 (2019) 729-742.
[58] L. Zhao, N. Park, Y. Tian, A. Shibata, N. Tsuji, Deformation-assisted diffusion for the enhanced kinetics of dynamic phase transformation, Mater. Res. Lett. 6(11) (2018) 641-647.

Suporting Information

Table S1 Nominal composition (at.%) and average SEM-EDS measured compositions of the Ta25-HT, Ta20-HT, Ta15-HT, Ta10-HT and Ta5-HT MEAs.

Alloy designation and composition		Ti (at.%)	Zr (at.%)	Nb (at.%)	Ta (at.%)
Ta25-HT	Nominal	25	25	25	25
	EDS	25.1±0.6	25 ± 2	25.8±0.9	25±2
Ta20-HT	Nominal	30	25	25	20
	EDS	30.5±0.3	25±1	24.5±0.5	19.9±0.8
Ta15-HT	Nominal	35	25	25	15
	EDS	35.1±0.3	24.8±0.7	25±0.4	15.1±0.5
Ta10-HT	Nominal	40	25	25	10
	EDS	39.9±0.3	25.2±0.3	25.1±0.3	9.8±0.2
Ta5-HT	Nominal	45	25	25	5
	EDS	45.1±0.3	24.9±0.3	24.9±0.3	5.1±0.2

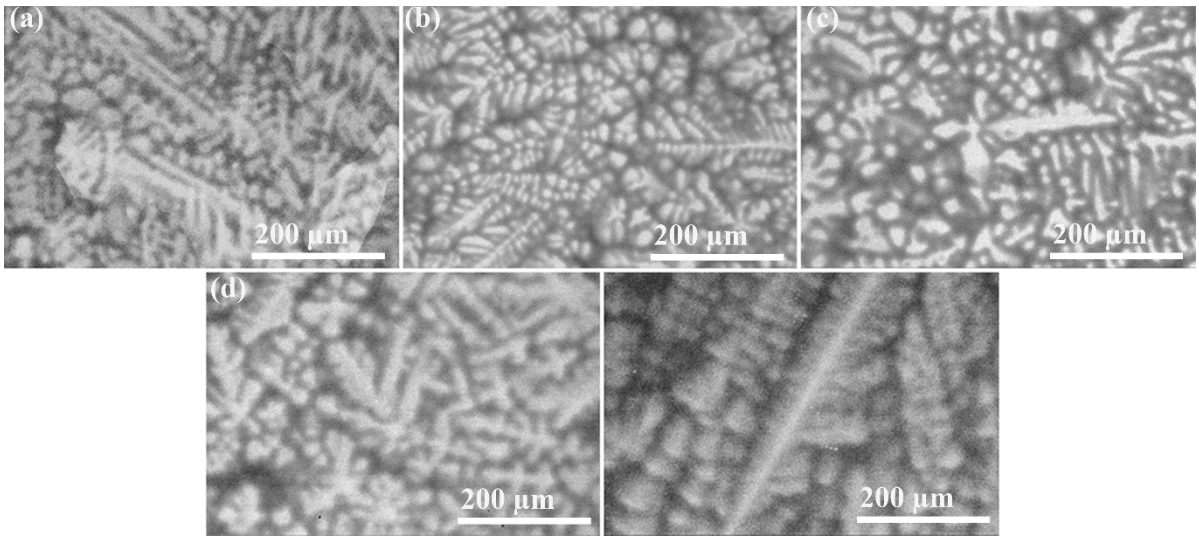

Figure S1 SEM-BSE images of as-cast MEAs: (a) Ti25, (b) Ti20, (c) Ta15, (d) Ta10, and (e) Ta5.

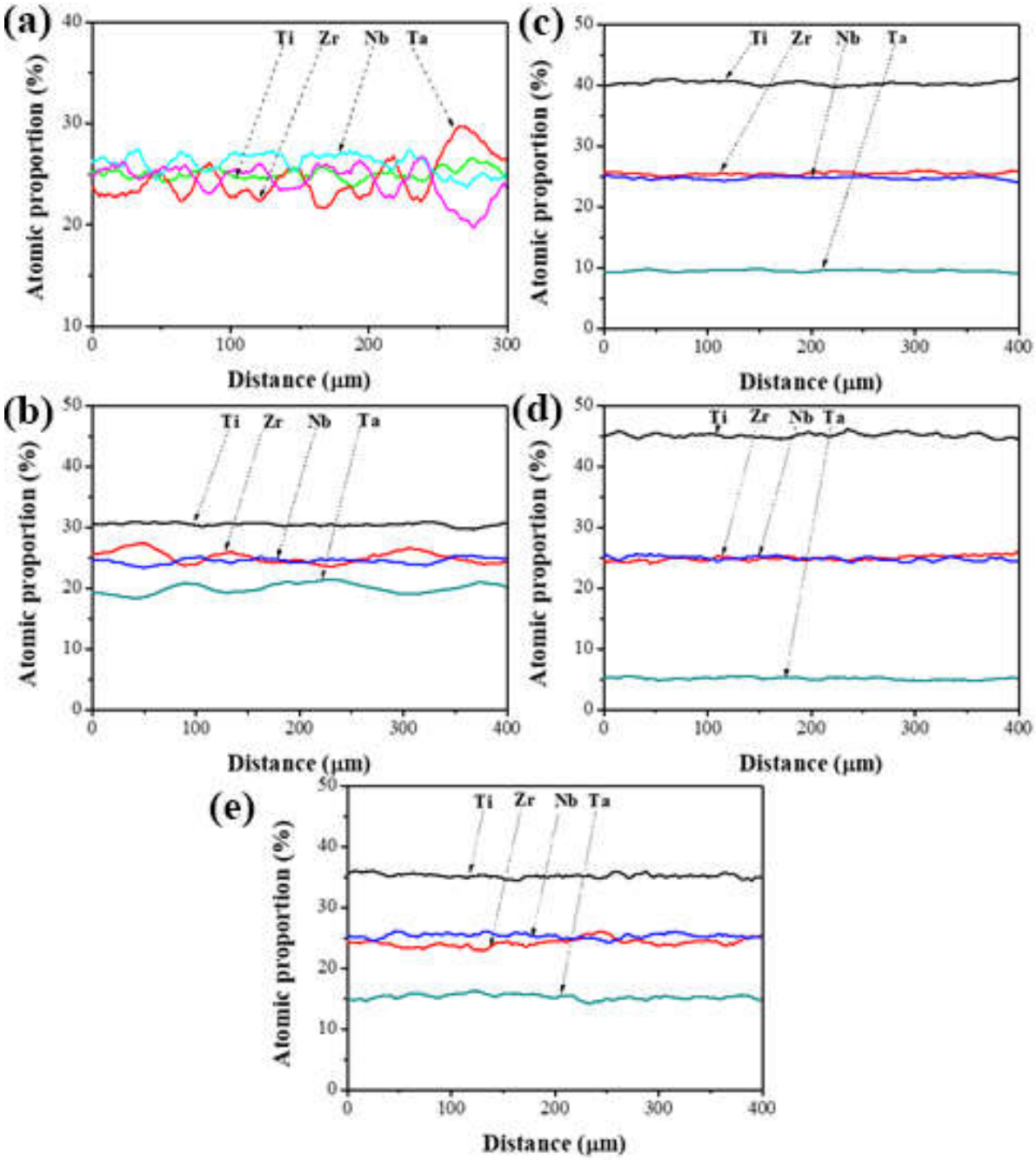

Figure S2 EDS line-scan profiles taken from (a) Ta25-HT, (b) Ta20-HT, (c) Ta15-HT, (d) Ta10-HT and (e) Ta5-HT. This figure have the sole purpose of indicating all constitutional elements distributed more homogeneous in Ta10-HT and Ta5-HT than in Ta25-HT, Ta20-HT, and Ta15-HT after they were annealed at 1200ºC for 8 hours.

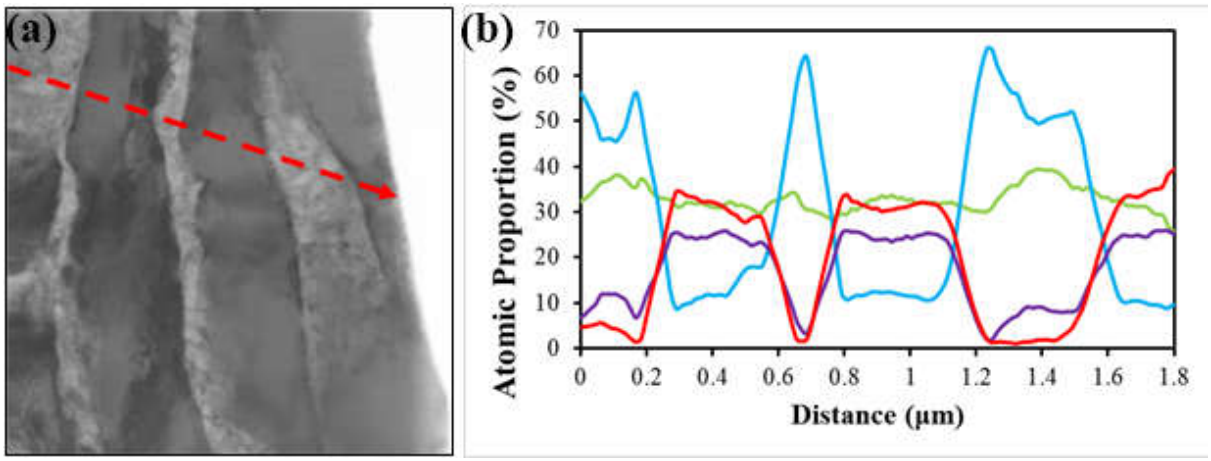

Figure S3 (a) STEM-BF image of lamellar structure at GBs of Ta25-HT24 MEA; (b) is the corresponding EDS line-scan taken from the red arrow in (a).

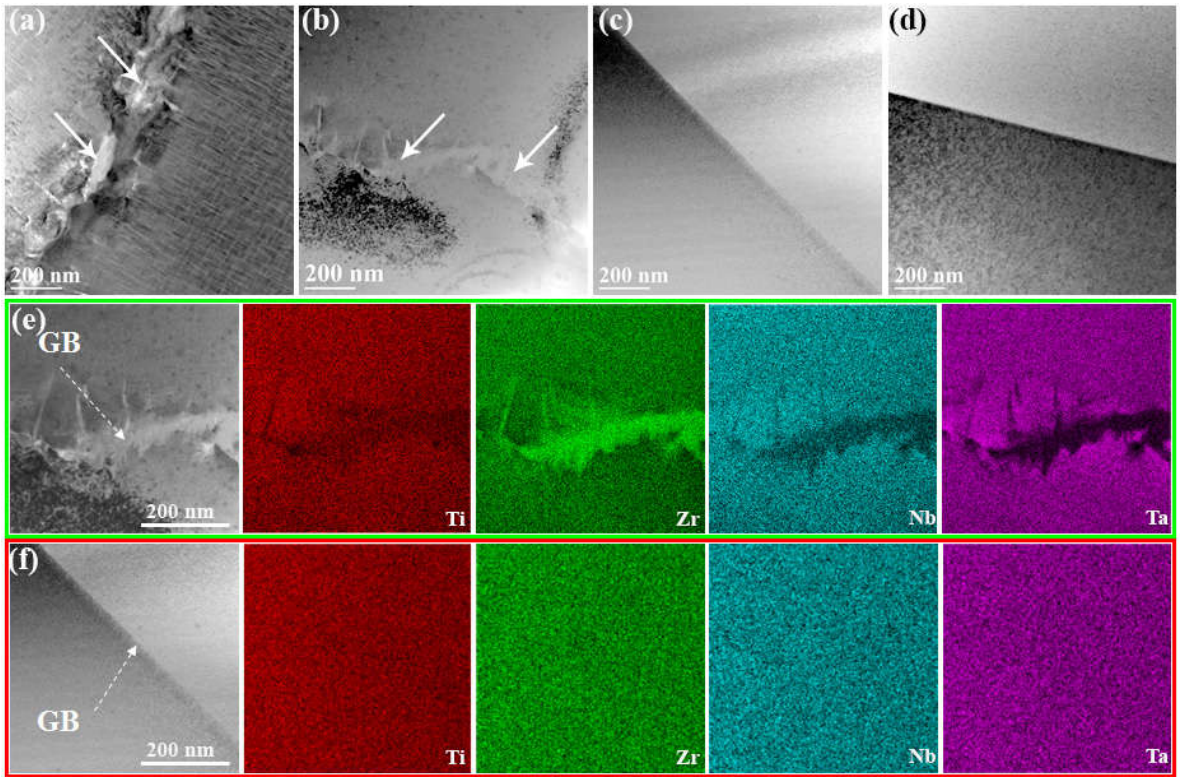

Figure S4 TEM-BF images taken from typical GBs of (a) Ta20-HT, (b) Ta15-HT, (c) Ta10-HT, and (d) Ta5-HT. (e) and (f) show the EDS mapping at typical GB areas of Ta15-HT and Ta10-HT MEAs, respectively.

TEM characterization was also performed in the GB regions of Ta20-HT, Ta15-HT, Ta10-HT and Ta5-HT MEAs as shown in Fig. S4. The secondary phase was observed at the GBs of Ta20-HT and Ta15-HT, as indicated by the white arrows in Fig. S4 (a) and (b). The STEM-EDS mapping was carried out at a GB region in Ta15-HT and confirms that this second phase was

rich in Zr (Fig. S4 (e)). However, no such secondary phase was observed when the Ta content is lower than 15 at.% as in Ta10-HT and Ta5-HT (Fig. S4 (c), (d), and (f)). This indicates that the BCC phase of Ta10 and Ta5 MEAs was stable after heat-treatment at 1200 ºC for 8 h at a cooling rate of 4 ºC/min.

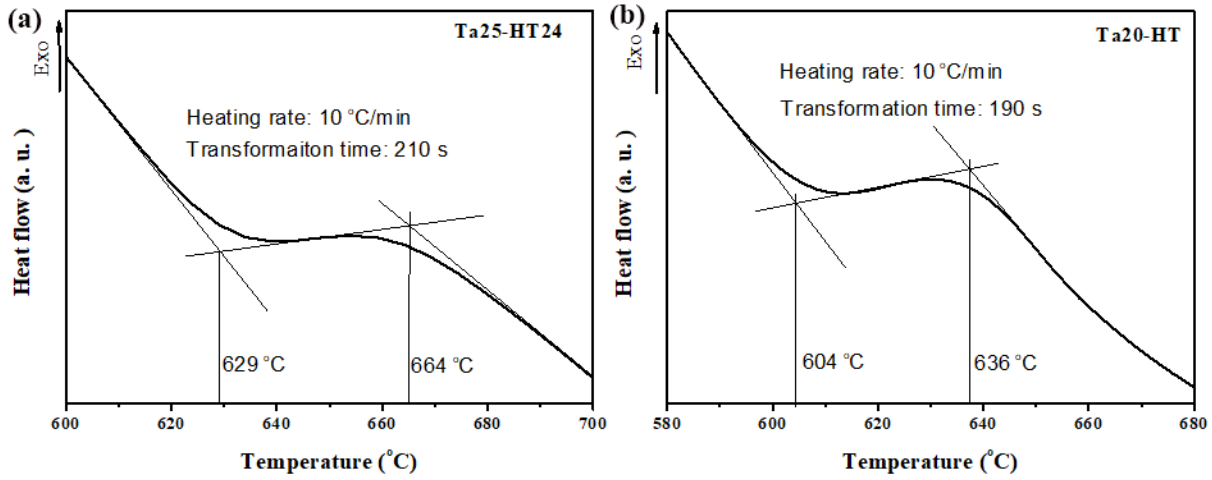

Figure S5 Zoomed-in endothermic peak in DSC analysis of (a) Ta25-HT24 and (b) Ta20-HT.

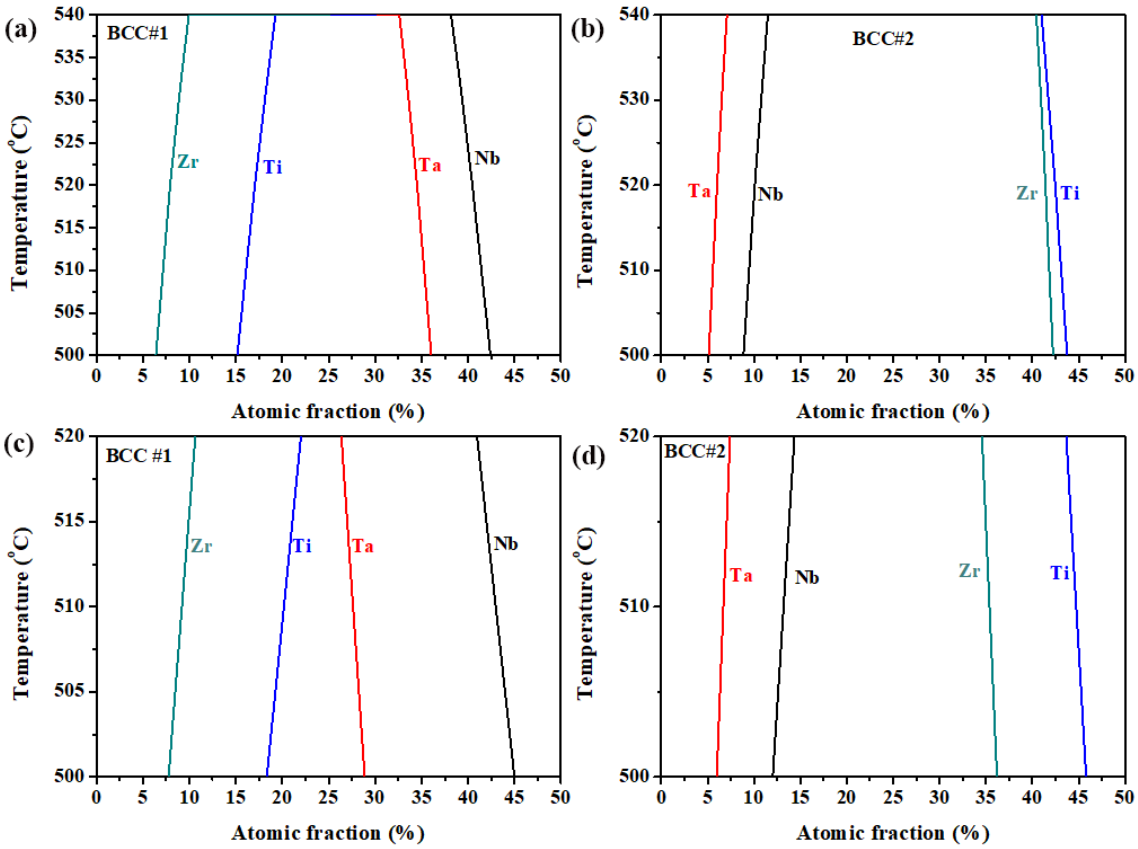

Figure S6 Temperature dependence of solubility of the alloying elements in (a) BCC#1 and (b) BCC#2 of Ta20 MEA; (c) BCC#1 and (d) BCC#2 of Ta15 MEA.

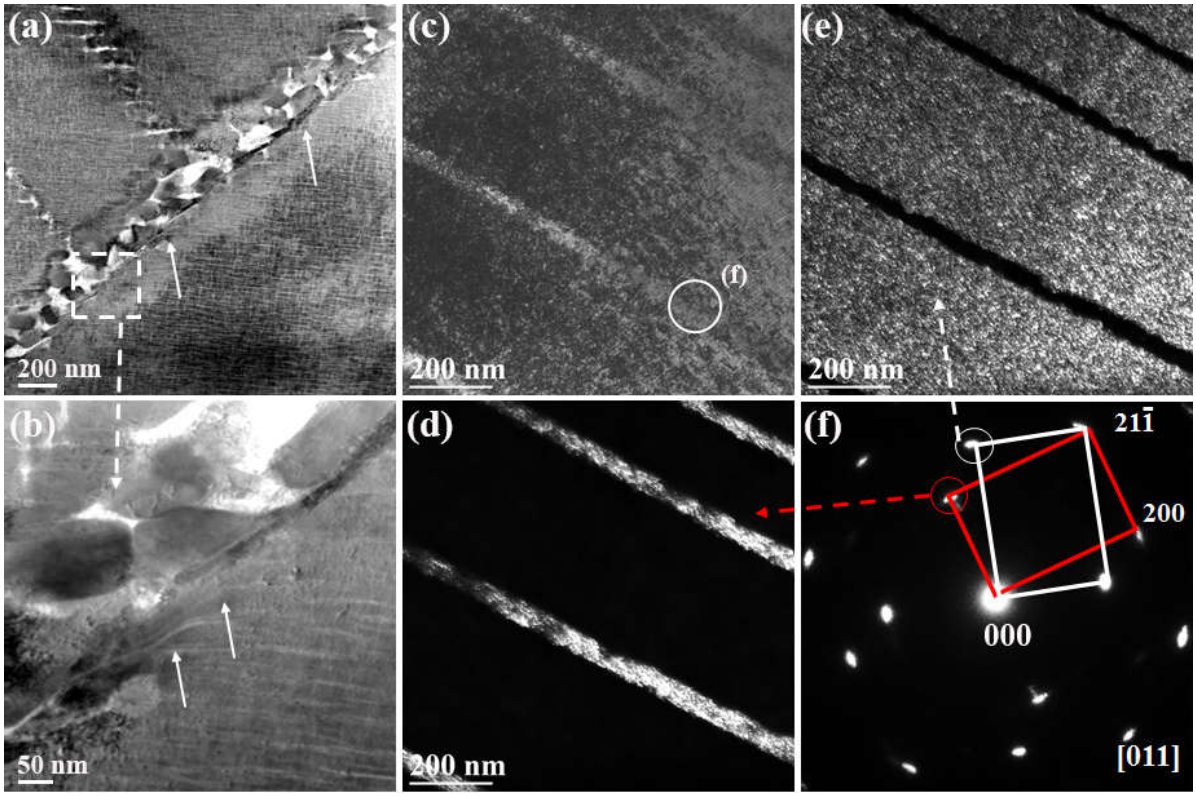

Figure S7 shows the TEM characterization for Ta20-HT after compression testing. Fig. S7 (a) is a TEM-BF image of a selected GB area, and Fig. S7 (b) shows the enlarged image of an area as marked-out in Fig. S7 (a). Shear traces indicated by white arrows in Fig. S7 (a) and (b) were clearly observed at the GBs in which the Zr-rich phase heterogeneously segregated during heat treatment. This indicates that the stress concentrated at the boundaries between the Zr-rich phase and the matrix is causing the failure of the Ta20-HT MEA during plastic deformation. Fig. S7 (c) depicts a TEM-BF image taken from the matrix area which reveals a lamella structure with a thickness of ~30 nm. Fig. S7 (f) shows the [011] zone-axis SAED pattern taken from the area as marked-out in Fig. S7 (c), which confirms the 112<111>-type twinning relationship between the matrix and the thin lamellae. Fig. S7 (d) and (e) depict the corresponding dark field TEM images.

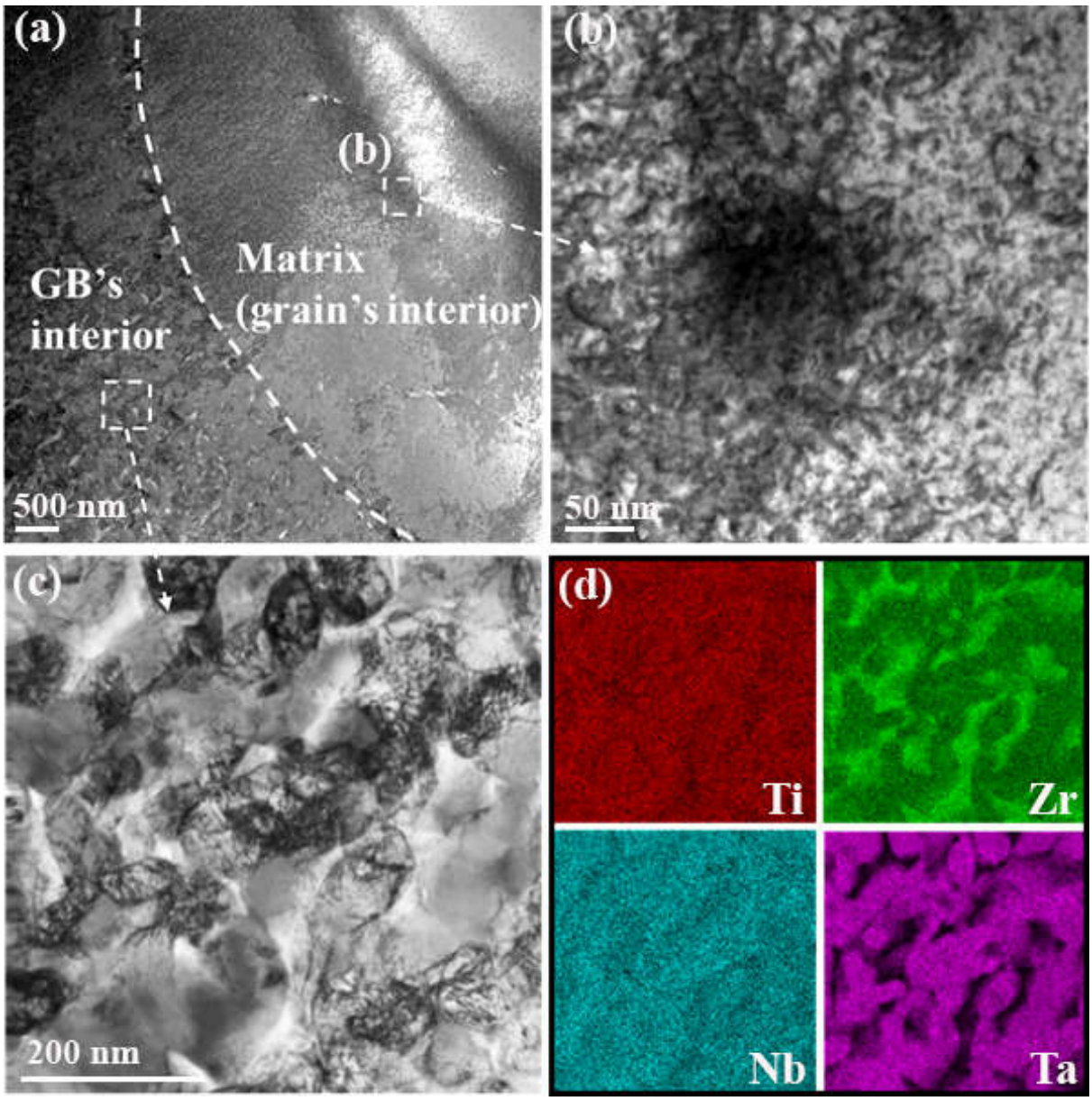

Figure S8 STEM characterization of Ta25-HT24 sample after compression by 30% plastic strain at 800 ºC. (a) is a STEM-BF image of a typical GB region; (b) is a STEM-BF image of a grain interior; (c) and (d) are a STEM-BF image and the corresponding STEM-EDS mapping of GB interior, respectively.

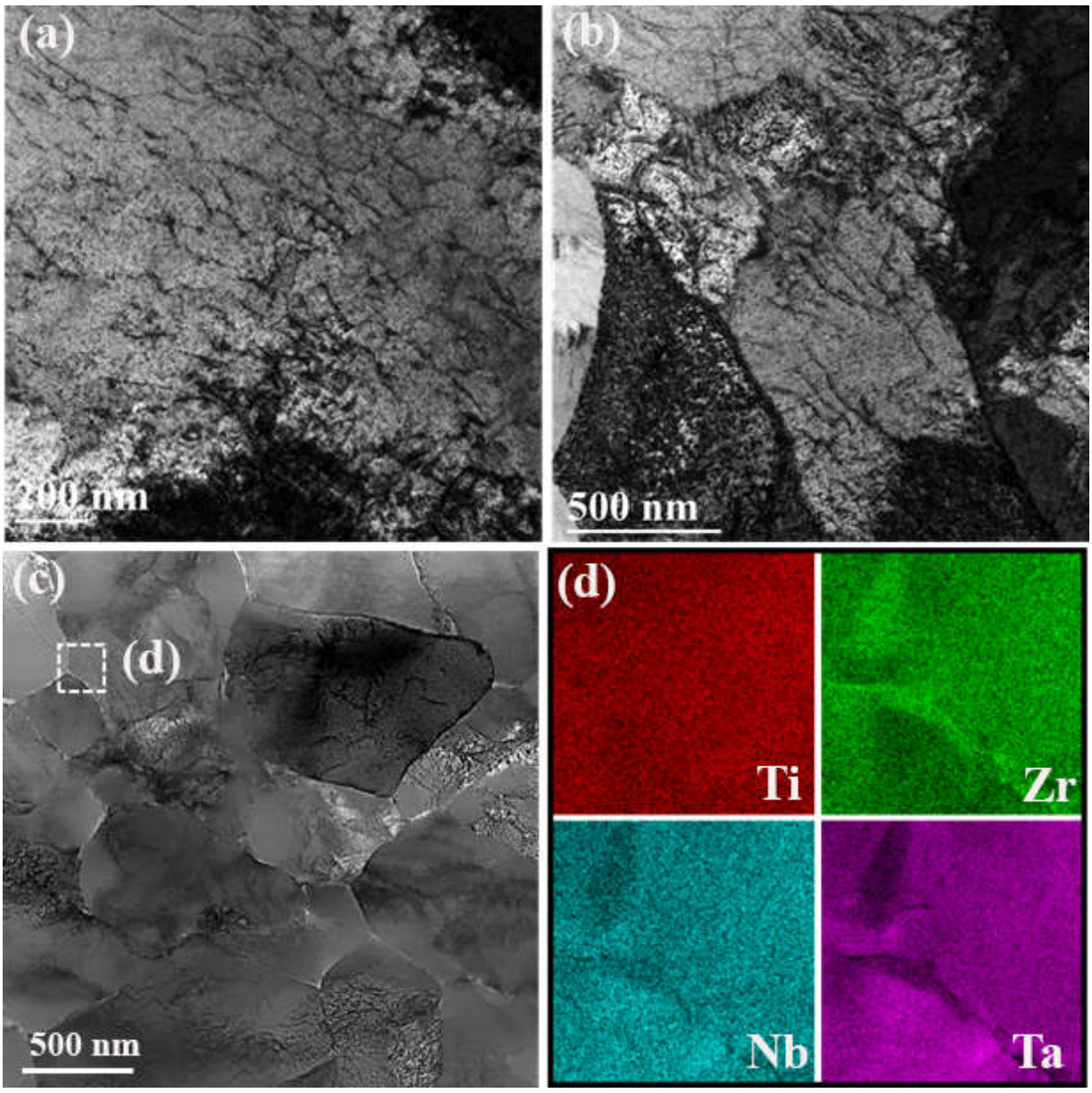

Figure S9 TEM characterization of Ta25-HT24 sample after compression by 30% plastic strain at 1000 ºC. (a) is a TEM-BF image of the matrix; (b) is a TEM-BF image of GB interior; (c) and (d) are the STEM-BF image and the corresponding EDS mapping of the GB interior, respectively.

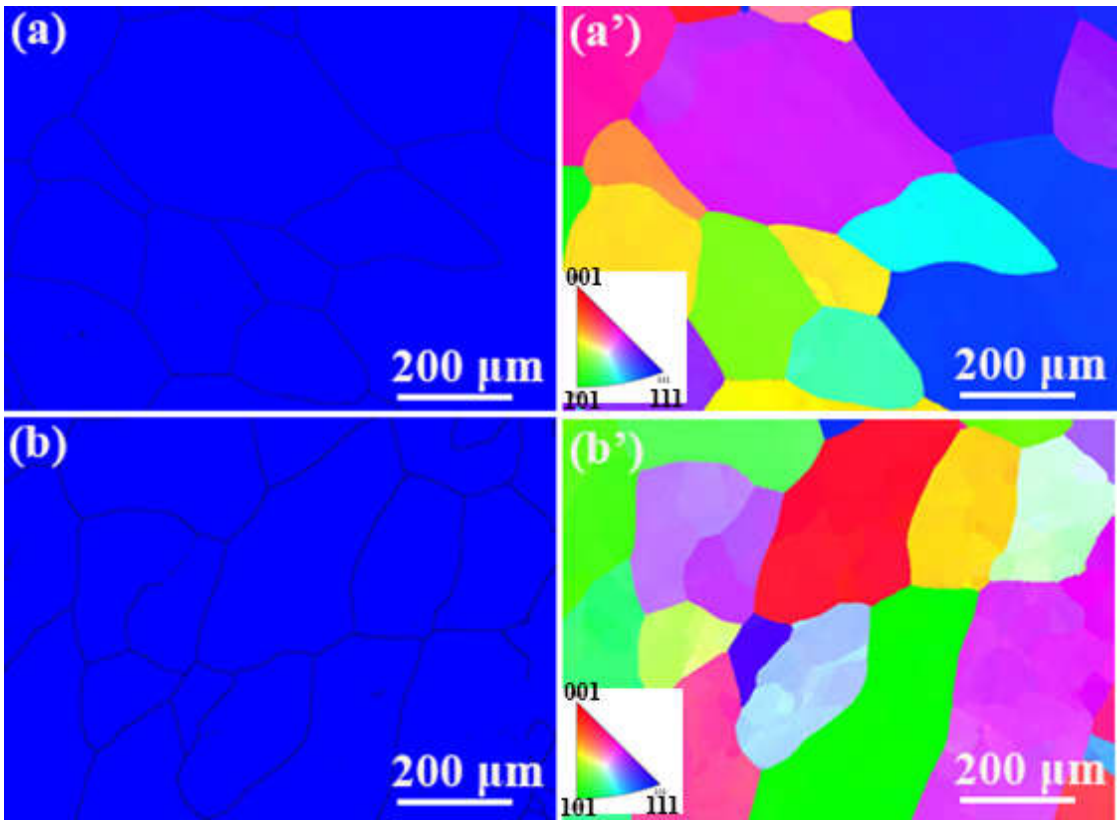

Figure S10 Phase map and IPF images: (a, a′) for Ta10-HT and (b, b′) for Ta5-HT. After annealing at 1200ºC for 8 hours under vacuum condition, both Ta10-HT and Ta5-HT exhibited a equiaxed-grain microstructure with single BCC solid solution as indication by blue color in the EBSD phase map (a) for Ta10-HT and (b) for Ta5-HT.

Chapter 7 Summary and future works.

7.1 Summary

In this research, two peer-reviewed articles have been published and one manuscript have been submitted. This research has successfully fabricated novel equiatomic and non-equiatomic Ti-Zr-Nb-Ta MEAs which possess promising properties for bio-application as well as structural applications at elevated temperatures. The study has focused on microstructure, mechanical properties and deformation mechanisms of MEAs in both as-cast and as-heat-treated conditions. The outcomes of this study are summarized as follows:

A novel quaternary equiatomic Ti-Zr-Nb-Ta (δ = 4.8 %) MEA, has been redesigned from a quinary equiatomic Ti-Zr-Nb-Ta-Mo (δ = 5.5 %) HEA, for much improved strength-ductility combinations by reducing the atomic mismatch (δ) through excluding Mo and for potentially improved biocompatibility.

A nanocuboidal structure in the matrix and a lamellar structure at the grain boundary region were revealed in the equiatomic Ti-Zr-Nb-Ta MEAs after heat treatment at 1200 ºC, for either 8 or 24 h, and at a heating/cooling rate of 4 ºC/min. This nanostructure is responsible for a significant increase in compression yield strength from 1100 ± 90 MPa to 1760 ± 30 MPa compared to its as-cast counterpart. The nature of high mixing enthalpies as well as the large differences in atomic size between Zr and other constituent elements i.e., Ta, Ti, and Nb likely induced the formation of the cuboidal-like nanostructure and the lamellar structure. The 112<111>-type twinning deformation governed the plastic deformation of the cuboidal-like nanostructure.

As-annealed equiatomic Ti-Zr-Nb-Ta MEA exhibits excellent softening resistance at high temperatures. Its yield strength, $\sigma_{0.2}$, decreased by about half, from ~1760 MPa to ~800 MPa, with deformation temperature increasing from the room temperature to 600ºC. However, this as-annealed MEA still exhibited excellent softening resistance at elevated temperatures, e.g., $\sigma_{0.2}$ remained at ~410 MPa at 1000 ºC and ~210 MPa at 1200 ºC.

New non-equiatomic $Ti_{(25+x)}$-Zr_{25}-Nb_{25}-$Ta_{(25-x)}$ (x = 0, 5, 10, 15, 20, in at. %) MEAs have been successfully derived from the equiatomic Ti-Zr-Nb-Ta MEA using the atomic mismatch (δ) approach. Each non-equiatomic MEA solidified as a single solid-solution phase, which was predicted by Pandat^{TM} simulation and the empirical rule. In particular, a brittle-to-ductile transition was observed with decreasing Ta content. As a result, both the as-cast Ti_{40}-Zr_{25}-Nb_{25}-

Ta_{10} and Ti_{45}-Zr_{25}-Nb_{25}-Ta_5 MEAs exhibited excellent tensile strain to fracture (>18%) and tensile strength (>900 MPa) with much reduced density compared to the brittle Ti_{25}-Zr_{25}-Nb_{25}-Ta_{25} MEA. They are both among a very small number of strong and ductile (tensile strain >15%) HEAs reported to date.

The non-equiatomic single BCC phase $Ti_{25+x}Zr_{25}Nb_{25}Ta_{25-x}$ (x= 5, 10, 15, 20, at. %) MEAs were stabilized with increasing replacement of Ta with Ti. After homogenisation at 1200ºC, a cuboidal-like nanostructure formed in the matrix and a secondary phase precipitated at the grain boundary in the homogenized $Ta_{20}Zr_{25}Nb_{25}Ti_{30}$ (Ta20-HT) and $Ta_{15}Zr_{25}Nb_{25}Ti_{35}$ (Ta15-HT). In contrast, the homogenized $Ta_{10}Zr_{25}Nb_{25}Ti_{40}$ (Ta10-HT) and $Ta_5Zr_{25}Nb_{25}Ti_{45}$ (Ta5-HT) showed a stable single BCC solid-solution phase up to 1200ºC. In addition, both Ta20-HT and Ta15-HT exhibited a high compression yield strength, but limited ductility at room temperature. On the other hand, Ta10-HT and Ta5-HT showed excellent ductility at room temperature in both tension and compression conditions.

7.2 Future works

Based on this study, a few topics can be proposed for further studies as follows:

1. Since the MEAs studied in this thesis were fabricated from Ti, Zr, Nb, and Ta, they have the potential to be used as novel implant alloys. Consequently, their biological properties need to be characterized in the future.
2. Non-equiatomic $Ta_{10}Zr_{25}Nb_{25}Ti_{40}$ (Ta10-HT) and $Ta_5Zr_{25}Nb_{25}Ti_{45}$ (Ta5-HT) MEAs have both shown good tensile strength (>900 MPa) and tensile strain at room temperature (~22%) in the as-cast state. This implies that these alloys have the potential to be 3D-printed into intricate components or device geometries. The microstructure and mechanical properties of both alloys in the 3D-printed state should be explored in the future.
3. New alloying elements can be introduced to the non-equiatomic Ti-Zr-Nb-Ta MEAs to further improve their mechanical properties at room temperature and elevated temperatures. In addition, thermomechanical processing could be applied to these alloys to manipulate their phase stability, microstructure, and mechanical properties.